THE UNIVERSITY *of* EDINBURGH

Fundamental Solutions for Beams, Plates, and Shells Under Thermomechanical Actions

Payam Khazaeinejad

A thesis submitted for the degree of
Doctor of Philosophy (PhD)

School of Engineering
College of Science and Engineering
The University of Edinburgh
2015

Dedication

To my dear parents, Parvaneh and Bahram
for their love, support and encouragement with my studies

and

To my dear wife, Leila
whose patience and understanding made this possible

Abstract

As the engineering profession moves from prescriptive or "deemed-to-satisfy" approaches towards design methodologies based on quantification of performance, sophisticated modelling tools are increasingly needed, especially when complex combinations of demand and capacity are encountered. Recourse is invariably made to advanced computational tools to provide high fidelity solutions to large and complex problems, such as the response of structural systems or components to thermomechanical actions. Software packages based on the finite element method are most commonly used for such analyses. There are some essential prerequisites to effective use of advanced computational software for complex nonlinear problems, which are often ignored, particularly in professional practice. These include a thorough understanding of the underlying mechanics of the problem under consideration; a good appreciation of the approximation methods for modelling the problem properly (e.g. the choice between elements, continuum or structural, low or high order interpolation, degree of mesh refinement necessary and so on); and perhaps most importantly ensuring that the software is reliable and is able to reproduce established fundamental solutions to an acceptable degree of accuracy.

This thesis attempts to address most of these issues but focusses primarily on the last mentioned prerequisite and provides a range of novel and unprecedented fundamental solutions for beams, plates, and shallow shells subject to moderate or extreme thermomechanical loads such as those resulting from a fire. Geometric and material nonlinearities are included in the proposed formulations along with the most common idealised boundary conditions. Thermally induced deformations generate large displacements and require the solutions to account for geometric nonlinearity,

while material nonlinearity arises from the degradation of the material at elevated temperatures. In the context of structural performance under extreme thermal action (such as fire), a finite element procedure is employed to analytically characterise generic temperature distributions through the thickness of a structural component arising from different types of fire exposure conditions including: a "short hot" fire leading to a high compartment temperature over a relatively short duration; and a "long cool" fire with lower compartment temperatures, but over a longer duration.

Results have shown that despite the larger area under the long cool fire time-temperature curve, which traditionally represented the fire severity, the effect of the short hot fire on the nonlinear responses of beams, plates, and shallow shells is more pronounced. Also, the effect of temperature-dependent material properties is found to be more pronounced during the short hot fire rather than the long cool fire. Comparison studies have confirmed that while the current numerical and theoretical approaches for analysing of thin plates and shells are often computationally intensive, the proposed approach offers an adequate level of accuracy with a rapid convergence rate for such structures. The solutions developed can be used to: verify software used for modelling structural response to thermomechanical actions; help students and professionals appreciate the fundamental mechanics better; provide relatively quick solutions for component level analyses; and visualise internal load paths and stress trajectories in complex structural components such as composite shells that can help engineers develop deeper insights into the relevant mechanics. The formulations developed are versatile and can be used for other applications such as laminated composite or orthotropic shallow shells. A very significant by-product of developing such fundamental solutions is their potential use in the development of highly accurate hybrid elements for very efficient modelling of large problems. While this has not been fully developed and implemented in the current work, the requisite theoretical framework has been developed and reported in one of the appendices, which can be used to develop such elements and implement on an appropriate software platform.

Lay Summary

A series of novel and unprecedented studies were designed to establish robust theoretical formulations to study the nonlinear behaviour of beams, plates, and shallow shells exposed to varying regimes of external heating, while also externally loaded. The solutions developed can be used to: verify software used for modelling structural response to thermomechanical actions; help students and professionals appreciate the fundamental mechanics better; provide relatively quick solutions for component level analyses; and visualise internal load paths and stress trajectories in complex structural components such as composite shells that can help engineers develop deeper insights into the relevant mechanics. A very significant by-product of developing such fundamental solutions is their potential use in the development of highly accurate computational approaches for very efficient modelling of large problems.

Acknowledgements

I would like to express my deep gratitude and appreciation to my supervisor, Professor Asif S. Usmani, for suggesting this research problem and for his support and encouragement throughout my PhD. His kindness, enthusiasm and faith in me have been extremely helpful. The good advice, support and friendship of my co-supervisor, Professor Omar Laghrouche of Heriot-Watt University, has also been invaluable, for which I am extremely grateful. He generously gave me insightful comments and valuable suggestions. I wish to appreciate the support and encouragement provided by the former and current University of Edinburgh OpenSees Group members that I worked with, Dr Shaun Devaney, Dr Jian Zhang, Dr Yaqiang Jiang, Dr Panagiotis Kotsovinos, Dr Jian Jiang, Liming Jiang, Dr Paraveen Kamath, Xu Dai, Jiayu Hu, and Zhujun Zhang.

I would also like to convey my most sincere thanks to Elizabeth and Thomas Burns, Saadia Usmani, Andrea Costa, Daniela Zampieri, Dr Mohammadreza Ebrahimi, Jiaming Xu, Dr Doug Aitken, Dr Calos Labra, Dr Colin Brett, Dr Yu Dong, Dr Prashant Gupta, Pratap Reddy Kasina, Dr Alisdair MacLeod, Dr John Paul Morrissey, Kevin Tierney, and Jillian and Ian Devay for making the environment more enjoyable throughout the years of my studies in Edinburgh. Certainly the greatest contribution to this effort has been the support and encouragement of my family from far away. The research reported herein was financially supported by the Edinburgh Research Partnership in Engineering (ERPE) funding which is greatly acknowledged.

Declaration

This thesis is the result of my own work except where specific reference has been made to the work of others. It has not been submitted for any other degree or professional qualification. The author of this thesis (including the appendices) owns any copyright in it and he has given the University of Edinburgh the right to use such copyright for any administrative, promotional, educational and/or teaching purposes. This excludes materials already published in academic journals, for which the copyright belongs to the corresponding publisher.

Journal Publications:

- P. Khazaeinejad, P., A.S. Usmani, O. Laghrouche, 2012, Nonlinear stress analysis of plates under thermomechanical loads, *Journal of Physics: Conference Series*, 382, 012022.

- P. Khazaeinejad, A.S. Usmani and O. Laghrouche, 2014, An analytical study of the nonlinear thermo-mechanical behaviour of thin isotropic rectangular plates, *Computers and Structures*, 141, 1-8 (selected as one of the Top 25 Hottest Articles of the journal from July to September 2014).

- P. Khazaeinejad, A.S. Usmani and O. Laghrouche, 2015, Temperature-dependent nonlinear behaviour of thin rectangular plates exposed to through-depth thermal gradients, *Composite Structures*, 132, 652-664.

- P. Khazaeinejad and A.S. Usmani, 2016, On thermo-mechanical nonlinear behaviour of shallow shells, *International Journal of Non-Linear Mechanics*, in press.

- P. Khazaeinejad and A.S. Usmani, 2016, Temperature-dependent nonlinear analysis of shallow shells: A theoretical approach, *Composite Structures*, in press.

- P. Khazaeinejad and A.S. Usmani, Temperature-dependent analysis of shallow shells and plates subjected to fire induced three-dimensional thermal gradients, in preparation to submit for review and publication.

- P. Khazaeinejad and A.S. Usmani, Nonlinear analysis of heated beams: Modelling benchmarks, in preparation to submit for review and publication.

Conference Publications:

- J. Jiang, P. Khazaeinejad and A.S. Usmani, 2012, Nonlinear analysis of shell structures in fire using OpenSees, *Proceedings of the 20th UK Conference of the Association for Computational Mechanics in Engineering (ACME2012)*, March 27-28, The University of Manchester, Manchester, UK.

- P. Khazaeinejad, A.S. Usmani and O. Laghrouche, 2012, Nonlinear stress analysis of plates under thermo-mechanical loads, *Modern Practice in Stress and Vibration Analysis Conference*, August 29-31, University of Glasgow, Glasgow, UK.

- S. Devaney, P. Khazaeinejad and A. Usmani, 2013, A practical approach to large deflections of thermomechanically loaded rectangular plates, *Infrastructure and Environment Scotland 1st Postgraduate Conference*, June 3, Heriot-Watt University, Edinburgh, UK.

- P. Khazaeinejad, A.S. Usmani and O. Laghrouche, 2013, Transient thermoelastic analysis of plates by hybrid-Trefftz method, *11th International Conference on Vibration Problems*, September 9-12, Lisbon, Portugal.

- P. Khazaeinejad, 2013, Thermo-mechanical analysis of shells using a hybrid-Trefftz formulation, *Proceedings of the 15th Young Researchers' Conference*, March 14, London, UK.

- P. Khazaeinejad, A.S. Usmani, 2014, Analytical solutions for nonlinear response of plates under thermal loading, *Proceedings of the 8th International Conference on Structures in Fire (SiF'14)*, June 11-13, Shanghai, China.

- P. Khazaeinejad, A.S. Usmani and O. Laghrouche, 2014, On nonlinear thermo-mechanical response of plates, *Infrastructure and Environment Scotland 2nd Postgraduate Conference*, September 2, The University of Edinburgh, Edinburgh, UK.

- P. Khazaeinejad, 2014, Demystifying the compressive ring in slabs under fire, *Proceedings of the 16th Young Researchers' Conference*, March 5, London, UK.

- P. Khazaeinejad, X. Dai, A.S. Usmani, 2015, Analysis of heated beams: Modelling benchmarks, *The First International Conference on Structural Safety under Fire and Blast*, September 2–4, Glasgow, UK.

- P. Khazaeinejad, A.S. Usmani, 2016, Visualisation of internal structures in thin composite plates and shells, *2nd International Conference on Mechanics of Composites*, July 11–14, Porto, Portugal.

Payam Khazaeinejad

September 2015

List of Figures

List of Tables

Notations

The following abbreviations and symbols will be addressed several times throughout this thesis. Rarely occurring abbreviations and symbols are noted in the corresponding context.

Abbreviations

BC	Boundary Condition
CMA	Compressive Membrane Action
DoFs	Degrees of Freedom
FE	Finite Element
FEM	Finite Element Method
FG	Functionally Graded
HFS-FEM	Hybrid Fundamental Solution-Based Finite Element Method
HT	Hybrid Trefftz
HT-FEM	Hybrid Trefftz Finite Element Method
MLPG	Meshless Local Petrov-Galerkin Method
OpenSees	Open System for Earthquake Engineering Simulation
TDMP	Temperature-Dependency of Material Properties
TMA	Tensile Membrane Action
UDL	Uniformly Distributed Load
YLA	Yield Line Analysis

Latin Symbols

A	Cross-sectional area of the beam
a	Length of the plate or shell's rectangular planform
b	Width of the plate or shell's rectangular planform
D	Flexural rigidity
E	Elastic modulus

F	Stress function
h	Thickness of the beam, plate, or shell
I	Moment of inertia of the beam
k_{rl}	Rotational spring constant at the left end of the beam
k_{rr}	Rotational spring constant at the right end of the beam
k_t	Translational spring constant
κ	Curvature of the beam
L	Length of the beam
M	Moment resultant
N	Force resultant
m, n	Integers in the Fourier series
P_x, P_y	Reaction loads along the beam, plate, or shell boundaries
q	Intensity of uniformly distributed load
R_x, R_y, R_{xy}	Shell curvatures
t	Time variable
u	Displacement component in x direction
v	Displacement component in y direction
w	Displacement component in z direction, or Transverse deflection
x, y, z	Cartesian coordinates

Greek Symbols

α	Coefficient of thermal expansion
ε	Normal strain
γ	Shear strain
σ	Normal stress
τ	Shear stress
θ	Temperature
θ_b	Temperature at the bottom surface of the beam, plate, or shell
θ_t	Temperature at the top surface of the beam, plate, or shell
θ_{max}	Maximum temperature
ν	Poisson's ratio
$\zeta_1, \zeta_2, \zeta_3$	Curvilinear coordinates

Contents

Chapter 1

Introduction

1.1 General background

Contemporary design of engineering structures has evolved into a highly scientific art underpinned by the laws of mechanics and mathematics, and armed with an expanding array of technologies. This has led to a steady movement towards loosening the straitjacket of codes and standards enabling flexibility and encouraging creativity. Modern Eurocodes have been one of the first international codes to allow engineers to "demonstrate safety" using "alternative approaches" based on "first principles" and "advanced calculation procedures" (Eurocode, 2002). This has become known rather loosely as "performance-based design" or "performance-based engineering".

In order to implement the process of performance-based engineering, sophisticated modelling tools are increasingly needed, especially when complex combinations of demand and capacity are encountered. Catastrophic events such as the multiple collapses of the World Trade Centre on September 11, 2001, Hurricane Katrina in 2005 and the 2011 Tokyo earthquake and tsunami revealed that even the most highly developed nations were short of preparedness and foresight in their ability to cope with the effects of catastrophic events that inevitably occur from time to time. The recent failure incidents have also highlighted the importance of accurate estimation of the response of all types of infrastructure to moderate or extreme loading conditions. This can be achieved through accurate prediction of potential failure mechanisms of infrastructural elements (bridges, buildings, dams etc.) and their main structural

components (beams, plates, shells etc.) under different thermomechanical actions. According to a recent review of bridge failure statistics (Imam and Chryssanthopoulos, 2010), the most important causes leading to collapse of metallic bridges had been design errors and limited knowledge (see Figure 1.1).

Considering the enormous variability in the intensity and characteristics of hazard events, recourse is invariably made to advanced computational tools to provide high fidelity solutions to large and complex problems. Software packages based on the finite element method (FEM) are most commonly used for such analyses. There are, however, some essential prerequisites to effective use of advanced computational software for complex nonlinear problems, which are often ignored, particularly in professional practice. These include a thorough understanding of the underlying mechanics of the problem under consideration; a good appreciation of the approximation methods for modelling the problem properly (e.g. the choice between elements, continuum or structural, low or high order interpolation, degree of mesh refinement necessary and so on); and perhaps most importantly ensuring that the software is reliable and is able to reproduce established fundamental solutions to an acceptable degree of accuracy.

Suitably inspired by this need, this thesis attempts to address most of these issues but focuses primarily on the last mentioned prerequisite and provides a range of novel and

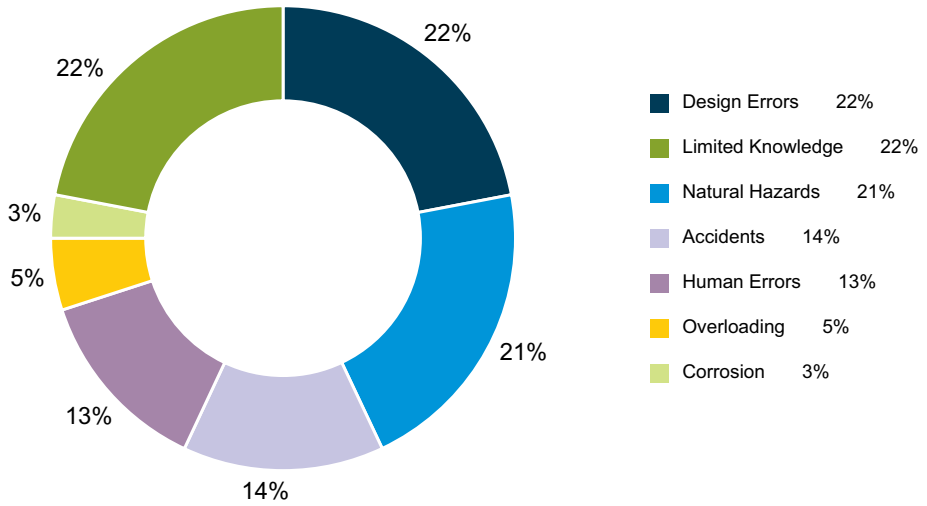

Figure 1.1 Key factors contributing to collapse of metallic bridges (Imam and Chryssanthopoulos, 2010). The majority of these collapses has occurred in the USA (36%) and UK (20%).

unprecedented fundamental solutions for beams, plates, and shallow shells subject to moderate or extreme thermomechanical actions such as those resulting from a fire.

1.2 Research motivation

The following observations provided the inspiration for the current research:

- Full-scale fire tests (Gillie *et al.*, 2004) have clearly demonstrated that slabs may be able to support loads much higher than those predicted by the well-established Yield Line Analysis (YLA) (up to 4 times when compressive membrane action (CMA) can be mobilised (Johansen, 1962)).

- The rich theory of classical numerical methods such as weighted residual and Rayleigh-Ritz, which are the foundations of the powerful FEM, suggests that a good approximation method for estimating structural forces and deformations depends upon using trial functions that are able to represent the deformed geometry of a structure as closely as possible. In this context the use of YLA for large deflection analysis of slabs subjected to thermal gradients may not have adequate mathematical justification as YLA is really only applicable under the assumption of very small displacements, which is almost never the case with floor slabs subjected to flashover fires. However, YLA may have some practical engineering justification for purposes of expediency as many engineering solutions for large displacements membrane dominated behaviour of slabs in fire have been proposed and are being used within certain limitations (see e.g., Bailey (2001) and Bailey (2004)).

- The change of shape of a slab because of significant thermal bowing in fire allows the tensile membrane action (TMA) to occur more naturally resulting in enhanced load-carrying capacity, even if there is loss of strength (Usmani *et al.*, 2000; Gillie *et al.*, 2002).

- Recently published books (see e.g., Qin (2000) and Wang *et al.* (2014)) and articles (see e.g., Qin (2005b), Dang and Hung (2013), Mohamed *et al.* (2013), and Cao and Qin (2015)) have raised the awareness of the engineering community towards benefits of employing hybrid-type computational approaches to

address the most complex engineering problems effectively. Such approaches permit avoiding important limitations of the conventional FEMs, as reported in Appendix A. Fundamental based solutions have been commonly used to construct advanced basis functions for such approaches.

1.3 Research objectives

The principle objective of this research is to develop a range of consistent methodologies to deal with structural nonlinearities in common structural components under thermomechanical actions. This is also important for understanding the mathematical underpinnings of engineering concepts such as the "thermal snap-through" and "thermal snap-back" in shells undergoing large thermomechanical displacements and the "compressive ring" supporting TMA in slabs in fire which has been experimentally recognised as an important load-carrying mechanism (Usmani *et al.*, 2000). In the first step, which is presented in this thesis, high quality fundamental solutions are developed for beams, plates, and shallow shells subject to moderate or extreme thermomechanical actions. These solutions can later be used as advanced basis functions to develop highly accurate hybrid elements for very efficient modelling of large and complex structures.

1.4 Significance of the current research

In most engineering structures, there are circumstances where structural components are exposed to non-uniform thermal gradients, while externally loaded. The most common applications are oil platforms or large compartments in buildings which are occasionally subjected to fire conditions, or aerospace vehicles which are subjected to aerodynamic heating upon reentry into the earth atmosphere. Such loading conditions typically induce two effects on the structures; deformation or geometry change (due to thermal expansion) and reduction of strength and stiffness of the structures (due to material degradation). As a consequence, there are two concurrent actions associated with thermally induced displacements and load induced displacements. At an early stage of thermal exposure, the structural behaviour is dominated by the latter, however, close to structure failure when material properties have significantly degraded, it is dominated by the former.

Such a mechanism was proposed by Usmani *et al.* (2003) to explain how and why the Twin Towers of the World Trade Center in New York collapsed as a result of the terrorist attack. However, full exploitation of the new understanding developed from that research and other relevant research in this area requires further more detailed investigations on the nonlinear response of shell structures to more realistic thermomechanical loads, so it could lead to designing safer structures. The research presented in this thesis is an attempt to address this issue for beams, plates, and shells as the most common structural components. It is novel in the following aspects:

- The current study accounts for the effect of the degradation of material properties at elevated temperatures. This effect is largely ignored in most nonlinear formulations in the literature.

- It considers thermal gradients in shell structures that represents a wide range of fire exposures, including a "short hot" fire leading to a high compartment temperature over a relatively short duration; and a "long cool" fire with lower compartment temperatures, but over a longer duration.

- It provides relatively quick solutions for component level analyses. This is vital when computational effort, mostly in terms of analyst effort, is a concern, or when an alternative approach is required to validate and corroborate the results from more rigorous numerical analyses or experimental tests.

- It can bridge the gap between the theory and black box software in order to understand the mechanics of highly deformable beams, plates, and shallow shells. The mathematical fundamentals of software packages have been underpinned mainly by FEM. These packages are used as black boxes and often their inputs and outputs are obscured by fancy GUIs which maybe convenient but it is also pedagogically counterproductive. The solutions developed in this thesis should help students and professionals appreciate the fundamental mechanics better.

- It can assist developers of performance-based engineering frameworks such as OpenSees (an open source software framework designed at University of California, Berkeley, for simulating nonlinear response of structures to earthquakes)

by supplying a hereto unavailable data set with which to validate models. This is particularly helpful since a wide range of solutions available in the literature are not easy to use for such purposes.

- The formulations developed are versatile and can be used for other applications, such as visualising internal load paths and stress trajectories in laminated composite or functionally graded (FG) orthotropic plates and shells that can help engineers develop deeper insights into the relevant mechanics.

- A very significant by-product of developing such fundamental solutions is their potential use in the development of highly accurate hybrid elements for very efficient modelling of large problems. For example, in earthquake engineering simulations of structural frames, the floor plates are usually modelled as a rigid diaphragm resulting in a massive reduction in the number of degrees of freedom (DoFs) required, thus making the simulation of large whole building frames possible. This is not possible in the simulation of frames under fire action as the deformations in the floor plate (especially where it is exposed to fire) must also be simulated accurately, thus requiring an adequate number of shell elements for modelling the floor plate. This problem will be exacerbated considerably in the context of performance-based engineering where travelling fires may be considered (Stern-Gottfried and Rein, 2012) to the extent where a large scale simulation would become prohibitively expensive. However, if hybrid elements based on fundamental solutions are used, the additional number of DOFs required could be brought to the level where structural fire simulations would not be much more expensive than seismic response simulations. While this idea has not been fully developed and implemented in the current work, the requisite theoretical framework has been developed and reported in Appendix A, which can be used to develop such elements and implement on an appropriate software platform.

1.5 Outline of the thesis

This thesis comprises nine chapters. Following this introductory chapter, in Chapter 2, a brief account of key concepts that are the foundation for the remaining chapters is given. Those concepts include the structural nonlinearities, the temperature-

dependency of material properties (TDMP), FG materials, OpenSees software framework, and the verification and validation. Chapter 3 describes fundamental theories governing thin beam, plate, and shell problems, including the corresponding kinematic relations and constitutive equations. Knowledge of these theories are deemed necessary to understand the mechanics of structural components as they form the basis for the nonlinear formulations.

In Chapter 4, a mathematical model is developed for the geometrically nonlinear analysis of beams subject to thermomechanical loads. The most common idealised boundary conditions (BCs) for single beam elements in frame structures are considered in the analysis. In the context of structural performance under extreme thermal action (such as fire), a finite element procedure is employed to analytically characterise generic temperature distributions through the thickness of the beam arising from different types of fire exposure conditions including: a “short hot” fire leading to a high compartment temperature over a relatively short duration; and a “long cool” fire with lower compartment temperatures, but over a longer duration. Results obtained from OpenSees are also presented for comparison.

Chapter 5 deals with the geometrically nonlinear analysis of rectangular plates. A set of nonlinear equations are solved simultaneously assuming quasi-static conditions to determine the plate responses to through-depth temperature fields and/or transverse mechanical loadings. The plate is assumed to be unrestrained or restrained against lateral translation (in the plane of the plate) at all boundaries and free to rotate about the axes coincident with each boundary. Results are validated extensively and their accuracy is measured against reliable solutions. Comparison is also made with results obtained from OpenSees. Chapter 6 is devoted to the development of accurate theoretical studies of solving geometrically and materially nonlinear problems of thin rectangular plates subject to different thermal and/or mechanical loadings. For the mechanical loading of the plate, a transverse load is assumed, while for the thermal loading, a full non-uniform temperature field across the surface and through the depth of the plate is considered. The material nonlinearity arises from the degradation of the material at elevated temperatures. Several examples related to nonlinear analysis of plate structures are solved, including examples for plates with laterally restrained

and unrestrained BCs under uniformly distributed loads (UDLs) or extreme thermal actions (such as short hot and long cool fire conditions). The evolution of the shape of the compressive zone supporting TMA in laterally unrestrained plates under large displacements is also graphically illustrated, while also considering nonlinear and temperature-dependent material behaviour.

In Chapter 7, a nonlinear mathematical model is presented for large displacement analysis of shallow shells with single and double curvatures (i.e. shallow cylindrical, spherical, and hyperbolic paraboloidal shells) under through-depth thermomechanical actions. Similar to the plate analysis, two limiting cases are considered for the shell BCs, assuming the shell edges to be either unrestrained or restrained against lateral translation, while rotations parallel to the shell boundary are assumed to be free. The validity and reliability of the proposed approach is assessed by considering several numerical examples for shallow shells under thermal and/or mechanical loads. In Chapter 8, the shallow shell formulation is further developed to account for the material nonlinearity arising from degradable material behaviour at elevated temperatures. Results are presented for shallow shells with either the laterally unrestrained or restrained BC under uniformly distributed loads (UDLs) or extreme thermal actions (such as short hot and long cool fire conditions).

Finally, the thesis closes in Chapter 9 with conclusions and a number of recommendations for future research on the topic. Suggestions are also made for possible further works to benefit from combination of the advantages of the solutions developed in this thesis and advanced FE approaches.

Chapter 2

Preliminary Concepts

2.1 Introduction

In the formulation of structural engineering problems, two theories are basically used: small deformation theory and large deformation theory. In the small deformation theory, the deformation of a structure is assumed to remain small (infinitesimal) even with increasing loading, therefore the geometry of the structure is assumed to remain unchanged before and after loading. Nevertheless, this theory provides good approximation for stress analysis of structures made of relatively stiff elastic materials. The large deformation theory, however, investigates circumstances under which a structure exhibits a nonlinear behaviour, while resisting the applied loads. In such circumstances, if the applied loads on the structure continuously increase, this may lead to a reduction of the strength and stiffness of the structure and development of large displacements, leading to the failure of the structure under the most severe cases of loading. This clearly increases the complexity of the structural analysis. The nonlinearity in structures is typically seen as a combination of various structural nonlinearities.

2.2 Structural nonlinearities

The structural nonlinearities can arise from a number of causes and therefore should be addressed in the design of structures. The most common types of structural nonlinearities encountered in solid and structural problems are geometric nonlinearity, boundary nonlinearity, and material nonlinearity. These are highlighted in the so-

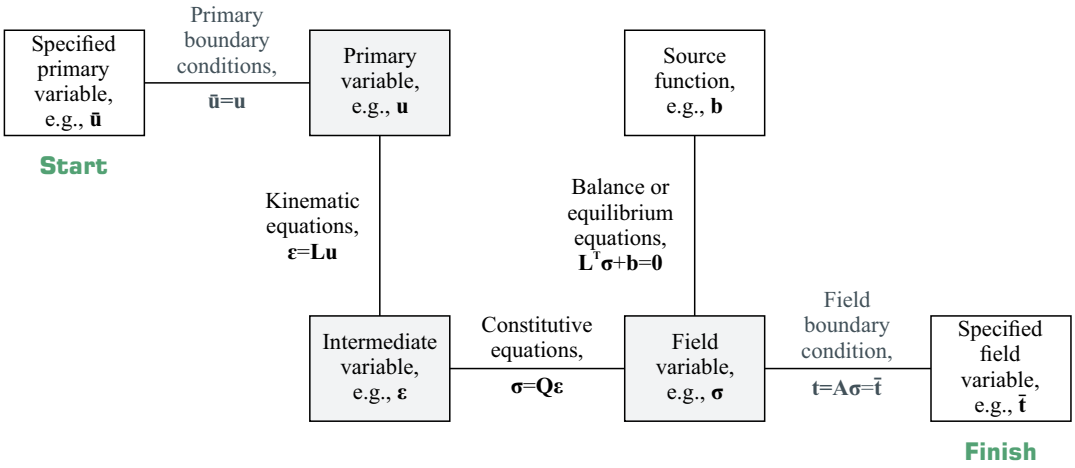

(a) Classification of variables and fields

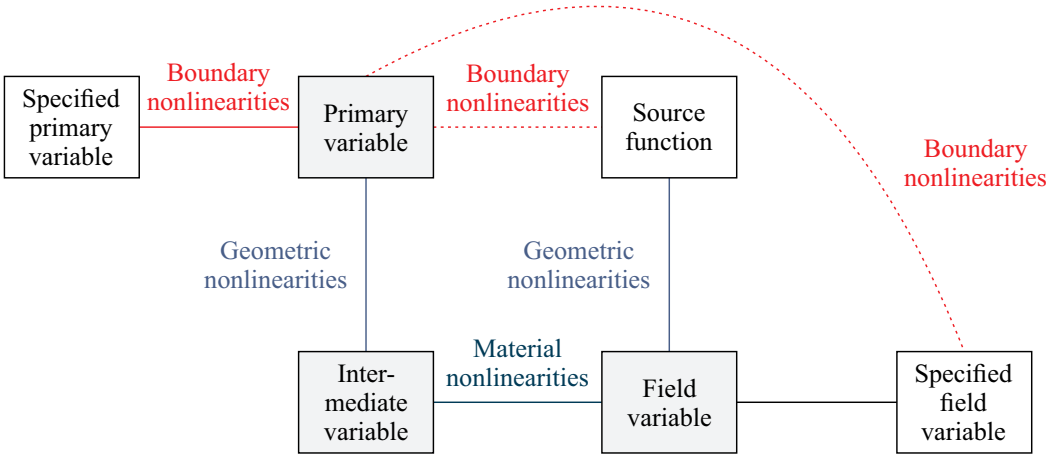

(b) Depiction of common sources of nonlinearities

Figure 2.1 Typical Tonti diagrams in nonlinear solid and structural mechanics problems. Quantities $\mathbf{u}$, $\bar{\mathbf{u}}$, $\boldsymbol{\varepsilon}$, $\boldsymbol{\sigma}$, $\mathbf{b}$, $\mathbf{t}$, and $\bar{\mathbf{t}}$ denote vectors of generalised displacements, prescribed displacements, strains, stresses, body forces, traction, and prescribed traction, respectively; $\mathbf{L}$, $\mathbf{Q}$, and $\mathbf{A}$ are differential operator matrix, constitutive coefficient matrix, and transformation matrix, respectively.

called Tonti diagrams in Figure 2.1 for solid and structural mechanics problems. The structural nonlinearities often preclude employing mathematical models to solve complex nonlinear structural problems. Their concepts are discussed in more detail in the following subsections.

2.2.1 Geometric nonlinearity

Geometric nonlinearity in a structure stems from a significant change in the geometry of the structure. When the magnitude of the maximum displacements of the structure is so large that the assumptions of the small deformation theory are no longer valid,

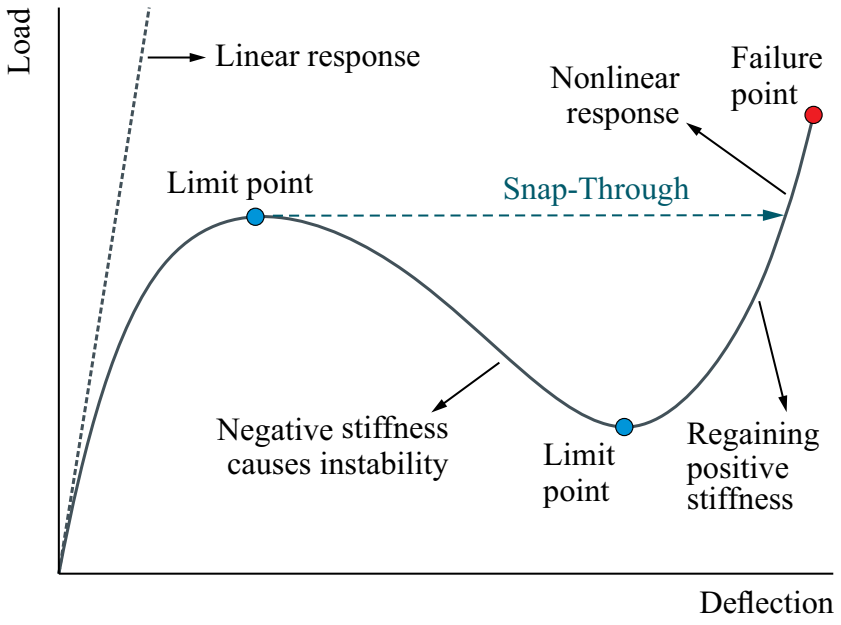

(a) Snap-Through instability

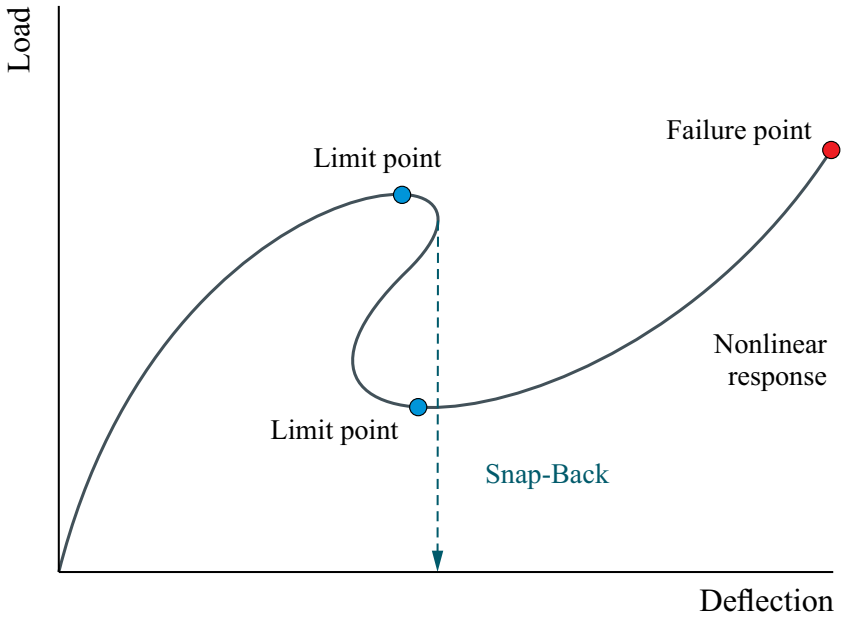

(b) Snap-Back instability

Figure 2.2 Typical response patterns in structural mechanics problems. At limit points the structure's stiffness is dramatically decreased due to increasing load.

recourse to a large displacement theory is then required. It may also be required to account for the effects of membrane forces and coupling between the axial forces and displacements of the structure. Mathematically this nonlinearity appears in the kinematic equations which relate the strain tensor to the displacement field.

Figure 2.2 shows such response patterns in structural mechanics problems. As shown in this figure, in a nonlinear system the structure may snap between two states, either

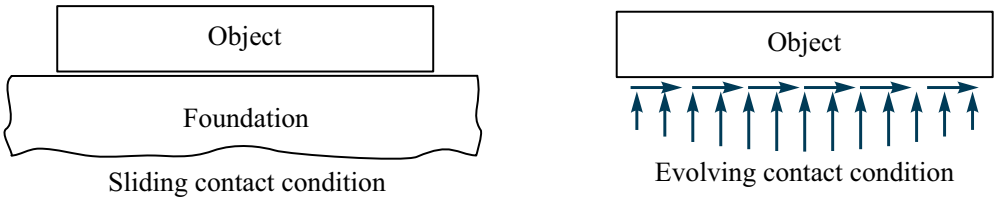

Figure 2.3 Demonstration of the boundary nonlinearity in a contact mechanics problem. At sliding contact condition, a new condition implies at the contact boundary. This condition then changes with deformation.

using a “snap-through” or a “snap-back” instability mechanism. These phenomena are often seen in loaded shell structures. However, these topics are beyond the scope of this study and therefore are not presented in this thesis. It should also be noted that there may be circumstances where large displacements are associated with plastic deformations, but in the present study, it is assumed that large displacements remain within the elastic (but not necessarily linear) range.

2.2.2 Boundary nonlinearity

Boundary nonlinearity may arise from a change in boundary or initial conditions of a structure. In such cases, boundary or initial conditions depend upon the deformation of the structure. The most common examples of the boundary nonlinearity are seen in contact mechanics problems, as illustrated in Figure 2.3. It is often argued that this type of nonlinearity can be classified as a geometric nonlinearity since any movement in the boundaries of a structure may be related to the geometry or deformation of the structure. This type of nonlinearity is not considered in this research.

2.2.3 Material nonlinearity

Material nonlinearity occurs when the material behaviour in an engineering system is either nonlinear elastic, elasto-plastic, or visco-elastic, as shown in Figure 2.4 for a one-dimensional spring device. Unlike linear systems, the stiffness matrix of a nonlinear system is not constant and may change with the deformation of the system. In the case of nonlinear elastic materials, the stress-strain behaviour is nonlinear even at small strains. For various hyperelastic material models, however, the stress-strain curves are nonlinear at moderate to large strains.

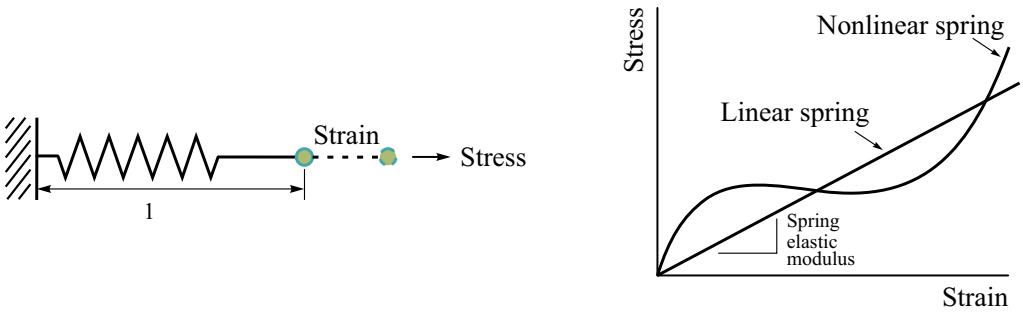

(a) Linear and nonlinear elastic spring models

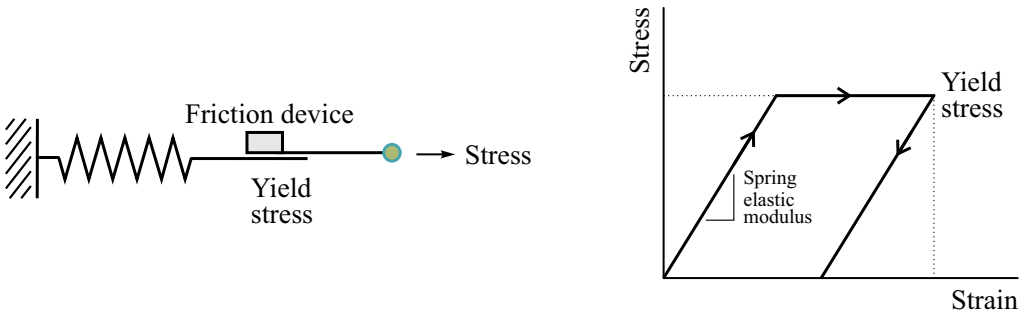

(b) An elasto-plastic spring model

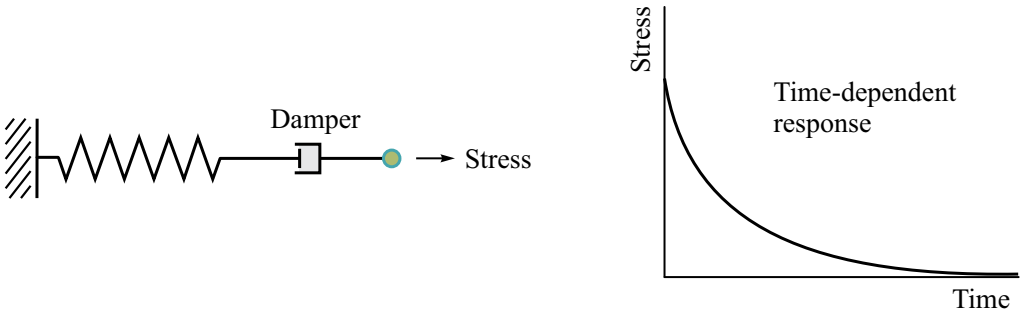

(c) A visco-elastic spring model

Figure 2.4 Demonstration of the material nonlinearity models using a one-dimensional spring device. The figure is adapted from Kim (2015). Both the length and cross-sectional area of the device are assumed to be unitary, hence displacement is replaced with strain and applied load is replaced with stress.

In structures where severe thermal loading (high temperature) is present, consequent material nonlinearity may need to be included in the formulation. In this thesis, the elastic material nonlinearity arising from the change of material properties with temperature will be considered, as discussed in the next section.

2.3 Temperature-dependency of material properties[1]

In order to determine the actual load-carrying capacity of structures, variation in mechanical and thermal properties of the material at elevated temperatures should be considered in the structural analysis. This requires appropriate expressions in the formulation to account for the nonlinear behaviour of material properties at elevated temperatures. Eurocode (2005) provides empirical data for the reduction in the stiffness of structural steel (see Appendix B) and concrete (see Appendix C) as two common constructional materials at elevated temperatures, whereas Australian Standards give the following expressions for the elastic modulus of structural steel (Standards Australia, 1998)

$$E(\theta) = E_0 \begin{cases} 1 + \frac{\theta}{2000 \ln \frac{\theta}{1100}}, & 0^\circ\text{C} < \theta \leq 600^\circ\text{C} \\ \frac{690\left(1-\frac{\theta}{1000}\right)}{\theta - 53.5}, & 600^\circ\text{C} \leq \theta \leq 1000^\circ\text{C} \end{cases} \tag{2.1}$$

and for the elastic modulus of concrete (Standards Australia, 2001)

$$E(\theta) = E_0 \begin{cases} 1, & 0^\circ\text{C} \leq \theta \leq 60^\circ\text{C} \\ \frac{720-\theta}{660}, & 60^\circ\text{C} \leq \theta \leq 720^\circ\text{C} \end{cases} \tag{2.2}$$

where in both expressions E_0 is the elastic modulus of the corresponding material at ambient temperature and $E(\theta)$ is its corresponding modulus at elevated temperature. The dependence of temperature on the Poisson's ratio could be considered negligible, hence in this thesis it is assumed equal to 0.3 unless otherwise stated. In Figures 2.5a and 2.5b, acquired data for the elastic modulus from both standards are plotted for comparison. Suitable curves are constructed in these figures to have the best fit to the series of data points provided. The corresponding mathematical expressions for these curves are

$$E(\theta) = E_0 \exp\left[-\left(\frac{\theta - 54.6}{523.8}\right)^2\right] \tag{2.3}$$

for steel and

$$E(\theta) = E_0 \exp\left[-\left(\frac{\theta - 52.06}{532}\right)^2\right] \tag{2.4}$$

for concrete.

[1] Based on the work reported by Khazaeinejad *et al.* (2015)

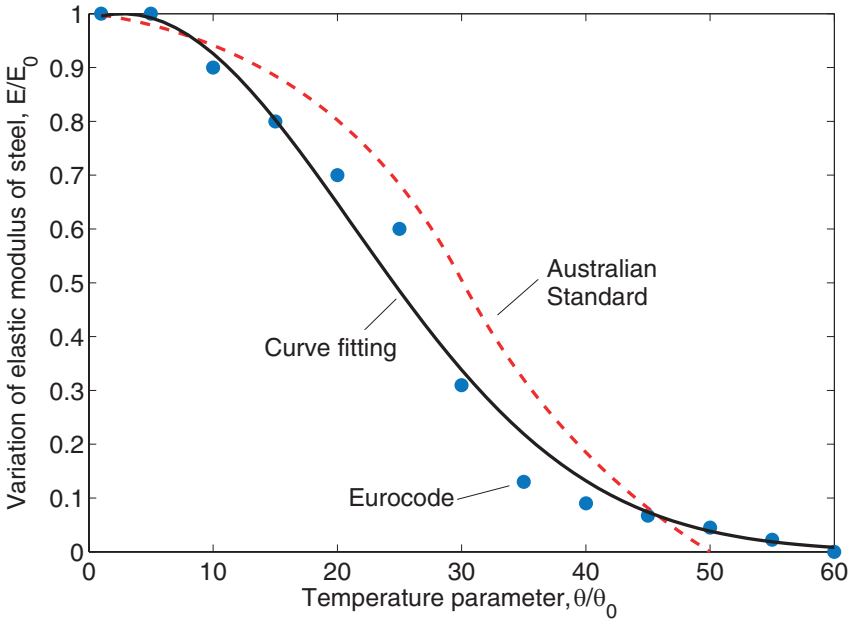

(a) Structural steel

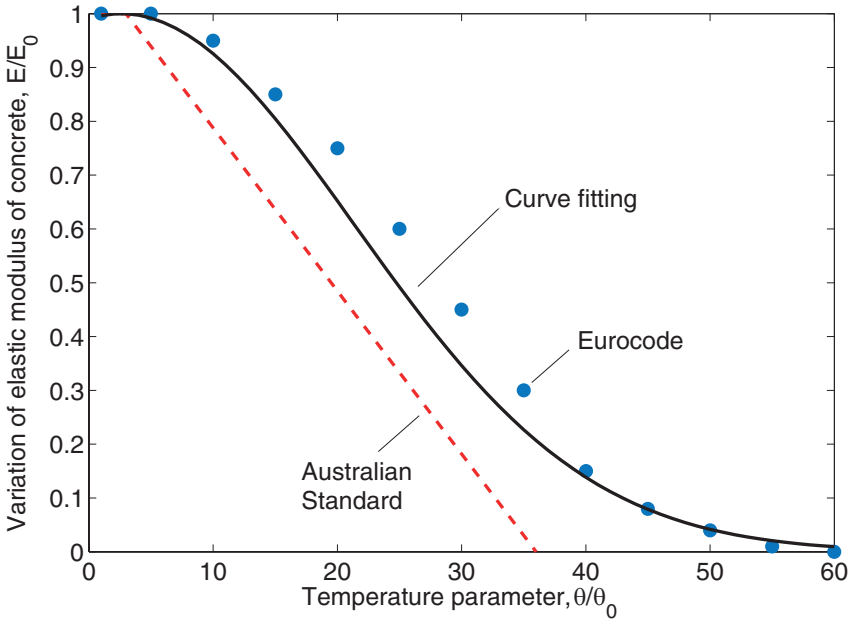

(b) Concrete

Figure 2.5 Degradation of elastic modulus at elevated temperatures for structural steel and concrete. The elastic modulus rapidly decreases with temperature for both materials.

The coefficient of thermal expansion of lightweight concrete is constant and equal to $8 \times 10^{-6}(1/^{\circ}\mathrm{C})$, but no expression is reported in Eurocode and Australian Standard for the variation of the coefficient of thermal expansion of steel and normal weight concrete with temperature. Nevertheless, the first derivative of the thermal elongation given in Eurocode (2005) can be used to obtain an expression representing the

reduction of the coefficient of thermal expansion at elevated temperatures. Such an expression is therefore obtained as

$$\alpha(\theta) = \begin{cases} 1.2 \times 10^{-5} + 0.8 \times 10^{-8}\theta, & 20^{\circ}\text{C} < \theta \leq 750^{\circ}\text{C} \\ 0, & 750^{\circ}\text{C} < \theta \leq 860^{\circ}\text{C} \\ 2 \times 10^{-5}, & 860^{\circ}\text{C} < \theta \leq 1200^{\circ}\text{C} \end{cases} \tag{2.5}$$

for steel and

$$\alpha(\theta) = \begin{cases} 9 \times 10^{-6} + 6.9 \times 10^{-11}\theta^2, & 20^{\circ}\text{C} \leq \theta \leq 700^{\circ}\text{C} \\ 0, & 700^{\circ}\text{C} < \theta \leq 1200^{\circ}\text{C} \end{cases} \tag{2.6}$$

for normal weight concrete. In both expressions, α_0 is the coefficient of thermal expansion of the corresponding material at ambient temperature and $\alpha(\theta)$ is its counterpart at elevated temperature. As shown in Figures 2.6a and 2.6b, the coefficient of thermal expansion increases smoothly for structural steel and dramatically for normal weight concrete with temperature. It drops to zero as for steel it undergoes phase change from ferrite-pearlite microstructure to a high temperature phase called austenite and for normal weight concrete it is due to a phase change arising from loss of chemically bound water at high temperatures. To improve the TDMP of structural components in thermal environment, functionally graded materials are commonly used.

2.4 Functionally graded materials

The concept of FG material was first introduced in Japan in 1984 as a thermal barrier material capable of withstanding a surface temperature of 2000 Kelvin and a temperature gradient of 1000 Kelvin across a cross section less than 10 mm (Koizumi, 1997). Since then it has been widely used to analyse various types of structures in thermal environments. A typical FG material is compositionally graded from a refractory ceramic to metal.

Due to lack of adequate information about the geometry of particles in composite materials, their effective properties are often evaluated based on the volume fraction of constituents and the size and shape of the dispersed phase (Vel and Batra, 2002). Accordingly, various models are proposed to represent the volume fraction of

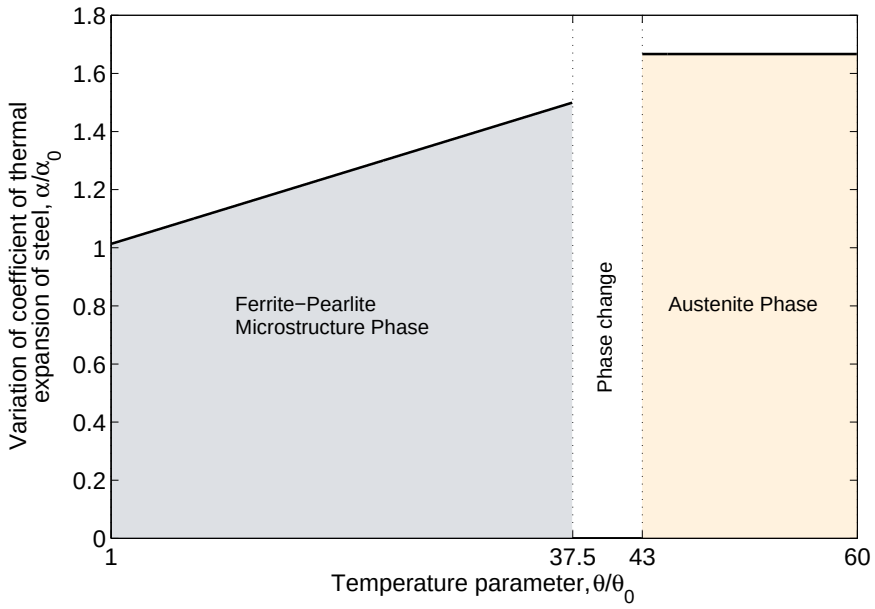

(a) Structural steel

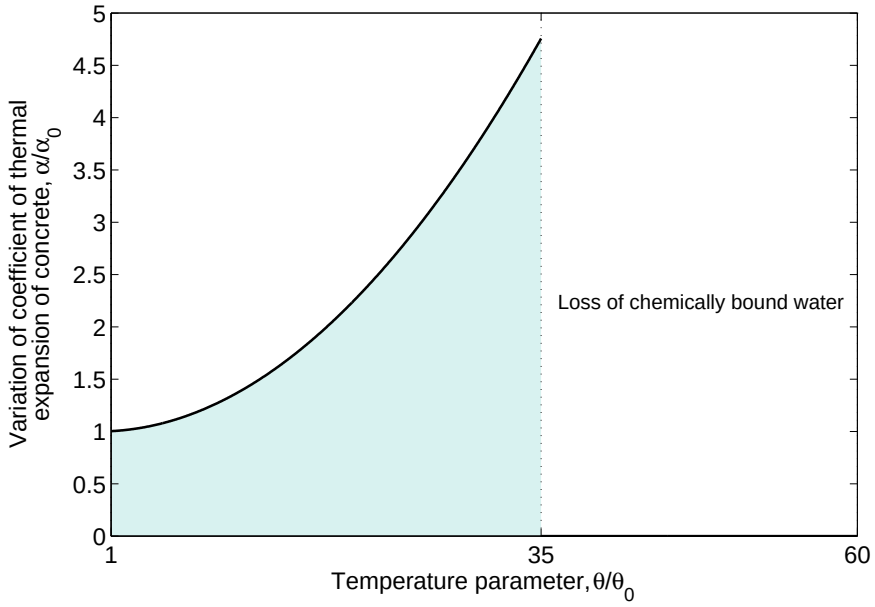

(b) Concrete

Figure 2.6 Degradation of coefficient of thermal expansion at elevated temperatures for structural steel and concrete. For both materials, the coefficient of thermal expansion increases with temperature.

constituents in FG materials such as the self-consistent method (Hill, 1965), the Mori-Tanaka scheme (Mori and Tanaka, 1973), the exponential distribution (Khazaeinejad and Najafizadeh, 2010), and the power-law distribution (Reddy, 2000; Javaheri and Eslami, 2002; Najafizadeh *et al.*, 2009; Khazaeinejad *et al.*, 2010; Najafizadeh *et al.*,

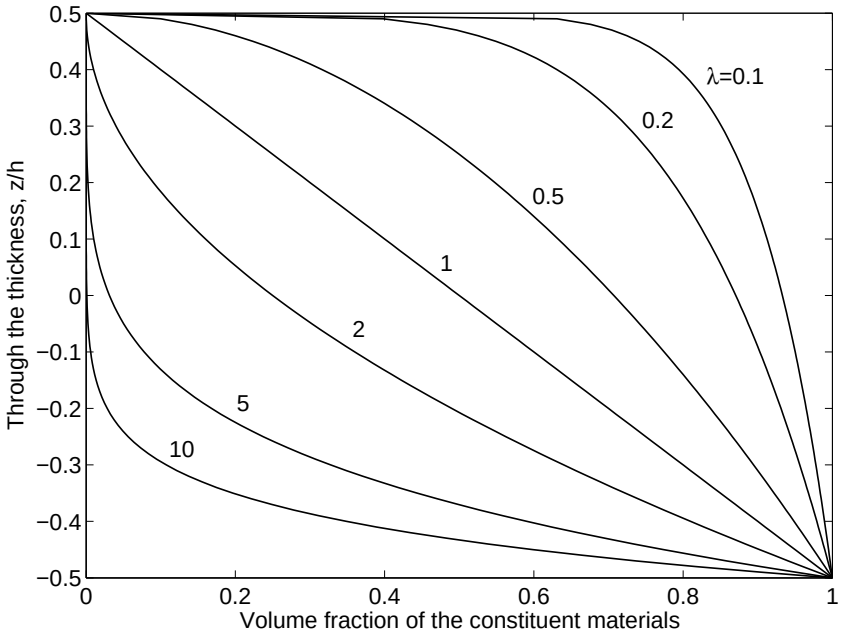

Figure 2.7 Variation of the volume fraction of an FG material in the thickness direction of a structural component. The volume fraction index is indicated by λ.

2010). In the latter which is most commonly used in the literature the volume fraction of a FG structural component varies through its depth by the following expression

$$V = \left(\frac{1}{2} - \frac{z}{h}\right)^{\lambda} \tag{2.7}$$

where $\lambda(\geq 0)$ denotes the volume fraction index. The variation of this function over the thickness is shown in Figure 2.7 for a range of volume fraction indices. The effective material property P of an FG material is then expressed either as

$$P(\theta, z) = (P_t - P_b)V + P_b \tag{2.8}$$

in which $P = P_b$ at $z = h/2$ and $P = P_t$ at $z = -h/2$, or

$$P(\theta, z) = (P_b - P_t)V + P_t \tag{2.9}$$

in which $P = P_t$ at $z = h/2$ and $P = P_b$ at $z = -h/2$. In equations (2.8) and (2.9), P represents an arbitrary material property such as elastic modulus or coefficient of thermal expansion, and P_t and P_b denote the material properties of the top and bottom surfaces of the structural components, respectively.

Table 2.1 Coefficients of temperature for a range of popular materials (Reddy and Chin, 1998)

Quantity	Coefficients				
	P_0	P_{-1}	P_1	P_2	P_3
Stainless Steel (SUS304)					
E (in Pa)	201.04×10^{9}	0	3.079×10^{-4}	-6.534×10^{-7}	0
α (in 1/K)	12.330×10^{-6}	0	8.086×10^{-4}	0	0
Aluminum Oxide					
E (in Pa)	349.55×10^{9}	0	-3.853×10^{-4}	4.027×10^{-7}	-1.673×10^{-10}
α (in 1/K)	6.8269×10^{-6}	0	1.838×10^{-4}	0	0
Nickel					
E (in Pa)	223.95×10^{9}	0	-2.794×10^{-4}	3.998×10^{-9}	0
α (in 1/K)	6.8269×10^{-6}	0	1.838×10^{-4}	0	0
Zirconia					
E (in Pa)	244.27×10^{9}	0	-1.371×10^{-3}	1.214×10^{-6}	-3.681×10^{-10}
α (in 1/K)	12.766×10^{-6}	0	-1.491×10^{-3}	1.006×10^{-5}	-6.778×10^{-11}
Silicon Nitride (Si_3N_4)					
E (in Pa)	348.43×10^{9}	0	-3.070×10^{-4}	2.160×10^{-7}	-8.946×10^{-11}
α (in 1/K)	9.9209×10^{-6}	0	8.705×10^{-4}	0	0
Ti-6A1-4V					
E (in Pa)	122.56×10^{9}	0	-4.586×10^{-4}	0	0
α (in 1/K)	7.5788×10^{-6}	0	6.638×10^{-4}	-3.147×10^{-6}	0

For taking into account the TDMP in FG materials, the following expression (Touloukian, 1967) is commonly used

$$P(\theta) = P_0\left(P_{-1}\theta^{-1} + 1 + P_1\theta + P_2\theta^2 + P_3\theta^3\right) \tag{2.10}$$

where P_0, P_{-1}, P_1, P_2, and P_3 are coefficients of environment temperature θ in Kelvin (K) and are unique for each material. Typical values for these coefficients can be found in the literature (see e.g., Reddy and Chin (1998)). For common structural metals and ceramics, these values are listed in Table 2.1. By substituting the values in this table in either equation (2.8) or (2.9), depending upon the sign convention assumed in the chosen coordinates system, expressions to account for the TDMP can be obtained. These expressions are plotted in Figures 2.8 and 2.9 using the first mentioned equation. As can be seen from the figures, the elastic modulus of materials

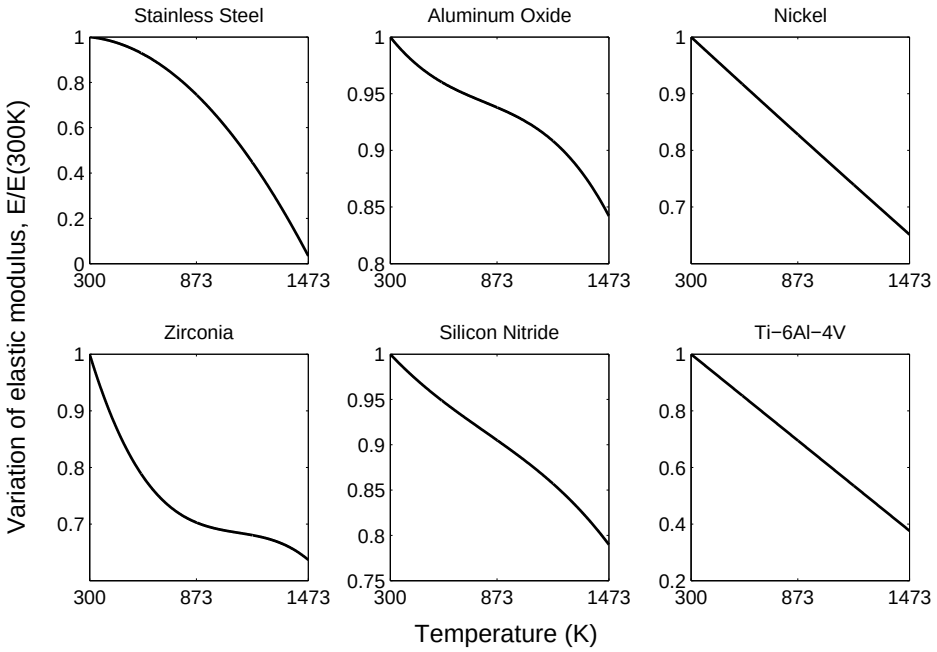

Figure 2.8 Degradation of elastic modulus for common metals and ceramics at elevated temperatures based on the model presented by Touloukian (1967).

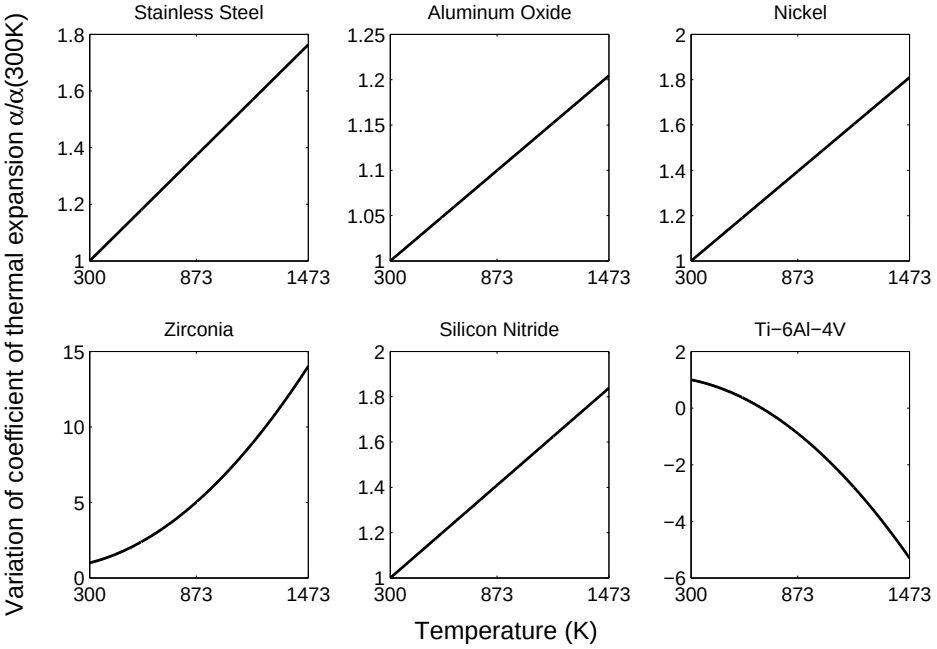

Figure 2.9 Degradation of coefficient of thermal expansion for common metals and ceramics at elevated temperatures based on the model presented by Touloukian (1967).

is reduced at high temperatures, whereas the coefficient of thermal expansion is increased at elevated temperatures.

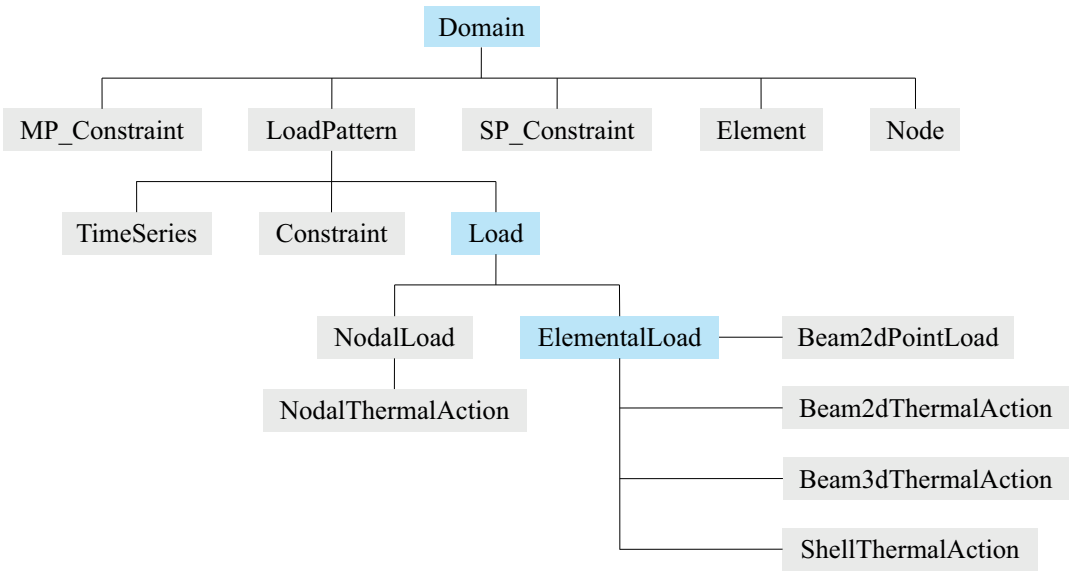

Figure 2.10 Class diagram for thermal loading in OpenSees.

Software packages based on the FEM are most commonly used for structural analysis. The OpenSees software framework will be used for comparison studies in the following chapters, therefore it is briefly introduced in the following section.

2.5 OpenSees software framework

A large number of specialist FE programs have been developed over the years to simulate the behaviour of complex structures under different thermomechanical actions. The most commonly used ones include VULCAN (Bailey, 1995), ADAPTIC (Izzuddin, 1996), and SAFIR (Franssen, 2011). In recent years, an open-source object-oriented software framework known as OpenSees (open system for earthquake engineering simulation) has attracted a rapidly growing community of users and developers. It has been initially developed at the University of California, Berkeley, with the aim of providing an advanced computational tool to simulate nonlinear response of structures to seismic excitations. For analysis of structural frames, its capabilities exceed that of commercial software in some cases. As shown in Figure 2.10, over the past years, thermal capabilities have been added to the OpenSees by developers at the University of Edinburgh.

The performance of the new developed thermal elements in OpenSees is routinely tested against analytically derived benchmark solutions (Jiang *et al.*, 2012), computer simulations (Jiang and Usmani, 2013) and experimental test results (Jiang *et al.*, 2014; Khorasani *et al.*, 2015). After verifying and validating such thermal elements, users

will be able to model structures in fire conditions through defining arbitrary non-uniform temperature distributions across and along an element, while also considering the TDMP. The verification and validation are often misunderstood as their meanings change to fit different contexts. The distinction between these two terms is briefly explained in the following section.

2.6 Verification and validation

In the context of testing, verification and validation are two different procedures which are commonly used in engineering analyses to meet the intended specifications and requirements. The former is carried out at initial stages of the development process of models and codes. The latter, however, is generally carried out after verification. In the verification process, the reliability and robustness of models and codes are checked against a series of benchmark tests and analytical solutions. As such, the solutions used for comparison are not necessarily realistic. However, validation is a procedure to estimate the accuracy of simulation software and codes against reliable sources such as real test data or rigorous computer models.

In general, the verification process ensures that computational models and codes and their associated data accurately represent the conceptual description and specifications of their developer, but validation basically determines the degree to which a model accurately represents realistic problems (Oberkampf *et al.*, 1998). Hence, the outcome of the validation process is meaningless if it is not preceded by a verification process.

Chapter 3

Fundamental Theories

3.1 Introduction

The mathematical descriptions of the mechanics of structures are reflected in fundamental theories that have been developed for various types of structural components. In structural mechanics, three general theories are used for the analysis of deformed structures:

- Infinitesimal strain theory, which is also known as small strain theory, small deformation theory, small displacement theory, or small displacement-gradient theory, can be used where the magnitude of the maximum out-of-plane displacement of a slender structural component is less than its thickness. In such circumstances, both strains and rotations are small and the coupling between axial and transverse motions is ignored. Accordingly, the load-deflection relationship may be considered linear. This theory is not capable of predicting nonlinear displacements of structures and thus is often referred to as the linear theory of structures.

- Finite strain theory, which is also known as large strain theory, large deformation theory, or large displacement-gradient theory, deals with large deflections and strains in a structure where its maximum displacements are significantly greater or of the same order of magnitude as the original dimensions of the structure.

This theory is primarily applied to forging and forming problems involving very large strains and in general not used for structural applications.

- Large displacement/rotation theory, which is a specialised version of the finite strain theory and is used for large displacements with small strains and moderate or large rotations. This theory is widely used for predicting nonlinear responses of structures under mechanical and thermal loads.

Elastic deformation theories assume that once the load has been removed the deformed structure will return to its original shape. However, there may be circumstances where the shape of a structure is permanently changed without fracture under the action of a sustained load. In such circumstances, plastic deformation theory, which is also known as plasticity, is used. The plasticity is beyond the scope of the current study and therefore in the following sections, relevant large elastic displacement theories for beams, plates, and shells are discussed.

3.2 Large displacement theory of beams

Euler–Bernoulli beam theory, which is also known as the classical beam theory, is the most commonly used theory for calculation of displacements and forces in beam problems. In spite of the fact that changes of the beam cross-sectional depth or thickness are neglected in this theory, it provides reasonable predictions for the behaviour of beams under different loading and boundary conditions. This theory is based on the following assumptions:

- Plane sections normal to the beam longitudinal axis remain plane and normal during and after the beam deformation;

- The first assumption implies that the Euler-Bernoulli theory is suitable for slender beams only where shear deformations in the beam are negligible;

- As the beam is under small displacements, geometry of the beam remains unchanged during and after the loading process.

With these assumptions, the Euler–Bernoulli beam theory is only suitable for analysing beams with small displacements. A modified version of this theory is the Timoshenko

beam theory which takes into account the effects of shear deformation and rotational inertia (i.e. resistance of a rotated beam to a change in its state or rate of rotation), making it suitable for the analysis of short beams. In this theory, plane sections normal to the beam longitudinal axis remain plane but not necessarily normal after deformation. These limitations have led to the development of refined theories such as the higher order shear deformation theories, which are beyond the scope of this study.

Under large displacements, axial (membrane) force in the beam is no longer negligible and the coupling between the axial force and the out-of-plane displacement of the beam must be considered in the beam theory. Consequently, axial BCs must be specified for the beam. The nonlinearity appears in the kinematic relations which relate the strain tensor to the displacement field.

3.2.1 Kinematic relationships

Consider a beam of uniform thickness and rectangular cross section in a Cartesian coordinates system where the x axis is along with the length of the beam (longitudinal direction), the y axis is along with the width of the beam (lateral direction), and the z axis is along with the thickness of the beam (transverse or vertical direction). Using the Timoshenko hypothesis, the displacement components of an arbitrary point in the beam can be expressed by

$$\begin{Bmatrix} \breve{u} \\ \breve{v} \\ \breve{w} \end{Bmatrix} = \begin{Bmatrix} u \\ v \\ w \end{Bmatrix} - z \begin{Bmatrix} \psi_x \\ \psi_y \\ 0 \end{Bmatrix} \tag{3.1}$$

where u, v, and w are the middle plane displacement components of the beam in the x, y, and z directions, respectively, and ψ_x and ψ_y represent the slopes (rotations) of the deformed beam.

In general, the total strain in a structural component is the sum of mechanical and thermal strains. The former is caused by stress resulting from external loads and

the latter is caused by temperature change. Using the Green's strain tensor, the strain-displacement relation for a beam can be written as

$$\varepsilon_{xx} = \frac{\partial \breve{u}}{\partial x} + \frac{1}{2}\left[\left(\frac{\partial \breve{u}}{\partial x}\right)^2 + \left(\frac{\partial \breve{v}}{\partial x}\right)^2 + \left(\frac{\partial \breve{w}}{\partial x}\right)^2\right] \tag{3.2}$$

Considering the small strain and finite rotation assumption, for moderately large displacements of beams this strain component can be rewritten as

$$\varepsilon_{xx} = \frac{\partial \breve{u}}{\partial x} + \frac{1}{2}\left(\frac{\partial \breve{w}}{\partial x}\right)^2 \tag{3.3}$$

Substituting from equation (3.1) into equation (3.3), an expression can be obtained for the normal strain of an arbitrary point in the beam

$$\begin{aligned} \varepsilon_{xx} &= \frac{\partial u}{\partial x} + \frac{1}{2}\left(\frac{\partial w}{\partial x}\right)^2 - z\frac{\partial \psi_x}{\partial x} \\ &= \frac{\partial u}{\partial x} + \frac{1}{2}\left(\frac{\partial w}{\partial x}\right)^2 - z\kappa \end{aligned} \tag{3.4}$$

The second term in the right hand side of the above equation arises from finite rotations of the beam.

Considering the assumptions of the Euler–Bernoulli beam theory (see Figure 3.1), the curvature of the beam is obtained as (Krenk, 2001)

$$\begin{aligned} \kappa &= \frac{\partial^2 w}{\partial x^2}\underbrace{\left[1 + \left(\frac{\partial w}{\partial x}\right)^2\right]^{-\frac{1}{2}}}_{\ll 1} \\ &\approx \frac{\partial^2 w}{\partial x^2} \end{aligned} \tag{3.5}$$

The thermally induced strain can be calculated by the following equation

$$\varepsilon_{xx}^{\theta} = \alpha\, \Delta\theta \tag{3.6}$$

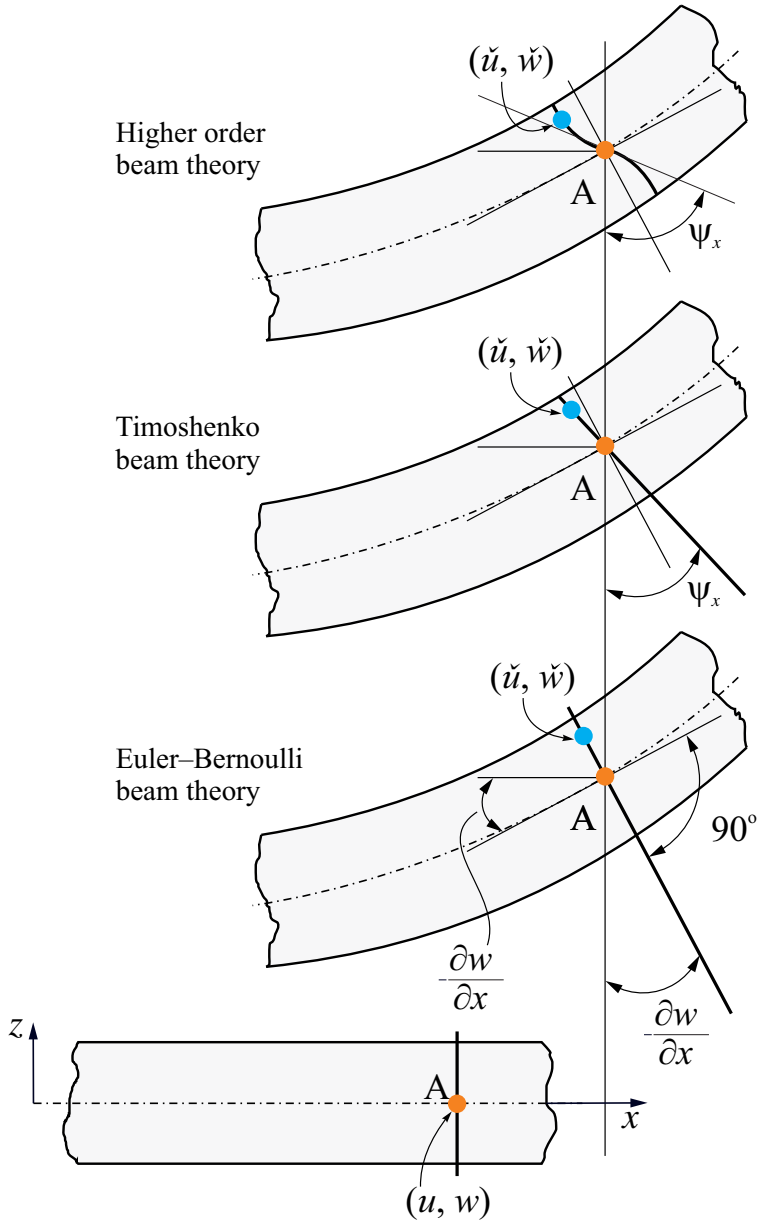

Figure 3.1 Kinematic parameters of various beam theories.

where superscript θ denotes the thermal strains, α is the coefficient of thermal expansion of the beam and $\Delta\theta$ represents the temperature changes in the beam.

As shown in Figure 3.1, according to the Euler–Bernoulli beam theory, the slopes of the deformed beam are related to the vertical (transverse) displacement of the beam as follows

$$\begin{Bmatrix} \check{u} \\ \check{v} \\ \check{w} \end{Bmatrix} = \begin{Bmatrix} u \\ v \\ w \end{Bmatrix} - z \begin{Bmatrix} \frac{\partial w}{\partial x} \\ \frac{\partial w}{\partial y} \\ 0 \end{Bmatrix} \tag{3.7}$$

3.2.2 Constitutive equations

The constitutive equation for beams under moderately large displacements are similar (but not identical) to that in the small displacement theory of beams. It can be described by the following equation for axial stress at any arbitrary point in the beam

$$\begin{aligned}\sigma_{xx} &= E\left(\varepsilon_{xx} - \varepsilon_{xx}^{\theta}\right) \\ &= E\left[\frac{\partial u}{\partial x} + \frac{1}{2}\left(\frac{\partial w}{\partial x}\right)^2 - z\kappa - \alpha\,\Delta\theta\right]\end{aligned} \tag{3.8}$$

where E is the elastic modulus of the beam. Note that, the normal and shear stresses in the y and z directions are neglected since they are small when compared to the axial stress in the beam. The resultant axial (membrane) force in the beam can be obtained by integrating the axial stress component of the beam over its cross section as follows

$$\begin{aligned}N &= \int_A \sigma_{xx}\,\mathrm{d}A \\ &= \int_A E\left[\frac{\partial u}{\partial x} + \frac{1}{2}\left(\frac{\partial w}{\partial x}\right)^2\right]\,\mathrm{d}A - \int_A E\kappa z\,\mathrm{d}A - N^{\theta}\end{aligned} \tag{3.9}$$

where N^{θ} is the thermal axial resultant which varies with temperature and is defined by

$$N^{\theta} = \int_A E\alpha\,\Delta\theta\,\mathrm{d}A \tag{3.10}$$

By integrating the resultant axial force over the thickness of the beam, the resultant bending moment of the beam is expressed as

$$\begin{aligned}M &= \int_A \sigma_{xx} z\,\mathrm{d}A \\ &= \int_A E\left[\frac{\partial u}{\partial x} + \frac{1}{2}\left(\frac{\partial w}{\partial x}\right)^2\right] z\,\mathrm{d}A - \int_A E\kappa z^2\,\mathrm{d}A - M^{\theta}\end{aligned} \tag{3.11}$$

where M^{θ} is the thermal bending moment which is temperature dependent and is defined by

$$M^{\theta} = \int_A E\alpha\,\Delta\theta z\,\mathrm{d}A \tag{3.12}$$

The aforementioned kinematic relations are used in the next chapter to derive equations governing nonlinear behaviour of beams under thermomechanical loads.

3.3 Large displacement theory of plates

Plates are typically classified as very thin when $\ell/h > 100$, moderately thin when $20 < \ell/h < 100$, and thick when $\ell/h < 20$, where ℓ and h denote the smallest in-plane dimension (length or width) and thickness of the plate, respectively. From numerous plate theories that have been developed for solid mechanics problems, the Kirchhoff-Love plate theory and the Mindlin-Reissner plate theory are the most widely used for analysing the plate problems. The former is the classical plate theory that neglects shear deformations and is limited to thin plate problems, while the latter, which is also known as the first order shear deformation theory of plates, takes into account the effects of transverse shear deformation and rotational inertia in plates and thus is more suitable for thick plate problems.

The classical linear theory of plates was initially introduced by Kirchhoff (1850). He proposed a mathematical formulation to describe the kinematic and constitutive relations in very thin or moderately thin plates subjected to forces and moments. Love (1888) extended the Kirchhoff's idea using the assumptions of the Euler-Bernoulli beam theory. It has been since known as the Kirchhoff-Love theory of plates. The theory could predict deformations and stresses in thin plates within the accuracy required for engineering purposes. However, it was incapable of describing the complicated states of deformation and stress in plates under large displacements. Later, the Kirchhoff-Love theory of plates was extended by von Kármán (1910) to include geometric nonlinearity in the plate problems. The von Kármán nonlinear theory of plates was applicable to situations where moderate rotations exist. The Kirchhoff–Love plate theory was extended for thick plates by Reissner (1945) and Mindlin (1951). In the so called Reissner-Mindlin plate theory, which is also known as the first order shear deformation theory of plates, shear deformations through the depth of the plate are considered.

3.3.1 Basic assumptions

The fundamental assumptions of the Kirchhoff-Love plate theory are:

- The deflection (the normal component of the displacement vector) of the middle surface of the plate is small when compared to the thickness of the plate. Therefore, the slope of the deflected surface is very small and as a consequence, the square of the slope is negligible in comparison with unity;

- Due to the small displacements of the plate, the middle surface remains unstrained subsequent to bending;

- The straight through-depth lines, initially normal to the middle surface plane before bending, remain unchanged and normal to that plane after deformation. As such, the out-of-plane shear strains are negligible and the normal strain in the thickness direction may also be omitted.

Under severe thermomechanical actions, the magnitude of the maximum displacement of the middle surface of a plate might exceed its thickness, though small in comparison to the other plate dimensions. In such circumstances, the plate structural response may change from linear to nonlinear. As a result, the plate experiences large displacements which requires using appropriate strain definitions, including mechanical and thermal strains. These strains should account for the stretching of the middle surface of the plate. Therefore, the first two assumptions of the classical plate theory are invalid and must be replaced with the following assumptions:

- The out-of-plane displacement of the middle surface of the plate is substantially greater than or of the same order as its thickness. Therefore, the slope of the deflected surface is considerable;

- Since the displacements of the plate are large, significant strains are generated in the middle surface of the plate after bending.

In such circumstances, the von Kármán nonlinear theory of plates (Timoshenko and Woinowsky-Krieger, 1959) is commonly used as a suitable theory.

3.3.2 Kinematic relationships

Based on the von Kármán theory, the nonlinear strain–displacement relations of a rectangular plate (with accounting for the stretching of the middle plane of the plate) are expressed as

$$\left\{\begin{array}{c}\varepsilon_{xx}\\ \varepsilon_{yy}\\ \gamma_{xy}\end{array}\right\}=\left\{\begin{array}{c}\frac{\partial u}{\partial x}+\frac{1}{2}\left(\frac{\partial w}{\partial x}\right)^2\\ \frac{\partial v}{\partial y}+\frac{1}{2}\left(\frac{\partial w}{\partial y}\right)^2\\ \frac{\partial u}{\partial y}+\frac{\partial v}{\partial x}+\left(\frac{\partial w}{\partial x}\right)\left(\frac{\partial w}{\partial y}\right)\end{array}\right\}+z\left\{\begin{array}{c}-\frac{\partial^2 w}{\partial x^2}\\ -\frac{\partial^2 w}{\partial y^2}\\ -2\frac{\partial^2 w}{\partial x\partial y}\end{array}\right\} \tag{3.13}$$

where u, v and w are the middle plane displacement components of the plate in x, y and z directions, respectively. In most structural materials, the thermally induced strains due to heating may be obtained by

$$\left\{\begin{array}{c}\varepsilon_{xx}^{\theta}\\ \varepsilon_{yy}^{\theta}\\ \gamma_{xy}^{\theta}\end{array}\right\}=\left\{\begin{array}{c}\alpha_{xx}\\ \alpha_{yy}\\ \alpha_{xy}\end{array}\right\}\Delta\theta \tag{3.14}$$

where α_{xx}, α_{yy}, and α_{xy} are the transformed coefficients of thermal expansion of the plate which may vary with temperature and $\Delta\theta$ represents the temperature increases in the plate.

3.3.3 Constitutive equations

The constitutive relations for a plate can then be written as

$$\left\{\begin{array}{c}\sigma_{xx}\\ \sigma_{yy}\\ \tau_{xy}\end{array}\right\}=\left(\begin{array}{ccc}Q_{11} & Q_{12} & Q_{16}\\ & Q_{22} & Q_{26}\\ \text{symm.} & & Q_{66}\end{array}\right)\left\{\begin{array}{c}\varepsilon_{xx}-\varepsilon_{xx}^{\theta}\\ \varepsilon_{yy}-\varepsilon_{yy}^{\theta}\\ \gamma_{xy}-\gamma_{xy}^{\theta}\end{array}\right\} \tag{3.15}$$

in which $Q_{ij}(i,j=1,2,6)$ are the stiffness coefficients associated with the material properties. Further normal and shear stresses can be integrated with respect to the thickness of the plate to obtain the stress resultants

$$\left\{\begin{array}{c}N_{xx}\\ N_{yy}\\ N_{xy}\end{array}\right\}=\int_{-h/2}^{h/2}\left\{\begin{array}{c}\sigma_{xx}\\ \sigma_{yy}\\ \tau_{xy}\end{array}\right\}\mathrm{d}z \tag{3.16}$$

and moment resultants in the plate

$$\begin{Bmatrix} M_{xx} \\ M_{yy} \\ M_{xy} \end{Bmatrix} = \int_{-h/2}^{h/2} \begin{Bmatrix} \sigma_{xx} \\ \sigma_{yy} \\ \tau_{xy} \end{Bmatrix} z \, \mathrm{d}z \tag{3.17}$$

Substituting equations (3.13)-(3.15) into equations (3.16) and (3.17), the stress and moment resultants acting on the plate can be obtained in terms of displacement components

$$\begin{Bmatrix} N_{xx} \\ N_{yy} \\ N_{xy} \end{Bmatrix} = \begin{pmatrix} A_{11} & A_{12} & A_{16} \\ & A_{22} & A_{26} \\ \text{symm.} & & A_{66} \end{pmatrix} \begin{Bmatrix} \frac{\partial u}{\partial x} + \frac{1}{2}\left(\frac{\partial w}{\partial x}\right)^2 \\ \frac{\partial v}{\partial y} + \frac{1}{2}\left(\frac{\partial w}{\partial y}\right)^2 \\ \frac{\partial u}{\partial y} + \frac{\partial v}{\partial x} + \left(\frac{\partial w}{\partial x}\right)\left(\frac{\partial w}{\partial y}\right) \end{Bmatrix} + \begin{pmatrix} B_{11} & B_{12} & B_{16} \\ & B_{22} & B_{26} \\ \text{symm.} & & B_{66} \end{pmatrix} \begin{Bmatrix} -\frac{\partial^2 w}{\partial x^2} \\ -\frac{\partial^2 w}{\partial y^2} \\ -2\frac{\partial^2 w}{\partial x \partial y} \end{Bmatrix} - \begin{Bmatrix} N_{xx}^{\theta} \\ N_{yy}^{\theta} \\ N_{xy}^{\theta} \end{Bmatrix} \tag{3.18}$$

$$\begin{Bmatrix} M_{xx} \\ M_{yy} \\ M_{xy} \end{Bmatrix} = \begin{pmatrix} B_{11} & B_{12} & B_{16} \\ & B_{22} & B_{26} \\ \text{symm.} & & B_{66} \end{pmatrix} \begin{Bmatrix} \frac{\partial u}{\partial x} + \frac{1}{2}\left(\frac{\partial w}{\partial x}\right)^2 \\ \frac{\partial v}{\partial y} + \frac{1}{2}\left(\frac{\partial w}{\partial y}\right)^2 \\ \frac{\partial u}{\partial y} + \frac{\partial v}{\partial x} + \left(\frac{\partial w}{\partial x}\right)\left(\frac{\partial w}{\partial y}\right) \end{Bmatrix} + \begin{pmatrix} D_{11} & D_{12} & D_{16} \\ & D_{22} & D_{26} \\ \text{symm.} & & D_{66} \end{pmatrix} \begin{Bmatrix} -\frac{\partial^2 w}{\partial x^2} \\ -\frac{\partial^2 w}{\partial y^2} \\ -2\frac{\partial^2 w}{\partial x \partial y} \end{Bmatrix} - \begin{Bmatrix} M_{xx}^{\theta} \\ M_{yy}^{\theta} \\ M_{xy}^{\theta} \end{Bmatrix} \tag{3.19}$$

where the extensional, coupling, and bending stiffnesses are respectively defined by

$$\begin{pmatrix} A_{11} & A_{12} & A_{16} \\ & A_{22} & A_{26} \\ \text{symm.} & & A_{66} \end{pmatrix} = \int_{-h/2}^{h/2} \begin{pmatrix} Q_{11} & Q_{12} & Q_{16} \\ & Q_{22} & Q_{26} \\ \text{symm.} & & Q_{66} \end{pmatrix} \mathrm{d}z \tag{3.20a}$$

$$\begin{pmatrix} B_{11} & B_{12} & B_{16} \\ & B_{22} & B_{26} \\ \text{symm.} & & B_{66} \end{pmatrix} = \int_{-h/2}^{h/2} \begin{pmatrix} Q_{11} & Q_{12} & Q_{16} \\ & Q_{22} & Q_{26} \\ \text{symm.} & & Q_{66} \end{pmatrix} z \, \mathrm{d}z \tag{3.20b}$$

$$\begin{pmatrix} D_{11} & D_{12} & D_{16} \\ & D_{22} & D_{26} \\ \text{symm.} & D_{26} & D_{66} \end{pmatrix} = \int_{-h/2}^{h/2} \begin{pmatrix} Q_{11} & Q_{12} & Q_{16} \\ & Q_{22} & Q_{26} \\ \text{symm.} & & Q_{66} \end{pmatrix} z^2 \, \mathrm{d}z \tag{3.20c}$$

The quantities N_{xx}^{θ}, N_{yy}^{θ}, and N_{xy}^{θ} are thermal stress resultants which are defined by

$$\begin{Bmatrix} N_{xx}^{\theta} \\ N_{yy}^{\theta} \\ N_{xy}^{\theta} \end{Bmatrix} = \int_{-h/2}^{h/2} \begin{pmatrix} Q_{11} & Q_{12} & Q_{16} \\ & Q_{22} & Q_{26} \\ \text{symm.} & & Q_{66} \end{pmatrix} \begin{Bmatrix} \alpha_{xx} \\ \alpha_{yy} \\ \alpha_{xy} \end{Bmatrix} \Delta\theta \, \mathrm{d}z \tag{3.21}$$

The quantities M_{xx}^{θ}, M_{yy}^{θ}, and M_{xy}^{θ} are thermal moment resultants which are given by

$$\begin{Bmatrix} M_{xx}^{\theta} \\ M_{yy}^{\theta} \\ M_{xy}^{\theta} \end{Bmatrix} = \int_{-h/2}^{h/2} \begin{pmatrix} Q_{11} & Q_{12} & Q_{16} \\ & Q_{22} & Q_{26} \\ \text{symm.} & & Q_{66} \end{pmatrix} \begin{Bmatrix} \alpha_{xx} \\ \alpha_{yy} \\ \alpha_{xy} \end{Bmatrix} \Delta\theta \, z \, \mathrm{d}z \tag{3.22}$$

For elastic plates, constitutive relations introduced in equation (3.15) may be written as

$$\begin{Bmatrix} \sigma_{xx} \\ \sigma_{yy} \\ \tau_{xy} \end{Bmatrix} = \begin{pmatrix} \bar{\lambda} + 2G & \bar{\lambda} & 0 \\ & \bar{\lambda} + 2G & 0 \\ \text{symm.} & & G \end{pmatrix} \begin{Bmatrix} \varepsilon_{xx} \\ \varepsilon_{yy} \\ \gamma_{xy} \end{Bmatrix} - (3\bar{\lambda} + 2G) \begin{Bmatrix} \varepsilon_{xx}^{\theta} \\ \varepsilon_{yy}^{\theta} \\ \gamma_{xy}^{\theta} \end{Bmatrix} \tag{3.23}$$

where λ and G are the Lame constants which have the following relations with elastic modulus E and Poisson's ratio ν

$$\bar{\lambda} = \frac{2\bar{\nu}}{1 - 2\bar{\nu}} G, \qquad G = \frac{E}{2(1 + \nu)} \tag{3.24}$$

in which

$$\bar{\nu} = \begin{cases} \frac{\nu}{1+\nu}, & \text{for plane stress} \\ \nu, & \text{for plane strain} \end{cases} \tag{3.25}$$

The stress and moment resultants can then be expressed by the following equations

$$\begin{aligned} \begin{Bmatrix} N_{xx} \\ N_{yy} \end{Bmatrix} &= h\left[\frac{\partial u}{\partial x} + \frac{1}{2}\left(\frac{\partial w}{\partial x}\right)^2\right]\begin{Bmatrix} \bar{\lambda}+2G \\ \bar{\lambda} \end{Bmatrix} \\ &\quad + h\left[\frac{\partial v}{\partial y} + \frac{1}{2}\left(\frac{\partial w}{\partial y}\right)^2\right]\begin{Bmatrix} \bar{\lambda} \\ \bar{\lambda}+2G \end{Bmatrix} \\ &\quad - (3\bar{\lambda}+2G)\int_{-h/2}^{h/2}\begin{Bmatrix} \alpha\Delta\theta \\ \alpha\Delta\theta \end{Bmatrix} dz \end{aligned} \tag{3.26a}$$

$$\begin{aligned} \begin{Bmatrix} M_{xx} \\ M_{yy} \end{Bmatrix} &= -\frac{h^3}{12}\frac{\partial^2 w}{\partial x^2}\begin{Bmatrix} \bar{\lambda} \\ \bar{\lambda}+2G \end{Bmatrix} - \frac{h^3}{12}\frac{\partial^2 w}{\partial y^2}\begin{Bmatrix} \bar{\lambda}+2G \\ \bar{\lambda} \end{Bmatrix} \\ &\quad - (3\bar{\lambda}+2G)\int_{-h/2}^{h/2}\begin{Bmatrix} \alpha\Delta\theta \\ \alpha\Delta\theta \end{Bmatrix} z dz \end{aligned} \tag{3.26b}$$

$$\begin{Bmatrix} N_{xy} \\ M_{xy} \end{Bmatrix} = h\left(\frac{\partial u}{\partial y} + \frac{\partial v}{\partial x} + \frac{\partial w}{\partial x}\frac{\partial w}{\partial y}\right)\begin{Bmatrix} G \\ 0 \end{Bmatrix} - \frac{h^3}{6}\frac{\partial^2 w}{\partial x \partial y}\begin{Bmatrix} 0 \\ G \end{Bmatrix} \tag{3.26c}$$

Considering the plane stress state, the stress resultants can be obtained as

$$N_{xx} = \frac{Eh}{1-\nu^2}\left[\frac{\partial u}{\partial x} + \nu\frac{\partial v}{\partial y} + \frac{1}{2}\left(\frac{\partial w}{\partial x}\right)^2 + \frac{\nu}{2}\left(\frac{\partial w}{\partial y}\right)^2\right] - N^\theta \tag{3.27a}$$

$$N_{yy} = \frac{Eh}{1-\nu^2}\left[\nu\frac{\partial u}{\partial x} + \frac{\partial v}{\partial y} + \frac{\nu}{2}\left(\frac{\partial w}{\partial x}\right)^2 + \frac{1}{2}\left(\frac{\partial w}{\partial y}\right)^2\right] - N^\theta \tag{3.27b}$$

$$N_{xy} = \frac{Eh}{2(1+\nu)}\left[\frac{\partial u}{\partial y} + \frac{\partial v}{\partial x} + \left(\frac{\partial w}{\partial x}\right)\left(\frac{\partial w}{\partial y}\right)\right] \tag{3.27c}$$

In a similar way, the moment resultants can also be obtained as

$$\begin{Bmatrix} M_{xx} \\ M_{yy} \\ M_{xy} \end{Bmatrix} = -D \begin{Bmatrix} \frac{\partial^2 w}{\partial x^2} + \nu \frac{\partial^2 w}{\partial y^2} \\ \nu \frac{\partial^2 w}{\partial x^2} + \frac{\partial^2 w}{\partial y^2} \\ (1-\nu) \frac{\partial^2 w}{\partial x \partial y} \end{Bmatrix} - M^{\theta} \begin{Bmatrix} 1 \\ 1 \\ 0 \end{Bmatrix} \tag{3.28}$$

where D is the flexural rigidity given by $Eh^3/12(1-\nu^2)$. The aforementioned kinematic relations are used in Chapters 5 and 6 to derive equations governing nonlinear behaviour of plates under thermomechanical loads.

3.4 Large displacement theory of shells

Essentially, a shell has either a single or double curvature (curved middle surface) in comparison to a plate-type structure, therefore a flat shell is also referred to as a plate. Shell equations are much more complicated than those developed for plates, especially when geometrical nonlinearity is included in the formulation. In this thesis, the 'shallow shell' version of shell equations are considered. This is because in many shell structures under localised loadings, the region of interest can be considered as a shallow shell even if the shell itself is non-shallow (Reissner, 1946; Flügge and Elling, 1972; Olszak, 1980). A shallow shell subjected to a transverse mechanical load, produces larger displacements in comparison with non-shallow shells. As such, the large displacement theory of shells is commonly used to deal with shallow shell problems.

3.4.1 Basic assumptions

Under the assumptions of the shallow shell theory, the rise of a shallow shell is relatively small in comparison to its other dimensions (see Figure 3.2 which is adapted from Donnell (1976) and illustrates schematically the ranges of applicability of various shell theories for modelling cylindrical shells). The nonlinear theory of shallow shells was initially proposed by Marguerre (1938). Its assumptions was later modified by Reissner (1946) and Flügge and Elling (1972). Since then, Marguerre nonlinear theory of shells has been widely used to deal with geometrical nonlinearity in shells with slight curvature.

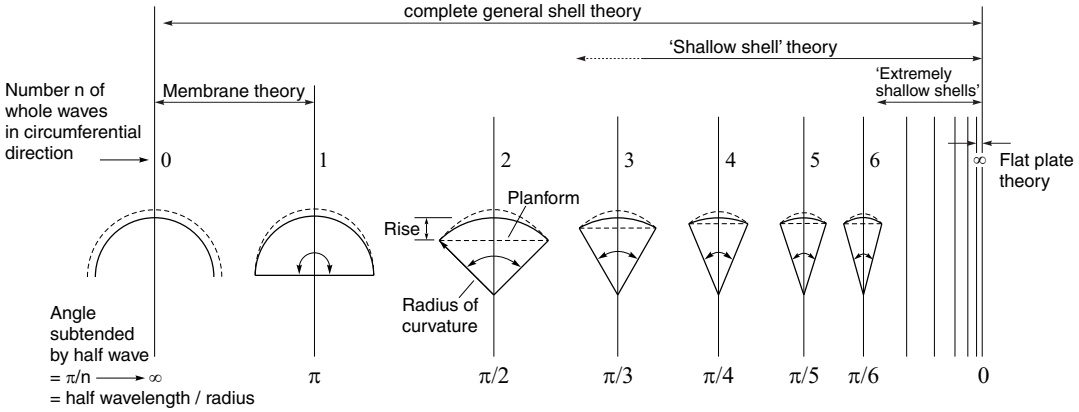

Figure 3.2 Hierarchy of various shell theories as function of their applicable ranges of subtended angle. The figure is adapted from (Donnell, 1976). In the case of 'extremely shallow shells', the minimum radius of curvature of the shell is more than two times larger than its maximum planform dimension (Qatu, 2004).

3.4.2 Kinematic relationships

In Figure 3.3, a schematic view of a shallow shell is shown. Due to its relatively small rise, the Cartesian coordinates (x, y, z) can be replaced with the curvilinear coordinates $(\zeta_1, \zeta_2, \zeta_3)$. A brief description of the Marguerre theory is given in the following (Chan and Chung, 1989). With respect to the Cartesian coordinates, the position of an arbitrary point, denoted by P in Figure 3.3, after deformation can be given by

$$\begin{aligned}\mathbf{r} &= \mathbf{r}_0 + \mathbf{U} \\ &= \begin{Bmatrix} x \\ y \\ z+\zeta \end{Bmatrix} + \begin{Bmatrix} u - z\frac{\partial w}{\partial x} \\ v - z\frac{\partial w}{\partial y} \\ w + \zeta \end{Bmatrix}\end{aligned} \tag{3.29}$$

where the first vector in the right hand side of the equation represents the position vector of point P before deformation, the second vector in the right hand side of the equation represents the displacement vector of point P, ζ is the rise of the shell, and z denotes the vertical distance of point P from the middle surface. Considering the Lagrangian description, the middle surface strain components ε_{xx}, ε_{yy} and γ_{xy} can be calculated from the following equation

$$\mathrm{d}s^2 - \mathrm{d}s_0^2 = 2\left(\varepsilon_x\,\mathrm{d}x^2 + \varepsilon_y\,\mathrm{d}y^2 + \gamma_{xy}\,\mathrm{d}x\,\mathrm{d}y\right) \tag{3.30}$$

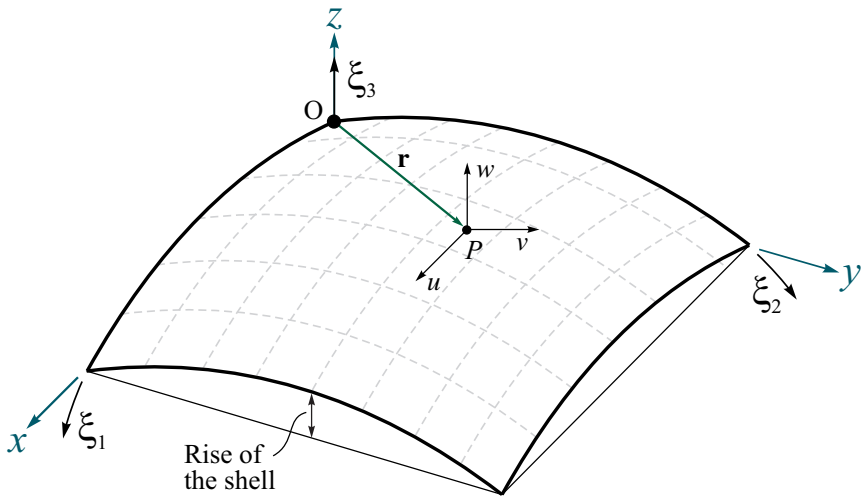

Figure 3.3 Configuration of a shallow shell.

where ds_0^2 is the square of differential line elements before deformation which is obtained as

$$\begin{aligned} ds_0^2 &= d\mathbf{r}_0 \cdot d\mathbf{r}_0 \\ &= \left\{1 + \left[\frac{\partial}{\partial x}(z+\zeta)\right]^2\right\} dx^2 + \left\{1 + \left[\frac{\partial}{\partial y}(z+\zeta)\right]^2\right\} dy^2 \\ &\quad + 2\left[\frac{\partial}{\partial x}(z+\zeta) + \frac{\partial}{\partial y}(z+\zeta)\right] dx\, dy \end{aligned} \tag{3.31}$$

whereas ds^2 is the square of differential line elements after deformation which is obtained as

$$\begin{aligned} ds^2 &= d\mathbf{r} \cdot d\mathbf{r} \\ &= \left\{\left[1+\frac{\partial u}{\partial x} - \frac{\partial}{\partial x}\left(z\frac{\partial w}{\partial x}\right)\right]^2 + \left[\frac{\partial v}{\partial x} - \frac{\partial}{\partial x}\left(z\frac{\partial w}{\partial y}\right)\right]^2 + \left[\frac{\partial}{\partial x}(z+\zeta+w)\right]^2\right\} dx^2 \\ &\quad + \left\{\left[1+\frac{\partial v}{\partial y} + \frac{\partial}{\partial y}\left(z\frac{\partial w}{\partial y}\right)\right]^2 + \left[\frac{\partial u}{\partial y} + \frac{\partial}{\partial y}\left(z\frac{\partial w}{\partial x}\right)\right]^2 + \left[\frac{\partial}{\partial y}(z+\zeta+w)\right]^2\right\} dy^2 \\ &\quad + 2\left\{\left[1+\frac{\partial u}{\partial x} - \frac{\partial}{\partial x}\left(z\frac{\partial w}{\partial x}\right)\right] \cdot \left[\frac{\partial u}{\partial y} + \frac{\partial}{\partial y}\left(z\frac{\partial w}{\partial x}\right)\right] + \left[1+\frac{\partial u}{\partial y} - \frac{\partial}{\partial y}\left(z\frac{\partial w}{\partial y}\right)\right] \right. \\ &\quad \left. \cdot \left[\frac{\partial v}{\partial x} - \frac{\partial}{\partial x}\left(z\frac{\partial w}{\partial y}\right)\right] + \left[\frac{\partial}{\partial x}(z+\zeta+w)\right] \cdot \left[\frac{\partial}{\partial y}(z+\zeta+w)\right]\right\} dx\, dy \end{aligned} \tag{3.32}$$

Substitution from equations (3.31) and (3.32) into equation (3.30) leads to the strain components of the shallow shell

$$\begin{aligned}\varepsilon_x = &\frac{\partial u}{\partial x} + \frac{1}{2}\left(\frac{\partial u}{\partial x}\right)^2 + \frac{1}{2}\left(\frac{\partial v}{\partial x}\right)^2 + \frac{1}{2}\left(\frac{\partial w}{\partial x}\right)^2 \\ &- z\frac{\partial^2 w}{\partial x^2} + \left(\frac{\partial w}{\partial x}\right)\frac{\partial \zeta}{\partial x} - \left(\frac{\partial u}{\partial x}\right)\frac{\partial}{\partial x}\left(z\frac{\partial w}{\partial x}\right) \\ &- \left(\frac{\partial v}{\partial x}\right)\frac{\partial}{\partial x}\left(z\frac{\partial w}{\partial y}\right) + \frac{1}{2}\left[\frac{\partial}{\partial x}\left(z\frac{\partial w}{\partial y}\right)\right]^2 + \frac{1}{2}\left[\frac{\partial}{\partial x}\left(z\frac{\partial w}{\partial x}\right)\right]^2\end{aligned} \tag{3.33a}$$

$$\begin{aligned}\varepsilon_y = &\frac{\partial v}{\partial y} + \frac{1}{2}\left(\frac{\partial u}{\partial y}\right)^2 + \frac{1}{2}\left(\frac{\partial v}{\partial y}\right)^2 + \frac{1}{2}\left(\frac{\partial w}{\partial y}\right)^2 \\ &- z\frac{\partial^2 w}{\partial y^2} + \left(\frac{\partial w}{\partial y}\right)\left(\frac{\partial \zeta}{\partial y}\right) - \left(\frac{\partial u}{\partial y}\right)\frac{\partial}{\partial y}\left(z\frac{\partial w}{\partial y}\right) \\ &+ \left(\frac{\partial v}{\partial y}\right)\frac{\partial}{\partial y}\left(z\frac{\partial w}{\partial x}\right) + \frac{1}{2}\left[\frac{\partial}{\partial y}\left(z\frac{\partial w}{\partial y}\right)\right]^2 + \frac{1}{2}\left[\frac{\partial}{\partial y}\left(z\frac{\partial w}{\partial x}\right)\right]^2\end{aligned} \tag{3.33b}$$

$$\begin{aligned}\varepsilon_{xy} = &\frac{\partial u}{\partial y} + \frac{\partial v}{\partial x} - 2z\frac{\partial^2 w}{\partial x \partial y} + \left(\frac{\partial u}{\partial x}\right)\left(\frac{\partial u}{\partial y}\right) + \left(\frac{\partial v}{\partial x}\right)\left(\frac{\partial v}{\partial y}\right) \\ &+ \left(\frac{\partial w}{\partial x}\right)\left(\frac{\partial w}{\partial y}\right) + \left(\frac{\partial \zeta}{\partial x}\right)\left(\frac{\partial w}{\partial y}\right) + \left(\frac{\partial w}{\partial x}\right)\left(\frac{\partial \zeta}{\partial y}\right) \\ &+ z\left[-\left(\frac{\partial u}{\partial x}\right)\left(\frac{\partial^2 w}{\partial x \partial y}\right) - \left(\frac{\partial v}{\partial y}\right)\left(\frac{\partial^2 w}{\partial x \partial y}\right) - \left(\frac{\partial u}{\partial y}\right)\left(\frac{\partial^2 w}{\partial x^2}\right)\right. \\ &\left. - \left(\frac{\partial v}{\partial x}\right)\left(\frac{\partial^2 w}{\partial y^2}\right)\right] + z^2\left[\left(\frac{\partial^2 w}{\partial x \partial y}\right)\left(\frac{\partial^2 w}{\partial y^2}\right) - \left(\frac{\partial^2 w}{\partial x^2}\right)\left(\frac{\partial^2 w}{\partial x \partial y}\right)\right]\end{aligned} \tag{3.33c}$$

The higher order terms in the above equations can be neglected due to their small magnitude compared to unity. Therefore, we obtain

$$\varepsilon_x = \frac{\partial u}{\partial x} + \frac{1}{2}\left(\frac{\partial w}{\partial x}\right)^2 + \left(\frac{\partial \zeta}{\partial x}\right)\left(\frac{\partial w}{\partial x}\right) - z\frac{\partial^2 w}{\partial x^2} \tag{3.34a}$$

$$\varepsilon_y = \frac{\partial v}{\partial y} + \frac{1}{2}\left(\frac{\partial w}{\partial y}\right)^2 + \left(\frac{\partial \zeta}{\partial y}\right)\left(\frac{\partial w}{\partial y}\right) - z\frac{\partial^2 w}{\partial y^2} \tag{3.34b}$$

$$\begin{aligned}\varepsilon_{xy} = &\frac{\partial u}{\partial y} + \frac{\partial v}{\partial x} + \left(\frac{\partial w}{\partial x}\right)\left(\frac{\partial w}{\partial y}\right) + \left(\frac{\partial w}{\partial x}\right)\left(\frac{\partial \zeta}{\partial y}\right) \\ &+ \left(\frac{\partial \zeta}{\partial x}\right)\left(\frac{\partial w}{\partial y}\right) - 2z\frac{\partial^2 w}{\partial x \partial y}\end{aligned} \tag{3.34c}$$

Using the von Kármán theory for moderately large deflections and small strains in shallow shells, the above strain-displacement relations can be written as

$$\left\{\begin{array}{c}\varepsilon_{xx}\\ \varepsilon_{yy}\\ \gamma_{xy}\end{array}\right\}=\left\{\begin{array}{c}\frac{\partial u}{\partial x}+\frac{1}{2}\left(\frac{\partial w}{\partial x}\right)^2\\ \frac{\partial v}{\partial y}+\frac{1}{2}\left(\frac{\partial w}{\partial y}\right)^2\\ \frac{\partial u}{\partial y}+\frac{\partial v}{\partial x}+\left(\frac{\partial w}{\partial x}\right)\left(\frac{\partial w}{\partial y}\right)\end{array}\right\}+\left\{\begin{array}{c}\frac{w}{R_x}\\ \frac{w}{R_y}\\ \frac{2w}{R_{xy}}\end{array}\right\}+z\left\{\begin{array}{c}-\frac{\partial^2 w}{\partial x^2}\\ -\frac{\partial^2 w}{\partial y^2}\\ -2\frac{\partial^2 w}{\partial x\partial y}\end{array}\right\} \tag{3.35}$$

where R_x and R_y are the radii of curvature of the undeformed shell, and R_{xy} is the corresponding parameter representing the twist of the middle surface of the shell. The above equation takes into account the stretching of the middle surface of the shallow shell.

3.4.3 Constitutive equations

The in-plane stresses vary linearly from the middle surface of the shell as follows

$$\begin{aligned}\left\{\begin{array}{c}\sigma_{xx}\\ \sigma_{yy}\\ \sigma_{xy}\end{array}\right\}=&\left(\begin{array}{ccc}Q_{11}&Q_{12}&Q_{13}\\ &Q_{22}&Q_{23}\\ \text{symm.}&&Q_{66}\end{array}\right)\left\{\begin{array}{c}\frac{\partial u}{\partial x}+\frac{1}{2}\left(\frac{\partial w}{\partial x}\right)^2+\frac{w}{R_x}\\ \frac{\partial v}{\partial y}+\frac{1}{2}\left(\frac{\partial w}{\partial y}\right)^2+\frac{w}{R_y}\\ \frac{\partial u}{\partial y}+\frac{\partial v}{\partial x}+\left(\frac{\partial w}{\partial x}\right)\left(\frac{\partial w}{\partial y}\right)+\frac{2w}{R_{xy}}\end{array}\right\}\\ &+z\left(\begin{array}{ccc}Q_{11}&Q_{12}&Q_{13}\\ &Q_{22}&Q_{23}\\ \text{symm.}&&Q_{66}\end{array}\right)\left\{\begin{array}{c}-\frac{\partial^2 w}{\partial x^2}\\ -\frac{\partial^2 w}{\partial y^2}\\ -2\frac{\partial^2 w}{\partial x\partial y}\end{array}\right\}\\ &+\left(\begin{array}{ccc}Q_{11}&Q_{12}&Q_{13}\\ &Q_{22}&Q_{23}\\ \text{symm.}&&Q_{66}\end{array}\right)\left\{\begin{array}{c}\alpha_{xx}\theta\\ \alpha_{yy}\theta\\ \alpha_{xy}\theta\end{array}\right\}\end{aligned} \tag{3.36}$$

It can be seen that the only difference between these equations and those introduced for plates is in the extra terms which are due to the shell curvature. The membrane

tractions (forces) for the shallow shell can be obtained by integrating the in-plane stresses of the shell over its depth

$$\begin{Bmatrix} N_{xx} \\ N_{yy} \\ N_{xy} \end{Bmatrix} = \begin{pmatrix} A_{11} & A_{12} & A_{16} \\ & A_{22} & A_{26} \\ \text{symm.} & & A_{66} \end{pmatrix} \begin{Bmatrix} \frac{\partial u}{\partial x} + \frac{1}{2}\left(\frac{\partial w}{\partial x}\right)^2 + \frac{w}{R_x} \\ \frac{\partial v}{\partial y} + \frac{1}{2}\left(\frac{\partial w}{\partial y}\right)^2 + \frac{w}{R_y} \\ \frac{\partial u}{\partial y} + \frac{\partial v}{\partial x} + \left(\frac{\partial w}{\partial x}\right)\left(\frac{\partial w}{\partial y}\right) + \frac{2w}{R_{xy}} \end{Bmatrix} + \begin{pmatrix} B_{11} & B_{12} & B_{16} \\ & B_{22} & B_{26} \\ \text{symm.} & & B_{66} \end{pmatrix} \begin{Bmatrix} -\frac{\partial^2 w}{\partial x^2} \\ -\frac{\partial^2 w}{\partial y^2} \\ -2\frac{\partial^2 w}{\partial x \partial y} \end{Bmatrix} - \begin{Bmatrix} N^{\theta}_{xx} \\ N^{\theta}_{yy} \\ N^{\theta}_{xy} \end{Bmatrix} \tag{3.37}$$

The moment resultants can also be obtained by twice integrating the in-plane stresses over the depth of the shell as follows

$$\begin{Bmatrix} M_{xx} \\ M_{yy} \\ M_{xy} \end{Bmatrix} = \begin{pmatrix} B_{11} & B_{12} & B_{16} \\ & B_{22} & B_{26} \\ \text{symm.} & & B_{66} \end{pmatrix} \begin{Bmatrix} \frac{\partial u}{\partial x} + \frac{1}{2}\left(\frac{\partial w}{\partial x}\right)^2 + \frac{w}{R_x} \\ \frac{\partial v}{\partial y} + \frac{1}{2}\left(\frac{\partial w}{\partial y}\right)^2 + \frac{w}{R_y} \\ \frac{\partial u}{\partial y} + \frac{\partial v}{\partial x} + \left(\frac{\partial w}{\partial x}\right)\left(\frac{\partial w}{\partial y}\right) + \frac{2w}{R_{xy}} \end{Bmatrix} + \begin{pmatrix} D_{11} & D_{12} & D_{16} \\ & D_{22} & D_{26} \\ \text{symm.} & & D_{66} \end{pmatrix} \begin{Bmatrix} -\frac{\partial^2 w}{\partial x^2} \\ -\frac{\partial^2 w}{\partial y^2} \\ -2\frac{\partial^2 w}{\partial x \partial y} \end{Bmatrix} - \begin{Bmatrix} M^{\theta}_{xx} \\ M^{\theta}_{yy} \\ M^{\theta}_{xy} \end{Bmatrix} \tag{3.38}$$

where the extensional, coupling, and bending stiffnesses are the same as those defined for the plate. Depending upon the type of material used for a shallow shell, the above equations can be simplified. For example, for an orthotropic shell, the stiffness coefficients may be given by

$$\begin{pmatrix} Q_{11} & Q_{12} & Q_{13} \\ & Q_{22} & Q_{23} \\ \text{symm.} & & Q_{66} \end{pmatrix} = \begin{pmatrix} \frac{E1}{1-\nu_{12}\nu_{21}} & \frac{E2\nu_{12}}{1-\nu_{12}\nu_{21}} & 0 \\ & \frac{E2}{1-\nu_{12}\nu_{21}} & 0 \\ \text{symm.} & & \frac{E2}{2(1+\nu_{12})} \end{pmatrix} \tag{3.39}$$

in which $E1$ and $E2$ are elastic moduli referring to the axes x and y, or for elastic shells, the shell stiffness matrix can be given in the following form

$$\begin{pmatrix} Q_{11} & Q_{12} & Q_{13} \\ & Q_{22} & Q_{23} \\ \text{symm.} & & Q_{66} \end{pmatrix} = \begin{pmatrix} \frac{E}{1-\nu^2} & \frac{\nu E}{1-\nu^2} & 0 \\ & \frac{E}{1-\nu^2} & 0 \\ \text{symm.} & & \frac{E}{2(1+\nu)} \end{pmatrix} \tag{3.40}$$

Accordingly, the axial force resultants are written as

$$N_{xx} = \frac{Eh}{1-\nu^2}\left[\frac{\partial u}{\partial x} + \nu\frac{\partial v}{\partial y} + \frac{1}{2}\left(\frac{\partial w}{\partial x}\right)^2 + \frac{\nu}{2}\left(\frac{\partial w}{\partial y}\right)^2 + \frac{w}{R_x} + \nu\frac{w}{R_y}\right] - N^{\theta} \tag{3.41a}$$

$$N_{yy} = \frac{Eh}{1-\nu^2}\left[\nu\frac{\partial u}{\partial x} + \frac{\partial v}{\partial y} + \frac{\nu}{2}\left(\frac{\partial w}{\partial x}\right)^2 + \frac{1}{2}\left(\frac{\partial w}{\partial y}\right)^2 + \nu\frac{w}{R_x} + \frac{w}{R_y}\right] - N^{\theta} \tag{3.41b}$$

$$N_{xy} = \frac{Eh}{2(1+\nu)}\left[\frac{\partial u}{\partial y} + \frac{\partial v}{\partial x} + \left(\frac{\partial w}{\partial x}\right)\left(\frac{\partial w}{\partial y}\right) + \frac{2w}{R_{xy}}\right] \tag{3.41c}$$

The moment resultants are the same as those introduced in equation (3.28). The basic relations developed in this section are used in Chapters 7 and 8 to study the geometrically and materially nonlinear behaviour of shallow shells under thermomechanical loads.

3.5 Summary

The fundamental theories of thin elastic beams, plates, and shallow shells including kinematic relationships and constitutive equations were presented. These theories will be used in the next chapters to derive the governing nonlinear equations of beams, plates, and shells.

Chapter 4

Geometrically Nonlinear Behaviour of Beams

4.1 Introduction

Beams and columns are useful structural components that can transfer applied loads to adjacent structural members, thereby playing an important role in the load-carrying mechanism of large-scale structures. This has motivated many researchers to propose a number of different approaches for determining the nonlinear response of beams to different thermomechanical loads. In the following, an overview of the most important contributions in this area is presented.

Venkateswara Rao and Kanaka Ruju (1984), Kaju and Venkateswara Kao (1984), and Kanaka Raju and Venkateswara Rao (1993) employed a Rayleigh-Ritz method to numerically investigate the thermal post-buckling behaviour of uniform and tapered columns. In their formulation, the geometric nonlinearity due to the curvature of the centroidal axis of the column was ignored. Je˛kot (1996) used a similar assumption to evaluate the thermal post-buckling behaviour of beams made of a nonlinear thermoelastic material. Considering the curvature of the beam due to heating, Coffin and Bloom (1999) presented an elliptic integral solution for the post-buckling response of an elastic and hygrothermal fully restrained beam against axial expansion. They found that contrary to predictions of classical studies, the axial load in the post-buckling regime is not constant and its magnitude decreases as the potential for free expansion is increased.

Based on the geometrically nonlinear theory of extensible beams, Shirong and Changjun (2000) and Li *et al.* (2002) carried out computational analyses for the thermal post-buckling behaviour of Euler-Bernoulli beams with pinned-pinned, fixed-fixed, and pinned-fixed BCs. The resulting nonlinear boundary value problems were reduced to initial value problems using a shooting method in conjunction with concepts of analytical continuation. Accounting for the effects of shear flexibility on the beam deformation, the work was then extended for bending and buckling analysis of nonlinear Timoshenko beams subjected to mechanical and thermal loads (Li and Zhou, 2003). Numerical results were presented for a pinned–fixed beam under a static transversely non-uniform temperature rise. The equilibrium paths of a beam subjected to a transversely non-uniform temperature rise were found similar to that of a beam under an axially distributed mechanical force with initial deflection or geometrical imperfections. Shepherd and Burgess (2011) developed an analytical model to investigate the effect of axial restraint in the buckling of steel columns subject to heating. They showed that the most dominant factor influencing the buckling magnitude in the columns is temperature and the effect of the axial restraint itself is not that much effective.

Abu-Farsakh *et al.* (2000) studied the effect of material nonlinearity and fiber orientation on the static response of unidirectional composite beams. They reported that with an increase in the angle of fiber orientation in a composite beam, its stiffness decreases, leading to larger deflections for the beam. Katsikadelis and Tsiatas (2003) employed a direct solution for the nonlinear analysis of Euler-Bernoulli beams with variable stiffness and general nonlinear BCs. The governing coupled nonlinear differential equations of the problem were solved using a boundary element method based on analog equation method, thereby the coupled nonlinear equations with variable coefficients were converted into uncoupled linear ones with fictitious loads. This methodology was then extended by Tsiatas (2010) to include beams resting on a nonlinear elastic foundation.

Sokolinsky *et al.* (2003) experimentally and theoretically studied the mechanical response of sandwich beams subject to localised loads. Four-point bending tests were conducted on sandwich beam specimens comprised of aluminum face sheets

and a PVC foam core using a universal test machine. The experimental results were compared with the analytical predictions based on the classical sandwich theory, and linear and a geometrically nonlinear higher order sandwich panel theory. Comparison studies showed that the classical sandwich theory underestimates the vertical displacements of sandwich beam specimens by more than 20%. It was also reported that this theory has failed to model the core indentation phenomenon in sandwich beams under concentrated loads. As an alternative, authors suggested the linear higher order theory for predicting bending deflections of sandwich beams under concentrated loads. Sze *et al.* (2004) presented a geometric nonlinear benchmark solution for a cantilever subjected to end shear force and end moment.

Erkmen and Bradford (2009) developed a three-dimensional geometrically nonlinear FE formulation to investigate the effects of initial curvature, geometric nonlinearity, and partial interaction on the behaviour of composite curved beams. Their numerical results showed that composite curved beams become significantly softer as their initial curvature increases. Based on a non-classical continuum theory called modified couple stress theory, Asghari *et al.* (2010) developed a nonlinear size-dependent formulation for Timoshenko beams with two immovable (laterally restrained) supports. The nonlinearity due to the middle plane stretching of the beam during deflection was included in their formulation. The governing partial differential equations and the corresponding BCs were derived using the Hamilton principle.

Usmani *et al.* (2001) presented some fundamental concepts involving the thermal loading of steel columns from the perspective of fire attack. A nonlinear transient FE model was proposed by Di Capua and Mari (2007) to predict the temperature distribution of a reinforced concrete cross-section exposed to fire. The model proposed showed a very good agreement with the experimentally measured temperature distributions under fire conditions. Wang *et al.* (2012c) conducted experimental and numerical studies to investigate the failure pattern and damage phenomenon of fire insulation on steel columns under monotonic and cyclic loads at ambient conditions. Their experimental tests showed that the adhesion of fire insulation with steel columns is generally weak. Jang (2013) developed a nonlinear method for the moderately large deflection analysis of infinite nonlinear beams on an elastic foundation under

localised external loads. The geometrical nonlinearity was based on the von Kármán type of large deformation theory. Recently, Cheng *et al.* (2015) carried out a numerical analysis on the buckling behaviour cold-formed steel channel-section beams subjected to uniformly distributed loads when exposed to fire on its one side. The analysis was performed using combined finite strip analysis and classical Fourier series solutions, considering the TDMP. They concluded that the buckling behaviour of the beam with temperature variation in its section is quite different from that of the beam with a constant uniform temperature in its section.

Most fire design codes are based on isolated single element testing under a standard fire curve (e.g. ISO834). In recent years, more and more criticism has been raised in the steel industry as this approach to structural fire resistance design is too conservative and wasteful. One of the seminal events that illustrated this, was the Broadgate phase 8 fire in London in the late 80s. Another shortcoming of the standard fire test is that the tested element is simply supported, which is unrealistic for most members of real steel frame structures under fire conditions. Therefore, a more realistic case is considering beams with finite end restraints.

Hence, in this chapter, a mathematical model is developed for determining the nonlinear response of beams with finite end restraint to transverse mechanical loads and through-depth thermal gradients. The finite end restraint is modelled using translational and rotational springs at the end of the beam. In the context of structural performance under extreme thermal actions (such as fire), the beam nonlinear response is studied under "short hot" and "long cool" fire exposure conditions discussed. The former is under a high temperature over a short post-flashover duration (Drysdale, 2011) and the latter is under a lower temperature over a longer post-flashover period (Drysdale, 2011).

4.2 Basic relations

As mentioned in the previous chapter, in the case of large displacements in beams, the coupling between the axial force in the beam and the out-of-plane displacement

of the beam must be considered in the beam theory. Using equations (3.3) and (3.5), the strain and curvature in an elastic nonlinear beam can be written as

$$\varepsilon_{xx} = \frac{\partial u}{\partial x} + \frac{1}{2}\left(\frac{\partial w}{\partial x}\right)^2 \tag{4.1a}$$

$$\kappa = \frac{\mathrm{d}^2 w}{\mathrm{d}x^2} \tag{4.1b}$$

The axial resultant force and the bending moment of the cross section of the beam in equations (3.9) and (3.11) can then be simplified as:

$$\begin{aligned} N_x &= N \\ &= EA\varepsilon_{xx} - N^\theta \end{aligned} \tag{4.2a}$$

$$\begin{aligned} M_x &= M \\ &= -EI\kappa - M^\theta \end{aligned} \tag{4.2b}$$

where A represents the area of the cross section of the beam and I is the moment of inertia that is defined by

$$I = \int_A z^2 \mathrm{d}A \tag{4.3}$$

In the next section, the governing equations of a beam under thermomechanical loads are derived.

4.3 Derivation of governing equations

For a beam subject to axial and transverse forces, a deformed beam element of length '$\mathrm{d}x$' is depicted in Figure 4.1. In this figure, P and q refer to the intensity of the axial and transverse forces (per unit length), respectively, w, Q, N, and M are the out-of-plane displacement of the beam, the internal shear force, the membrane force, and the bending moment of the beam, respectively. From equilibrium conditions in the vertical direction, we obtain

$$Q + \frac{\partial Q}{\partial x}\,\mathrm{d}x - Q + P\frac{\partial w}{\partial x}\,\mathrm{d}x + q\,\mathrm{d}x = 0 \tag{4.4}$$

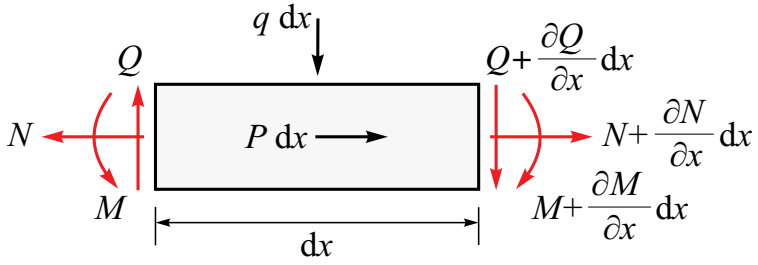

Figure 4.1 Stress and moment resultants in a small element cut from a beam subjected to axial and transverse forces.

which can be rearranged as

$$\frac{\partial Q}{\partial x} + P\frac{\partial w}{\partial x} + q = 0 \tag{4.5}$$

By taking a moment about the centre of the beam element, an equilibrium equation can be obtained as follows

$$\begin{aligned} M - \left(M + \frac{\partial M}{\partial x}\mathrm{d}x\right) + \left(Q + \frac{\partial Q}{\partial x}\mathrm{d}x\right)\frac{\mathrm{d}x}{2} + Q\frac{\mathrm{d}x}{2} \\ - \left(N + \frac{\partial N}{\partial x}\mathrm{d}x\right)\left(\frac{\partial w}{\partial x} + \frac{\partial^2 w}{\partial x^2}\mathrm{d}x\right)\frac{\mathrm{d}x}{2} - N\left(\frac{\partial w}{\partial x}\right)\frac{\mathrm{d}x}{2} = 0 \end{aligned} \tag{4.6}$$

It is important to note that the right hand side of the above equation is zero due to neglecting the rotatory inertia. The terms of order $(\mathrm{d}x)^2$ and $(\mathrm{d}x)^3$ are small when compared to unity and can be neglected from the equation. Therefore, we obtain

$$Q = \frac{\partial M}{\partial x} + N\frac{\partial w}{\partial x} \tag{4.7}$$

Substituting equation (4.7) into equation (4.5) leads to a general governing equation for the beam

$$\frac{\partial^2 M}{\partial x^2} + \frac{\partial}{\partial x}\left(N\frac{\partial w}{\partial x}\right) + P\frac{\partial w}{\partial x} + q = 0 \tag{4.8}$$

Using the equations (4.2) and (4.8), the out-of-plane displacement of a beam of uniform cross section under thermomechanical loads must satisfy the following differential equation

$$\frac{\mathrm{d}^4 w}{\mathrm{d}x^4} - \frac{N}{EI}\frac{\mathrm{d}^2 w}{\mathrm{d}x^2} + \frac{1}{EI}\left(\frac{\mathrm{d}^2 M^{\theta}}{\mathrm{d}x^2} + q\right) = 0 \tag{4.9}$$

The second term in the above equation accounts for the coupling between the axial force and the out-of-plane displacement of the beam. It makes the governing equation more complicated since the axial force is also directly related to the out-of-plane displacement. The left hand side of this equation requires appropriate conditions at the beam boundaries.

4.4 Boundary conditions

A range of idealised BCs for single beam elements in frame structures are considered in this study. These BCs are modelled using translational and rotational springs at the end of the beam as illustrated in Figure 4.2. As such, any beam solution must satisfy the following conditions:

$$u|_{x=0} = 0 \tag{4.10a}$$

$$w|_{x=0} = 0 \tag{4.10b}$$

$$M_l = EI\left[\frac{\mathrm{d}^2 w}{\mathrm{d}x^2}\right]_{x=0} = k_{rl}\left[\frac{\mathrm{d}w}{\mathrm{d}x}\right]_{x=0} \tag{4.10c}$$

and

$$k_t\, u|_{x=L} = N \tag{4.11a}$$

$$w|_{x=L} = 0 \tag{4.11b}$$

$$M_r = EI\left[\frac{\mathrm{d}^2 w}{\mathrm{d}x^2}\right]_{x=L} = -\,k_{rr}\left[\frac{\mathrm{d}w}{\mathrm{d}x}\right]_{x=L} \tag{4.11c}$$

Note that, regarding the BC (4.11a), the following two cases must be considered:

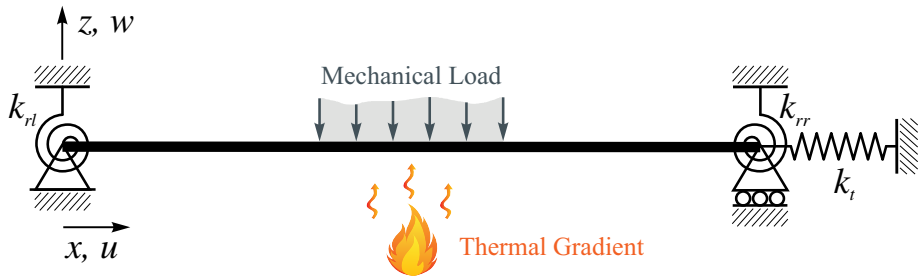

Figure 4.2 A beam with translational and rotational springs subject to a transverse mechanical load and a thermal gradient.

1. For a laterally unrestrained beam where the axial force is zero, the horizontal displacement is nonzero.

2. For a fixed beam where the horizontal displacement is zero, the axial force is nonzero.

4.5 Solution of governing equations

In the absence of in-plane forces, the beam in-plane equation of force is given by

$$\frac{\partial N}{\partial x} = 0 \qquad \text{or} \qquad N = \text{constant} \tag{4.12}$$

Considering the fact that the axial force in the beam does not vary along the length of the beam, the following equation can be derived upon integration of equation (4.2a)

$$\frac{NL}{EA} = u|_{x=L} - u|_{x=0} - \frac{N^{\theta}L}{EA} + \frac{1}{2}\int_0^L \left(\frac{\mathrm{d}w}{\mathrm{d}x}\right)^2 \mathrm{d}x \tag{4.13}$$

Upon substitution from equation (4.11a) in the above equation, we obtain a nonlinear equation for the axial force in the beam

$$N = \frac{EAk_t}{Lk_t - EA}\left[-\frac{N^{\theta}L}{EA} + \frac{1}{2}\int_0^L \left(\frac{\mathrm{d}w}{\mathrm{d}x}\right)^2 \mathrm{d}x\right] \tag{4.14}$$

The reaction forces and bending moments at the beam supports can also be obtained from the equilibrium equations. As illustrated in Figure 4.3, these equations are:

$$P_l + P_r - qL = 0 \tag{4.15a}$$

$$M_l - M_r - P_r L + \frac{qL^2}{2} = 0 \tag{4.15b}$$

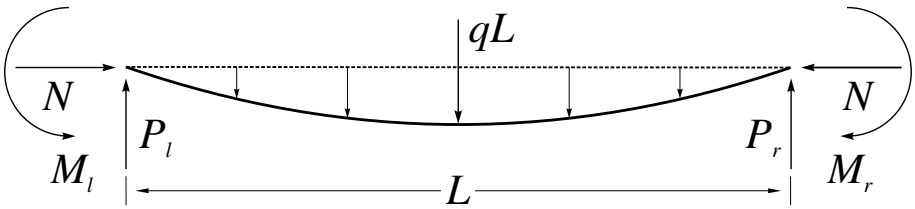

Figure 4.3 Free body diagram of a beam with finite end restraints subject to a transverse mechanical load.

Different transverse mechanical loading conditions can be considered by expressing the quantity q in a Fourier series as

$$q(x) = \sum_{m=1}^{\infty} q_m \sin \frac{m\pi x}{L} \tag{4.16}$$

where its coefficient is given by

$$q_m = \frac{2}{L} \int_0^L q(x) \sin \frac{m\pi x}{L} \, \mathrm{d}x \tag{4.17}$$

The following loading conditions can then be considered:

For UDL of magnitude q:

$$q_m = q \tag{4.18}$$

For sinusoidal loading of magnitude q where $m = 1$:

$$q_m = \frac{4q}{\pi} \tag{4.19}$$

For point load of q applied at an arbitrary point x_0 along the length of the beam:

$$q_m = \frac{2q}{L} \sin \frac{m\pi x_0}{L} \tag{4.20}$$

The thermally induced resultant moment M^θ which is associated with a change in temperature can be taken in the same form as the transverse mechanical loading

$$M^\theta(x) = \sum_{m=1}^{\infty} M_m^\theta \sin \frac{m\pi x}{L} \tag{4.21}$$

where its coefficient is calculated by performing the Fourier integration as follows

$$M_m^\theta = \frac{4M^\theta}{\pi} \tag{4.22}$$

Upon substitution of equations (4.16) and (4.21) into equation (4.9), we obtain the following governing equation for single beams under thermomechanical loads

$$\frac{\mathrm{d}^4 w}{\mathrm{d}x^4} - \frac{N}{EI}\frac{\mathrm{d}^2 w}{\mathrm{d}x^2} + \frac{1}{EI}\left(-\frac{\pi^2 M_m^\theta}{L^2} + q_m\right)\sin\frac{m\pi x}{L} = 0 \tag{4.23}$$

The solution of this equation consists of two parts, a homogenous solution, denoted by w_h and a particular solution, denoted by w_p as follows

$$w = w_h + w_p \tag{4.24}$$

The particular solution can be described as

$$w_p = C_0 \sin\frac{m\pi x}{L} \tag{4.25}$$

with the constant C_0 taken in the form of

$$C_0 = \frac{\pi^2 L^2 M_m^\theta - q_m L^4}{EIm^4\pi^4 + m^2\pi^2 L^2 N} \tag{4.26}$$

The homogeneous solution, however, can be taken in the following form

$$w_h = C_1 + C_2 x + C_3 \sinh\sqrt{\frac{N}{EI}}x + C_4 \cosh\sqrt{\frac{N}{EI}}x \tag{4.27}$$

where the four constants C_0, C_1, C_2, C_3, and C_4 can be determined from the four BCs given by equations (4.10b), (4.10c), (4.11b), and (4.11c). The total out-of-plane displacement of the beam can then be written as

$$w = C_0 \sin\frac{m\pi x}{L} + C_1 + C_2 x + C_3 \sinh\sqrt{\frac{N}{EI}}x + C_4 \cosh\sqrt{\frac{N}{EI}}x \tag{4.28}$$

The four constants C_1, C_2, C_3, and C_4 can be determined by applying the BCs (4.10) and (4.11) as follows:

From the BC (4.10b), we obtain

$$C_1 + C_4 = 0 \tag{4.29}$$

From the BC (4.10c), we obtain

$$C_4 N - k_{rl}\left(C_0\frac{\pi}{L} + C_2 + C_3\sqrt{\frac{N}{EI}}\right) = 0 \tag{4.30}$$

From the BC (4.11b), we obtain

$$C_1 + C_2 L + C_3 \sinh\sqrt{\frac{N}{EI}}L + C_4 \cosh\sqrt{\frac{N}{EI}}L = 0 \tag{4.31}$$

From the BC (4.11c), we obtain

$$\begin{aligned} &C_3 N \sinh\sqrt{\frac{N}{EI}}L + C_4 N \cosh\sqrt{\frac{N}{EI}}L \\ &+ k_{rr}\left(-C_0\frac{\pi}{L} + C_2 + C_3\sqrt{\frac{N}{EI}}\cosh\sqrt{\frac{N}{EI}}L + C_4\sqrt{\frac{N}{EI}}\sinh\sqrt{\frac{N}{EI}}L\right) = 0 \end{aligned} \tag{4.32}$$

These four equations can be reduced by substituting $C_1 = -C_4$ from equation (4.29) into the other three equations as follows:

$$-\frac{k_{rl}\pi}{L}C_0 - NC_1 - k_{rl}C_2 - k_{rl}\sqrt{\frac{N}{EI}}C_3 = 0 \tag{4.33a}$$

$$\left(1 - \cosh\sqrt{\frac{N}{EI}}L\right)C_1 + C_2 L + C_3 \sinh\sqrt{\frac{N}{EI}}L = 0 \tag{4.33b}$$

$$\begin{aligned} &-\frac{k_{rr}\pi}{L}C_0 - \left(N\cosh\sqrt{\frac{N}{EI}}L + k_{rr}\sqrt{\frac{N}{EI}}\sinh\sqrt{\frac{N}{EI}}L\right)C_1 \\ &+ k_{rr}C_2 + \left(N\sinh\sqrt{\frac{N}{EI}}L + k_{rr}\sqrt{\frac{N}{EI}}\cosh\sqrt{\frac{N}{EI}}L\right)C_3 = 0 \end{aligned} \tag{4.33c}$$

By solving these nonlinear equations and equation (4.14) simultaneously, the four constants C_0, C_1, C_2, C_3, and the axial force N are determined. By substituting the resulting values into equations (4.28), the out-of-plane displacement and the corresponding axial force in the beam are obtained.

Table 4.1 Definitions of dimensionless quantities for geometrically nonlinear beam problems

Description	Quantity	Definition
Dimensionless centre deflection	$\bar{w}$	w/h
Dimensionless axial force	$\bar{N}$	NL^2/EI
Dimensionless translational spring constant	$\bar{k}_t$	kEA/L
Dimensionless x-coordinate parameter	$\bar{x}$	x/a

In order to investigate the performance of the proposed approach, a number of examples are calculated in the following. Quantities are presented in a dimensionless form as listed in Table 4.1.

4.5.1 Beam subject to idealised temperature distributions

For the nonlinear analysis of beams under linear thermal loading, the following temperature field is assumed for the beam

$$\theta = \left(\frac{1}{2} - \frac{z}{h}\right)\theta_b + \left(\frac{1}{2} + \frac{z}{h}\right)\theta_t \tag{4.34}$$

where θ_b and θ_t are the temperatures at the bottom and top surfaces of the beam. As shown in Figure 4.4, a realistic through-depth temperature distribution can be represented by an equivalent mean temperature corresponding to the thermal expansion and an average thermal gradient (Usmani *et al.*, 2001).

A beam is subjected to a UDL of 1.2 kPa, while being under three linear temperature fields through its depth, as shown in Figure 4.5. The influence of three different finite end restraints on the beam nonlinear response are investigated. Each of these provides a certain degree of restraint to the beam. For all the considered examples, results

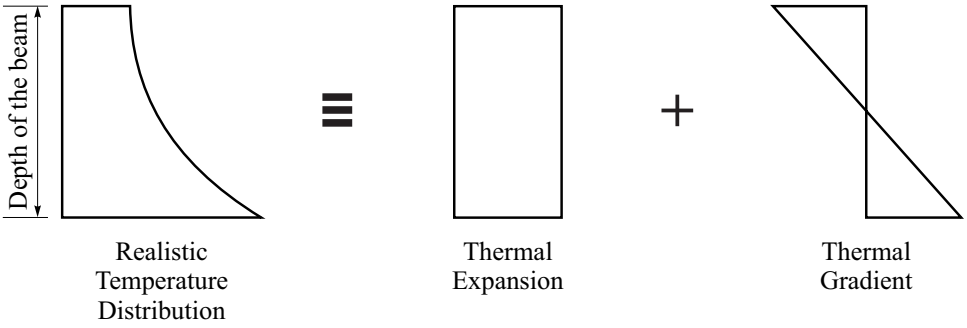

Figure 4.4 Equivalent through-depth temperature distribution in structural members.

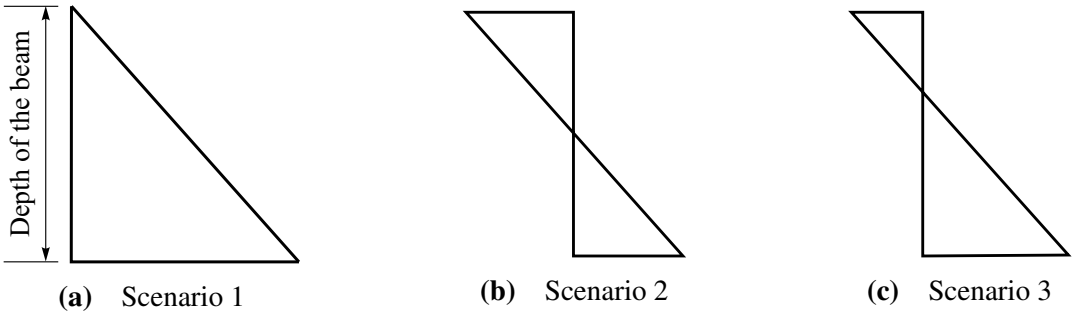

Figure 4.5 Through-depth thermal loading considered for the beam.

obtained from OpenSees are presented for comparison studies. The data used for analysing the beam are listed in Table 4.2.

In the first scenario, the temperature at the top surface of the beam is assumed to be zero, while it varies linearly through the depth of the beam to a temperature of 1000°C. Results are presented for three mechanically loaded beams with different elastically restrained ends (see Figure 4.6). Figures 4.7 and 4.8 show a pattern of development for transverse deflection and axial force with an increase in the temperature for these beams. These BCs are achieved by setting appropriate values for the spring constant. In the case of the laterally unrestrained beam (BC1), both the translational and rotational spring constants are zero. In the case of horizontally restrained beam by a spring (BC2), the lateral translation is fixed. The rotational spring constant is zero but the dimensionless translational spring constant $\bar{k}_t$ is taken as 0.2. In the case of fully restrained beam against horizontal movement (BC3), the rotational spring constant is zero, while the dimensionless translational spring constant is set to be 500.

In the case of BC1, the central deflection of the beam increases linearly as the temperature at the bottom surface increases. For the beam with BC2 and BC3, lack of rotational end restraints has resulted in a higher central deflection. In particular, for the beam with BC3, the value of deflection is larger than that of the other cases. In Figure 4.8, the dimensionless axial forces in the beams with the three different

Table 4.2 Geometrical and material properties of the beam considered in OpenSees

L (m)	b (m)	h (m)	E (N/m^2)	α (1/°C)	ν
6	0.1	0.2	200	12×10^{-6}	0.3

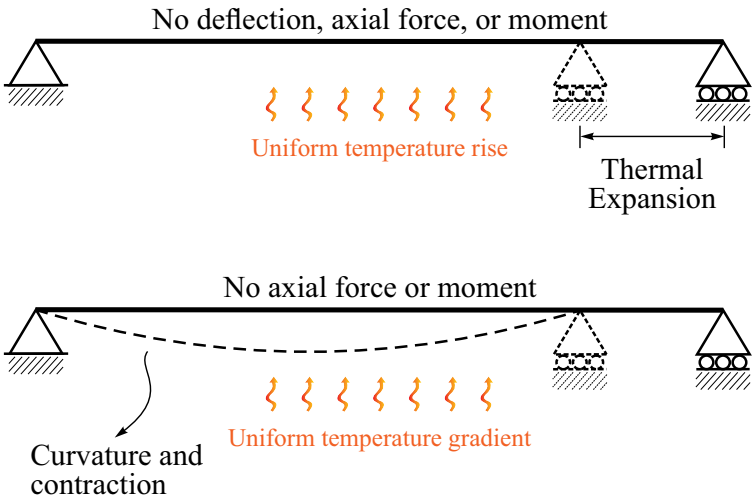

(a) Beam with laterally unrestrained end

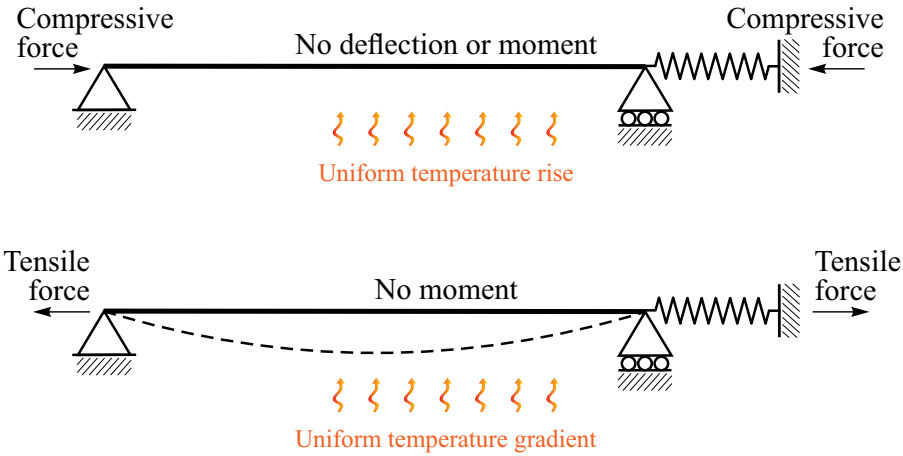

(b) Beam with finite restrained end

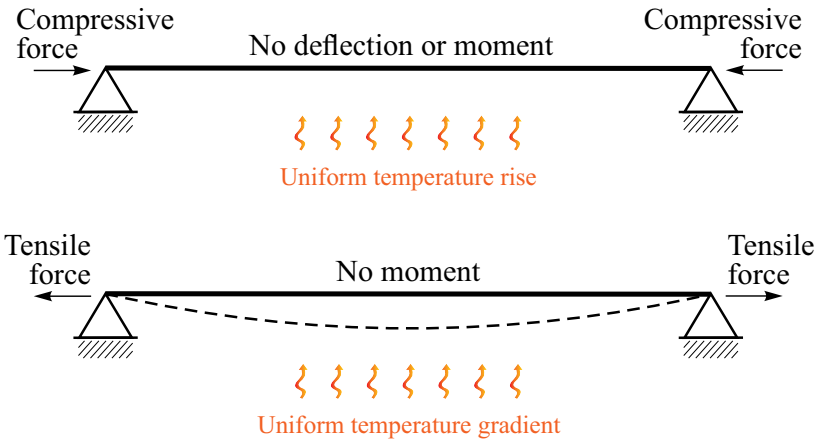

(c) Beam with axially restrained end

Figure 4.6 Single beams under different elastically restrained ends.

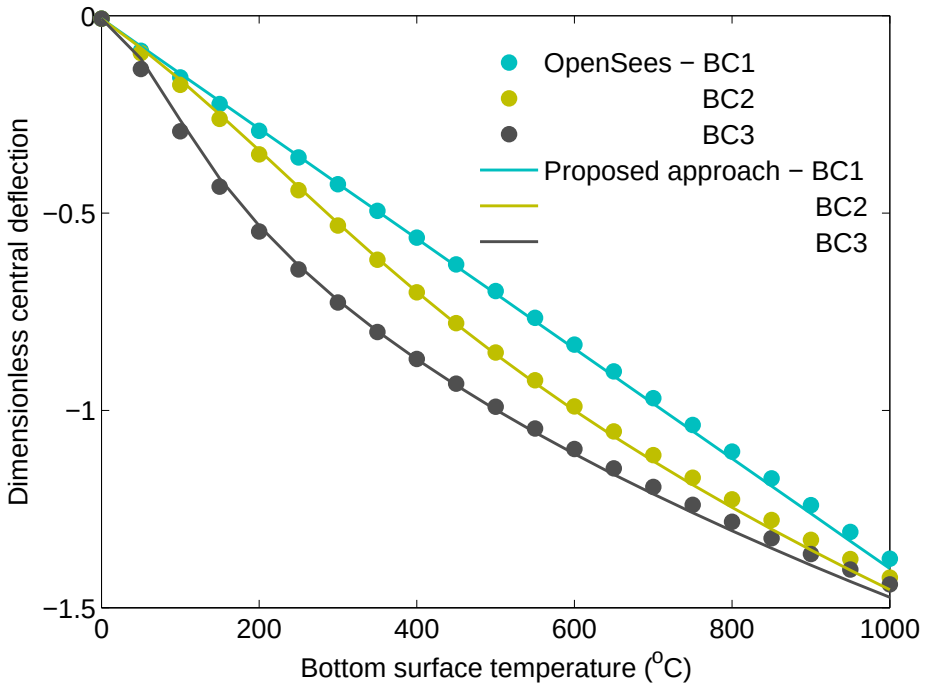

Figure 4.7 Dimensionless central deflection of a heated beam subject to the loading scenario 1.

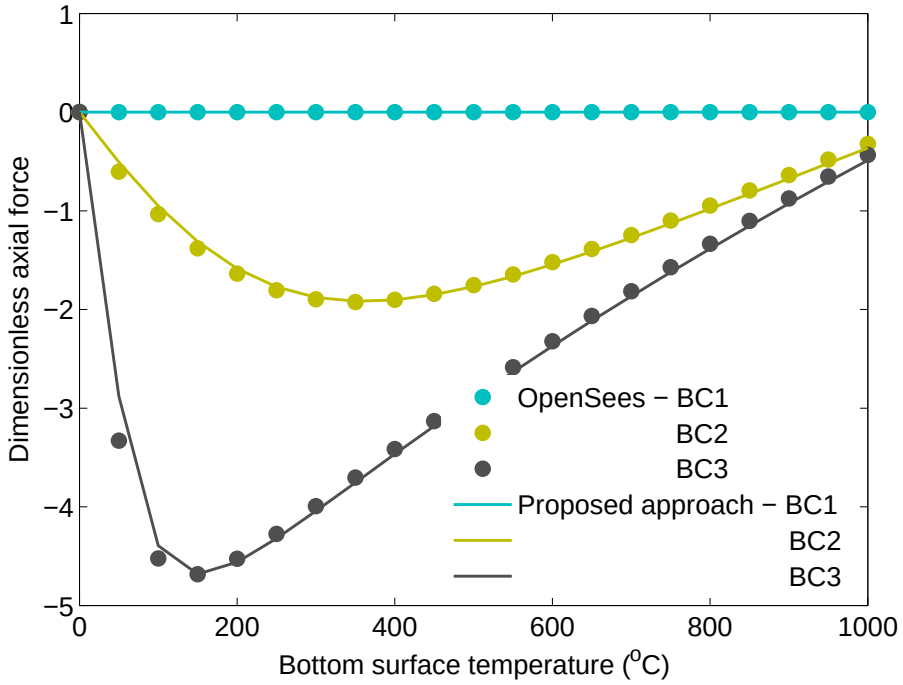

Figure 4.8 Dimensionless axial force in a heated beam subject to the loading scenario 1.

elastically restrained ends are plotted. As expected, the axial force for the beam with BC1 is zero even when the deflection keeps increasing. In contrast with this case, a compressive axial force is produced in the beams with BC2 and BC3. By

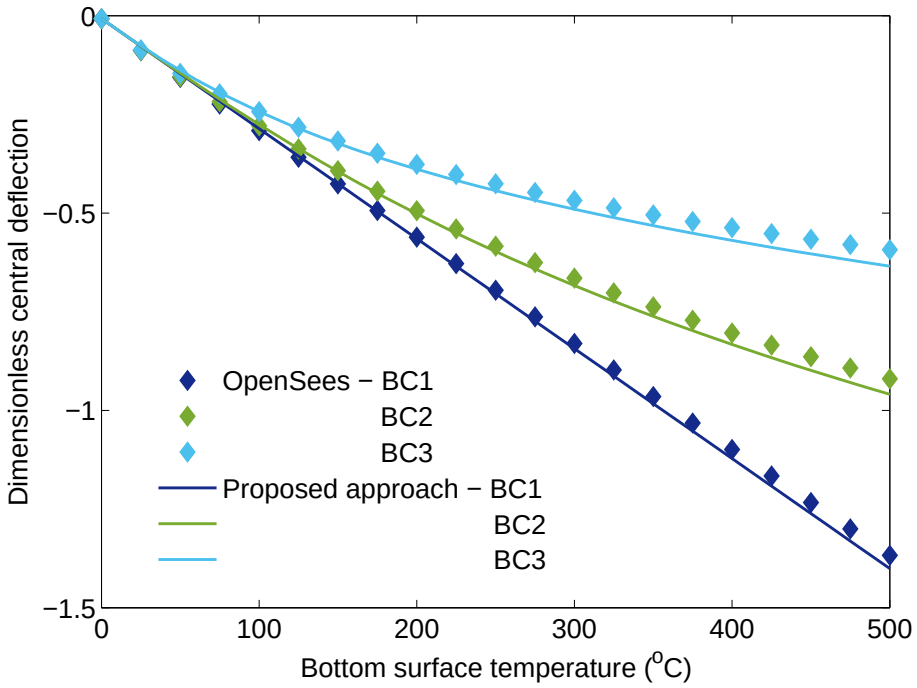

Figure 4.9 Dimensionless central deflection of a heated beam subject to the loading scenario 2.

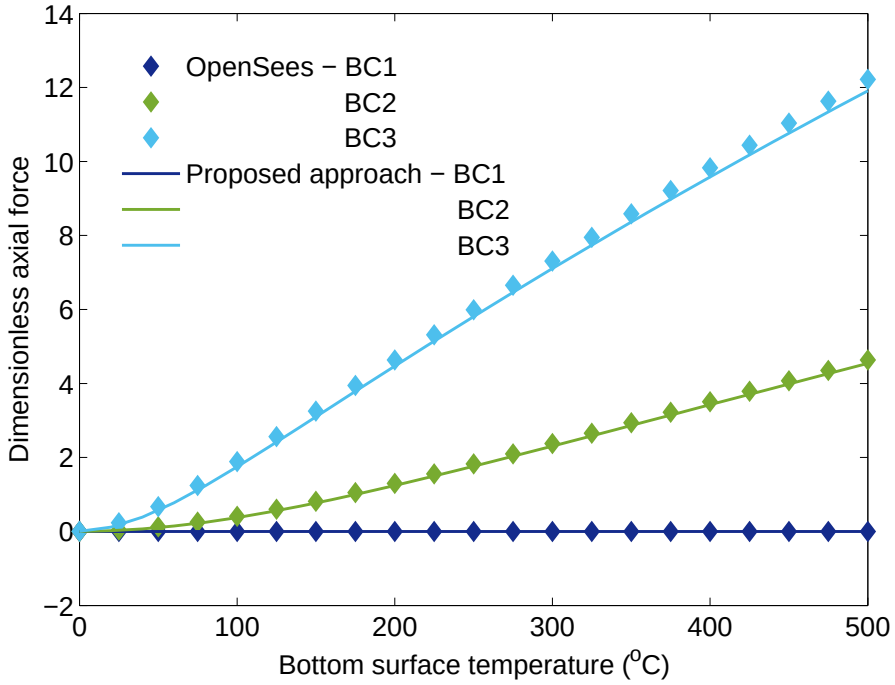

Figure 4.10 Dimensionless axial force in a heated beam subject to the loading scenario 2.

adding restraint to the thermal expansion, this force sharply rises up and then reduces dramatically when the temperature at the bottom surface of the beam reaches to 400°C for BC2 and 180°C for BC3. For the latter case, this is because the compressive axial

force sharply builds up before temperature increases to 150°C, and when it reaches its peak the beam buckles, thereby releasing the compressive axial force in the beam.

In the the second scenario, the temperature at the top surface of the beam varies from 0 to -500°C, while its bottom surface temperature varies from 0 to 500°C. Figures 4.9 and 4.10 show the transverse deflection and axial force in a beam for this scenario. The influence of the thermal bowing in the same beams is shown in Figures 4.9 and 4.10. It has resulted in different central deflection values for the chosen BCs. Unlike for scenario 1, the deflection of simply supported beam was much larger than that in finite and fully fixed end beams. As there is not any thermal expansion in the beam, the tensile forces in the beams increase linearly as the temperature at the bottom surface of the beam increases. The largest axial force is produced for the beam with fully fixed end.

In the third scenario, the temperature at the top surface of the beam varies from 0 to -300°C, while its bottom surface temperature varies from 0 to 700°C. Figures 4.11 and 4.12 show the dimensionless central deflection and axial force in the beams with the chosen BCs against temperature for the thermal loading scenario 3. As the temperature at the bottom surface increases until 300°C, the deflection at middle span of the fully fixed end beam is slightly larger than that in the other beams, but this changes when the temperature reaches 700°C and the deflection of the simply supported beam becomes larger. In the case of the axially restrained beam, the beam is in compression, indicating that the thermal expansion is the dominant effect. When the temperature reaches 100°C, the thermal bowing effect cancels off the thermal expansion effect. As shown in the axial force history after 100°C, the compressive axial force releases and the tensile force builds up in the beam. It can be seen that the response determined for the beam with finite axial restraint is in the middle between those of laterally unrestrained and axially restrained beams.

As can be seen, for all the boundary cases, there has been very good agreement between the deflection and axial force results obtained using the proposed method and those obtained from OpenSees.

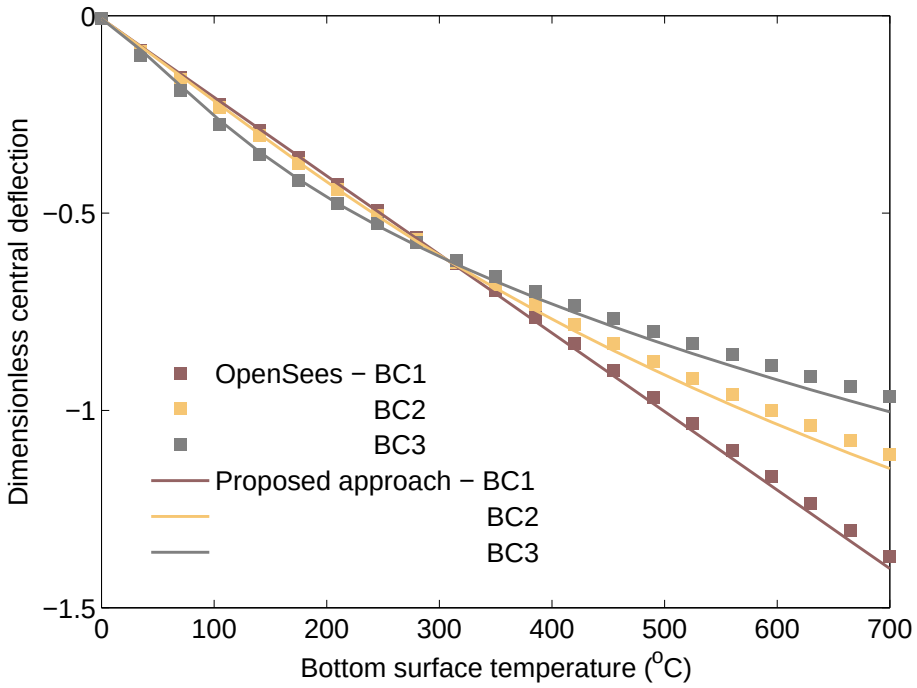

Figure 4.11 Dimensionless central deflection of a heated beam subject to the loading scenario 3.

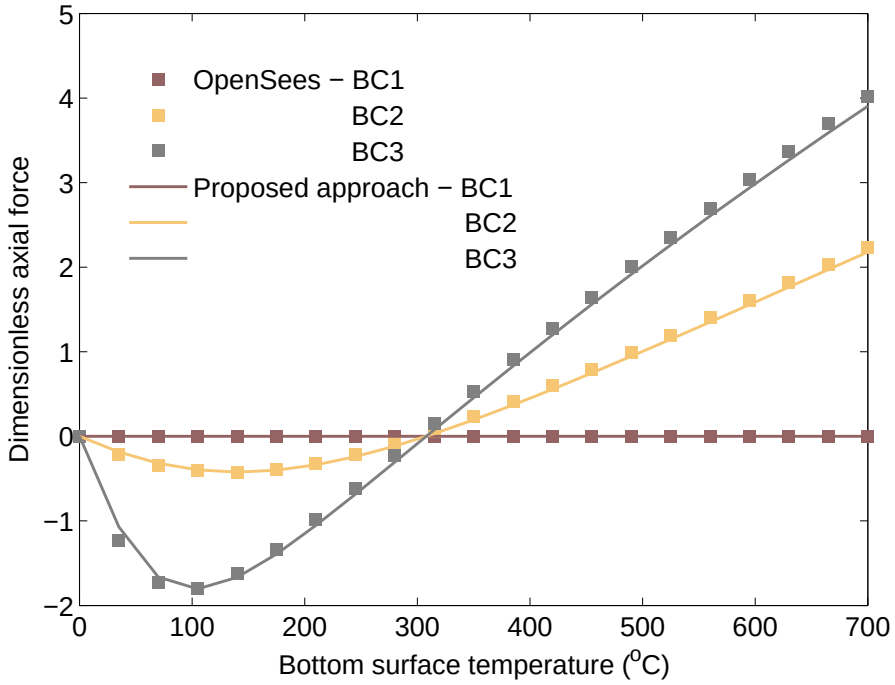

Figure 4.12 Dimensionless axial force in a heated beam subject to the loading scenario 3.

4.5.2 Beam subject to transversely non-unform heating

For the analysis of thermally induced large displacements of beams, interest lies mainly in the variation of temperature through the depth of the beam. Since the

aim is examining the effect of different non-uniform temperature profiles on the beam response, steady-state conditions are assumed. There are various methods for determining such a one-dimensional temperature profile. A popular method is carrying out an FE heat transfer analysis.

Within the context of structural performance in fire, the Fortran FE code reported by Huang and Usmani (1994) is chosen as an efficient approach. The data are calculated for a beam with thickness of 0.2m using a typical exponential time-temperature relation for the gas temperature in a compartment given as (Usmani *et al.*, 2003)

$$\theta(t) = \theta_0 + (\theta_{max} - \theta_0)\,[1 - \exp(-\eta t)] \tag{4.35}$$

where θ_0 is the ambient temperature (20°C), θ_{max} is the maximum temperature, η is a parameter controlling the 'rate of heating', and t is an artificial time variable considered to only provide a sensitivity analysis to the current computation. Imposing fire at the bottom surface of the beam, two extreme cases of high and low rates of heating are studied:

1. A "short hot" exponential fire representing a high heating rate ($\eta = 0.005$) with a maximum temperature of 1000°C when the bottom surface of the beam is heated for 1,200 s.

2. A "Long cool" exponential fire representing a low heating rate ($\eta = 0.001$) with a maximum temperature of 650°C when the bottom surface of the beam is heated for 21,600 s.

Accordingly, the imposed heating may vary slowly with time or may be sustained over long periods of time as illustrated in Figures 4.13 and 4.14. The through-depth temperature distributions in the beam for both fire conditions are determined and are shown in Figures 4.15 and 4.16 for different times during heating. As shown in Figure 4.17, a further analysis is carried out for the particular cases of heating rate parameter η fitting the chosen fire time-temperature curves. The generalised expression is obtained as

$$\theta(z) = \theta_0 + (\theta_{max} - \theta_0)\exp\left[\mu\left(\frac{z}{h} + \frac{1}{2}\right)\right] \tag{4.36}$$

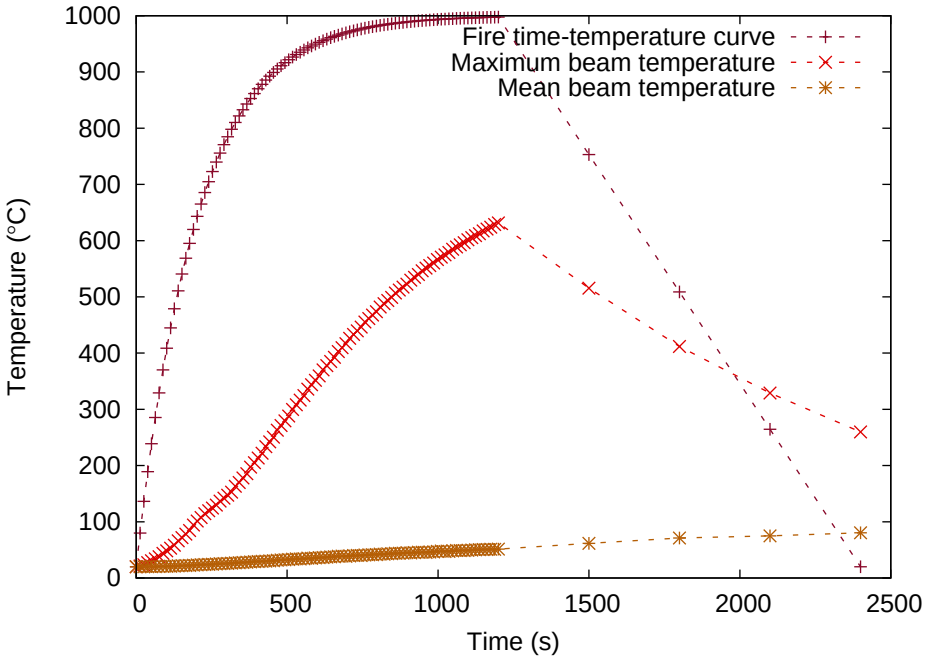

(a) Maximum and minimum temperatures

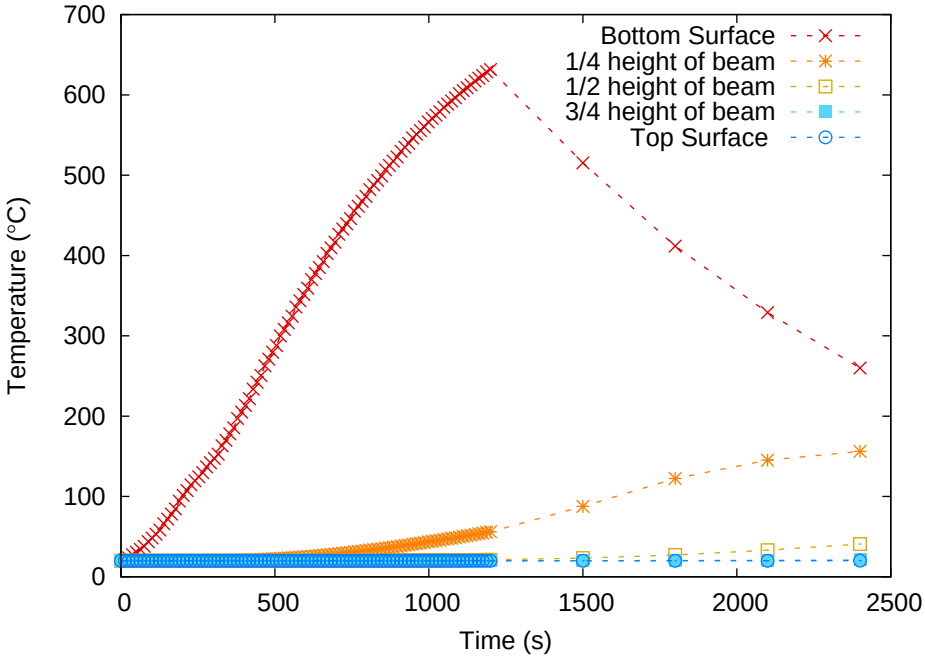

(b) Temperature at various heights

Figure 4.13 Time-temperature curves for a beam subject to the short hot fire scenario.

where the rate of change in the temperature is governed by the dimensionless parameter μ. Clearly, the thermal curvature is greater when μ is higher. Note that, the temperature distribution is constant for $\mu = 0$. For the chosen fire scenarios, the

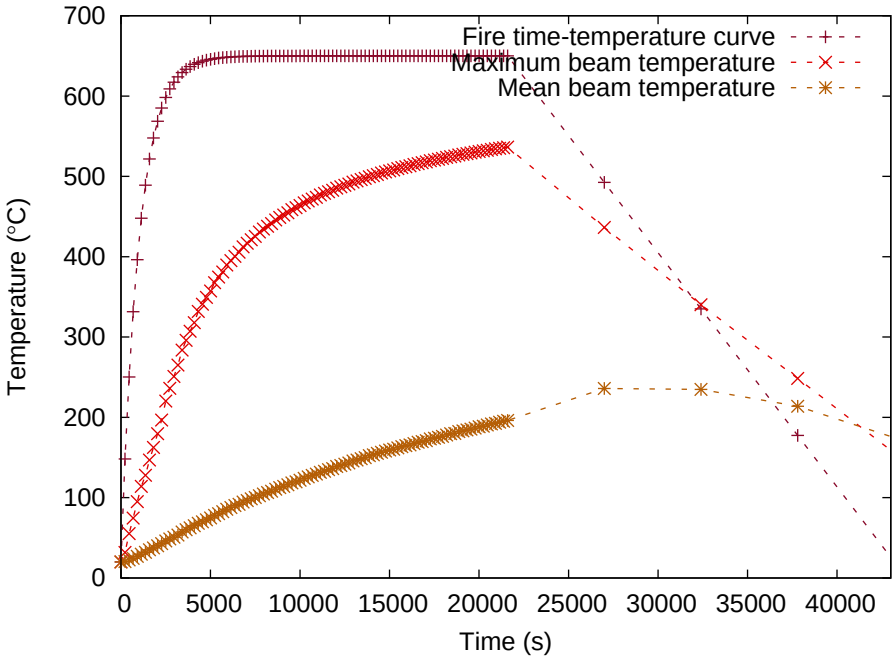

(a) Maximum and minimum temperatures

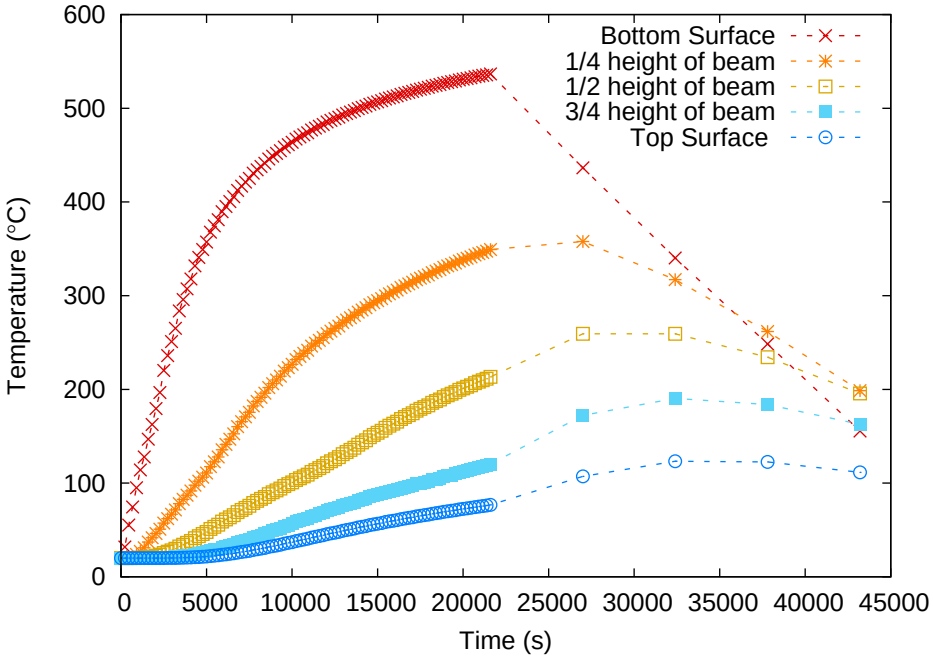

(b) Temperature at various heights

Figure 4.14 Time-temperature curves for a beam subject to the long cool fire scenario.

through-depth temperature profiles are achieved by the following expressions for the low heating rate

$$\theta(z) = 20.37 + 275.54 \exp\left[-6\left(\frac{z}{h} + \frac{1}{2}\right)\right] \tag{4.37}$$

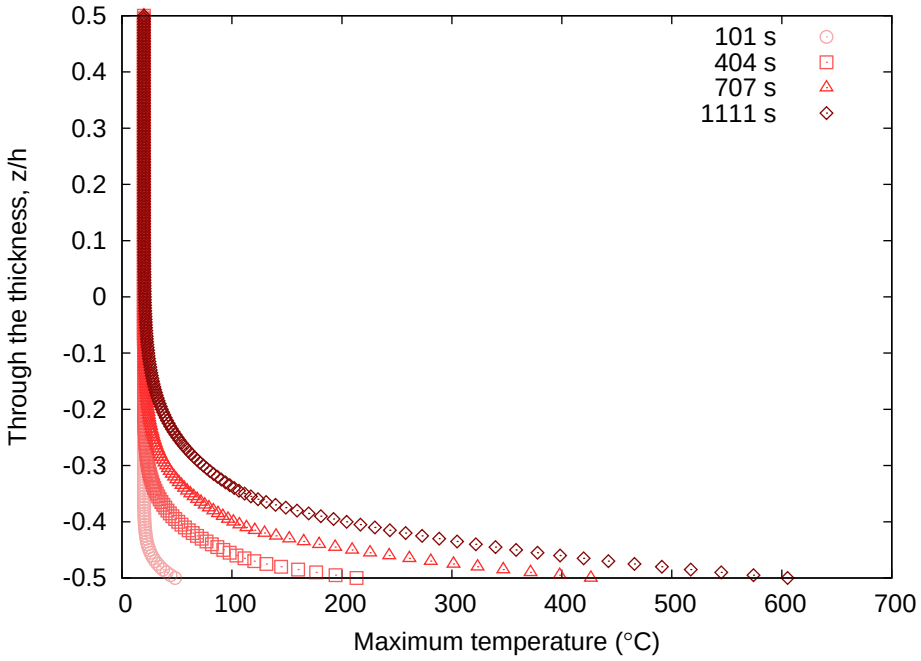

Figure 4.15 Fire induced through-depth temperature distribution for a beam under the short hot fire.

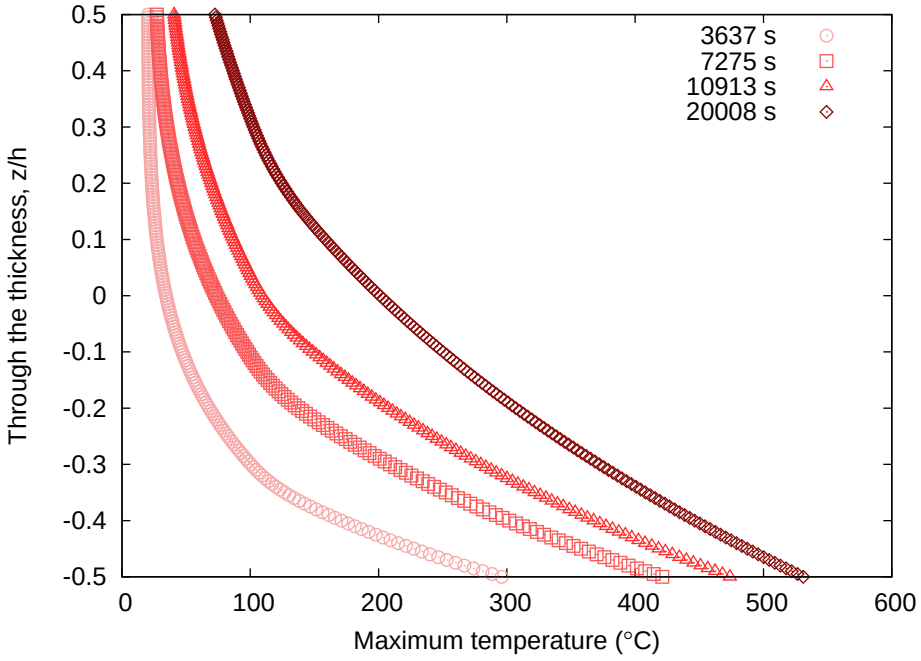

Figure 4.16 Fire induced through-depth temperature distribution for a beam under the long cool fire.

and for the high heating rate

$$\theta(z) = 20 + 585.27 \exp\left[-12.5\left(\frac{z}{h} + \frac{1}{2}\right)\right] \tag{4.38}$$

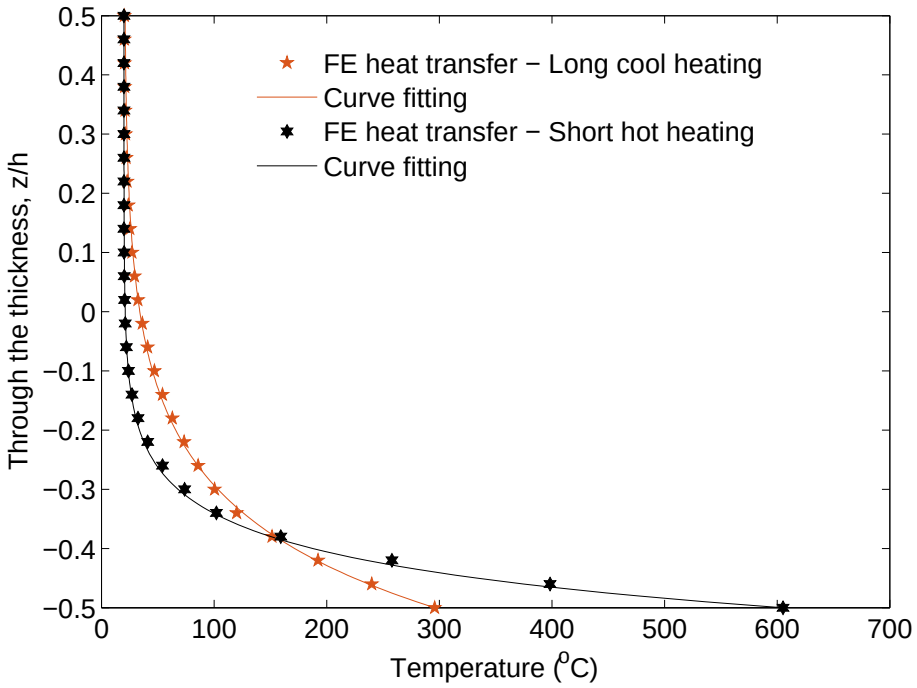

Figure 4.17 Non-uniform temperature distributions over the thickness of the beam using the FE heat transfer analysis. The assumed curve fitting functions correspond to the high and low rates of heating.

In Figure 4.18, the dimensionless central deflection of a beam with the chosen BCs under both the short hot and long cool fire conditions is plotted. As can be seen, the

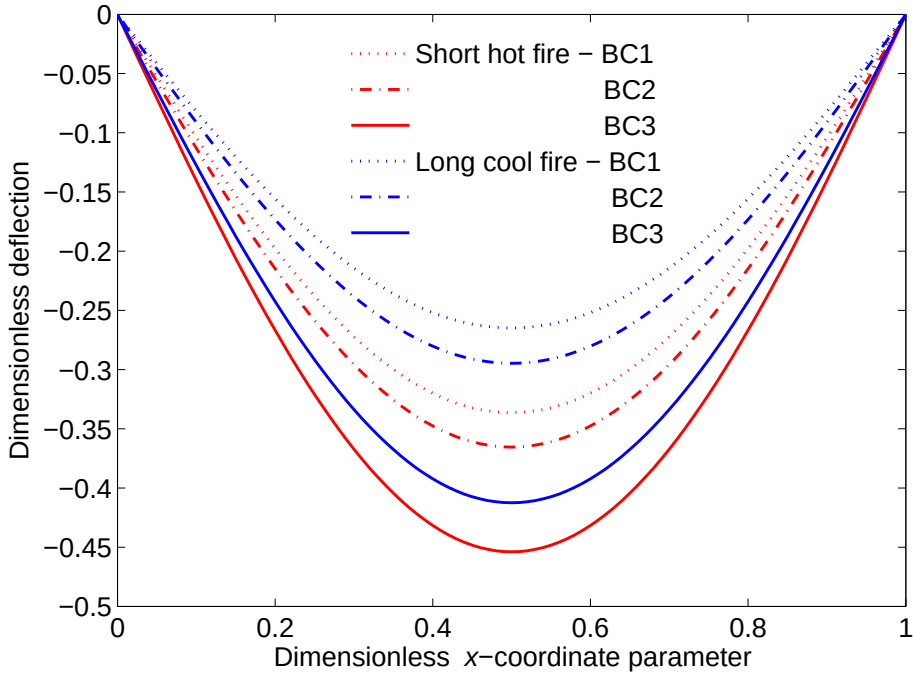

Figure 4.18 Dimensionless deflection profile of a beam with three different elastically restrained ends under short hot and long cool fire conditions.

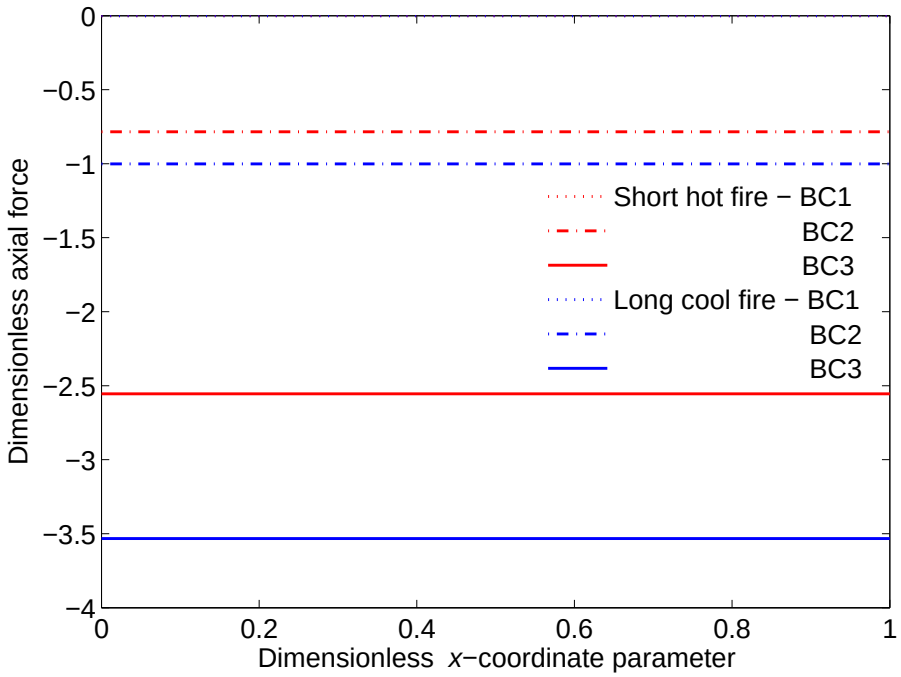

Figure 4.19 Dimensionless axial force in a beam with three different elastically restrained ends under short hot and long cool fire conditions.

beam with BC3 has the largest deflection compared with that for other BCs. Moreover, the short hot fire has resulted in larger deflection for the beams. Figure 4.19 shows the dimensionless axial forces in the same beams. As expected, the axial force in the beams are constant. Unlike the deflection, the largest axial forces are produced in the case of the long cool fire condition. That is because under the short hot fire condition, the thermal bowing effect is more dominant in the beam when compared with the beam under the long cool fire condition and thus most of the thermal expansion effect is cancelled out, producing less axial force.

4.6 Summary

A series of fundamental solutions were presented for single beams with finite end restraint subject to thermomechanical loads. The performance of the implemented codes for thermal beam element in OpenSees was verified well in comparison with the theoretical analyses. Only one term was used in the displacement series to achieve the final solutions. The examples considered emphasised on the greatest contribution of the thermal gradient to the beam nonlinear response. The proposed formulation is very useful for verification of other new software packages based on the FEM.

Chapter 5

Geometrically Nonlinear Behaviour of Rectangular Plates[1]

5.1 Introduction

A preliminary study of the large deflections of plate structures was presented by Levy (1942) who employed the double Fourier series for analysis of simply supported plates. Berger (1955) presented relatively accurate solutions for deflections and stresses of a flat plate with large deflections. He simplified the differential governing equations of the problem by neglecting terms in the strain energy. Timoshenko and Woinowsky-Krieger (1959) made a significant contribution to the understanding of the response of plates to various forces and moments. A combination of trigonometric and hyperbolic functions was used by Iyengar and Naqvi (1966) to study the nonlinear response of plates with either laterally unrestrained or restrained BCs.

The complexity caused by the nonlinear out-of-plane (or transverse) displacements often precludes employing analytical techniques to solve engineering problems. Recourse is made to numerical techniques, such as the FEMs (Zienkiewicz *et al.*, 1971; Hughes *et al.*, 1977; Belytschko *et al.*, 1981; Lee and Wong, 1982; Belytschko and Tsay, 1983; Bathe and Dvorkin, 1985; Bathe and Dvorkin, 1986; Hinton and Huang, 1986; Batoz and Lardeur, 1989; Oñate *et al.*, 1992; Zienkiewicz *et al.*, 1993; Ibrahimbegović, 1993; Katili, 1993b; Katili, 1993a; Taylor and Auricchio, 1993; Ayad *et al.*, 1998; Soh *et al.*, 1999; Ayad and Rigolot, 2002; Zhang and Kuang, 2007; Plaut,

[1] Based on the works reported by Khazaeinejad *et al.* (2012) and Khazaeinejad *et al.* (2014).

2014) or meshless methods (Sladek and Sladek, 2003; Sladek *et al.*, 2008c; Sladek *et al.*, 2013) to achieve solutions but this may not always be the best approach in practical applications. Nonlinear problems are, however, difficult to handle by means of current numerical methods. Application of hybrid Trefftz FEMs (HT-FEMs) to nonlinear problems was first introduced by Qin (1995). He developed a triangular HT element with 5 DoFs at each corner node for post-buckling analysis of thin plates subjected to uniform compressive loads. Nonlinear terms due to geometric nonlinearity were treated as pseudo-distributed loads by using the incremental form of governing equations of the problem. As a result, in-plane and out-of-plane displacements were uncoupled and an iterative approach was then used to evaluate the nonlinear terms. A modified variational principle (Qin, 1994) was used to construct the HT formulation. Qin used a similar approach to develop a quadrilateral HT element for the numerical solution of post-buckling analysis of thin plates resting on elastic foundations (Qin, 1997), a quadrilateral HT element (with 5 DoFs at each corner node and 1 DoF at each mid-side node) for nonlinear analysis of thick plates based on the Reissner-Mindlin plate theory (Qin, 1996a), and a HT-FE model with p-method capabilities for thick plates on elastic foundations (Qin and Diao, 1996).

An application of the boundary element method to nonlinear large deformation analysis of Reissner-Mindlin plate was presented by Wen *et al.* (2005). A load incremental technique was employed to solve the nonlinear equations. The domain integrals containing the nonlinear terms were transformed to boundary integrals using the dual reciprocity method. The efficiency and accuracy of this method was demonstrated for a simply supported square plate and a clamped circular plate both subjected to a uniform load. It was later extended by Wen *et al.* (2006) to account for the nonlinear response of plates to in-plane edge loads with imperfections initiated by small pressure load normal to the plate. The load increment procedure used was simple and not efficient for plates under large loads due to the geometric nonlinearity in the problem. Wen and Hon (2007) extend the meshless collocation method to develop a geometrically nonlinear analysis for large deformations of Reissner plate bending problems. They used load increment algorithm and full load algorithm to solve the nonlinear equations. Their method was simple and efficient for treating

certain complex problems, but it required a considerable number of collocation points to achieve the final solution when large loads were applied in the problem.

Using the discrete singular convolution and harmonic differential quadrature methods, Civalek (2007) numerically solved the geometrically nonlinear static and dynamic problems of thin rectangular plates resting on elastic foundation. The governing nonlinear partial differential equations of the plate were discretised in space and time domains using the discrete singular convolution algorithm and harmonic differential quadrature method, respectively. It was found that lower damping coefficient results in larger deflections for the plate. Zhao *et al.* (2008) used a linearly conforming radial point interpolation method to study the geometric nonlinear problem of plates. The nonlinearity was considered in the membrane strain, while the bending and shear strains were assumed linear. Both the radial and polynomial basis functions were employed to construct the shape functions. Al-Gahtani and Naffa'a developed a meshless formulation for the large deflection analysis of thin plates with laterally unrestrained BC (Al-Gahtani and Naffa'a, 2009) and restrained BC (Al-Gahtani and Naffa'a, 2009) subjected to a uniform load. A fifth-order polynomial radial basis function used to approximate displacement components of the plate. The maximum error for solutions were found near the corners of the plate. Based on the known flexural stiffness for a bimodular thin plate in small-deflection bending, He *et al.* (2012) obtained the von Kármán equations with different moduli in tension and compression. The perturbation method and the displacement variation method were used to solve the governing equations. They reported that the introduction of different moduli will eventually influence the yield stress at the edge and centre of the plate.

Sun *et al.* (2012) used a static-dynamic approach to extend the capability of the Vulcan software to model the static and dynamic behaviour of steel structures during both local and global progressive collapse of the structures under fire conditions. Alongside the advances in computational tools, analytical and semi-analytical techniques have also extensively been used for analysing nonlinear plate problems. Luo (2000) introduced an approximate theory for the geometrically nonlinear analysis of plates. The exact geometry of the deformed middle surface of the plate was used for the determination of the physical strains and equilibrium equations of the plates. Using

the Love–Kirchoff assumption, Byklum and Amdahl (2002) presented a simplified computational model for the elastic large deflection analysis of plates and stiffened panels due to buckling. The edges of the plate were laterally unrestrained, but forced to remain straight after deformation, representing the support from neighboring plates in large structures. The energy equations were integrated analytically, but were solved numerically.

De Holanda and Gonçalves (2003) developed a nonlinear FE formulation based on the Marguerre's nonlinear shallow shell theory (a modified version of Mindlin's hypothesis) to model the buckling and the large deflection post-buckling behaviour of perfect and geometrically imperfect plates on a tensionless elastic foundation subjected to in-plane compressive forces. They reported that in practical applications where the supporting media cannot provide tensile reactions, the unilateral character of the foundation should properly be taken into account in the analysis to avoid errors. An analytical work by Wang and El-Sheikh (2005) on the mechanical aspect of the nonlinear response of rectangular plates showed the significant effects of the degree of restraint at the plate boundaries on the development of large displacements in the plate. This is, however, not been fully investigated on plates under thermomechanical loads and there is relatively scant research in this area in the literature (Lin *et al.*, 1994; Ma and Wang, 2003; Abu *et al.*, 2013). In fact, more often the mechanical and thermal aspects of the plate nonlinear response are investigated separately using either analytical approaches or numerical methods.

Motivated by this opportunity, a mathematical model is developed in this chapter to analyse the large displacements of thin rectangular plates under thermal, mechanical and combined thermomechanical loading. The temperature profile is assumed to vary non-uniformly over the plate thickness.

5.2 Basic relations

A rectangular plate of length a, width b, and uniform thickness h subjected to a UDL and a thermal gradient (caused by a heat source) across its thickness is considered as shown in Figure 5.1, where the Cartesian coordinates system (x, y, z) is set on the middle surface of the plate. The plate experiences large displacements which requires using appropriate strain definitions, including mechanical and thermal strains.

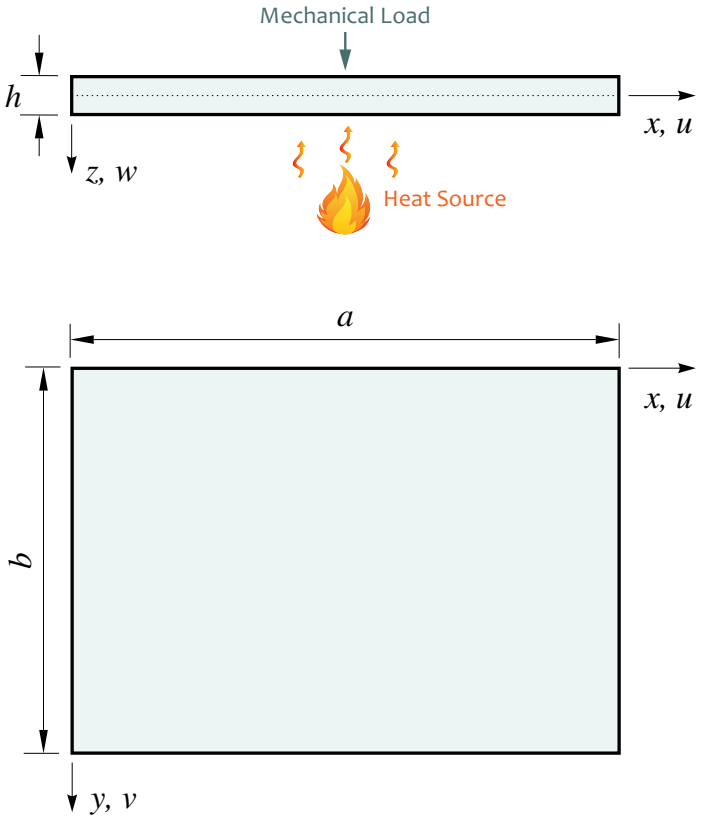

Figure 5.1 A schematic view of a rectangular plate subjected to a UDL and a thermal gradient across its thickness.

The former is caused by stress resulting from external loads or restraint to thermal expansion and the latter is caused by thermal expansion. To formulate the kinematic relations, the von Kármán type of large displacement theory is employed.

By combining equations (3.27a)-(3.27c), the membrane strain components (including thermal strains) are written as

$$\begin{Bmatrix} \varepsilon_{xx} \\ \varepsilon_{yy} \\ \gamma_{xy} \end{Bmatrix} = \frac{1}{Eh} \begin{Bmatrix} N_{xx} - \nu N_{yy} + N^{\theta} \\ N_{yy} - \nu N_{xx} + N^{\theta} \\ 2(1+\nu)N_{xy} \end{Bmatrix} \tag{5.1}$$

where h is the plate thickness, E is the elastic modulus of the plate, ν is the Poisson's ratio of the plate, α is the coefficient of thermal expansion of the plate, θ describes

the temperature changes across the plate thickness, and N_{xx}, N_{yy} and N_{xy} are forces defined via stress function F as follows

$$\begin{Bmatrix} N_{xx} \\ N_{yy} \\ N_{xy} \end{Bmatrix} = h \begin{Bmatrix} \frac{\partial^2 F}{\partial y^2} \\ \frac{\partial^2 F}{\partial x^2} \\ -\frac{\partial^2 F}{\partial x \partial y} \end{Bmatrix} \tag{5.2}$$

The stress function F is an unknown parameter that will be determined based on the BCs assumed at the plate boundaries.

To quantify the nonlinear distribution of membrane and bending stresses within an elastic rectangular plate due to thermomechanical loads, the compatibility and equilibrium equations must be solved simultaneously. The former relates the axial forces to the out-of-plane displacement of the plate whereas the latter relates the internal membrane forces due to large displacements to the out-of-plane displacement of the plate.

5.3 Derivation of governing equations

The compatibility equation can be obtained by taking the second derivatives of the strains and combining the resulting expressions as follows

$$\frac{\partial^2 \varepsilon_{xx}}{\partial y^2} + \frac{\partial^2 \varepsilon_{yy}}{\partial x^2} - \frac{\partial^2 \gamma_{xy}}{\partial x \partial y} = \left(\frac{\partial^2 w}{\partial x \partial y}\right)^2 - \left(\frac{\partial^2 w}{\partial x^2}\right)\left(\frac{\partial^2 w}{\partial y^2}\right) \tag{5.3}$$

Substituting equations (5.1) into equation (5.3), we obtain

$$\begin{aligned} &\frac{\partial^4 F}{\partial x^4} + 2\frac{\partial^4 F}{\partial x^2 \partial y^2} + \frac{\partial^4 F}{\partial y^4} - E\left[\left(\frac{\partial^2 w}{\partial x \partial y}\right)^2 - \left(\frac{\partial^2 w}{\partial x^2}\right)\left(\frac{\partial^2 w}{\partial y^2}\right)\right] \\ &+ \frac{1}{h}\left(\frac{\partial^2 N^\theta}{\partial x^2} + \frac{\partial^2 N^\theta}{\partial y^2}\right) = 0 \end{aligned} \tag{5.4}$$

In considering the bending of plates under the combined action of transverse loads and forces in the middle plane of the plate, the contribution of the latter forces must be taken into account in the formulation. The system of these forces for a small element cut from the plate are shown in Figure 5.2. Their magnitudes per unit length

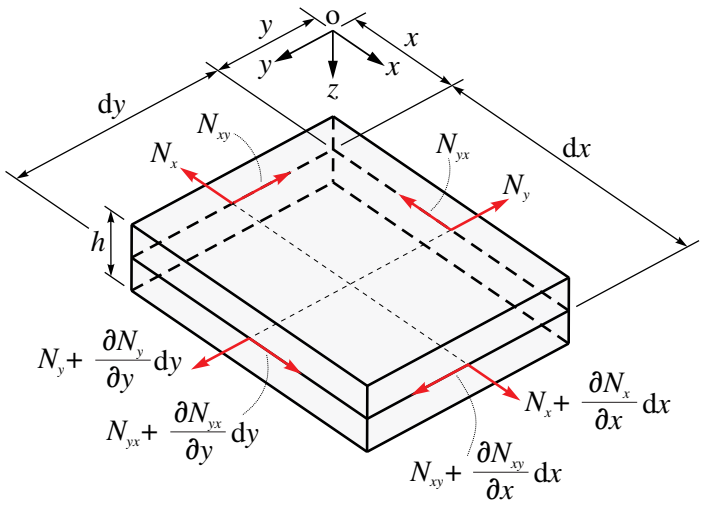

Figure 5.2 Stress resultants in a small element cut from a plate subject to a transverse mechanical load.

are denoted by N_x, N_y, and N_{xy}. The sign convention adopted here for the shear forces and the twisting moments is that the vectors along the $+z$ axis produce positive shear force and moment. Accordingly, all the moments and shear forces acting on the plate element in Figure 5.3 are taken as positive. For such system of forces, considering all the forces on the x and y axes and in the absence of body forces, the following equilibrium equations are obtained:

$$N_x + \frac{\partial N_x}{\partial x}\,dx + \frac{\partial N_{xy}}{\partial y}\,dx = 0 \tag{5.5a}$$

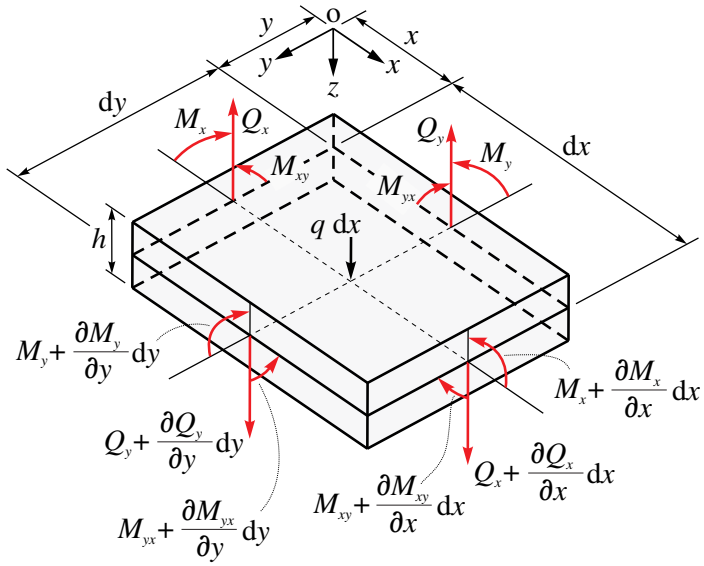

Figure 5.3 Moment and shear force resultants in a small element cut from a plate subject to a transverse mechanical load.

$$N_y + \frac{\partial N_y}{\partial y}\,\mathrm{d}y + \frac{\partial N_{xy}}{\partial x}\,\mathrm{d}x = 0 \tag{5.5b}$$

from which we can obtain the following equations

$$\frac{\partial N_x}{\partial x} + \frac{\partial N_{xy}}{\partial y} = 0 \tag{5.6a}$$

$$\frac{\partial N_{xy}}{\partial x} + \frac{\partial N_y}{\partial y} = 0 \tag{5.6b}$$

The contribution of the normal and shear forces to the bending of the plate are as follows:

i. Contribution of N_x in the z axis:

$$-N_x\,\mathrm{d}y\,\frac{\partial w}{\partial x} + \left(N_x + \frac{\partial N_x}{\partial x}dx\right)\left(\frac{\partial w}{\partial x} + \frac{\partial^2 w}{\partial x^2}\right)\,\mathrm{d}y \tag{5.7}$$

It can be simplified by neglecting the higher order terms which are small when compared to unity

$$N_x\frac{\partial^2 w}{\partial x^2}\,\mathrm{d}x\,\mathrm{d}y + \frac{\partial N_x}{\partial x}\frac{\partial w}{\partial x}\,\mathrm{d}x\,\mathrm{d}y \tag{5.8}$$

ii. Contribution of N_y in the z axis:

$$-N_y\,\mathrm{d}y\,\frac{\partial w}{\partial x} + \left(N_x + \frac{\partial N_x}{\partial x}\,\mathrm{d}x\right)\left(\frac{\partial w}{\partial x} + \frac{\partial^2 w}{\partial x^2}\right)\,\mathrm{d}y \tag{5.9}$$

which can be simplified as

$$N_y\frac{\partial^2 w}{\partial y^2}\,\mathrm{d}x\,\mathrm{d}y + \frac{\partial N_y}{\partial y}\frac{\partial w}{\partial y}\,\mathrm{d}x\,\mathrm{d}y \tag{5.10}$$

iii. Contribution of N_{xy} in the z axis:

$$\begin{aligned} &N_{xy}\,\mathrm{d}x\,\frac{\partial w}{\partial y} + \left(N_{xy} + \frac{\partial N_{xy}}{\partial x}\,\mathrm{d}x\right)\left(\frac{\partial w}{\partial y} + \frac{\partial^2 w}{\partial x \partial y}\,\mathrm{d}x\right)\,\mathrm{d}y \\ &+ N_{yx}\,\mathrm{d}y\,\frac{\partial w}{\partial x} + \left(N_{yx} + \frac{\partial N_{yx}}{\partial y}\,\mathrm{d}y\right)\left(\frac{\partial w}{\partial x} + \frac{\partial^2 w}{\partial x \partial y}\,\mathrm{d}y\right)\,\mathrm{d}x \end{aligned} \tag{5.11}$$

which can be simplified as

$$2N_{xy}\frac{\partial^2 w}{\partial x \partial y}\,\mathrm{d}x\,\mathrm{d}y + \frac{\partial N_{xy}}{\partial x}\frac{\partial w}{\partial y}\,dx\,dy + \frac{\partial N_{xy}}{\partial y}\frac{\partial w}{\partial x}\,\mathrm{d}x\,\mathrm{d}y \tag{5.12}$$

Thus, the total contribution of normal and shear forces in the z axis can be expressed by

$$\begin{aligned} &N_x\frac{\partial^2 w}{\partial x^2}\,\mathrm{d}x\,\mathrm{d}y + N_y\frac{\partial^2 w}{\partial y^2}\,\mathrm{d}x\,\mathrm{d}y + 2N_{xy}\frac{\partial^2 w}{\partial x \partial y}\,\mathrm{d}x\,\mathrm{d}y \\ &+ \underbrace{\left(\frac{\partial N_x}{\partial x} + \frac{\partial N_{xy}}{\partial y}\right)}_{=0,\text{ from equation}(5.6a)}\frac{\partial w}{\partial x}\,\mathrm{d}x\,\mathrm{d}y + \underbrace{\left(\frac{\partial N_y}{\partial y} + \frac{\partial N_{xy}}{\partial x}\right)}_{=0,\text{ from equation}(5.6b)}\frac{\partial w}{\partial y}\,\mathrm{d}x\,\mathrm{d}y \end{aligned} \tag{5.13}$$

Considering the forces and moments shown in Figure 5.3, the following three independent conditions of equilibrium can be obtained:

i. Force equilibrium in the z axis including the contribution of normal and shear forces in equation (5.13)

$$\begin{aligned} &\frac{\partial Q_x}{\partial x}\,\mathrm{d}x\,\mathrm{d}y + \frac{\partial Q_y}{\partial y}\,\mathrm{d}y\,\mathrm{d}x + N_x\frac{\partial^2 w}{\partial x^2}\,\mathrm{d}x\,\mathrm{d}y \\ &+ N_y\frac{\partial^2 w}{\partial y^2}\,\mathrm{d}x\,\mathrm{d}y + 2N_{xy}\frac{\partial^2 w}{\partial x \partial y}\,\mathrm{d}x\,\mathrm{d}y + q\,\mathrm{d}x\,\mathrm{d}y = 0 \end{aligned} \tag{5.14}$$

from which the following equation can be obtained

$$\frac{\partial Q_x}{\partial x} + \frac{\partial Q_y}{\partial y}N_x\frac{\partial^2 w}{\partial x^2} + N_y\frac{\partial^2 w}{\partial y^2} + 2N_{xy}\frac{\partial^2 w}{\partial x \partial y} + q = 0 \tag{5.15}$$

where q represents the UDL.

ii. Moment equilibrium about the x axis

$$\frac{\partial M_{xy}}{\partial x}\,\mathrm{d}x\,\mathrm{d}y + \frac{\partial M_y}{\partial y}\,\mathrm{d}x\,\mathrm{d}y - Q_y\,\mathrm{d}x\,\mathrm{d}y = 0 \tag{5.16}$$

from which the following equation can be obtained

$$\frac{\partial M_{xy}}{\partial x} + \frac{\partial M_y}{\partial y} - Q_y = 0 \tag{5.17}$$

iii. Moment equilibrium about the y axis

$$\frac{\partial M_{yx}}{\partial y}\,\mathrm{d}x\,\mathrm{d}y + \frac{\partial M_x}{\partial x}\,\mathrm{d}x\,\mathrm{d}y - Q_x\,\mathrm{d}x\,\mathrm{d}y = 0 \tag{5.18}$$

from which the following equation can be obtained

$$\frac{\partial M_{yx}}{\partial y} + \frac{\partial M_x}{\partial x} - Q_x = 0 \tag{5.19}$$

From the equations (5.17) and (5.19), the shear forces can be expressed by

$$Q_x = \frac{\partial M_{yx}}{\partial y} + \frac{\partial M_x}{\partial x} \tag{5.20a}$$

$$Q_y = \frac{\partial M_{xy}}{\partial x} + \frac{\partial M_y}{\partial y} \tag{5.20b}$$

Substituting equation (5.20) into equation (5.15), yields the following equilibrium equation:

$$\frac{\partial^2 M_{xx}}{\partial x^2} + 2\frac{\partial^2 M_{xy}}{\partial x \partial y} + \frac{\partial^2 M_{yy}}{\partial y^2} + N_{xx}\frac{\partial^2 w}{\partial x^2} + N_{yy}\frac{\partial^2 w}{\partial y^2} + 2N_{xy}\frac{\partial^2 w}{\partial x \partial y} + q = 0 \tag{5.21}$$

After substitution from equations (3.28) into equation (5.21) and taking into account that $M_{xy} = M_{yx}$, the equilibrium equation for large displacements of elastic plates is given by (Timoshenko and Woinowsky-Krieger, 1959)

$$\begin{aligned}
&\frac{\partial^4 w}{\partial x^4} + 2\frac{\partial^4 w}{\partial x^2 \partial y^2} + \frac{\partial^4 w}{\partial y^4} - \frac{h}{D}\left[\frac{q}{h} + \left(\frac{\partial^2 F}{\partial y^2}\right)\left(\frac{\partial^2 w}{\partial x^2}\right)\right. \\
&\left. - 2\left(\frac{\partial^2 F}{\partial x \partial y}\right)\left(\frac{\partial^2 w}{\partial x \partial y}\right) + \left(\frac{\partial^2 F}{\partial x^2}\right)\left(\frac{\partial^2 w}{\partial y^2}\right)\right] \\
&+ \frac{1}{D}\left(\frac{\partial^2 M^\theta}{\partial x^2} + \frac{\partial^2 M^\theta}{\partial y^2}\right) = 0
\end{aligned} \tag{5.22}$$

In order to solve the resulting governing equations, BCs must be specified.

5.4 Boundary conditions

For the kind of problems considered in the paper, two common types of support conditions are considered. The in-plane displacements are:

i. unrestrained against lateral translations, while the out-of-plane displacement is zero along the plate boundaries and rotations are free (Woo and Meguid, 2001; Li *et al.*, 2004). In plates with such constraints undergoing large displacements, a degree of TMA can still occur. A feature of this mechanism is the appearance of a "compressive ring" in the plate as a manifestation of compressive

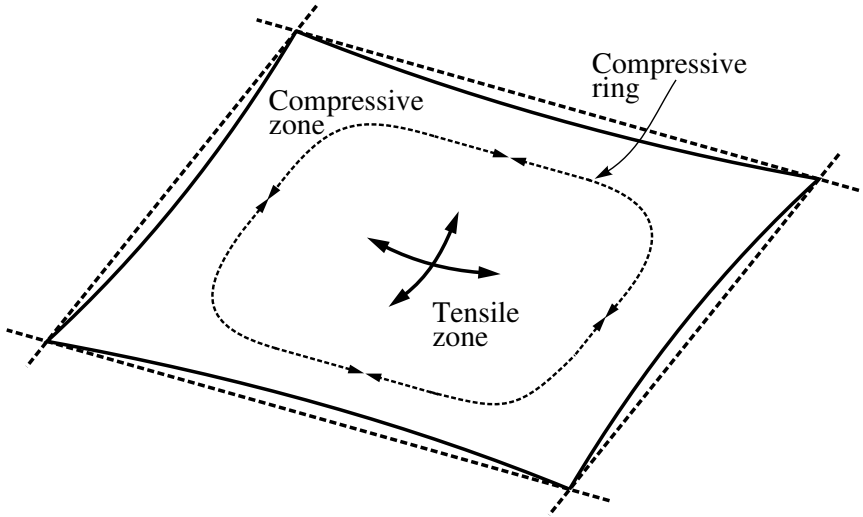

(a) Laterally unrestrained BC

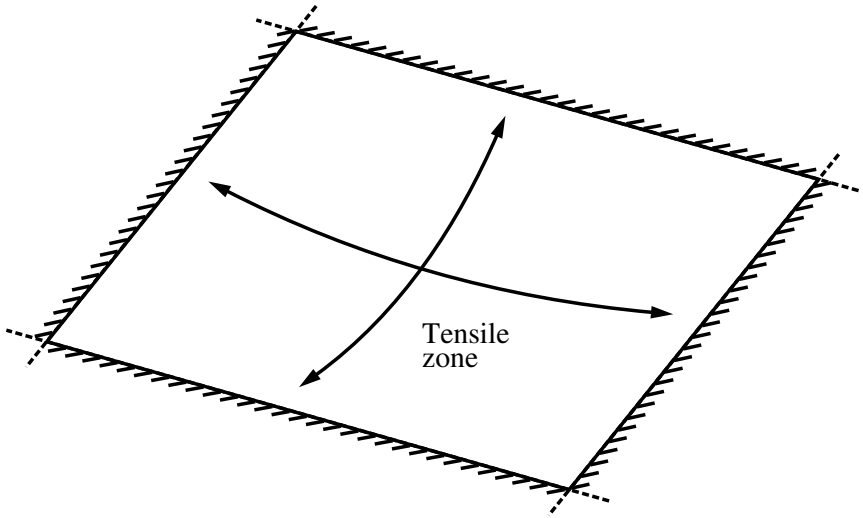

(b) Laterally restrained BC

Figure 5.4 Schematic views of the BCs specified for the plate. At large vertical displacements, TMA typically develops through restraining lateral translation at the boundaries, however, when translation across boundaries is unrestrained, a "compressive ring" appears which provides restraint to TMA occurring in the central region of the plate.

membrane action in the outer regions of the plate which provides restraint to TMA occurring in the central region of the plate, not dissimilar to the relatively rigid ring surrounding a trampoline. These features are shown schematically in Figure 5.4a. This boundary case can be used to analyse simply supported slabs where under large displacement conditions the plate flexural resistance may be supplemented by TMA supported by a ring of compression around it. This BC is referred to as the 'laterally unrestrained' BC.

ii. restrained to lateral translations, while the out-of-plane displacement is zero along the plate boundaries and rotations are free (Levy, 1942; Timoshenko and Woinowsky-Krieger, 1959; Wang and El-Sheikh, 2005; Alinia and Ghannadpour, 2009; Jayakumar *et al.*, 2013). In this case, TMA typically develops at large out-of-plane displacements, anchored by restraint to lateral translation at the boundaries as shown in Figure 5.4b. This type of BC can be used to analyse slabs or floor systems restrained by the surrounding structure. This type of BC is referred to as the 'laterally restrained' BC.

The aforementioned BCs are reasonable limiting cases bracketing the conditions that may be found in real structural frames. These BCs allow investigating the influence of in-plane conditions on the nonlinear response of plates.

5.5 Solution of governing equations

To solve the governing equations, the out-of-plane displacement can be expanded using a double Fourier series as follows

$$w(x,y) = \sum_{m=1}^{\infty}\sum_{n=1}^{\infty} w_{mn} S_{mn} \tag{5.23}$$

where $S_{mn} = \sin(m\pi x/a)\sin(n\pi y/b)$. In a similar way, different transverse mechanical loading conditions can be considered by expanding the traction q in equation (5.15) into a double Fourier series as follows

$$q(x,y) = \sum_{m=1}^{\infty}\sum_{n=1}^{\infty} q_{mn} S_{mn} \tag{5.24}$$

where the coefficient of the series is given by (Timoshenko and Woinowsky-Krieger, 1959)

$$q_{mn} = \frac{4}{ab}\int_0^a \int_0^b q(x,y) S_{mn}\, \mathrm{d}y\, \mathrm{d}x \tag{5.25}$$

The following loading conditions can be derived for the plate:

For uniform loading of magnitude q_0:

$$q_{mn} = \frac{4[-1+(-1)^m][-1+(-1)^n]}{mn\pi^2} q_0 \tag{5.26}$$

For sinusoidal loading of magnitude q_0 where $m = n = 1$:

$$q_{mn} = q_0 \tag{5.27}$$

For point load of q_0 applied at coordinates (x_0,y_0):

$$q_{mn} = \frac{4q_0}{ab} \sin\frac{m\pi x_0}{a} \sin\frac{n\pi y_0}{b} \tag{5.28}$$

The thermal resultants N^θ and M^θ may also be taken in the same form as the mechanical loading

$$\left\{ \begin{array}{c} N^\theta(x,y) \\ M^\theta(x,y) \end{array} \right\} = \sum_{m=1}^{\infty}\sum_{n=1}^{\infty} \left\{ \begin{array}{c} N^\theta_{mn} \\ M^\theta_{mn} \end{array} \right\} S_{mn} \tag{5.29}$$

where the coefficients N^θ_{mn} and M^θ_{mn} can be calculated by performing the Fourier integration:

$$\begin{aligned} \left\{ \begin{array}{c} N^\theta_{mn} \\ M^\theta_{mn} \end{array} \right\} &= \frac{4}{ab}\int_0^a \int_0^b \left\{ \begin{array}{c} N^\theta \\ M^\theta \end{array} \right\} S_{mn}\, \mathrm{d}y\, \mathrm{d}x \\ &= \frac{4(-1+(-1)^m)(-1+(-1)^n)}{mn\pi^2} \left\{ \begin{array}{c} N^\theta \\ M^\theta \end{array} \right\} \end{aligned} \tag{5.30}$$

For the Airy stress function, an expression satisfying the stress-free edges case (for the laterally unrestrained BC) and undeformed edges case (for the laterally restrained BC) may then be taken as

$$F(x,y) = \frac{P_x y^2}{2bh} + \frac{P_y x^2}{2ah} + \sum_{m=1}^{\infty}\sum_{n=1}^{\infty} F_{mn} S_{mn} \tag{5.31}$$

where P_x and P_y are the total loads that prevent the edges from moving in the axial direction, applied at $x = 0, a$ and $y = 0, b$, respectively. For the laterally unrestrained BC, such loads are zero. In contrast, if the support conditions corresponding to the laterally restrained BC are imposed, then P_x and P_y are nonzero and can be obtained via the elongation of the plate in the x and y directions as follows

$$\int_0^a \frac{\partial u}{\partial x} \mathrm{d}x = \int_0^a \left\{ \frac{1}{E}\left(\frac{\partial^2 F}{\partial y^2} - \nu \frac{\partial^2 F}{\partial x^2}\right) - \frac{1}{2}\left(\frac{\partial w}{\partial x}\right)^2 + \frac{N^\theta}{Eh} \right\} \mathrm{d}x \tag{5.32a}$$

$$\int_0^b \frac{\partial v}{\partial y} \mathrm{d}y = \int_0^b \left\{ \frac{1}{E}\left(\frac{\partial^2 F}{\partial x^2} - \nu \frac{\partial^2 F}{\partial y^2}\right) - \frac{1}{2}\left(\frac{\partial w}{\partial y}\right)^2 + \frac{N^\theta}{Eh} \right\} \mathrm{d}y \tag{5.32b}$$

For the laterally restrained BC, setting the edge displacements to zero after substitution of equations (5.23)-(5.31) into equation (5.32) results in the following expressions for P_x and P_y

$$\begin{Bmatrix} P_x \\ P_y \end{Bmatrix} = \frac{Eh\pi^2 w_{mn}^2}{8(1-\nu^2)} \begin{Bmatrix} b(\frac{m^2}{a^2} + \nu\frac{n^2}{b^2}) \\ a(\nu\frac{m^2}{a^2} + \frac{n^2}{b^2}) \end{Bmatrix} - \frac{N^\theta}{(1-\nu)} \begin{Bmatrix} b \\ a \end{Bmatrix} + \frac{hF_{mn}\left(-1+(-1)^m\right)\left(-1+(-1)^n\right)}{mn} \begin{Bmatrix} \frac{n^2}{b} \\ \frac{m^2}{a} \end{Bmatrix} \tag{5.33}$$

By taking account of the mathematical coupling between higher order terms in the governing equations more than two indices must be used for representing the series solution terms (Timoshenko and Woinowsky-Krieger, 1959; Wang and El-Sheikh, 2005). Substituting equations (5.23)-(5.31) and equation (5.33) into equations (5.4) and (5.22) leads to the following coupled equations

$$h\left(\frac{m^2}{a^2}+\frac{n^2}{b^2}\right)^2 F_{mn}S_{mn}-\left(\frac{m^2}{a^2}+\frac{n^2}{b^2}\right)\frac{N^{\theta}_{mn}S_{mn}}{\pi^2} - \frac{Eh}{a^2b^2}\left(mnrs\ C_{mn}C_{rs}-m^2s^2\ S_{mn}S_{rs}\right)w_{mn}w_{rs}=0 \tag{5.34a}$$

$$\left[D\left(\frac{m^2}{a^2}+\frac{n^2}{b^2}\right)^2+\frac{1}{ab\pi^2}\left(\frac{m^2P_x}{a}+\frac{n^2P_y}{b}\right)\right]w_{mn}S_{mn} - \left(\frac{m^2}{a^2}+\frac{n^2}{b^2}\right)\frac{M^{\theta}_{mn}S_{mn}}{\pi^2}-\frac{q_{mn}S_{mn}}{\pi^4} - \frac{h\left[(m^2s^2+r^2n^2)\ S_{mn}S_{rs}-2mrns\ C_{mn}C_{rs}\right]}{a^2b^2}F_{rs}w_{mn}=0 \tag{5.34b}$$

where $C_{mn}=\cos(m\pi x/a)\cos(n\pi y/b)$. For any assumed number of terms in the series solutions, a set of nonlinear algebraic equations will be established. A flow chart of this solution procedure is shown in Figure 5.5. For instance, for two terms in the series solutions, the following four compatibility equations

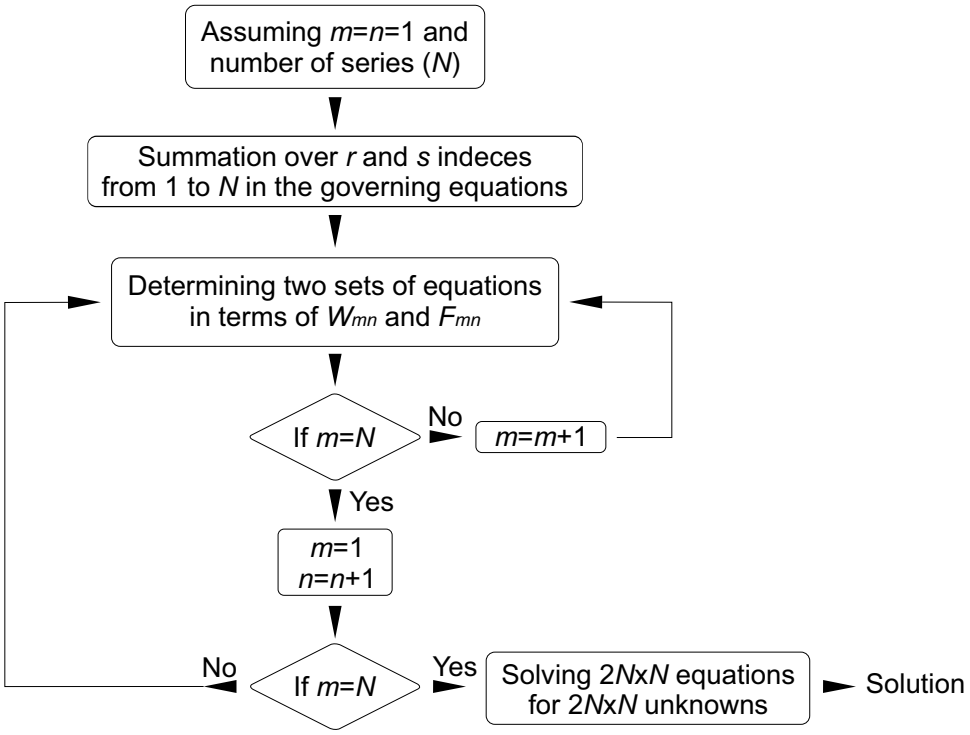

Figure 5.5 A flow chart of the programme for the solution of the governing equations considering the mathematical coupling between higher order terms.

$$h\left(\frac{1}{a^2}+\frac{1}{b^2}\right)^2 F_{11}S_{11}-\left(\frac{1}{a^2}+\frac{1}{b^2}\right)\frac{N_{11}^{\theta}S_{11}}{\pi^2} \tag{5.35a}$$
$$-\frac{Eh\left(C_{11}(C_{11}+2C_{12}+2C_{21}+4C_{22})-S_{11}(S_{11}+4S_{12}+S_{21}+4S_{22})\right)}{a^2b^2}$$
$$\times w_{11}(w_{11}+w_{12}+w_{21}+w_{22})=0$$

$$h\left(\frac{1}{a^2}+\frac{4}{b^2}\right)^2 F_{12}S_{12}-\left(\frac{1}{a^2}+\frac{4}{b^2}\right)\frac{N_{12}^{\theta}S_{12}}{\pi^2} \tag{5.35b}$$
$$-\frac{Eh\left(2C_{12}(C_{11}+2C_{12}+2C_{21}+4C_{22})-S_{12}(S_{11}+4S_{12}+S_{21}+4S_{22})\right)}{a^2b^2}$$
$$\times w_{12}(w_{11}+w_{12}+w_{21}+w_{22})=0$$

$$h\left(\frac{4}{a^2}+\frac{1}{b^2}\right)^2 F_{21}S_{21}-\left(\frac{4}{a^2}+\frac{1}{b^2}\right)\frac{N_{21}^{\theta}S_{21}}{\pi^2}$$
$$-\frac{2Eh\left(C_{21}(C_{11}+2C_{12}+2C_{21}+4C_{22})-2S_{21}(S_{11}+4S_{12}+S_{21}+4S_{22})\right)}{a^2b^2}$$
$$\times w_{21}(w_{11}+w_{12}+w_{21}+w_{22})=0 \tag{5.35c}$$

$$h\left(\frac{4}{a^2}+\frac{4}{b^2}\right)^2 F_{22}S_{22}-\left(\frac{4}{a^2}+\frac{4}{b^2}\right)\frac{N_{22}^{\theta}S_{22}}{\pi^2} \tag{5.35d}$$
$$-\frac{4Eh\left(C_{22}(C_{11}+2C_{12}+2C_{21}+4C_{22})-S_{22}(S_{11}+4S_{12}+S_{21}+4S_{22})\right)}{a^2b^2}$$
$$\times w_{22}(w_{11}+w_{12}+w_{21}+w_{22})=0$$

and the following four equilibrium equations are derived

$$\left(D\left(\frac{1}{a^2}+\frac{1}{b^2}\right)^2+\frac{1}{ab\pi^2}\left(\frac{P_x}{a}+\frac{P_y}{b}\right)\right)w_{11}S_{11}-\left(\frac{1}{a^2}+\frac{1}{b^2}\right)\frac{M_{11}^{\theta}S_{11}}{\pi^2}-\frac{q_{11}S_{11}}{\pi^4}$$
$$-\frac{h\left(S_{11}(2S_{11}+5S_{12}+5S_{21}+8S_{22})-2C_{11}(C_{11}+2C_{12}+2C_{21}+4C_{22})\right)}{a^2b^2}$$
$$\times w_{11}(F_{11}+F_{12}+F_{21}+F_{22})=0 \tag{5.36a}$$

$$\left(D\left(\frac{1}{a^2}+\frac{4}{b^2}\right)^2+\frac{1}{ab\pi^2}\left(\frac{P_x}{a}+\frac{4P_y}{b}\right)\right)w_{12}S_{12}-\left(\frac{1}{a^2}+\frac{4}{b^2}\right)\frac{M_{12}^{\theta}S_{12}}{\pi^2}-\frac{q_{12}S_{12}}{\pi^4}$$
$$-\frac{h\left(S_{12}(5S_{11}+8S_{12}+17S_{21}+20S_{22})-4C_{12}(C_{11}+2C_{12}+2C_{21}+4C_{22})\right)}{a^2b^2}$$
$$\times w_{12}(F_{11}+F_{12}+F_{21}+F_{22})=0 \tag{5.36b}$$

$$\left(D\left(\frac{4}{a^2}+\frac{1}{b^2}\right)^2+\frac{1}{ab\pi^2}\left(\frac{4P_x}{a}+\frac{P_y}{b}\right)\right)w_{21}S_{21}-\left(\frac{4}{a^2}+\frac{1}{b^2}\right)\frac{M^{\theta}_{21}S_{21}}{\pi^2}-\frac{q_{21}S_{21}}{\pi^4}$$
$$-\frac{h\left(S_{21}(5S_{11}+17S_{12}+8S_{21}+20S_{22})-4C_{21}(C_{11}+2C_{12}+2C_{21}+4C_{22})\right)}{a^2b^2}$$
$$\times w_{21}(F_{11}+F_{12}+F_{21}+F_{22})=0 \tag{5.36c}$$

$$\left(D\left(\frac{4}{a^2}+\frac{4}{b^2}\right)^2+\frac{1}{ab\pi^2}\left(\frac{4P_x}{a}+\frac{4P_y}{b}\right)\right)w_{22}S_{22}-\left(\frac{4}{a^2}+\frac{4}{b^2}\right)\frac{M^{\theta}_{22}S_{22}}{\pi^2}-\frac{q_{22}S_{22}}{\pi^4}$$
$$-\frac{4h\left(S_{22}(2S_{11}+5S_{12}+5S_{21}+8S_{22})-2C_{22}(C_{11}+2C_{12}+2C_{21}+4C_{22})\right)}{a^2b^2}$$
$$\times w_{22}(F_{11}+F_{12}+F_{21}+F_{22})=0 \tag{5.36d}$$

The aforementioned mathematical coupling raises the computational cost and time needed to solve the derived system of equations. Moreover, its contribution to the final solution might be negligible as shown in the following section. Considering one term approximation case (i.e., $m=r$ and $n=s$) results in the following simplified governing equations

$$h\left(\frac{m^2}{a^2}+\frac{n^2}{b^2}\right)^2F_{mn}S_{mn}-\left(\frac{m^2}{a^2}+\frac{n^2}{b^2}\right)\frac{N^{\theta}_{mn}S_{mn}}{\pi^2}-\frac{Ehm^2n^2(C^2_{mn}-S^2_{mn})}{a^2b^2}w^2_{mn}=0 \tag{5.37a}$$

$$\left(D\left(\frac{m^2}{a^2}+\frac{n^2}{b^2}\right)^2+\frac{1}{ab\pi^2}\left(\frac{m^2P_x}{a}+\frac{n^2P_y}{b}\right)\right)w_{mn}S_{mn}$$
$$-\left(\frac{m^2}{a^2}+\frac{n^2}{b^2}\right)\frac{M^{\theta}_{mn}S_{mn}}{\pi^2}-\frac{q_{mn}S_{mn}}{\pi^4}-\frac{2hm^2n^2(S^2_{mn}-C^2_{mn})}{a^2b^2}F_{mn}w_{mn}=0 \tag{5.37b}$$

To expand the trigonometric functions over infinite sums, expansion theorem is applied for the modal functions defined in equation (5.29). If a generic function is expressed by $\Psi(x,y)=\sum_{m=1}^{\infty}\sum_{n=1}^{\infty}\psi_{mn}S_{mn}(x,y)$, for normalised modal function $S_{mn}(x,y)$ over an orthogonal basis, we have

$$\begin{aligned}\psi_{mn}&=\frac{\langle\Psi(x,y),S_{mn}(x,y)\rangle}{\langle S_{mn}(x,y),S_{mn}(x,y)\rangle}\\&=\frac{4}{ab}\int_0^a\int_0^b\Psi(x,y)S_{mn}(x,y)\,\mathrm{d}y\,\mathrm{d}x\end{aligned} \tag{5.38}$$

where the modal function satisfies the following condition

$$\begin{aligned}\langle S_{mn}(x,y), S_{mn}(x,y)\rangle &= \int_0^a \int_0^b S_{mn}(x,y) S_{mn}(x,y)\ \mathrm{d}y\ \mathrm{d}x \\ &= 1\end{aligned} \tag{5.39}$$

Having used the expansion theorem, if the left part of equations (5.37a) and (5.37b) are denoted by X_1 and X_2, respectively, then from the following equations

$$\int_0^a \int_0^b \left\{ \begin{array}{c} X_1 \\ X_2 \end{array} \right\} S_{mn} = 0 \tag{5.40a}$$

the following two equations are derived

$$h\left(\frac{m^2}{a^2}+\frac{n^2}{b^2}\right)^2 F_{mn} - \left(\frac{m^2}{a^2}+\frac{n^2}{b^2}\right)\frac{N^{\theta}_{mn}}{\pi^2} - 4EhH_{mn}\left(\frac{mn}{ab}\right)^2 w_{mn}^2 = 0 \tag{5.41a}$$

$$\begin{aligned} &D\left(\left(\frac{m^2}{a^2}+\frac{n^2}{b^2}\right)^2 + \frac{1}{ab\pi^2}\left(\frac{m^2 P_x}{a}+\frac{n^2 P_y}{b}\right)\right) w_{mn} \\ &- \left(\frac{m^2}{a^2}+\frac{n^2}{b^2}\right)\frac{M^{\theta}_{mn}}{\pi^2} - \frac{q_{mn}}{\pi^4} + 8hF_{mn}H_{mn}\left(\frac{mn}{ab}\right)^2 w_{mn} = 0 \end{aligned} \tag{5.41b}$$

where

$$\begin{aligned} &H_{mn} \\ &= \frac{-1+2(-1)^m+2(-1)^n-(-1)^{3m}-(-1)^{3n}-3(-1)^{m+n}+(-1)^{3m+n}+(-1)^{m+3n}}{3mn\pi^2} \end{aligned} \tag{5.42}$$

By substituting equation (5.41a) into equation (5.41b) an algebraic equation is derived for large displacements of thin rectangular plates

$$A\ w_{mn}^3 + B\ w_{mn} + C = 0 \tag{5.43}$$

where

$$A = \frac{32Ehm^4n^4H_{mn}^2}{\left(m^2b^2+n^2a^2\right)^2} \tag{5.44a}$$

$$B = D\left(\frac{m^2}{a^2}+\frac{n^2}{b^2}\right)^2 + \frac{8N_{mn}^{\theta}H_{mn}m^2n^2}{\pi^2(m^2b^2+n^2a^2)} + \frac{1}{\pi^2ab}\left(\frac{m^2P_x}{a}+\frac{n^2P_y}{b}\right) \tag{5.44b}$$

$$C = -\left(\frac{m^2}{a^2}+\frac{n^2}{b^2}\right)\frac{M_{mn}^{\theta}}{\pi^2} - \frac{q_{mn}}{\pi^4} \tag{5.44c}$$

Once the material and geometric parameters are known, the deflection corresponding to a specified load is determined through the use of the expression given in equation (5.23) for the out-of-plane deflection. It should be calculated for adequate series terms (m and n) to make the final solution more accurate for the both chosen BCs.

The in-plane stresses at the middle surface of the plate and the extreme-fibre bending stresses due to the plate deflection can be calculated from

$$\begin{Bmatrix} \sigma_{xx}^m(x,y) \\ \sigma_{yy}^m(x,y) \\ \tau_{xy}^m(x,y) \end{Bmatrix} = \begin{Bmatrix} \frac{P_x}{bh} \\ \frac{P_y}{ah} \\ 0 \end{Bmatrix} - \sum_{m=1}^{\infty}\sum_{n=1}^{\infty} \begin{Bmatrix} \frac{n^2\pi^2}{b^2}\, S_{mn}\, F_{mn} \\ \frac{m^2\pi^2}{a^2}\, S_{mn}\, F_{mn} \\ \frac{mn\pi^2}{ab}\, C_{mn}\, F_{mn} \end{Bmatrix} \tag{5.45}$$

and

$$\begin{Bmatrix} \sigma_{xx}^b(x,y) \\ \sigma_{yy}^b(x,y) \\ \tau_{xy}^b(x,y) \end{Bmatrix} = \frac{Eh}{2(1-\nu^2)} \sum_{m=1}^{\infty}\sum_{n=1}^{\infty} \begin{Bmatrix} \pi^2\left(\frac{m^2}{a^2}+\nu\frac{n^2}{b^2}\right) w_{mn}\, S_{mn} \\ \pi^2\left(\frac{n^2}{b^2}+\nu\frac{m^2}{a^2}\right) w_{mn}\, S_{mn} \\ \frac{mn\pi^2(\nu-1)}{ab}\, C_{mn}\, w_{mn} \end{Bmatrix} - \sum_{m=1}^{\infty}\sum_{n=1}^{\infty} \begin{Bmatrix} \frac{6M_{mn}^{\theta}}{h^2}\, S_{mn} \\ \frac{6M_{mn}^{\theta}}{h^2}\, S_{mn} \\ 0 \end{Bmatrix} \tag{5.46}$$

In the case of small deformations, there is no need to retain the nonlinear terms associated with large displacements. Accordingly, the reaction loads are simplified as

$$\left\{ \begin{array}{c} P_x \\ P_y \end{array} \right\} = \frac{hF_{mn}\left(-1+(-1)^m\right)\left(-1+(-1)^n\right)}{mn} \left\{ \begin{array}{c} \frac{n^2}{b} \\ \frac{m^2}{a} \end{array} \right\} - \frac{N^\theta}{(1-\nu)} \left\{ \begin{array}{c} b \\ a \end{array} \right\} \tag{5.47}$$

and the stress function and deflection are given by the following equations

$$F_{mn} = \frac{a^2 b^2 N^\theta_{mn}}{h\pi^2(m^2b^2+n^2a^2)} \tag{5.48}$$

$$w_{mn} = -\frac{C}{B} \tag{5.49}$$

where

$$B = D\left(\frac{m^2}{a^2}+\frac{n^2}{b^2}\right)^2 + \frac{1}{\pi^2 ab}\left(\frac{m^2P_x}{a}+\frac{n^2P_y}{b}\right) \tag{5.50a}$$

$$C = -\left(\frac{m^2}{a^2}+\frac{n^2}{b^2}\right)\frac{M^\theta_{mn}}{\pi^2} - \frac{q_{mn}}{\pi^4} \tag{5.50b}$$

Similarly, adequate series terms in the deflection and stress expressions should be used to ensure good accuracy of the final solution. To understand the features of the proposed nonlinear analysis and to demonstrate its performance, several examples are calculated in the following sections.

5.5.1 Plate subject to UDL

First, results from comparison studies are presented to investigate the mechanical aspect of the plate nonlinear response. In the analysis, quantities are represented in a dimensionless form as listed in Table 5.1. To investigate the effect of the mathematical coupling of higher order terms in governing equations on the final solutions, a comparison is made in Figure 5.6 with solutions for a square plate under UDL with laterally restrained and unrestrained BCs. As can be seen, the contribution

Table 5.1 Definitions of dimensionless quantities for geometrically nonlinear plate problems

Description	Quantity	Definition
Dimensionless UDL	$\bar{q}$	qa^4/Eh^4
Dimensionless horizontal displacement	$\bar{u}$	u/h
Dimensionless centre deflection	$\bar{w}$	w/h
Dimensionless bending stresses	$\bar{\sigma}^b$	$\sigma^b a^2/Eh^2$
	$\bar{\tau}^b$	$\tau^b a^2/Eh^2$
Dimensionless membrane stresses	$\bar{\sigma}^m$	$\sigma^m a^2/Eh^2$
	$\bar{\tau}^m$	$\tau^m a^2/Eh^2$

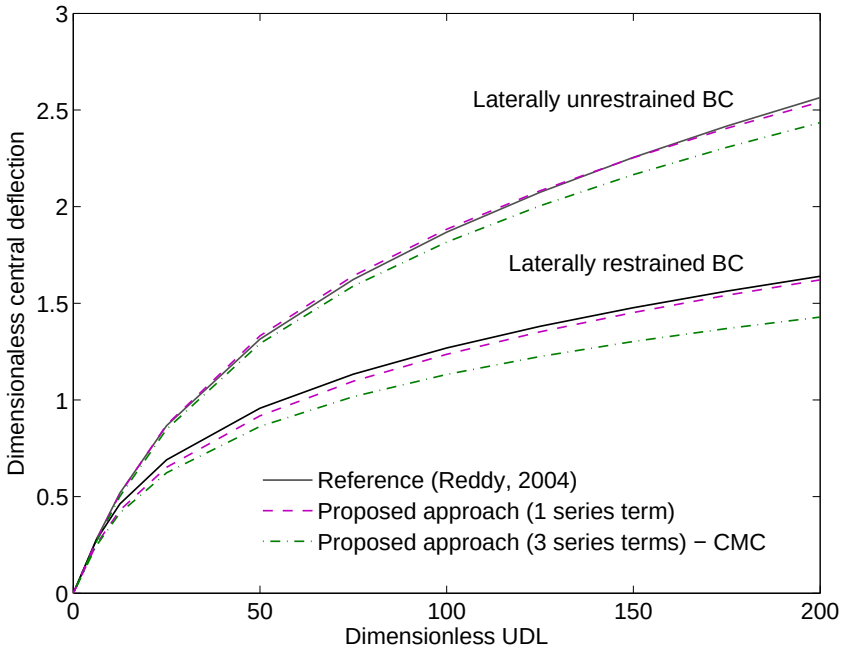

Figure 5.6 Convergence of the dimensionless central deflection for a square plate under UDL with considering the mathematical coupling (CMC) between higher order terms in the governing equations.

of the mathematical coupling to the final solution is not significant for both the chosen BCs.

In all the examples considered in the following, the dimensionless nonlinear central deflection of plates with the laterally unrestrained BC is calculated using one series term in the solution ($m = n = 1$) whereas for the plates with laterally restrained BC, it is calculated using three series terms in the solution ($m, n = 1, 2, 3$). These choices are based on the results plotted in Figure 5.7 which shows the convergence of the results to those obtained using an analytical method (Wang and El-Sheikh, 2005)

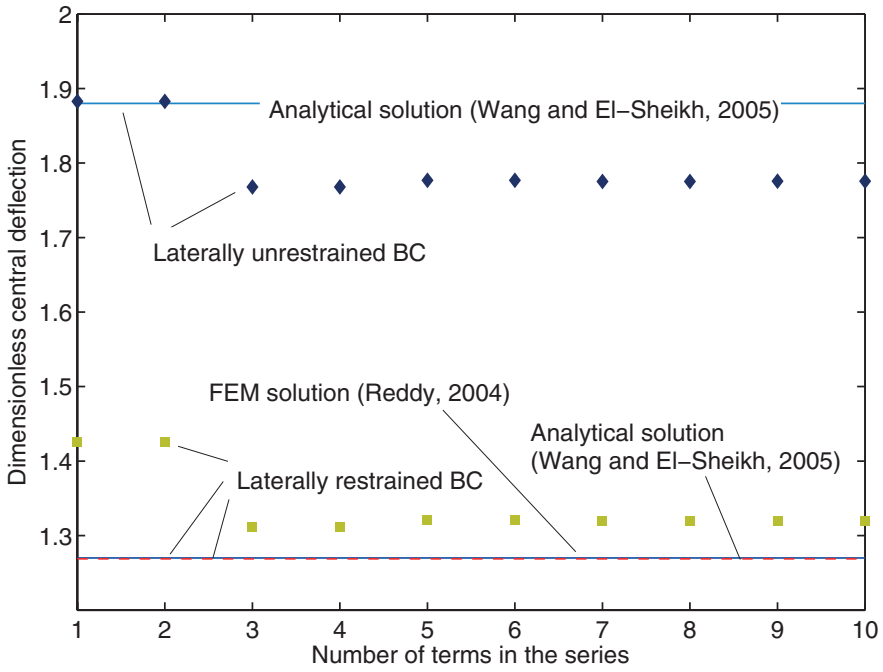

Figure 5.7 Convergence of the dimensionless nonlinear central deflection for a square plate ($a/h = 10$) under UDL ($\bar{q} = 100$). The FEM solution (Reddy, 2004) is obtained based on the first order shear plate theory with three iterations taken for convergence and the analytical solution (Wang and El-Sheikh, 2005) is obtained based on the von Kármán theory using six terms in the series for deflection and stress function (with CMC between higher order terms in the governing equations).

and FEM (Reddy, 2004). Table 5.2 shows the nonlinear responses of a square plate with laterally unrestrained and restrained BCs subject to UDL. In this table, the results obtained using the proposed method are compared with results derived by an analytical method (Wang and El-Sheikh, 2005) using the von Kármán theory. They agree very well with those listed in the table with almost zero error for the laterally unrestrained BC and 3.15% error for the restrained BC.

In Table 5.3, in addition to the nonlinear central deflection, dimensionless nonlinear membrane and extreme-fibre bending stresses (at the centre of the plate) are listed for a laterally restrained thin square plate subject to UDL and compared with FEM solutions (Al-Gahtani and Naffa'a, 2009). Reasonable agreement can be seen between the results with a maximum error of 4.4% for the central deflection, 0.74% for the membrane stress, and 0.87% for extreme-fibre bending stress. The comparison of the results also reveals that only one term in the series is sufficient for obtaining reasonably accurate nonlinear membrane stresses, while three terms should be considered for

Table 5.2 Comparison of dimensionless nonlinear central deflection for a square plate with laterally unrestrained and restrained BCs under UDL with $\bar{q} = 100$ and $h/a = 0.001$

Quantity	Reference*	Proposed approach	ABAQUS simulation
Laterally unrestrained BC			
$\bar{w}$	1.88 (6)†	1.88 (1)	1.78 (6) 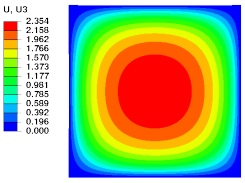
$\bar{u}$	—	-0.00770 (1)	-0.00779 (6) 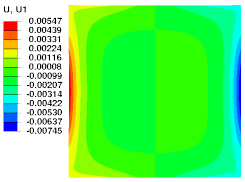
Laterally restrained BC			
$\bar{w}$	1.27 (6)†	1.31 (3)	1.32 (6) 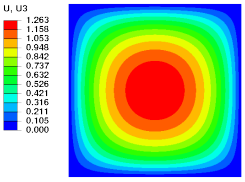
$\bar{u}$	—	0.00664 (3)	0.00671 (6) 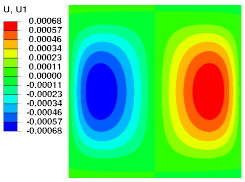

*Wang and El-Sheikh (2005), an analytical method based on the classical plate theory.

†The digits in parentheses are the number of terms in the series taken for convergence.

deflections and bending stresses. In Figure 5.8, the small and large deflection trends of a square plate under UDL are shown for both BCs. For higher values of UDL, nonlinear deflections deviate from the linear theory predictions, due to the effect of higher-order out-of-plane deformation terms. The nonlinear central deflections for the laterally unrestrained BC are obtained using one term in the series solutions, while for the laterally restrained BC the solutions are obtained using three terms in the series solutions.

Table 5.3 Comparison of dimensionless nonlinear centre deflection and stresses for a laterally restrained thin square plate under UDL

Dimensionless UDL	Central deflection			Membrane stress			Bending stress		
	ANSYS*	RBF*	Proposed approach†	ANSYS	RBF	Proposed approach†	ANSYS	RBF	Proposed approach†
1.375	0.0606	0.0607	0.0607	0.0112	0.0112	0.0099	0.3931	0.3925	0.3853
2.750	0.1195	0.1195	0.1198	0.0435	0.0435	0.0386	0.7734	0.7720	0.7602
4.125	0.1753	0.1752	0.1763	0.0937	0.0936	0.0837	1.1315	1.1291	1.1164
5.500	0.2272	0.2270	0.2295	0.1574	0.1572	0.1421	1.4623	1.4648	1.4492
6.875	0.2752	0.2748	0.2791	0.2311	0.2305	0.2104	1.7650	1.7653	1.7566
8.250	0.3194	0.3188	0.3251	0.3113	0.3103	0.2861	2.0407	2.0384	2.0390
9.625	0.3600	0.3594	0.3678	0.3960	0.4040	0.3668	2.2919	2.2868	2.2979
11.000	0.3977	0.3968	0.4074	0.4833	0.4810	0.4510	2.5212	2.5134	2.5353
12.375	0.4326	0.4314	0.4444	0.5720	0.5690	0.5374	2.7315	2.7212	2.7535
13.750	0.4650	0.4648	0.4788	0.6614	0.6625	0.6253	2.9249	2.9124	2.9544
15.125	0.4954	0.4947	0.5111	0.7508	0.7508	0.7138	3.1037	3.0893	3.1399
16.500	0.5238	0.5227	0.5415	0.8400	0.8388	0.8027	3.2696	3.2536	3.3118
17.875	0.5507	0.5492	0.5701	0.9287	0.9261	0.8916	3.4243	3.4070	3.4715
19.250	0.5760	0.5741	0.5972	1.0166	1.0127	0.9801	3.5691	3.5505	3.6202
20.625	0.6000	0.5978	0.6229	1.1038	1.0983	1.0683	3.7049	3.6935	3.7591
22.000	0.6229	0.6203	0.6473	1.1900	1.1831	1.1560	3.8328	3.8212	3.8892
23.375	0.6447	0.6417	0.6706	1.2753	1.2669	1.2430	3.9537	3.9331	4.0112
24.750	0.6656	0.6623	0.6928	1.3596	1.3498	1.3294	4.0683	4.0473	4.1259
26.125	0.6855	0.6819	0.7141	1.4431	1.4319	1.4150	4.1770	4.1559	4.2340
27.500	0.7047	0.7020	0.7345	1.5255	1.5139	1.5000	4.2805	4.2686	4.3359
28.875	0.7231	0.7189	0.7542	1.6070	1.5941	1.5842	4.3793	4.3688	4.4322
30.250	0.7409	0.7364	0.7731	1.6690	1.6717	1.6676	4.4552	4.4526	4.5233
31.625	0.7580	0.7533	0.7913	1.7672	1.7533	1.7504	4.5641	4.5434	4.6097
33.000	0.7746	0.7695	0.8089‡	1.8461	1.8295	1.8324‡	4.6509	4.6263	4.6916‡

*Al-Gahtani and Naffa'a (2009), Radial basis function (RBF) is based on the classical plate theory.

†The deflection and bending stress are obtained using three series terms, while membrane stress is obtained using one series term.

‡| (Present-ANSYS)/ANSYS | ×100 is 4.4%, 0.74% and 0.87%, respectively for deflection, membrane and bending stresses.

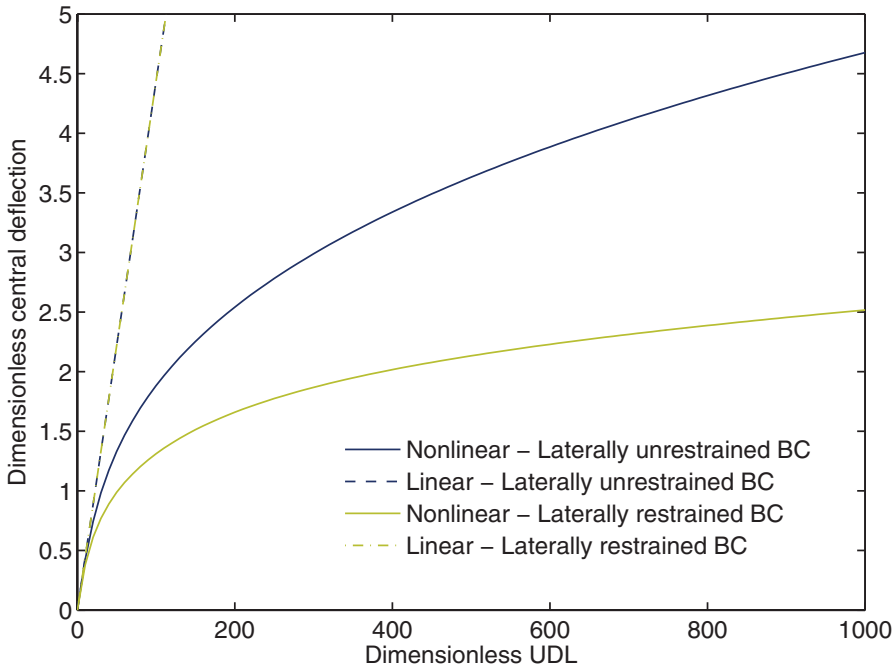

Figure 5.8 Dimensionless linear and nonlinear responses of a square plate ($a/h = 10$) over a wide range of UDL. The nonlinear central deflections for the laterally unrestrained case are obtained using one term in the series, while for the laterally restrained case the deflections are obtained using three series terms. For linear responses seven terms in the corresponding series are used.

5.5.2 Plate subject to thermal effects

To investigate the accuracy of the proposed method for plates under thermal loading, a laterally restrained square plate with a side length of 5 m, thickness of 0.1 m, elasticity modulus of 40 GPa, coefficient of thermal expansion of 8×10^{-6} /°C and Poisson's ratio of 0.3 is considered. A temperature distribution causing an equivalent thermal gradient of 5000 °C/m and an equivalent mean temperature of 200 °C is chosen. The acquired nondimensional central deflection using the method presented is 1.35 and using the ABAQUS FE package (Usmani and Cameron, 2004) is 1.36, whereas using Usmani and Cameron analytical method (Usmani and Cameron, 2004) is 1.48. Comparing the results obtained by these three methods reveals that the result predicted by the present method is in very good agreement with the one predicted by the FE analysis (Usmani and Cameron, 2004), indicating that this is the more accurate solution for determining the deflection in a plate subjected to elevated temperatures. It should be noted that three terms in the series were used to converge the result for this loading case as shown in Figure 5.9.

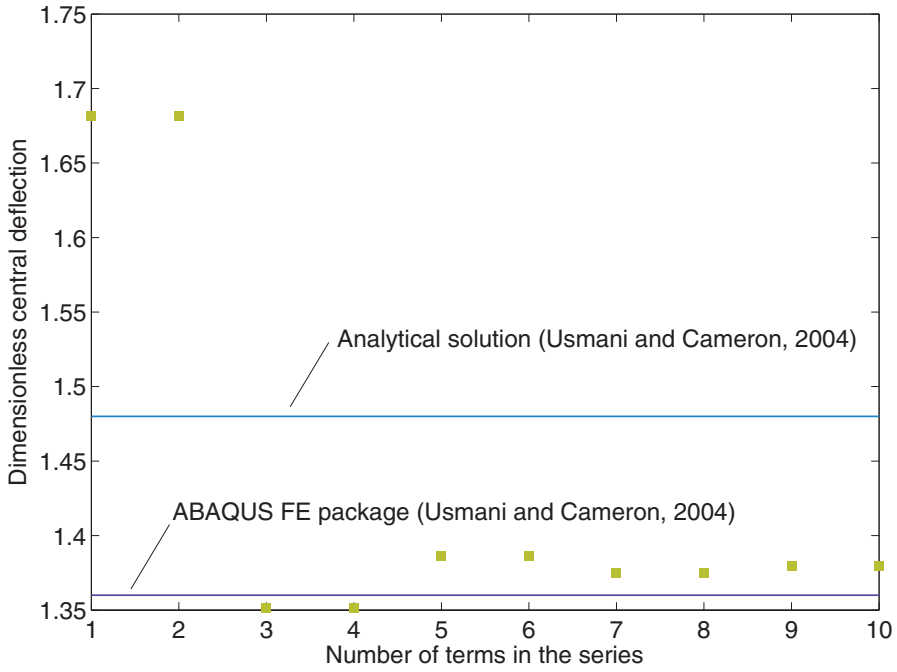

Figure 5.9 Convergence of the dimensionless nonlinear central deflection for a laterally restrained square plate ($a/h = 50$) under linear temperature gradient ($\theta(z) = 200 + 5000z$). The analytical solution (Usmani and Cameron, 2004) is obtained based on a simplified model using one term in the series for deflection.

5.5.3 Plate subject to combined thermomechanical loads

A square plate with aspect ration of 1, span-thickness of 60, modulus of elasticity of 200GPa, coefficient of thermal expansion of $12\times10^{-}6$ 1/°C, and Poisson ratio of 0.3 is considered. For the mechanical loading, a UDL of 1000 kN/m is applied, while for the thermal loading, the temperature at the top of the plate was assumed to be zero and it varied linearly over the depth of the plate to the temperature of 1000°C at the bottom (θ_b). The values of small deflection at the centre of the plate are shown in Figure 5.10. In this figure, OpenSees solutions are compared with analytical solutions. A mesh of 16×16 was used for the OpenSees model. There is a very good agreement between the OpenSees and analytical solutions.

For nonlinear case study, cubic equation (5.43) is solved to find the maximum deflection of the plate. The values of large deflection at the centre of the plate are shown in Figure 5.11. It is found that there is a very good agreement between the results when three terms are used in the series solution. As can be seen, there are clear differences between the results of small and large displacements. Large displacement of the plate

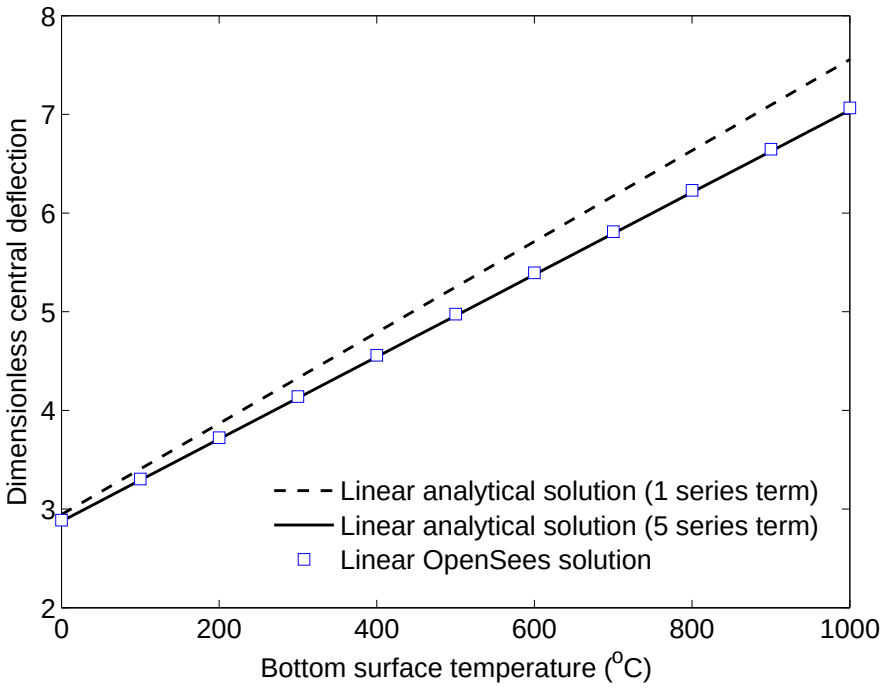

Figure 5.10 Comparison of the dimensionless linear central deflection for a laterally unrestrained square plate under UDL ($\bar{q} = 64.8$) and linear temperature gradient ($\theta(z) = (0.5 + z/h)\theta_b$) with OpenSees solution.

generates membrane tensions during the application of the UDL and this reduces the deflection when seen in comparison with the linear solution. For this loading case, the influence of the number of terms in the series on the nonlinear central deflection of a square plate subjected to thermomechanical loading is illustrated in Figure 5.12. For simplicity, final solutions are computed for only one term expansion of Fourier series. The dimensionless nonlinear central deflection, dimensionless membrane stress, and dimensionless extreme-fibre bending stress at the centre of a thin square plate subjected to UDL and a linear temperature field are calculated. Temperature profile is modelled by an equivalent thermal gradient of $\theta_{,z}$ and an equivalent mean temperature of $\Delta\theta$.

Figure 5.13 depicts the nonlinear central deflection responses of the plate for laterally unrestrained and restrained conditions. Only one series term is used in the analysis. The length-to-thickness ratio is $a/h = 50$. The results show that larger temperature gradients result in larger deflections. Adding lateral restraint at the edges of the plate results in lower values of central deflection than those obtained for the laterally unrestrained case. This could, however, change if the mean temperature is increased

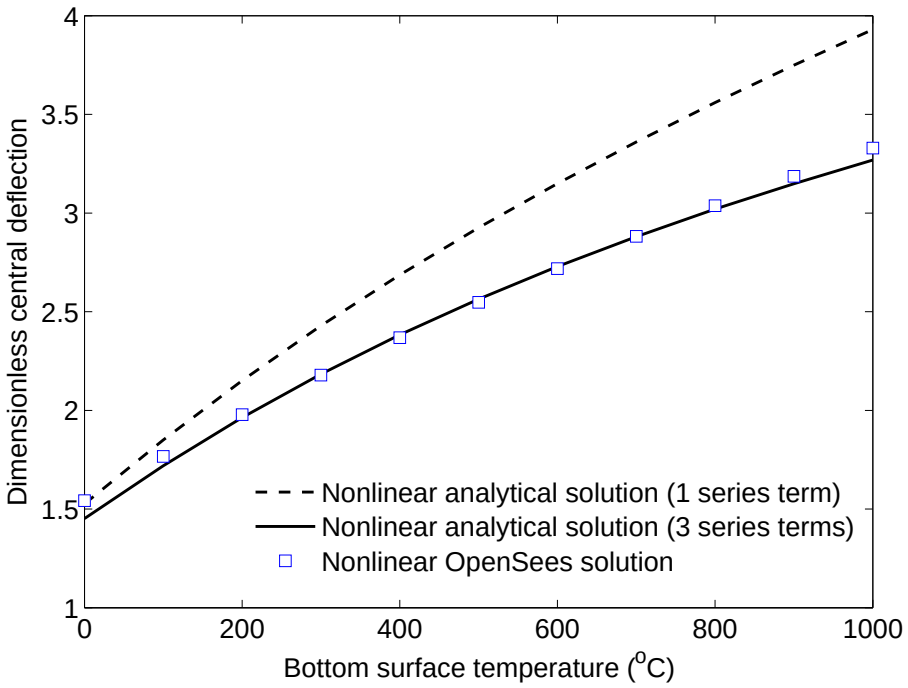

Figure 5.11 Comparison of the dimensionless nonlinear central deflection for a laterally unrestrained square plate under UDL ($\bar{q} = 64.8$) and linear temperature gradient ($\theta(z) = (0.5 + z/h)\theta_b$) with OpenSees solution.

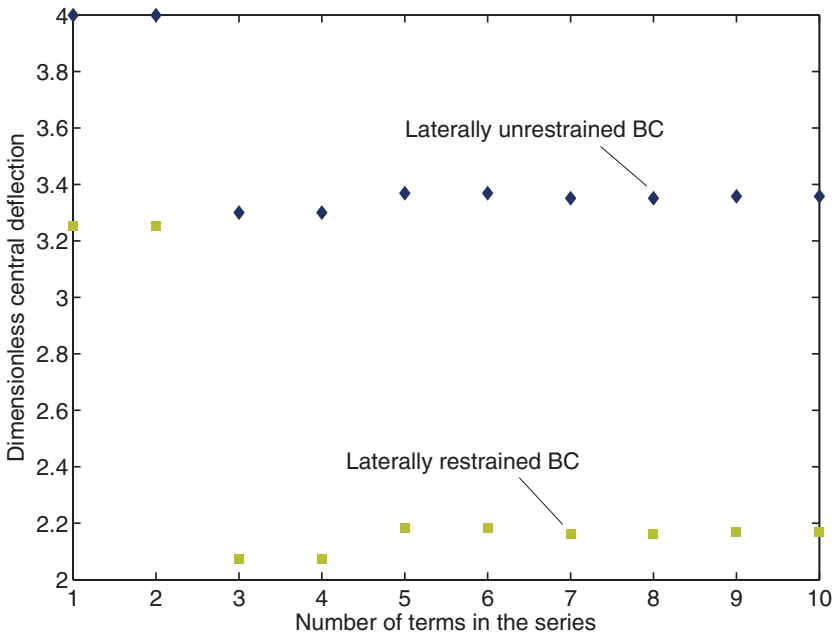

Figure 5.12 Dimensionless nonlinear central deflection for a square plate under thermomechanical loading having two BCs and $a/h = 50$. The plate is subjected to UDL ($\bar{q} = 500$) and linear temperature gradient ($\theta(z) = 200 + 3000z$).

relative to the temperature gradient. Figure 5.14 illustrates the membrane and extreme-fibre bending stress distribution of the same plate (at the centre) over a wide range

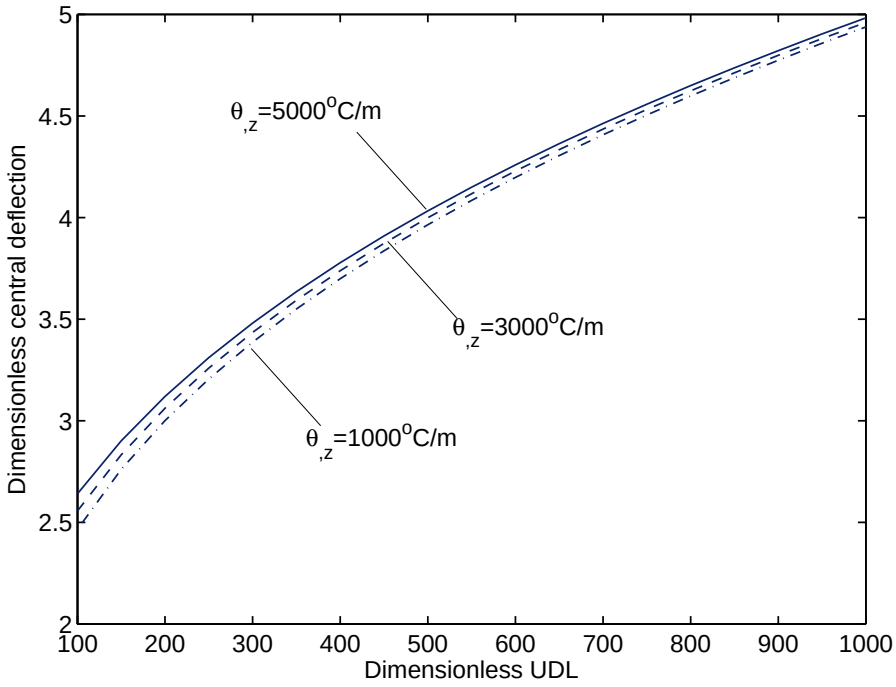

(a) Laterally unrestrained BC

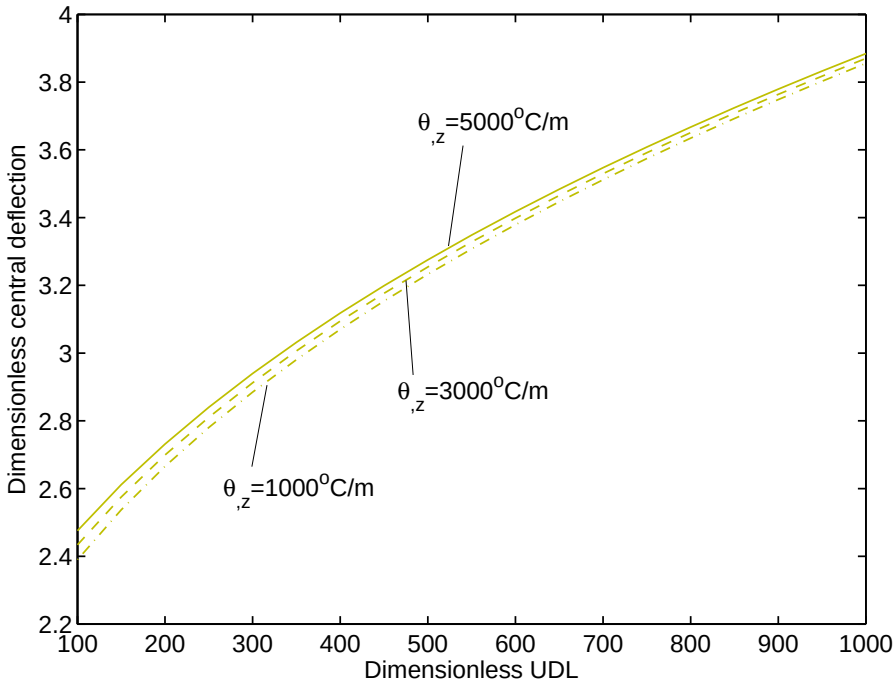

(b) Laterally restrained BC

Figure 5.13 Dimensionless nonlinear central deflection for a square plate ($a/h = 50$) under thermomechanical loading. The data are obtained using one term in the series and plotted over a wide range of UDL and temperature gradient ($\theta(z) = 200 + \theta_{,z} z$).

of UDL. The stresses are calculated for only one term of series and three different thermal gradients. It can also be seen that due to the existence of extension-bending

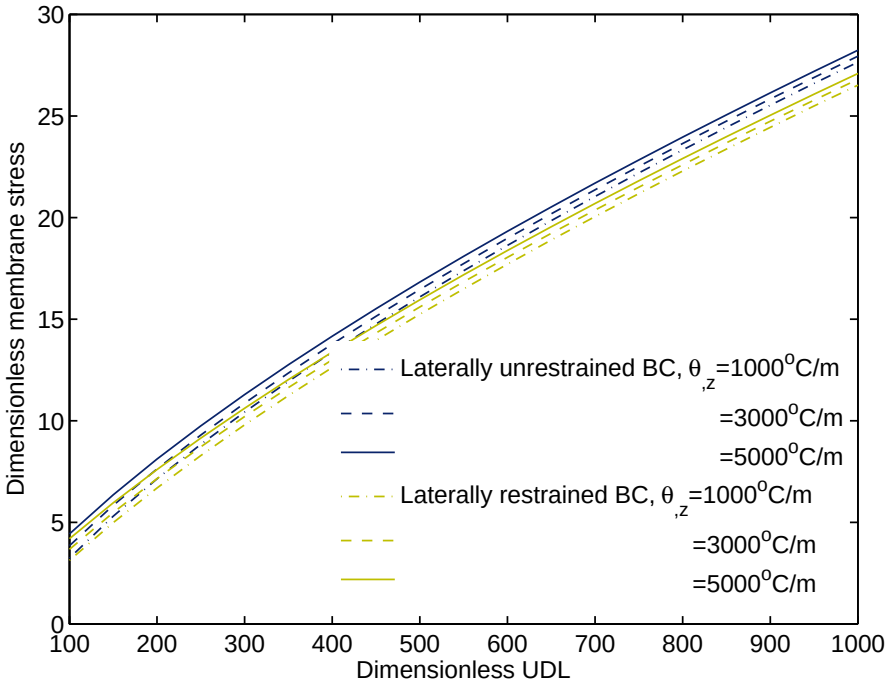

(a) Membrane stress at the centre

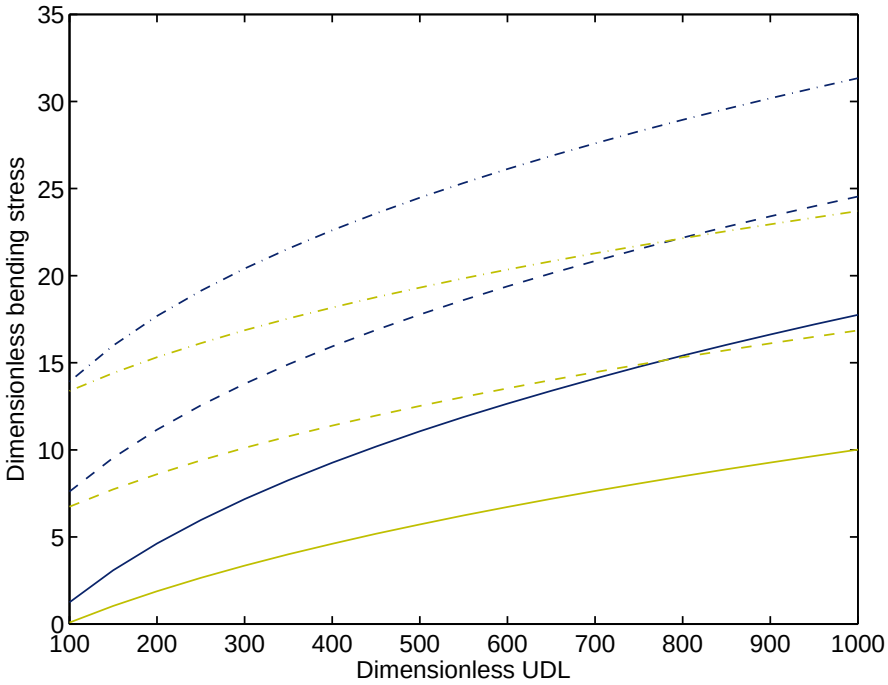

(b) Extreme-fibre bending stress

Figure 5.14 Dimensionless stresses for a square plate ($a/h = 50$) under thermomechanical loading. The stress distributions are obtained using one term in the series and plotted over a wide range of UDL and linear temperature gradient ($\theta(z) = 200 + \theta_{,z} z$).

coupling for a laterally unrestrained plate the predicted values of both stresses are higher than those predicted for the restrained plate. Moreover, it is observed that by

increasing the value of UDL, the plate is dominated by membrane stress. It can be concluded from observation that the restrained boundary condition case has significant influence on the bending stress distribution of the plate.

5.6 Summary

A novel mathematical model was presented for the geometrically nonlinear analysis of laterally unrestrained and/or restrained rectangular plates subjected to thermal and/or mechanical loading. The required computational time was minimised by neglecting the mathematical coupling between higher order terms in the governing equations due to their low contribution to the final solutions. The performance of the proposed method was demonstrated through several analysis examples. It was found that for the laterally unrestrained BC, one term might be sufficient to achieve reasonable accuracy. However, for the laterally restrained BC, three series terms were needed, particularly for higher thermomechanical loads. Despite the limitation of the present solution to simple geometries, it has potential for practical applications. The present analysis has wide applications for analysing plate-type structures in fire conditions, particularly when elements of fire compartment boundaries such as wall panels are subjected to high temperatures and thermal gradients resulting in large displacements. It may also be used in a performance-based engineering framework as an alternative for prescriptive methods.

Chapter 6

Geometrically and Materially Nonlinear Behaviour of Rectangular Plates[1]

6.1 Introduction

In large displacements of plates, the middle plane of the plate significantly stretches, thereby developing tensile membrane forces in the plate. As a result, the load-carrying capacity of the plate increases as deflection increases. This has been observed in full-scale fire tests such as Cardington (Martin and Moore, 1999). Motivated by this, Huang *et al.* (1999) developed a layered procedure for modelling the reinforced concrete slabs in fire with considering the nonlinear material properties of concrete and reinforcing steel at high temperatures. Bailey and Moore (2000) proposed a design method for calculating the load-carrying capacity of steel framed buildings with composite flooring systems subject to fire based on a series of full-scale fire tests on an eight-storey steel framed building. The composite floor plate was divided into several horizontally unrestrained fire-resisting slab panels of low aspect ratio, depending upon the strength of the composite slab which includes membrane action, the strength of the composite beams, the fire resistance period, and the allowable vertical displacement based on the ultimate structural collapse of the system. The method assumed a YLA type failure mechanism in which fracture can occur in reinforcement across the perimeter beams of the slab panels as a result of the large local hogging moments, as shown in Figure 6.1. The method was limited to isotropic

[1] Based on the work reported by Khazaeinejad and Usmani (2014) and Khazaeinejad *et al.* (2015).

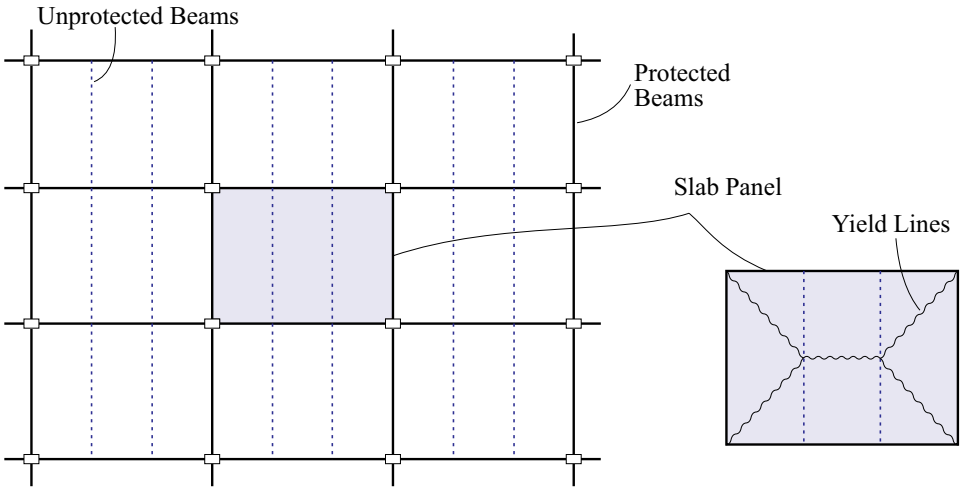

Figure 6.1 Configuration of the YLA for a composite floor slab.

reinforcement. Furthermore, assuming no horizontal restraint from the surrounding structures was conservative. Therefore, it was further developed by Bailey to allow the specification of orthotropic reinforcement (Bailey, 2003), to incorporate the membrane action of the slab and beam system acting compositely (Bailey, 2004), and to predict the membrane action of unrestrained composite floors in fire (Bailey and Toh, 2007).

Huang *et al.* (2003a) used a nonlinear layered FE procedure for predicting the structural response of reinforced concrete slabs both at ambient temperature and in fire conditions. Their proposed method was based on based on the Reissner-Mindlin theory, with considering both geometric and material nonlinearities. They compared their theoretical solutions with experimental results (Huang *et al.*, 2003b). Ignoring both the assumptions of YLA and laterally unrestrained BC in the Bailey's method, Usmani and Cameron (2004) proposed an analytical approach for calculating the load-carrying capacity of composite floor slabs in fire. They carried out their analysis based on the membrane capacity, assuming that most of the bending capacity of slabs is lost at elevated temperatures. Thermal deflections and stresses were determined for a laterally restrained slab subject to a linear temperature distribution through its depth. They considered the thermal loading as a mean temperature and a superposed thermal gradient (see Figure 4.4).

Over the past decades, a range of disparate approaches have been proposed by researchers to modelling composite plates (see e.g., Chia (1988), Lee and Reddy (2005),

Zhang and Yang (2009), Singha *et al.* (2011), Khandan *et al.* (2012), and Madhukar and Singha (2013)). Some of the most important recent contributions on nonlinear response of composite plates are introduced here. Shukla and Nath (2000) used an analytical technique to investigate the steady-state response of moderately thick laminated composite rectangular plates under various BCs undergoing moderately large deformations. The solution they proposed was based on the Chebyshev series solution technique. Yanga and Shen (2003) used the classical plate theory with von Kármán assumptions to study the nonlinear load-deflection and post-buckling responses of FG plates resting on an elastic foundation under in-plane and transverse loadings. A semi-analytical approach based on the DQM and Galerkin procedure was used to solve the governing equations. Ma and Wang (2003) investigated the nonlinear bending and thermal post-buckling behaviours of FG circular plates under mechanical and thermal loadings. The governing equations derived in the framework of the classical plate theory and von Kármán assumptions were numerically solved using a shooting method. Alinia and Ghannadpour (2009) used the same theory to investigate the nonlinear responses of FG plates under transverse pressure. They used the principle of minimum potential energy to obtain the analytical solutions of simply supported plates.

Na and Kim (2006) studied the nonlinear bending of laterally restrained FG plates subjected to uniform pressure and thermal loads using a three-dimensional FEM. The thermal loads were assumed to be uniform, linear, and quarter sine wave temperature distributions across the plate thickness. Shen (2007) presented an analytical method for thermal post-buckling analysis of a simply supported shear deformable FG plate under both in-plane non-uniform parabolic temperature distribution and heat conduction based on a higher order shear deformation plate theory. Li *et al.* (2007) studied the nonlinear post-buckling behavior of FG circular plate under mechanical and thermal loadings using the classical plate theory with von Kármán assumptions. The initial geometric imperfections of FG plates were taken into account in their study. Based on the von Kármán assumptions, Navazi and Haddadpour (2008) presented analytical solutions of the nonlinear cylindrical bending and post-buckling problems of shear deformable simply supported FG plates under mechanical loads. Sepahi *et al.* (2010) investigated the effects of thermal and combined thermomechanical loadings

on axisymmetric large deflection of a simply supported annular FG plate resting on an elastic foundation. The thermal loading was assumed to be non-uniform over the depth of the plate. The nonlinear behaviour of imperfect eccentrically stiffened FG panels resting on an elastic foundation was studied by Duc and Quan (2013), Duc and Quan (2014), and Duc and Thang (2014) using the classical plate theory and Lekhnitsky smeared stiffener technique.

An FE analysis was recently performed by Jeyaraj (2013) to study the critical buckling temperature and free vibration modes of isotropic plates under arbitrary varying temperature fields. Sabik and Kreja (2013) numerically investigated the load capacity of thermally loaded multi-layered plates under uniform thermal loading. Their formulation was based on the first order shear deformation theory, but the thermal degradation of material properties was not taken into account in their model. More recently, Salminen and Heinisuo (2014) proposed a design method for predicting the shear resistance of thin steel plates at non-uniform elevated temperatures. Nonlinear behaviour of steel at elevated temperatures was considered in their model according to Eurocode (2005). As reported in Thai and Kim (2015), the classical plate theory can accurately be applied for analysing FG thin plates and shells where the effects of the shear and normal deformations are negligible.

In this chapter, the formulation developed in the previous chapter for the laterally unrestrained and restrained rectangular plates is extended to account for the elastic material nonlinear behaviour of plates at elevated temperatures. Deflections of the plate are assumed to be large compared with the original dimensions of the plate and changes in stiffness and loads occur as the plate deforms. Hence, in addition to the geometric nonlinearity, the elastic material nonlinearity is also assumed which arises from considering the temperature-dependency of the mechanical and thermal properties used at elevated temperatures. Accordingly, the coefficients of the material stiffness matrix become dependent on both position and temperature. For the mechanical loading of the plate, a transverse load is assumed, while for the thermal loading, a full non-uniform temperature field across the surface and through the depth of the plate is considered. In the context of structural performance under extreme

thermal actions, the plate is analysed under the short hot and long cool fire conditions similar to those discussed in Chapter 4.

6.2 Derivation of governing equations

The force resultants may be expressed by the stress function F as follows

$$\begin{Bmatrix} N_{xx} \\ N_{yy} \\ N_{xy} \end{Bmatrix} = \begin{Bmatrix} \frac{\partial^2 F}{\partial y^2} \\ \frac{\partial^2 F}{\partial x^2} \\ -\frac{\partial^2 F}{\partial x \partial y} \end{Bmatrix} \tag{6.1}$$

By rearranging equation (3.18) and using equation (6.1), the middle plane strains in the plate can be expressed by

$$\begin{aligned} \begin{Bmatrix} \frac{\partial u}{\partial x} + \frac{1}{2}\left(\frac{\partial w}{\partial x}\right)^2 \\ \frac{\partial v}{\partial y} + \frac{1}{2}\left(\frac{\partial w}{\partial y}\right)^2 \\ \frac{\partial u}{\partial y} + \frac{\partial v}{\partial x} + \frac{\partial w}{\partial x}\frac{\partial w}{\partial y} \end{Bmatrix} &= \begin{pmatrix} a_{11} & a_{12} & a_{16} \\ & a_{22} & a_{26} \\ \text{symm.} & & a_{66} \end{pmatrix} \begin{Bmatrix} \frac{\partial^2 F}{\partial y^2} \\ \frac{\partial^2 F}{\partial x^2} \\ -\frac{\partial^2 F}{\partial x \partial y} \end{Bmatrix} \\ &+ \begin{pmatrix} b_{11} & b_{12} & b_{16} \\ & b_{22} & b_{26} \\ \text{symm.} & & b_{66} \end{pmatrix} \begin{Bmatrix} \frac{\partial^2 w}{\partial x^2} \\ \frac{\partial^2 w}{\partial y^2} \\ 2\frac{\partial^2 w}{\partial x \partial y} \end{Bmatrix} \\ &+ \begin{pmatrix} a_{11} & a_{12} & a_{16} \\ & a_{22} & a_{26} \\ \text{symm.} & & a_{66} \end{pmatrix} \begin{Bmatrix} N_{xx}^{\theta} \\ N_{yy}^{\theta} \\ N_{xy}^{\theta} \end{Bmatrix} \end{aligned} \tag{6.2}$$

in which the coefficients a_{ij} and b_{ij} are related to the stiffness coefficients A_{ij} and B_{ij} as defined in the following

$$\begin{pmatrix} a_{11} & a_{12} & a_{16} \\ & a_{22} & a_{26} \\ \text{symm.} & & a_{66} \end{pmatrix} = \begin{pmatrix} A_{11} & A_{12} & A_{16} \\ & A_{22} & A_{26} \\ \text{symm.} & & A_{66} \end{pmatrix}^{-1} \tag{6.3a}$$

$$\begin{pmatrix} b_{11} & b_{12} & b_{16} \\ & b_{22} & b_{26} \\ \text{symm.} & & b_{66} \end{pmatrix} = \begin{pmatrix} A_{11} & A_{12} & A_{16} \\ & A_{22} & A_{26} \\ \text{symm.} & & A_{66} \end{pmatrix}^{-1} \begin{pmatrix} B_{11} & B_{12} & B_{16} \\ & B_{22} & B_{26} \\ \text{symm.} & & B_{66} \end{pmatrix} \tag{6.3b}$$

Substituting equations (6.1) and (6.2) into the strain compatibility equation 5.3 leads to the following nonlinear equation:

$$\begin{aligned}
&a_{22}\frac{\partial^4 F}{\partial x^4} - 2a_{26}\frac{\partial^4 F}{\partial x^3 \partial y} + (2a_{12} + a_{66})\frac{\partial^4 F}{\partial x^2 y^2} - 2a_{16}\frac{\partial^4 F}{\partial x \partial y^3} + a_{11}\frac{\partial^4 F}{\partial y^4} - \left(\frac{\partial^2 w}{\partial x \partial y}\right)^2 \\
&+ \frac{\partial^2 w}{\partial x^2}\frac{\partial^2 w}{\partial y^2} + b_{12}\frac{\partial^4 w}{\partial x^4} + (2b_{26} - b_{16})\frac{\partial^4 w}{\partial x^3 \partial y} + (b_{11} + b_{22} - 2b_{66})\frac{\partial^4 w}{\partial x^2 \partial y^2} \\
&+ (2b_{16} - b_{26})\frac{\partial^4 w}{\partial x \partial y^3} + b_{12}\frac{\partial^4 w}{\partial y^4} = -a_{12}\frac{\partial^2 N^\theta_{xx}}{\partial x^2} + a_{16}\frac{\partial^2 N^\theta_{xx}}{\partial x \partial y} - a_{11}\frac{\partial^2 N^\theta_{xx}}{\partial y^2} \\
&\quad - a_{22}\frac{\partial^2 N^\theta_{yy}}{\partial x^2} + a_{26}\frac{\partial^2 N^\theta_{yy}}{\partial x \partial y} - a_{12}\frac{\partial^2 N^\theta_{yy}}{\partial y^2} - a_{26}\frac{\partial^2 N^\theta_{xy}}{\partial x^2} + a_{66}\frac{\partial^2 N^\theta_{xy}}{\partial x \partial y} - a_{16}\frac{\partial^2 N^\theta_{xy}}{\partial y^2}
\end{aligned} \tag{6.4}$$

It can be seen that the effect of TDMP is reflected in the coefficients a_{ij} and b_{ij}.

To establish the compatibility equation, the moment resultants (3.19) are rewritten as

$$\begin{aligned}
\begin{Bmatrix} M_{xx} \\ M_{yy} \\ M_{xy} \end{Bmatrix} &= \begin{pmatrix} c_{11} & c_{12} & c_{16} \\ & c_{22} & c_{26} \\ \text{symm.} & & c_{66} \end{pmatrix} \begin{Bmatrix} \frac{\partial^2 F}{\partial y^2} \\ \frac{\partial^2 F}{\partial x^2} \\ -\frac{\partial^2 F}{\partial x \partial y} \end{Bmatrix} \\
&+ \begin{pmatrix} d_{11} & d_{12} & d_{16} \\ & d_{22} & d_{26} \\ \text{symm.} & & d_{66} \end{pmatrix} \begin{Bmatrix} -\frac{\partial^2 w}{\partial x^2} \\ -\frac{\partial^2 w}{\partial y^2} \\ -2\frac{\partial^2 w}{\partial x \partial y} \end{Bmatrix} \\
&+ \begin{pmatrix} c_{11} & c_{12} & c_{16} \\ & c_{22} & c_{26} \\ \text{symm.} & & c_{66} \end{pmatrix} \begin{Bmatrix} N^\theta_{xx} \\ N^\theta_{yy} \\ N^\theta_{xy} \end{Bmatrix} - \begin{Bmatrix} M^\theta_{xx} \\ M^\theta_{yy} \\ M^\theta_{xy} \end{Bmatrix}
\end{aligned} \tag{6.5}$$

where the coefficient c_{ij} and d_{ij} are related to the stiffness coefficients A_{ij}, B_{ij}, and D_{ij} as follows

$$\begin{pmatrix} c_{11} & c_{12} & c_{16} \\ & c_{22} & c_{26} \\ \text{symm.} & & c_{66} \end{pmatrix} = \begin{pmatrix} B_{11} & B_{12} & B_{16} \\ & B_{22} & B_{26} \\ \text{symm.} & & B_{66} \end{pmatrix} \begin{pmatrix} A_{11} & A_{12} & A_{16} \\ & A_{22} & A_{26} \\ \text{symm.} & & A_{66} \end{pmatrix}^{-1} \tag{6.6a}$$

$$
\begin{pmatrix} d_{11} & d_{12} & d_{16} \\ & d_{22} & d_{26} \\ \text{symm.} & & d_{66} \end{pmatrix}
= \begin{pmatrix} D_{11} & D_{12} & D_{16} \\ & D_{22} & D_{26} \\ \text{symm.} & & D_{66} \end{pmatrix}
- \begin{pmatrix} B_{11} & B_{12} & B_{16} \\ & B_{22} & B_{26} \\ \text{symm.} & & B_{66} \end{pmatrix}
\begin{pmatrix} A_{11} & A_{12} & A_{16} \\ & A_{22} & A_{26} \\ \text{symm.} & & A_{66} \end{pmatrix}^{-1}
\begin{pmatrix} B_{11} & B_{12} & B_{16} \\ & B_{22} & B_{26} \\ \text{symm.} & & B_{66} \end{pmatrix} \tag{6.6b}
$$

Upon substitution of equation (6.5) into the equilibrium equation (5.21), the other nonlinear equation is established

$$
\begin{aligned}
&d_{11}\frac{\partial^4 w}{\partial x^4} + 2(d_{16}+d_{16})\frac{\partial^4 w}{\partial x^3 \partial y} + 2(d_{12}+4d_{66})\frac{\partial^4 w}{\partial x^2 y^2} + 4d_{26}\frac{\partial^4 w}{\partial x \partial y^3} + d_{22}\frac{\partial^4 w}{\partial y^4} \\
&- \frac{\partial^2 F}{\partial y^2}\frac{\partial^2 w}{\partial x^2} + 2\frac{\partial^2 F}{\partial x \partial y}\frac{\partial^2 w}{\partial x \partial y} - \frac{\partial^2 F}{\partial x^2}\frac{\partial^2 w}{\partial y^2} - c_{12}\frac{\partial^4 F}{\partial x^4} - (2c_{26}-c_{16})\frac{\partial^4 F}{\partial x^3 \partial y} \\
&- (c_{11}+c_{22}-2c_{66})\frac{\partial^4 F}{\partial x^2 y^2} - (2c_{16}-c_{26})\frac{\partial^4 F}{\partial x \partial y^3} - c_{12}\frac{\partial^4 F}{\partial y^4} = q + c_{11}\frac{\partial^2 N_{xx}^{\theta}}{\partial x^2} \\
&+ c_{12}\frac{\partial^2 N_{xx}^{\theta}}{\partial y^2} + 2c_{16}\frac{\partial^2 N_{xx}^{\theta}}{\partial x \partial y} + c_{12}\frac{\partial^2 N_{yy}^{\theta}}{\partial x^2} + c_{22}\frac{\partial^2 N_{yy}^{\theta}}{\partial y^2} + 2c_{26}\frac{\partial^2 N_{yy}^{\theta}}{\partial x \partial y} \\
&+ c_{16}\frac{\partial^2 N_{xy}^{\theta}}{\partial x^2} + c_{26}\frac{\partial^2 N_{xy}^{\theta}}{\partial y^2} + 2c_{66}\frac{\partial^2 N_{xy}^{\theta}}{\partial x \partial y} - \frac{\partial^2 M_{xx}^{\theta}}{\partial x^2} - \frac{\partial^2 M_{yy}^{\theta}}{\partial y^2} - 2\frac{\partial^2 M_{xy}^{\theta}}{\partial x \partial y}
\end{aligned} \tag{6.7}
$$

The most common way of solving such equations is to use trigonometric functions. In terms of how the support conditions are specified, sine and/or cosine series solutions might be considered.

6.3 Solution of governing equations

In the case of laterally restrained BC, the equivalent reaction loads at the plate boundaries can be obtained as

$$\int_0^a \frac{\partial u}{\partial x} dx = \int_0^a \left(a_{11} \frac{\partial^2 F}{\partial y^2} + a_{12} \frac{\partial^2 F}{\partial x^2} + b_{11} \frac{\partial^2 w}{\partial x^2} + b_{12} \frac{\partial^2 w}{\partial y^2} + a_{11} N_{xx}^{\theta} + a_{12} N_{yy}^{\theta} - \frac{1}{2} \left(\frac{\partial w}{\partial x} \right)^2 \right) \mathrm{d}x \tag{6.8a}$$

$$\int_0^b \frac{\partial v}{\partial y} dy = \int_0^b \left(a_{12} \frac{\partial^2 F}{\partial y^2} + a_{22} \frac{\partial^2 F}{\partial x^2} + b_{12} \frac{\partial^2 w}{\partial x^2} + b_{22} \frac{\partial^2 w}{\partial y^2} + a_{12} N_{xx}^{\theta} + a_{22} N_{yy}^{\theta} - \frac{1}{2} \left(\frac{\partial w}{\partial y} \right)^2 \right) \mathrm{d}y \tag{6.8b}$$

where setting the edge displacements to zero after substituting equations (5.23) and (5.31) into equations (6.8) and performing the integration, yields the following expressions for the reaction loads

$$P_x = F_{mn} \bar{n}^2 \frac{bh\zeta_2}{\zeta_1} + w_{mn} \frac{bh\zeta_3}{\zeta_1} + \frac{1}{2} w_{mn}^2 \frac{bh\zeta_4}{\zeta_1} - bhN_{xx}^{\theta} \tag{6.9a}$$

$$P_y = F_{mn} \bar{m}^2 \frac{ah\zeta_2}{\zeta_1} + w_{mn} \frac{ah\zeta_5}{\zeta_1} + \frac{1}{2} w_{mn}^2 \frac{ah\zeta_4}{\zeta_1} - ahN_{yy}^{\theta} \tag{6.9b}$$

where

$$\zeta_1 = \int_0^a \int_0^b \left(a_{11} a_{22} - a_{12}^2 \right) \mathrm{d}y \mathrm{d}x \tag{6.10a}$$

$$\zeta_2 = \int_0^a \int_0^b \left(a_{11} a_{22} - a_{12}^2 \right) S_{mn} \mathrm{d}y \mathrm{d}x \tag{6.10b}$$

$$\zeta_3 = \int_0^a \int_0^b \left[\left(a_{22} b_{11} - a_{12} b_{12} \right) \bar{m}^2 + \left(a_{22} b_{12} - a_{12} b_{22} \right) \bar{n}^2 \right] S_{mn} \mathrm{d}y \mathrm{d}x \tag{6.10c}$$

$$\zeta_4 = \int_0^a \int_0^b \left(a_{22} \bar{m}^2 \cos^2 \bar{m}x \sin^2 \bar{n}y - a_{12} \bar{n}^2 \sin^2 \bar{m}x \cos^2 \bar{n}y \right) \mathrm{d}y \mathrm{d}x \tag{6.10d}$$

$$\zeta_5 = \int_0^a \int_0^b \left[\left(a_{11} b_{12} - a_{12} b_{11} \right) \bar{m}^2 + \left(a_{11} b_{22} - a_{12} b_{12} \right) \bar{n}^2 \right] S_{mn} \mathrm{d}y \mathrm{d}x \tag{6.10e}$$

$$\zeta_6 = \int_0^a \int_0^b \left(a_{11} \bar{n}^2 \sin^2 \bar{m}x \cos^2 \bar{n}y - a_{12} \bar{m}^2 \cos^2 \bar{m}x \sin^2 \bar{n}y \right) \mathrm{d}y \mathrm{d}x \tag{6.10f}$$

For through-depth thermal loading conditions, these equations are simplified as

$$P_x = \frac{bh\left(a_{22}\bar{m}^2 - a_{12}\bar{n}^2\right)}{8\left(a_{11}a_{22} - a_{12}^2\right)} w_{mn}^2 + \frac{[-1+(-1)^m][-1+(-1)^n]\,bh\bar{n}^2}{mn\pi^2} F_{mn} \tag{6.11a}$$
$$+ \frac{bh[-1+(-1)^m][-1+(-1)^n]\left[(a_{22}b_{11} - a_{12}b_{12})\bar{m}^2 + (a_{12}b_{22} - a_{22}b_{12})\bar{n}^2\right]}{mn\pi^2\left(a_{11}a_{22} - a_{12}^2\right)} w_{mn}$$
$$- bhN_{xx}^{\theta}$$

$$P_y = \frac{ah\left(a_{11}\bar{n}^2 - a_{12}\bar{m}^2\right)}{8\left(a_{11}a_{22} - a_{12}^2\right)} w_{mn}^2 + \frac{[-1+(-1)^m][-1+(-1)^n]\,ah\bar{m}^2}{mn\pi^2} F_{mn} \tag{6.11b}$$
$$+ \frac{ah[-1+(-1)^m][-1+(-1)^n]\left[(a_{11}b_{12} - a_{12}b_{11})\bar{m}^2 + (a_{11}b_{22} - a_{12}b_{12})\bar{n}^2\right]}{mn\pi^2\left(a_{11}a_{22} - a_{12}^2\right)} w_{mn}$$
$$- ahN_{yy}^{\theta}$$

In contrast, when the laterally unrestrained BC is imposed, the reaction loads are zero at the plate boundaries and the following expressions can then be obtained for the in-plane displacements

$$u = \sum_{m=1}^{\infty}\sum_{n=1}^{\infty}\left[-\frac{\bar{m}^2}{4}\left(x + \frac{\sin 2\bar{m}x}{2\bar{m}}\right) w_{mn}^2 \sin^2 \bar{n}y + \eta_1 w_{mn} + \eta_2 F_{mn} + \eta_3\right] \tag{6.12a}$$

$$v = \sum_{m=1}^{\infty}\sum_{n=1}^{\infty}\left[-\frac{\bar{n}^2}{4}\left(y + \frac{\sin 2\bar{n}y}{2\bar{n}}\right) w_{mn}^2 \sin^2 \bar{m}x + \eta_4 w_{mn} + \eta_5 F_{mn} + \eta_6\right] \tag{6.12b}$$

where the coefficients are defined by

$$\eta_1 = -\int_0^a \left(\bar{b}_{11}\bar{m}^2 + \bar{b}_{12}\bar{n}^2\right) S_{mn}\mathrm{d}x \tag{6.13a}$$

$$\eta_2 = -\int_0^a \left(\bar{a}_{12}\bar{m}^2 + \bar{a}_{11}\bar{n}^2\right) S_{mn}\mathrm{d}x \tag{6.13b}$$

$$\eta_3 = \int_0^a \left(\bar{a}_{11}N_{xx}^{\theta} + \bar{a}_{12}N_{yy}^{\theta}\right)\mathrm{d}x \tag{6.13c}$$

$$\eta_4 = -\int_0^b \left(\bar{b}_{12}\bar{m}^2 + \bar{b}_{22}\bar{n}^2\right) S_{mn}\mathrm{d}y \tag{6.13d}$$

$$\eta_5 = -\int_0^b \left(\bar{a}_{22}\bar{m}^2 + \bar{a}_{12}\bar{n}^2\right) S_{mn}\mathrm{d}y \tag{6.13e}$$

$$\eta_6 = \int_0^b \left(\bar{a}_{12} N_{xx}^{\theta} + \bar{a}_{22} N_{yy}^{\theta}\right) \mathrm{d}y \tag{6.13f}$$

It is clear that the coefficients of the in-plane displacements are temperature-dependent. A simplified version of these expressions for the through-depth thermal loading can be given by

$$u = \sum_{m=1}^{\infty}\sum_{n=1}^{\infty}\left[-\frac{\bar{m}^2}{4} w_{mn}^2 \left(x + \frac{\sin 2\bar{m}x}{2\bar{m}}\right)\sin^2 \bar{n}y + \frac{b_{11}\bar{m}^2 + b_{12}\bar{n}^2}{\bar{m}} w_{mn} \cos \bar{m}x \sin \bar{n}y \right. \\ \left. + \frac{a_{12}\bar{m}^2 + a_{11}\bar{n}^2}{\bar{m}} F_{mn} \cos \bar{m}x \sin \bar{n}y + a a_{11} N_{xx}^{\theta} + a a_{12} N_{yy}^{\theta}\right] \tag{6.14a}$$

$$v = \sum_{m=1}^{\infty}\sum_{n=1}^{\infty}\left[-\frac{\bar{n}^2}{4} w_{mn}^2 \sin^2 \bar{m}x \left(y + \frac{\sin 2\bar{n}y}{2\bar{n}}\right) + \frac{b_{12}\bar{m}^2 + b_{22}\bar{n}^2}{\bar{n}} w_{mn} \sin \bar{m}x \cos \bar{n}y \right. \\ \left. + \frac{a_{22}\bar{m}^2 + a_{12}\bar{n}^2}{\bar{n}} F_{mn} \sin \bar{m}x \cos \bar{n}y + b a_{12} N_{xx}^{\theta} + b a_{22} N_{yy}^{\theta}\right] \tag{6.14b}$$

Having used the expansion theorem and by substituting expressions (5.23)-(5.31) into the governing equations (6.4) and (6.7), for a rectangular plate with temperature-dependent material properties the compatibility and equilibrium equations are established as

$$\sum_{m=1}^{\infty}\sum_{n=1}^{\infty}\left\{\chi_1 F_{mn} + \chi_2 W_{mn}^2 + \chi_3 W_{mn} + \chi_4\right\} = 0 \tag{6.15a}$$

$$\sum_{m=1}^{\infty}\sum_{n=1}^{\infty}\left\{\chi_5 W_{mn} + \chi_6 F_{mn} W_{mn} + \chi_7 F_{mn} + \chi_8\right\} = 0 \tag{6.15b}$$

where the coefficients are defined as

$$\chi_1 = \int_0^a \int_0^b \left[a_{22}\bar{m}^4 S_{mn}^2 + 2a_{26}\bar{m}^3 \bar{n} S_{mn} C_{mn} + (2a_{12} + a_{66})\bar{m}^2\bar{n}^2 S_{mn}^2 \right. \\ \left. + 2a_{16}\bar{m}\bar{n}^3 S_{mn} C_{mn} + a_{11}\bar{n}^4 S_{mn}^2\right] \mathrm{d}y\, \mathrm{d}x \tag{6.16a}$$

$$\chi_2 = \int_0^a \int_0^b \bar{m}^2\bar{n}^2 \left(S_{mn}^2 - C_{mn}^2\right) S_{mn}\, \mathrm{d}y\, \mathrm{d}x \tag{6.16b}$$

$$\chi_3 = \int_0^a \int_0^b \\ = \left[b_{12}\bar{m}^4 S_{mn}^2 - (2b_{26} - b_{16})\bar{m}^3 \bar{n} S_{mn} C_{mn} + (b_{11} + b_{22} - 2b_{66})\bar{m}^2\bar{n}^2 S_{mn}^2 \right. \\ \left. - (2b_{16} - b_{26})\bar{m}\bar{n}^3 S_{mn} C_{mn} + b_{12}\bar{n}^4 S_{mn}^2\right] \mathrm{d}y\, \mathrm{d}x \tag{6.16c}$$

$$\chi_4 = -\int_0^a \int_0^b \Big[(a_{12}N^{\theta}_{mnxx} + a_{22}N^{\theta}_{mnyy} + a_{26}N^{\theta}_{mnxy})\bar{m}^2 S^2_{mn} + (a_{11}N^{\theta}_{mnxx} + a_{12}N^{\theta}_{mnyy} + a_{16}N^{\theta}_{mnxy})\bar{n}^2 S^2_{mn} + (a_{16}N^{\theta}_{mnxx} + a_{26}N^{\theta}_{mnyy} + a_{66}N^{\theta}_{mnxy})\bar{m}\bar{n} S_{mn} C_{mn}\Big] \, \mathrm{d}y \, \mathrm{d}x \tag{6.16d}$$

$$\chi_5 = \int_0^a \int_0^b \Big[d_{11}\bar{m}^4 S^2_{mn} - 2d_{16}\bar{m}^3\bar{n} S_{mn} C_{mn} + (2d_{12} + 4d_{66}) S^2_{mn}\bar{m}^2\bar{n}^2 - 4d_{26}\bar{m}\bar{n}^3 S_{mn} C_{mn} + \bar{d}_{22}\bar{n}^4 S^2_{mn} + \frac{P_x\bar{m}^2}{bh} S^2_{mn} + \frac{P_y\bar{n}^2}{ah} S^2_{mn}\Big] \, \mathrm{d}y \, \mathrm{d}x \tag{6.16e}$$

$$\chi_6 = \int_0^a \int_0^b 2\bar{m}^2\bar{n}^2 \left(C^2_{mn} - S^2_{mn}\right) S_{mn} \, \mathrm{d}y \, \mathrm{d}x \tag{6.16f}$$

$$\chi_7 = \int_0^a \int_0^b \left[-c_{12}\bar{m}^4 S^2_{mn} + (2C_{26} - C_{16})\bar{m}^3\bar{n} S_{mn} C_{mn} - (c_{11} + c_{22} - 2c_{66})\bar{m}^2\bar{n}^2 S^2_{mn} + (2C_{16} - C_{26})\bar{m}\bar{n}^3 S_{mn} C_{mn} - c_{12}\bar{n}^4 S^2_{mn}\right] \mathrm{d}y \, \mathrm{d}x \tag{6.16g}$$

$$\chi_8 = \int_0^a \int_0^b \Big[(c_{11}N^{\theta}_{mnxx} + c_{12}N^{\theta}_{mnyy} + c_{16}N^{\theta}_{mnxy})\bar{m}^2 S^2_{mn} + (c_{12}N^{\theta}_{mnxx} + c_{22}N^{\theta}_{mnyy} + c_{26}N^{\theta}_{mnxy})\bar{n}^2 S^2_{mn} - 2(C_{16}N^{\theta}_{mnxx} + C_{26}N^{\theta}_{mnyy} + C_{66}N^{\theta}_{mnxy})\bar{m}\bar{n} S_{mn} C_{mn} - \bar{m}^2 M^{\theta}_{mnxx} S^2_{mn} - \bar{n}^2 M^{\theta}_{mnyy} S^2_{mn} - q_{mn} S^2_{mn}\Big] \, \mathrm{d}y \, \mathrm{d}x \tag{6.16h}$$

Considering only through-depth thermal loading, the governing equations are given subsequently

$$\begin{aligned} &\left[a_{22}\bar{m}^4 + (2a_{12} + a_{66})\bar{m}^2\bar{n}^2 + a_{11}\bar{n}^4\right] F_{mn} S_{mn} - \bar{m}^2\bar{n}^2 w^2_{mn}\left(C^2_{mn} - S^2_{mn}\right) \\ &+ \left[(b_{11} + b_{22} - 2b_{66})\bar{m}^2\bar{n}^2 + b_{12}\bar{m}^4 + b_{12}\bar{n}^4\right] w_{mn} S_{mn} \\ &- \left[\left(a_{12}N^{\theta}_{mnxx} + a_{22}N^{\theta}_{mnyy}\right)\bar{m}^2 + \left(a_{11}N^{\theta}_{mnxx} + a_{12}N^{\theta}_{mnyy}\right)\bar{n}^2\right] S_{mn} = 0 \end{aligned} \tag{6.17}$$

$$
\begin{aligned}
&\left[d_{11}\bar{m}^4 + (2d_{12} + 4d_{66})\bar{m}^2\bar{n}^2 + d_{22}\bar{n}^4\right] w_{mn}S_{mn} \\
&- \left[c_{12}\bar{m}^4 + (c_{11} + c_{22} - 2c_{66})\bar{m}^2\bar{n}^2 + c_{12}\bar{n}^4\right] F_{mn}S_{mn} \\
&+ \left(\frac{P_x\bar{m}^2}{bh} + \frac{P_y\bar{n}^2}{ah}\right) w_{mn}S_{mn} - 2\bar{m}^2\bar{n}^2F_{mn}w_{mn}\left(S_{mn}^2 - C_{mn}^2\right) \\
&+ \left[\left(c_{11}N_{mnxx}^{\theta} + c_{12}N_{mnyy}^{\theta}\right)\bar{m}^2 + \left(c_{12}N_{mnxx}^{\theta} + c_{22}N_{mnyy}^{\theta}\right)\bar{n}^2\right] S_{mn} \\
&- \left(\bar{m}^2M_{mnxx}^{\theta} + \bar{n}^2M_{mnyy}^{\theta}\right) S_{mn} - q_{mn}S_{mn} = 0
\end{aligned}
\tag{6.18}
$$

The stress function coefficient F_{mn} is then obtained as a function of the unknown coefficient w_{mn}

$$
\begin{aligned}
F_{mn} = \frac{1}{(a_{22}\bar{m}^4 + (2a_{12} + a_{66})\bar{m}^2\bar{n}^2 + a_{11}\bar{n}^4)} &\left[4\bar{m}^2\bar{n}^2H_{mn}w_{mn}^2\right. \\
&- \left[(b_{11} + b_{22} - 2b_{66})\bar{m}^2\bar{n}^2 + b_{12}\bar{m}^4 + b_{12}\bar{n}^4\right] w_{mn} \\
&\left.+ \left[\left(a_{12}N_{mnxx}^{\theta} + a_{22}N_{mnyy}^{\theta}\right)\bar{m}^2 + \left(a_{11}N_{mnxx}^{\theta} + a_{12}N_{mnyy}^{\theta}\right)\bar{n}^2\right]\right]
\end{aligned}
\tag{6.19}
$$

The load-deflection equation is also derived as

$$
\varsigma_1 w_{mn} + \varsigma_2 F_{mn} + \varsigma_3 F_{mn}w_{mn} + \varsigma_4 = 0 \tag{6.20}
$$

where

$$
\varsigma_1 = \frac{P_x\bar{m}^2}{bh} + \frac{P_y\bar{n}^2}{ah} + d_{11}\bar{m}^4 + (2d_{12} + 4d_{66})\bar{m}^2\bar{n}^2 + d_{22}\bar{n}^4 \tag{6.21a}
$$

$$
\varsigma_2 = -c_{12}\bar{m}^4 - (c_{11} + c_{22} - 2c_{66})\bar{m}^2\bar{n}^2 - c_{12}\bar{n}^4 \tag{6.21b}
$$

$$
\varsigma_3 = 8\bar{m}^2\bar{n}^2H_{mn} \tag{6.21c}
$$

$$
\begin{aligned}
\varsigma_4 = &\left[\left(c_{11}N_{mnxx}^{\theta} + c_{12}N_{mnyy}^{\theta}\right)\bar{m}^2 + \left(c_{12}N_{mnxx}^{\theta} + c_{22}N_{mnyy}^{\theta}\right)\bar{n}^2\right] \\
&- \left(\bar{m}^2M_{mnxx}^{\theta} + \bar{n}^2M_{mnyy}^{\theta}\right) - q_{mn}
\end{aligned}
\tag{6.21d}
$$

It should be noted that the required computational time is minimised by neglecting the mathematical coupling between higher order terms in the governing equations

due to their low contribution to the final solutions as discussed in the previous chapter. To achieve reasonable accuracy a limited number of terms are retained in the series solutions, depending upon the specified support conditions for the plate.

To assess the accuracy and performance of the proposed method, several numerical examples are presented.

6.3.1 Plate subject to UDL

In addition to the dimensionless parameters in Table 5.1, a list of new dimensionless parameters are given in Table 6.1.

Table 6.1 Definitions of dimensionless quantities for geometrically and materially nonlinear plate problems

Description	Definition
Aspect ratio	a/b
Thickness-span ratio	h/a
Dimensionless membrane force	Na^2/E_0h^3

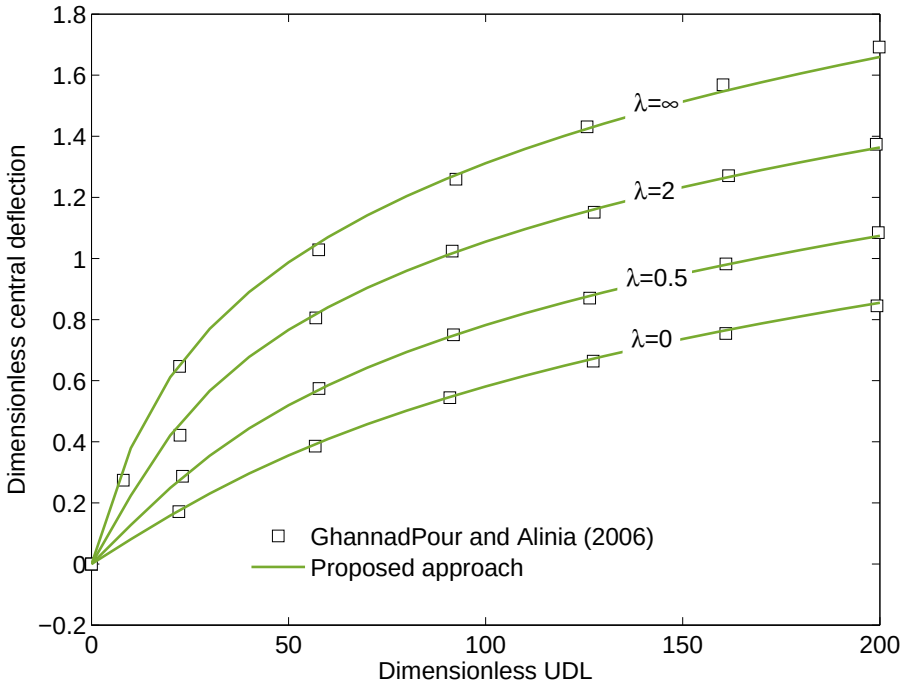

Figure 6.2 Dimensionless central deflection of a laterally restrained FG square plate ($h/a = 0.05$) over a wide range of non-dimensional UDL and volume fraction index λ. Results are obtained using three terms in the series solutions.

First, in Figure 6.2, load-deflection curves of a laterally restrained FG square plate with thickness-span ratio of 0.05 are shown for different volume fraction indices. The lower surface of the plate is assumed to be metal (aluminum) rich, while the upper surface is assumed to be pure ceramic (alumina). The elastic modulus is taken as 70 GPa and 380 GPa for aluminum and alumina, respectively. The UDL is non-dimensionalised using the aluminum's elastic modulus. It can be seen that the results obtained using the method presented are in very good agreement with those obtained from an analytical solution based on the classical plate theory (GhannadPour and Alinia, 2006).

6.3.2 Plate subject to full non-uniform temperature field

Consider a square plate with elasticity modulus of 380 GPa and Poisson's ratio of 0.3 under a sinusoidal thermal load as given below

$$\theta(x,y,z) = 2\theta_0 \frac{z}{h} \sin\frac{m\pi x}{a} \sin\frac{n\pi y}{b} \tag{6.22}$$

where θ_0 is the reference temperature. In Table 6.2, the calculated non-dimensional central deflection $(w/(h\alpha\theta_0))$ using the method presented (for only one term in the series solutions) is compared with analytical solutions of first order shear deformation theory (Mindlin, 1951), third order shear deformation theory (Ghugal and Kulkarni, 2011) and higher order shear deformation theory (Matsunaga, 2009). Comparing the results shows that the proposed method is accurate for determining the deflection of rectangular plates subjected to thermal loads.

Table 6.2 Comparisons of the non-dimensional transverse deflection at the centre of a square plate under a sinusoidal thermal load

Span-thickness ratio	Analytical solution sources	Deflection $w/(h\alpha\theta_0)$
10	Mindlin (1951)	13.1717
	Matsunaga (2009)	13.11
	Ghugal and Kulkarni (2011)	13.1719
	Proposed approach	13.17
100	Matsunaga (2009)	1317
	Proposed approach	1317

6.3.3 Plate subject to combined thermomechanical loads

As the first example for this loading case, in Figure 6.3 the dimensionless central deflection of an FG square plate is compared with deflections obtained from an analytical solution based on a higher order shear deformation plate theory (Shen and Wang, 2010). The plate is made of a mixture of silicon nitride and stainless steel with a volume fraction index of 2 and thickness-span ratio of 0.1. It is subjected to UDL in a thermal environmental condition at 300 K. The TDMP is also considered in the analysis and material properties are graded through the thickness of the plate according to the power-law distribution introduced in equation (8.19). The values of the coefficients of temperature in equation (2.10) are listed in Table 2.1. It is clearly seen that very good agreement is attained for this loading case.

In order to determine the fire induced through-depth temperature profile for the plate, the FE heat transfer analysis discussed in the Chapter 4 was carried out for a plate of 0.07 m thickness under the short hot and long cool fire scenarios. Figures 6.4 and 6.5 illustrate the time-temperature curves and through the depth temperature distributions for the plate under short hot fire and long cool fire, respectively. Both figures show

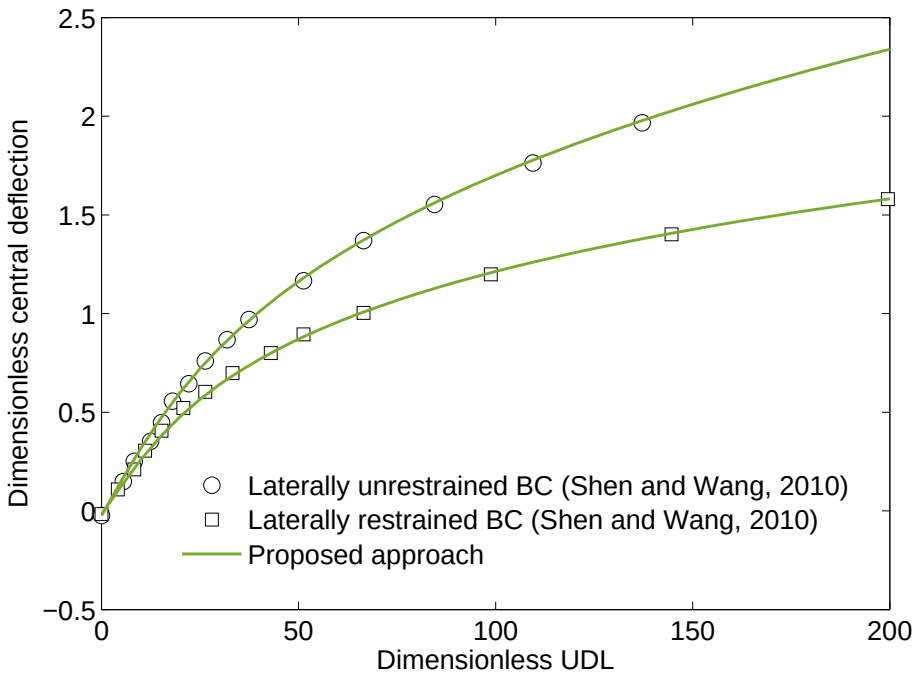

Figure 6.3 Dimensionless central deflection of an FG square plate ($h/a = 0.1$) having laterally unrestrained and restrained BCs under thermal environmental condition and a wide range of non-dimensional UDL.

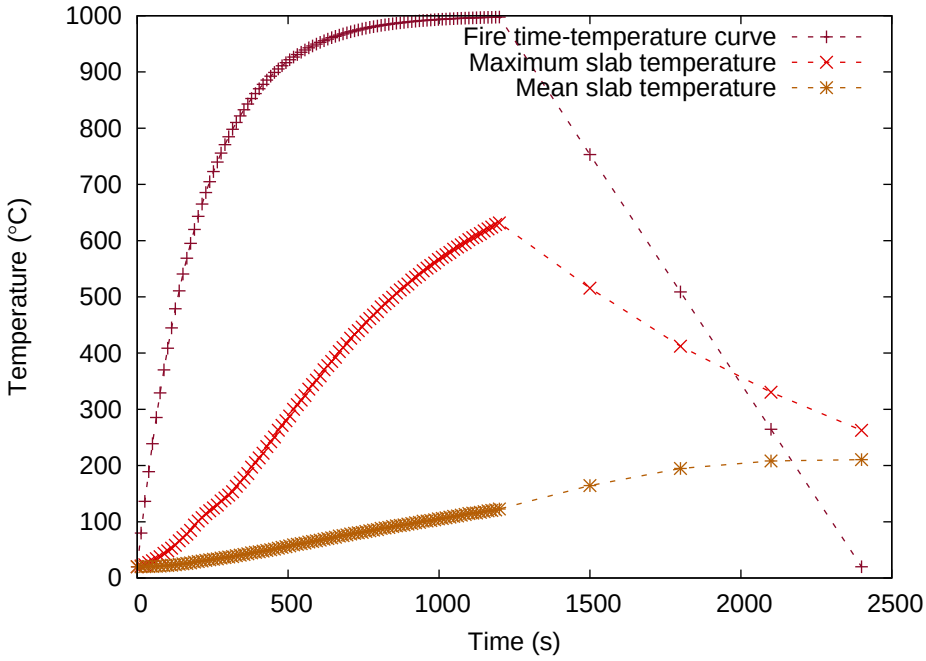

(a) Time-temperature curve

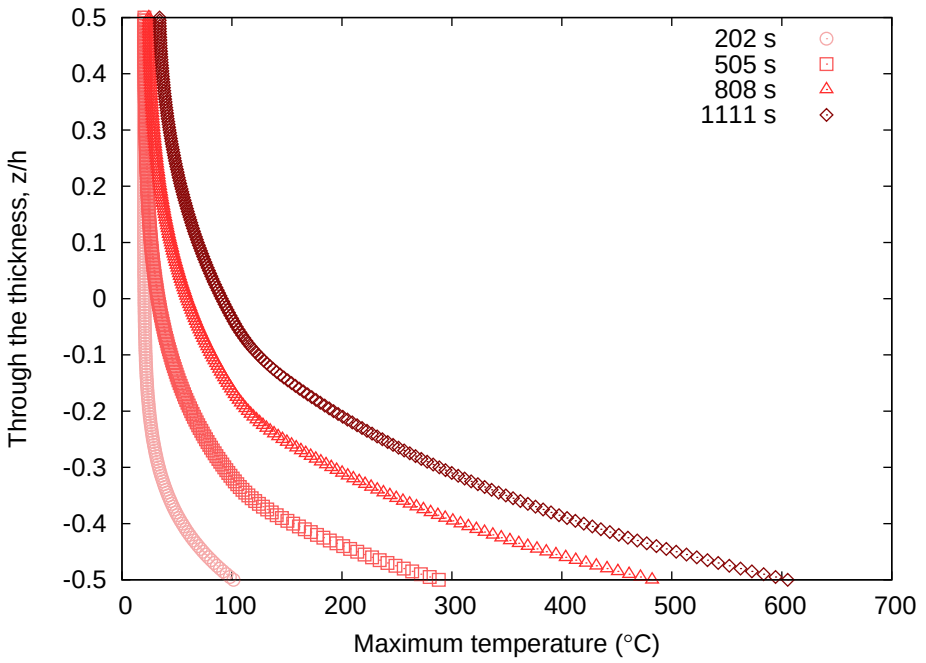

(b) Through-depth temperature

Figure 6.4 Time-temperature curve and through-depth temperature distribution for the short hot exponential fire.

the typical temperature distribution for plate structures under a one directional heat source which causes the temperature to decay exponentially over the thickness. As expected, the top surface is the coolest as it is the furthest from the heat source at the bottom surface. This approach allows the study of two extreme cases of high and low rates of heating. The two chosen temperature profiles from the FE heat

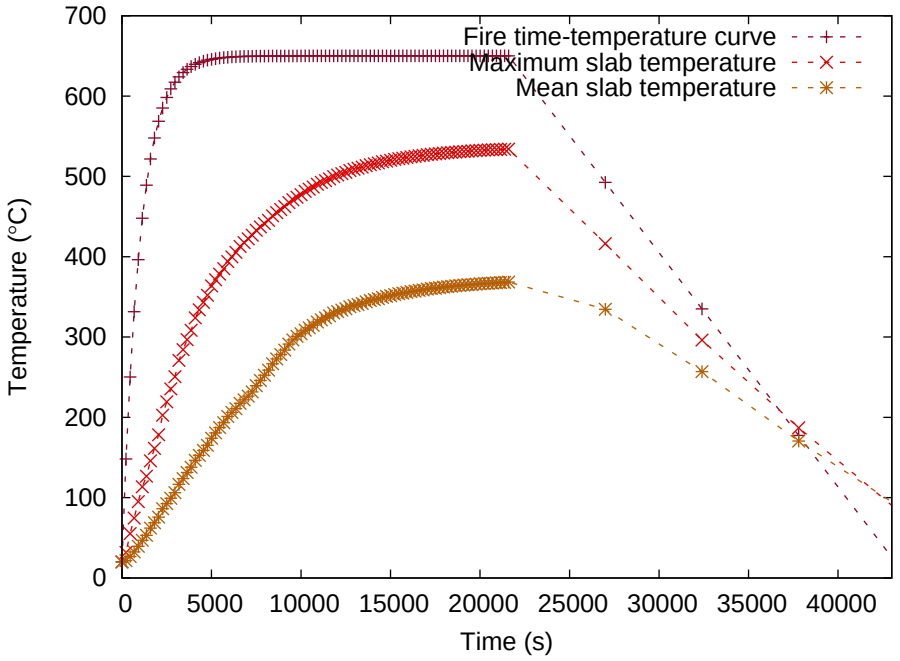

(a) Time-temperature curve

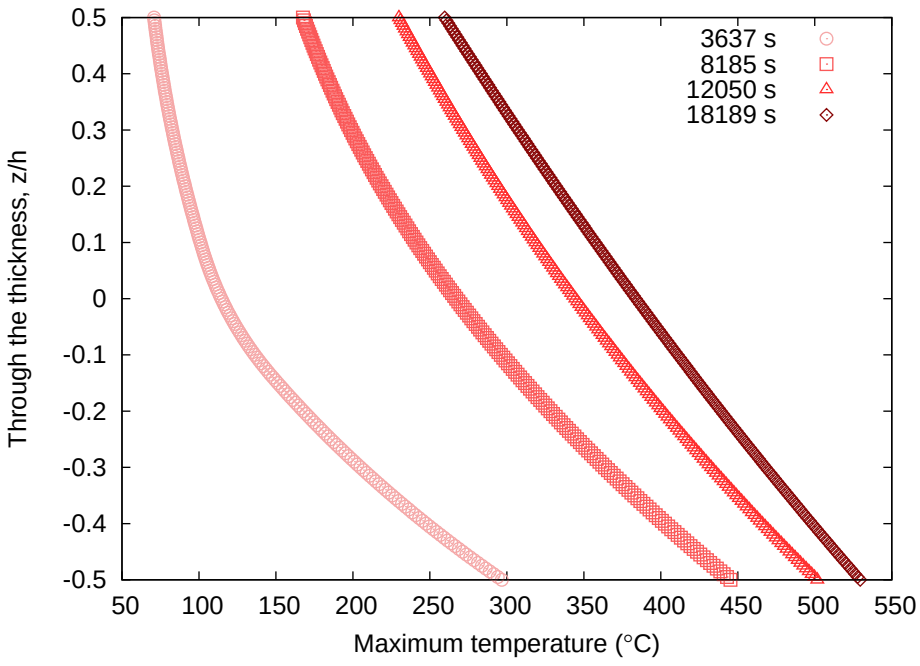

(b) Through-depth temperature

Figure 6.5 Time-temperature curve and through-depth temperature distribution for the long cool exponential fire.

transfer analysis are shown in Figure 6.6. Similar to the beam analysis, a generalised expression is obtained for the particular cases of heating rate parameter η fitting the chosen fire time-temperature curves as follows

$$\theta(z) = \theta_0 + (\theta_{max} - \theta_0)\exp\left[\mu\left(\frac{z}{h} - \frac{1}{2}\right)\right] \tag{6.23}$$

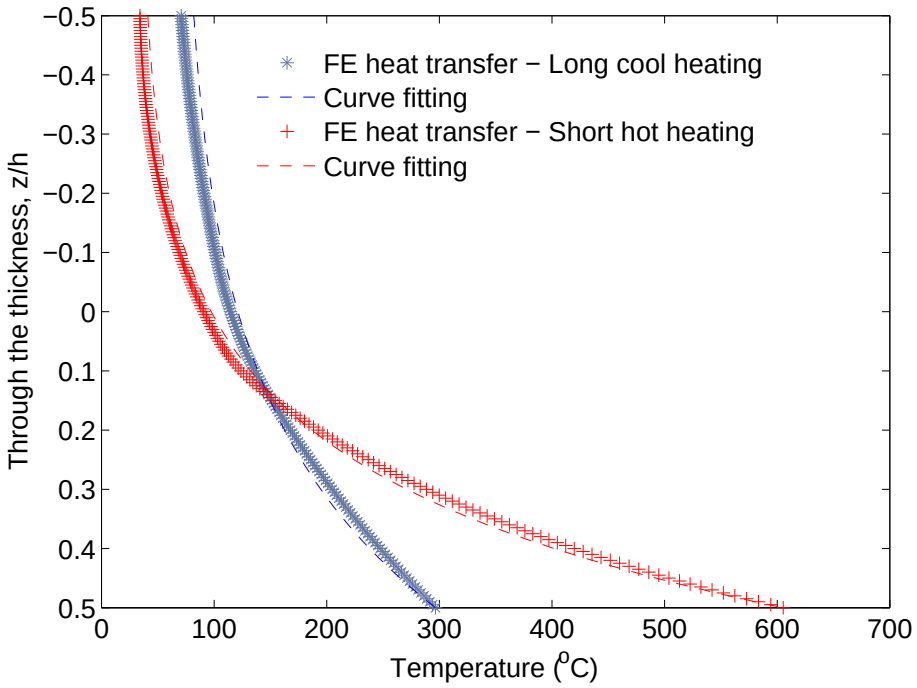

Figure 6.6 Non-uniform temperature distributions over the thickness of the plate using the FE heat transfer analysis. The assumed curve fitting functions correspond to the high and low rates of heating.

where the rate of change in the temperature is governed by the dimensionless parameter μ. For the chosen fire scenarios, the corresponding temperature profiles are achieved by the following expressions

$$\text{Low heating rate}: \theta(z)=70.81+225.87\exp\left[3\left(\frac{z}{h}-\frac{1}{2}\right)\right] \tag{6.24a}$$

$$\text{High heating rate}: \theta(z)=34.18+571.16\exp\left[4.4\left(\frac{z}{h}-\frac{1}{2}\right)\right] \tag{6.24b}$$

The assumed non-uniform temperature profiles can be used to study the structural behaviour of plates under most likely fire scenarios with different rates of heating. In the following, the nonlinear response of rectangular plates to short hot heating and long cool heating is studied. Due to inherent complexities in the problem studied, computational time increases when large number of terms are considered in the series solutions. To overcome this drawback, optimal number of terms are determined for both BC cases. In Figures 6.7 and 6.8, convergence of the series solutions is studied for the nonlinear central deflection of a square plate subjected to dimensionless UDL

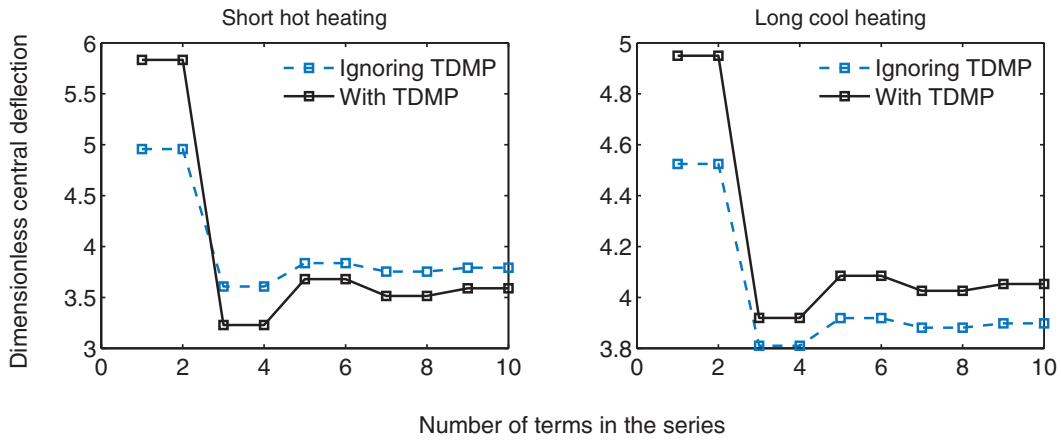

Figure 6.7 Convergence of the dimensionless nonlinear central deflection for a square plate ($h/a = 0.007$) with laterally unrestrained BC subject to UDL ($\bar{q}$=200) and two heating regimes. The Effect of TDMP is considered when calculating the solutions.

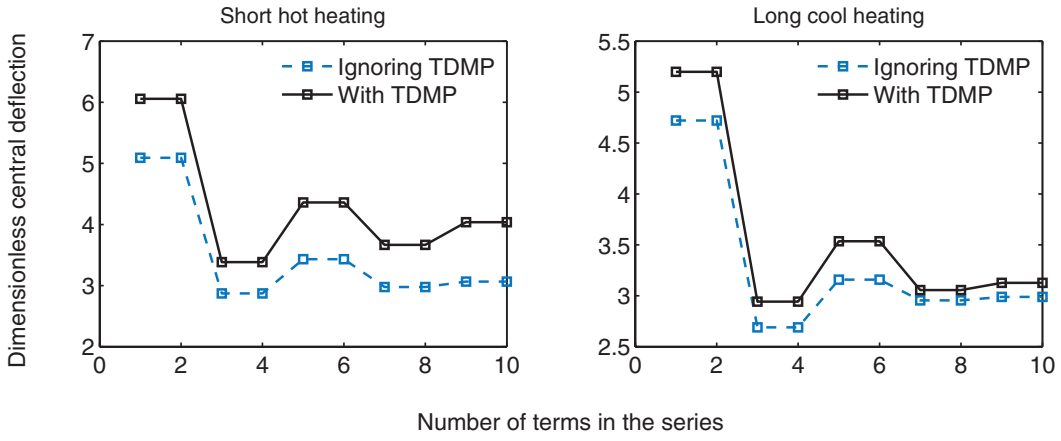

Figure 6.8 Convergence of the dimensionless nonlinear central deflection for a square plate ($h/a = 0.007$) with laterally restrained BC subject to UDL ($\bar{q}$=200) and two heating regimes. The Effect of TDMP is considered when calculating the solutions.

of 200 and short hot and long cool heating regimes for the laterally restrained and unrestrained BCs, respectively. The plate has thickness-span ratio of 0.007, elasticity modulus of 27 GPa (du Béton, 2010) and coefficient of thermal expansion of 9×10^{-6} (1/°C). The results are presented with and without considering the TDMP. It is found that for the laterally unrestrained BC, one term might be sufficient to achieve reasonable accuracy to the actual solutions, however, for the laterally restrained BC, three series terms are required.

To investigate the effect of the plate geometry, different aspect and thickness-span ratios are considered in Tables 6.3 and 6.4. As can be seen, both ratios have a nonlinear influence on the plate deflection. The central deflection for the plate with laterally

Table 6.3 Effect of the aspect and thickness-span ratios on the dimensionless central deflection of a plate under the short hot heating and UDL ($\bar{q}$=200)

Aspect ratio		Thickness-span ratio				
		0.005	0.007	0.008	0.01	0.015
Laterally unrestrained BC						
1	Ignoring TDMP	6.555	4.958	4.487	3.872	3.177
	With TDMP	7.771	5.834	5.252	4.475	3.562
2	Ignoring TDMP	10.010	7.219	6.338	5.094	3.423
	With TDMP	12.010	8.736	7.704	6.247	4.282
3	Ignoring TDMP	14.150	10.090	8.776	6.886	4.197
	With TDMP	17.120	12.390	10.880	8.718	5.688
Laterally restrained BC						
1	Ignoring TDMP	3.907	2.871	2.554	2.107	1.713
	With TDMP	4.622	3.384	3.006	2.490	1.803
2	Ignoring TDMP	2.935	2.123	1.869	1.510	0.967
	With TDMP	3.494	2.535	2.235	1.815	1.240
3	Ignoring TDMP	1.277	0.937	0.830	0.677	0.418
	With TDMP	1.538	1.136	1.010	0.832	0.580

Table 6.4 Effect of the aspect and thickness-span ratios on the dimensionless central deflection of a plate under the long cool heating and UDL ($\bar{q}$=200)

Aspect ratio		Thickness-span ratio				
		0.005	0.007	0.008	0.01	0.015
Laterally unrestrained BC						
1	Ignoring TDMP	5.959	4.524	4.114	3.591	3.026
	With TDMP	6.570	4.950	4.478	3.866	3.188
2	Ignoring TDMP	8.980	6.378	5.557	4.403	2.888
	With TDMP	10.010	7.162	6.263	4.999	3.317
3	Ignoring TDMP	12.530	8.700	7.458	5.654	3.063
	With TDMP	14.080	9.915	8.577	6.646	3.897
Laterally restrained BC						
1	Ignoring TDMP	3.646	2.689	2.397	1.965	1.774
	With TDMP	4.006	2.943	2.620	2.169	1.726
2	Ignoring TDMP	2.721	1.964	1.727	1.392	0.902
	With TDMP	3.003	2.169	1.909	1.544	0.990
3	Ignoring TDMP	1.166	0.850	0.751	0.609	0.338
	With TDMP	1.295	0.947	0.838	0.683	0.433

unrestrained BC is calculated using only one term in the series solutions, while for the laterally restrained plate it is calculated using three terms. This is justified through convergence studies and resulted in a considerable saving in computation time without losing accuracy.

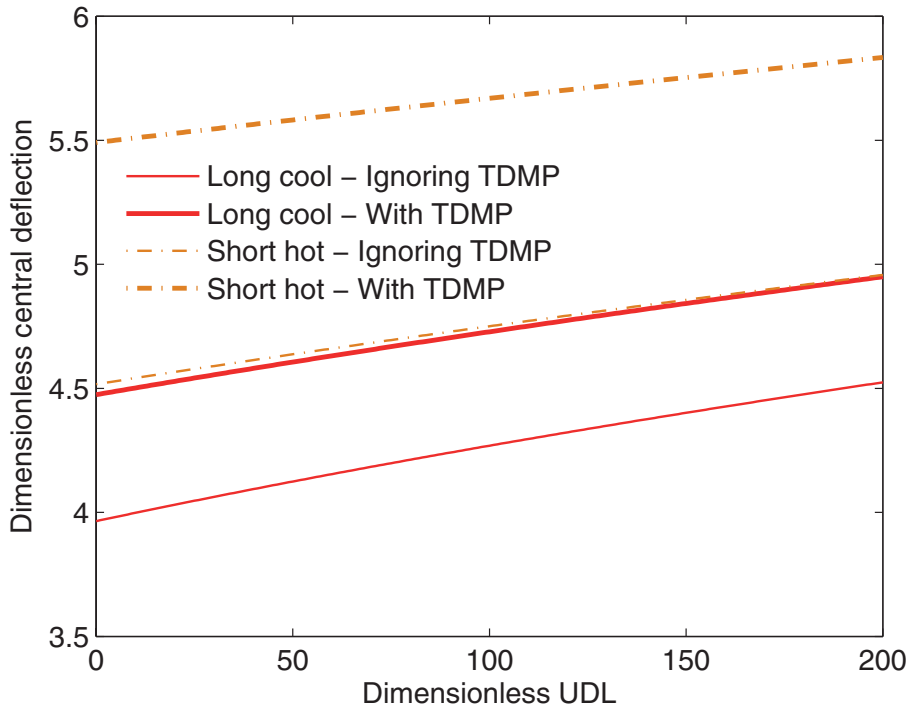

Figure 6.9 Dimensionless central deflection of a square plate ($h/a = 0.007$) with laterally unrestrained BC over a wide range of non-dimensional UDL. Results are obtained using one term in the series solutions with and without considering the TDMP.

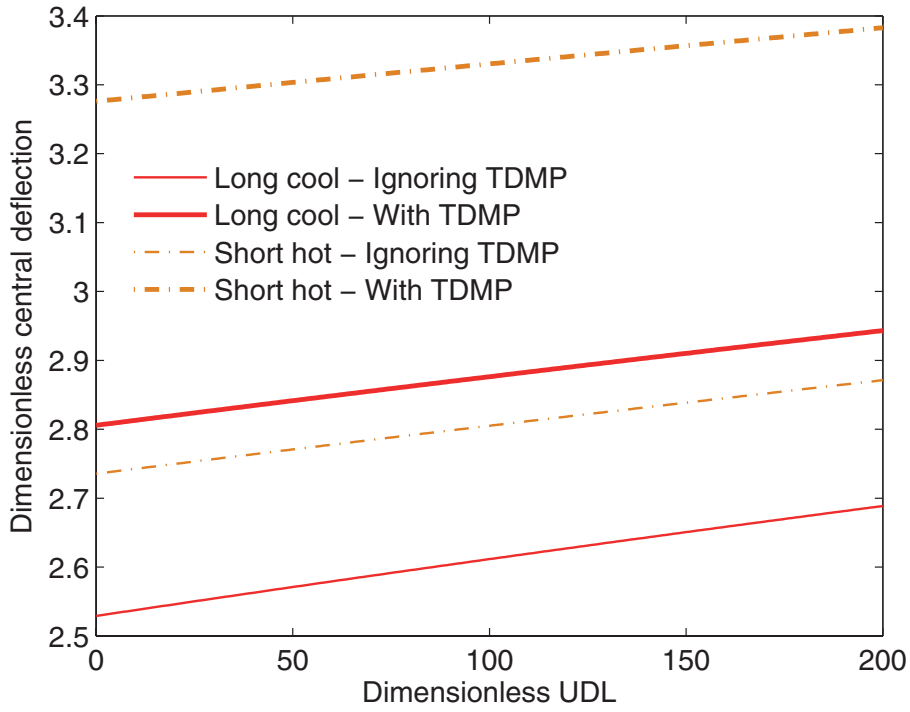

Figure 6.10 Dimensionless central deflection of a square plate ($h/a = 0.007$) with laterally restrained BC over a wide range of non-dimensional UDL. Results are obtained using three terms in the series solutions with and without considering the TDMP.

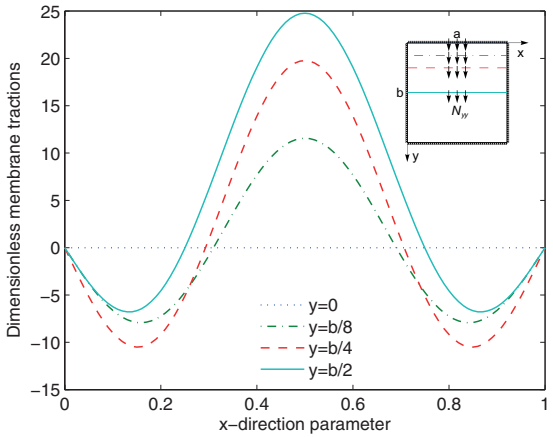

(a) Short hot fire with considering 3 series terms

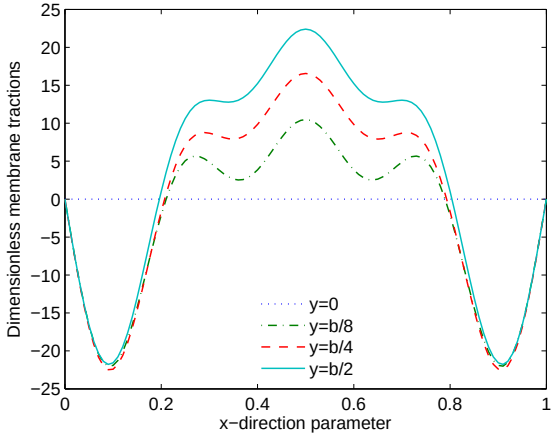

(b) Short hot fire with considering 7 series terms

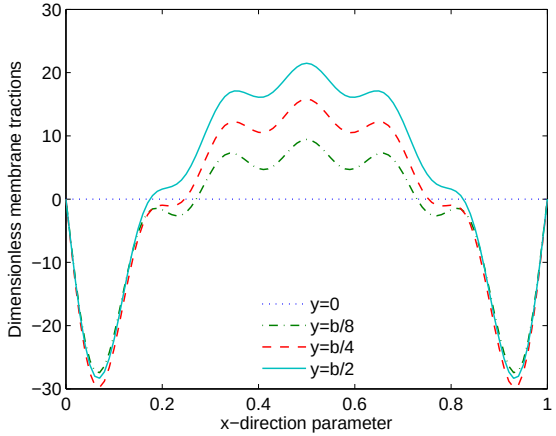

(c) Short hot fire with considering 11 series terms

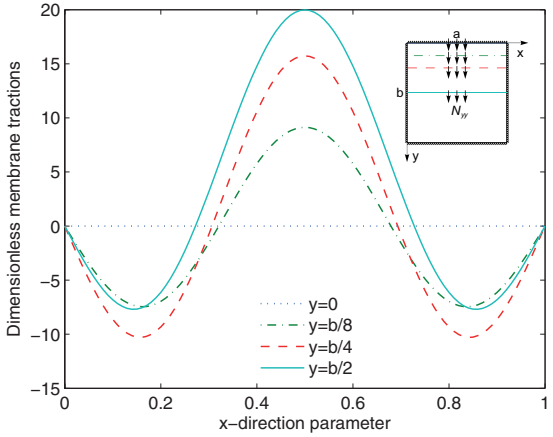

(d) Long cool fire with considering 3 series terms

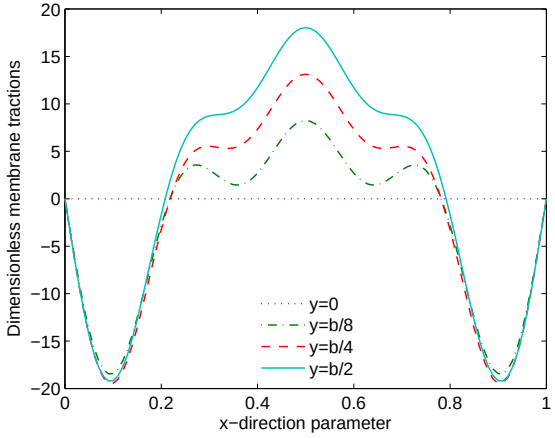

(e) Long cool fire with considering 7 series terms

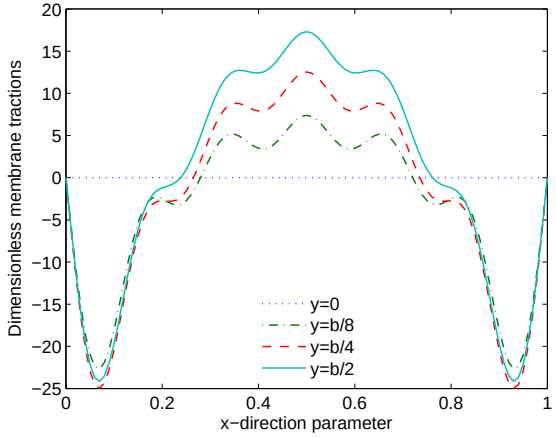

(f) Long cool fire with considering 11 series terms

Figure 6.11 Dimensionless membrane forces (N_{yy}) for a plate with laterally unrestrained BC across its span. The plate is subjected to two heating regimes and UDL ($\bar{q}$=200), while considering the TDMP.

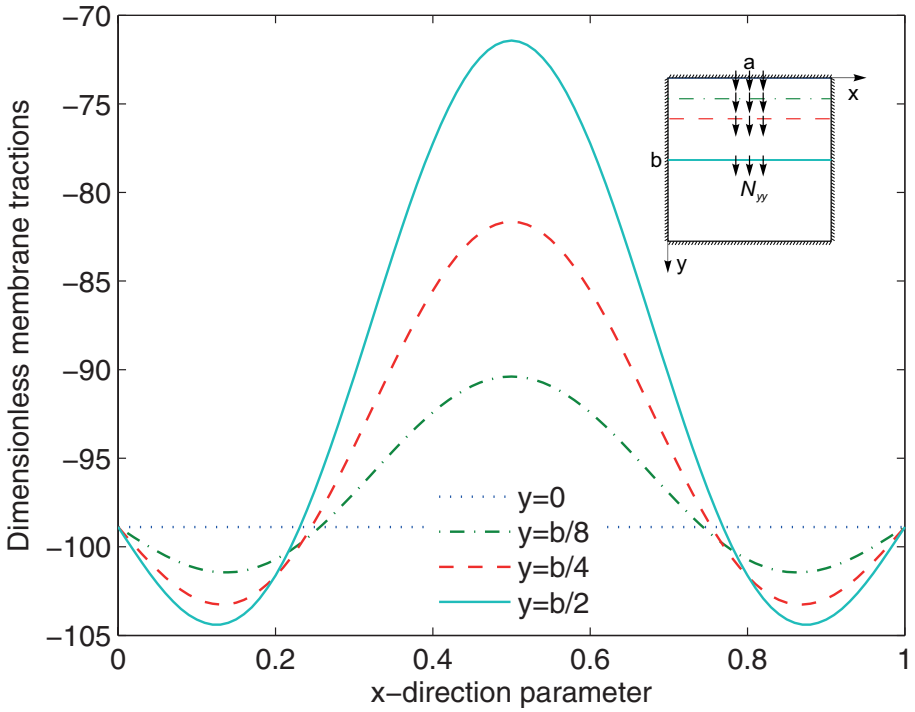

(a) Short hot fire

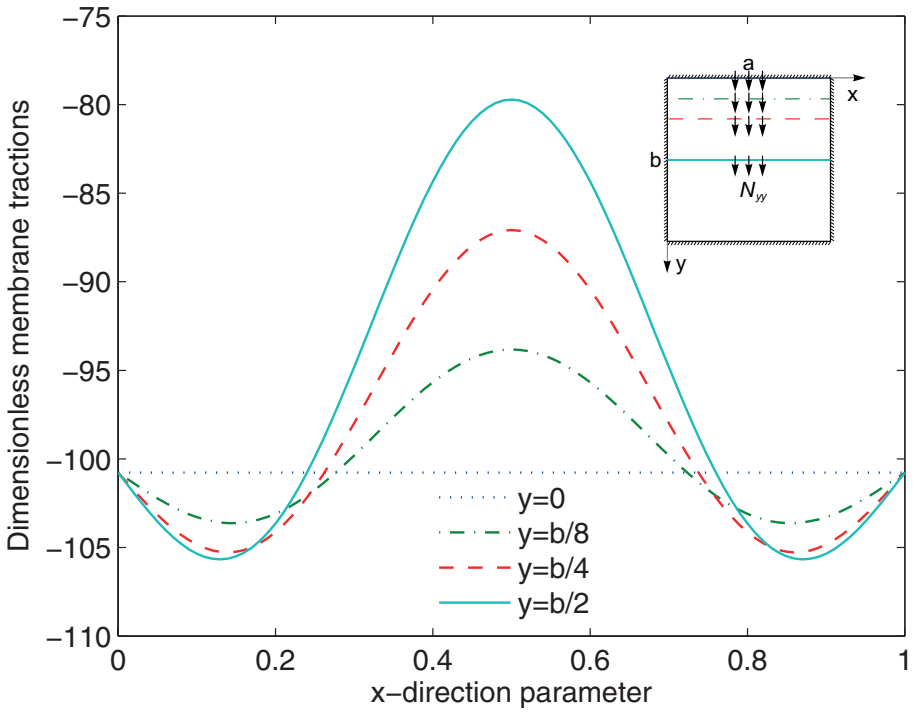

(b) Long cool fire

Figure 6.12 Dimensionless membrane forces (N_{yy}) for a plate with laterally restrained BC across its span. The plate is subjected to two heating regimes and UDL ($\bar{q}$=200), while considering TDMP. Three series terms are used in the proposed formulation to produce these figures.

Figures 6.9 and 6.10 show the variation of non-dimensional UDL parameter with the central deflection for laterally restrained and unrestrained BCs, respectively, with and without considering the TDMP. It can be seen that the effect of TDMP is significant in both boundary cases, in particular in the case of laterally unrestrained BC. The effect of the TDMP on the plate response is also highlighted by plotting dimensionless membrane forces (N_{yy}) in Figure 6.11 for a plate with laterally unrestrained BC and in Figure 6.12 for a plate with laterally restrained BC. Results are monitored in four different locations across the plate span for both heating regimes. The plate has the same material properties and geometry as mentioned in the last example and is subjected to the same UDL. In the case of long cool heating, it can be observed from the graphs that the difference between the results with and without considering the TDMP are not significant. However, in the case of short hot heating such a difference is found to be notable. This is mainly due to the fact that at high temperatures the material stiffness declines faster than at lower temperatures.

6.3.4 Development of tensile membrane action in plates

Membrane action in plates (for example reinforced concrete slabs) generally develops either in the form of CMA and/or TMA. The former develops at small vertical displacements of the plate under conditions of restraint to lateral translation, while the latter develops at large vertical displacements, also anchored by restraint to lateral translation at the boundaries. These phenomena are therefore naturally very sensitive to the boundary restraint conditions of the plate. It is well known that the development of both CMA and TMA can enhance the ultimate load-carrying capacity of floor slabs. As illustrated in Figure 5.4a, in slabs with laterally unrestrained BC undergoing large displacements, a “compressive ring” is formed in the slab as a manifestation of CMA in the outer regions of the slab which provides restraint to TMA occurring in the central region of the slab. This mechanism has, however, not been fully investigated and therefore has never been properly quantified.

In Figure 6.13, quiver plots of x, y, and z components of stress vector of a thin square temperature-dependent slab with laterally unrestrained BC subject to UDL of 100 under short hot fire condition is illustrated using GiD postprocessing framework. The figure shows the contribution of each stress components to the internal stress pattern

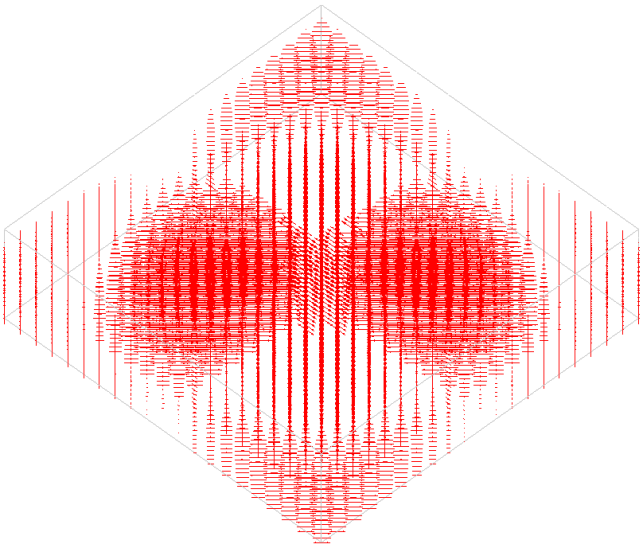

(a) The x component of principal stress in GiD

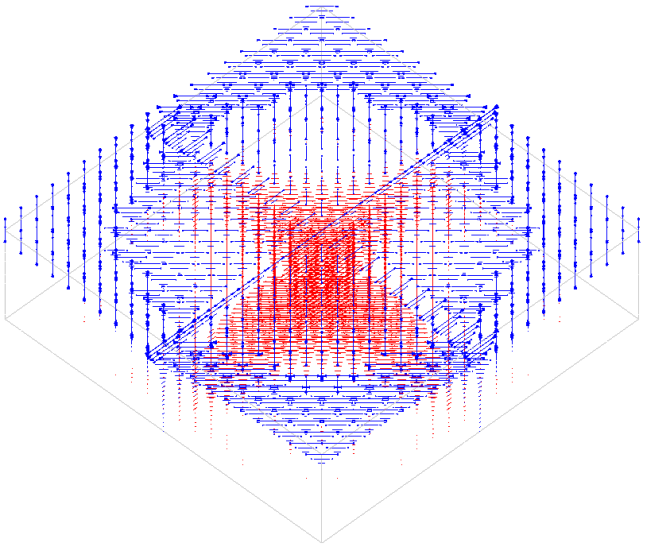

(b) The y component of principal stress in GiD

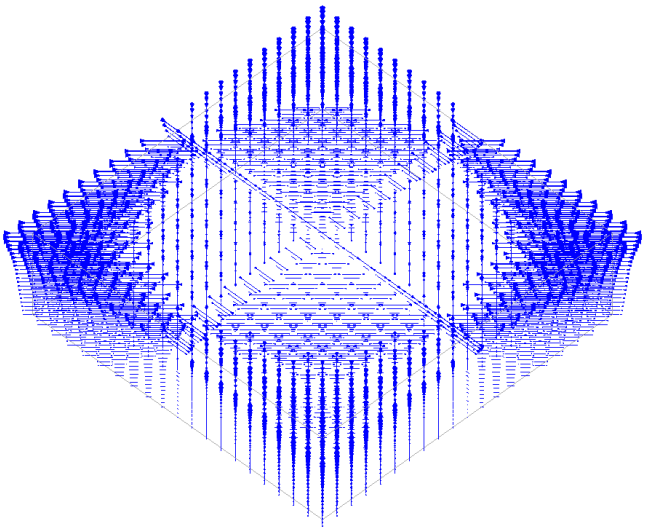

(c) The z component of principal stress in GiD

Figure 6.13 Quiver plots of principal stresses for a thin slab with temperature-dependent material properties under the short hot fire condition. Blue arrows represent compressive stresses and the red ones represent tensile stresses. Three series terms are used in the proposed formulation to produce the stress trajectories.

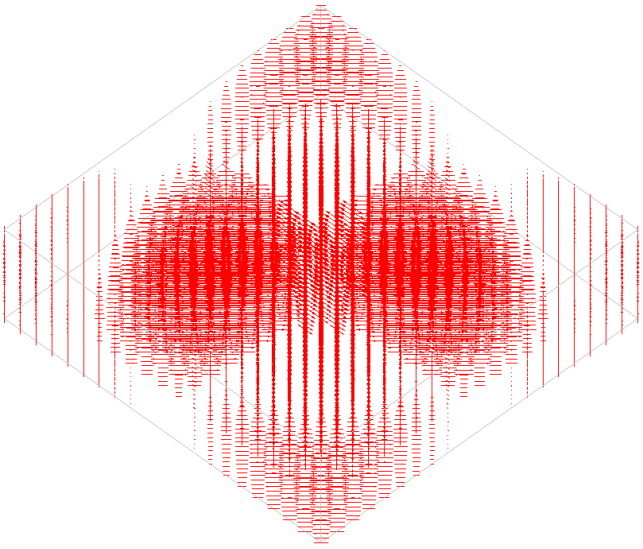

(a) The x component of principal stress in GiD

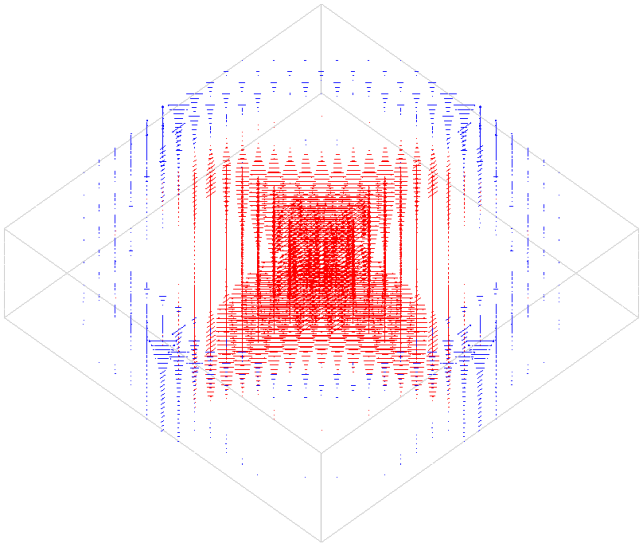

(b) The y component of principal stress in GiD

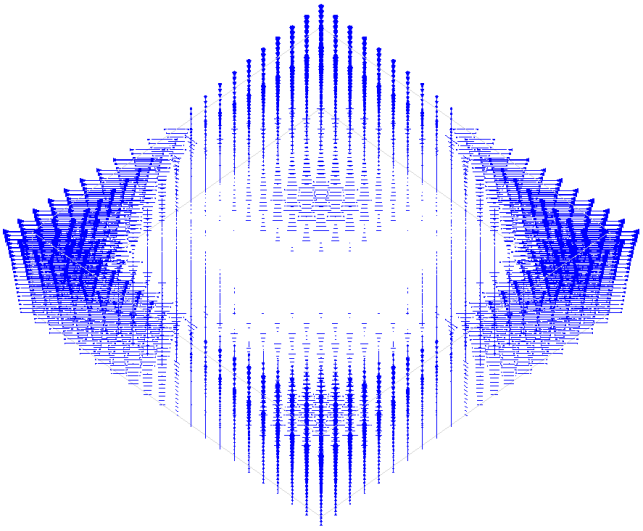

(c) The z component of principal stress in GiD

Figure 6.14 Quiver plots of principal stresses for a slab with temperature-dependent material properties under the long cool fire condition. Blue arrows represent compressive stresses and the red ones represent tensile stresses. Three series terms are used in the proposed formulation to produce the stress trajectories.

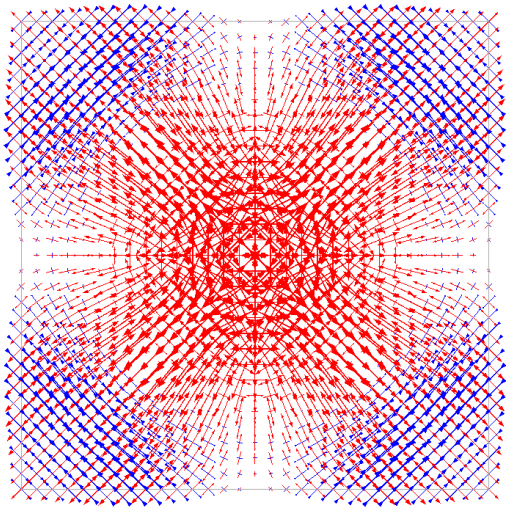

(a) After 202s, when the temperature at the top and bottom surfaces are 20°C and 101.41°C, respectively. The temperature field is taken as $20+81.41\exp[8(z/h-0.5)]$.

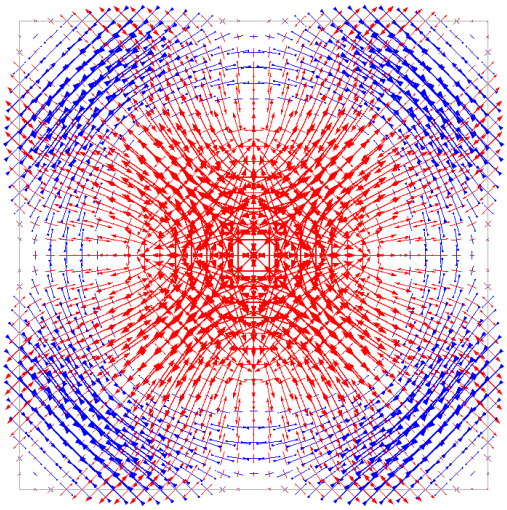

(b) After 505s, when the temperature at the top and bottom surfaces are 20.41°C and 288.12°C, respectively. The temperature field is taken as $20.41+267.71\exp[6.5(z/h-0.5)]$.

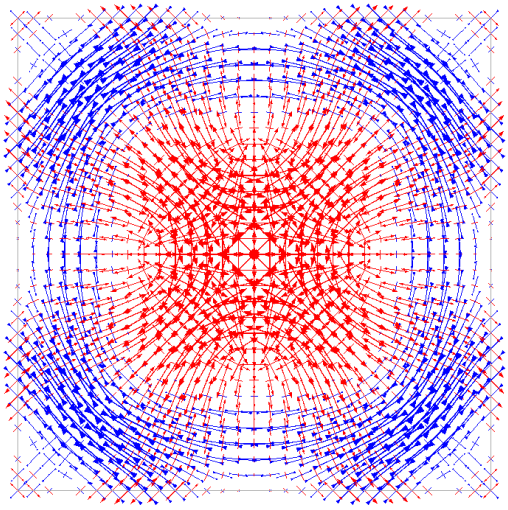

(c) After 808s, when the temperature at the top and bottom surfaces are 24.41°C and 482.13°C, respectively. The temperature field is taken as $24.41+457.72\exp[5.3(z/h-0.5)]$.

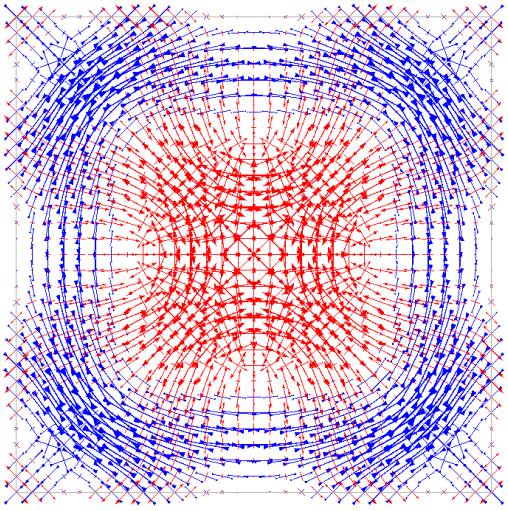

(d) After 1111s, when the temperature at the top and bottom surfaces are 34.18°C and 605.34°C, respectively. The temperature field is taken as $34.18+571.16\exp[4.4(z/h-0.5)]$.

Figure 6.15 Representation of compressive ring for a temperature-dependent slab under the short hot fire condition according to Figure 6.4b. Blue arrows represent compression and the red ones represent tension.

of the slab in fire. The lengths of the vectors are proportional to their magnitudes. A similar analysis is carried out for the same slab under long cool fire which is shown in Figure 6.14. Figures 6.15 and 6.16 illustrate the quiver plots of all dimensionless principal membrane forces for a square plate with unrestrained BC under the two heating regimes (short hot and long cool fire conditions) when TDMP is considered.

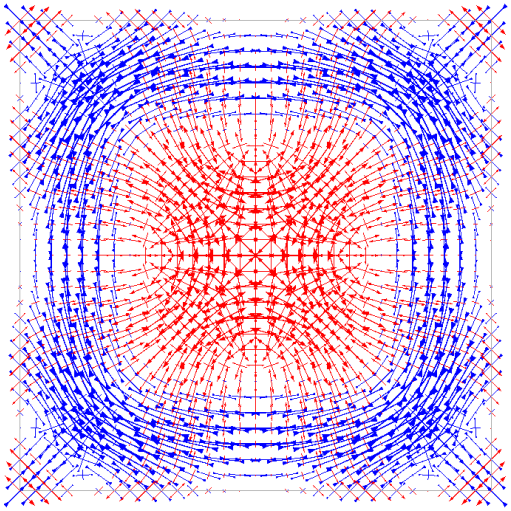

(a) After 3637s, when the temperature at the top and bottom surfaces are 70.81°C and 296.68°C, respectively. The temperature field is taken as $70.81 + 225.87\ \exp[3(z/h - 0.5)]$.

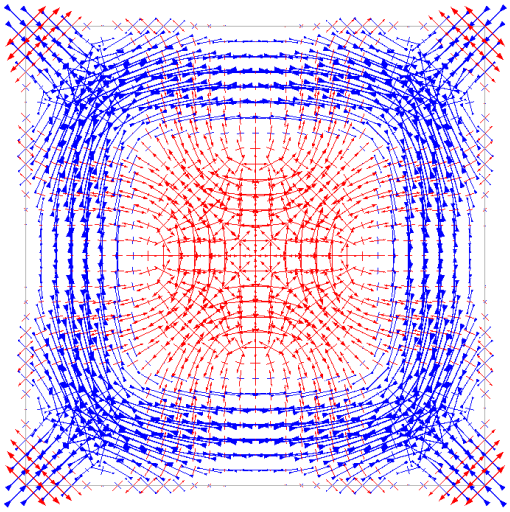

(b) After 8185s, when the temperature at the top and bottom surfaces are 167.53°C and 445.23°C, respectively. The temperature field is taken as $87.53 + 357.7\ \exp[1.4(z/h - 0.5)]$.

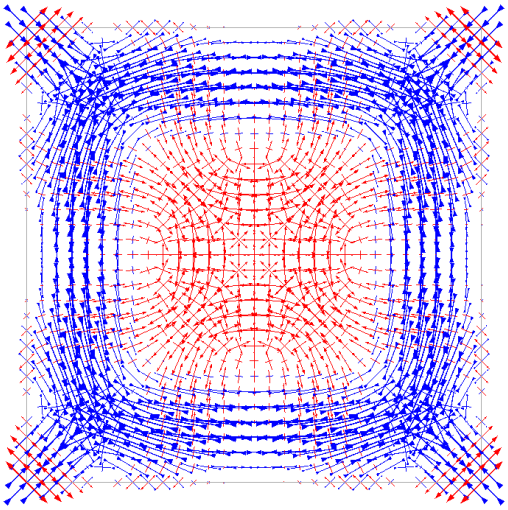

(c) After 12050s, when the temperature at the top and bottom surfaces are 229.88°C and 501.61°C, respectively. The temperature field is taken as $79.88 + 421.73\ \exp[(z/h - 0.5)]$.

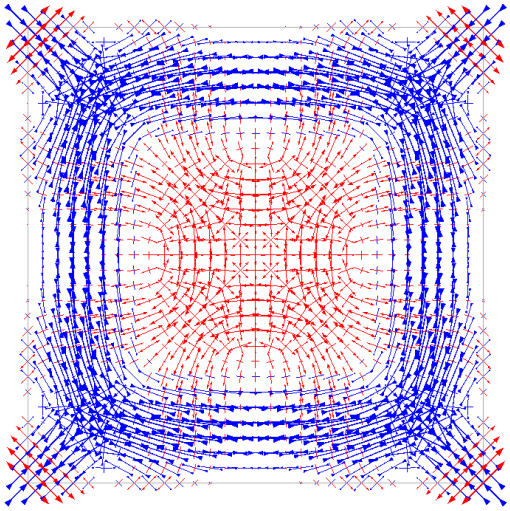

(d) After 18189s, when the temperature at the top and bottom surfaces are 259.59°C and 529.48°C, respectively. The temperature field is taken as $59.59 + 468.3\ \exp[0.8(z/h - 0.5)]$.

Figure 6.16 Representation of compressive ring for a temperature-dependent slab under the long cool fire condition according to Figure 6.5b. Blue arrows represent compression and the red ones represent tension.

The variation of the temperature are shown in these figures using a cartoon strip type approach.

As observed in Figure 6.11, the magnitude of the membrane forces are higher in the case of short hot fire than that of in the long cool fire. This can also be seen in

Figures 6.15 and 6.16. The reason for this is that higher gradients in the short hot fire creates larger curvatures, thereby increasing the contribution of membrane forces in carrying the load. However, lower deflections in the long cool fire mean that the contribution of bending resistance is relatively greater, therefore membrane forces are lower. Figures 6.15 and 6.16 clearly show TMA in the plate with tensile membrane stresses in the central zone and compressive membrane stresses around perimeter of the plate. The existence of both tension zone in the middle and compression zone around perimeter of the plate leads to the formation of a "compressive ring" which is highlighted with blue arrows in the figures. This phenomenon has been recognised as an important load-carrying mechanism of "last resort" in the full-scale fire tests at Cardington test in the UK (Usmani *et al.*, 2000).

6.4 Summary

New theoretical approaches were presented for the geometrically and materially nonlinear analysis of laterally unrestrained and restrained rectangular plates subjected to thermal and/or mechanical loading. The performance of the proposed method was demonstrated through several analysis examples. It was found that similar to the previous chapter, for the laterally unrestrained case, one term might be sufficient to achieve a reasonably accurate solution. However, for the laterally restrained case, three series terms were needed, particularly for higher thermomechanical loads. Although the numerical analysis is confined to the case of rectangular plates under two fire conditions based upon likely fires that could occur, the application of the method presented to other arbitrary non-uniform in-depth thermal gradients considering the TDMP is straightforward.

Chapter 7

Geometrically Nonlinear Behaviour of Shallow Shells[1]

7.1 Introduction

Shallow shells are widely used in the design of lightweight thin-walled structures. They can deliver useful load-carrying capacity by virtue of their curvatures, thereby effectively resisting the externally applied loads with optimum use of materials. This makes them practical and efficient structural components and of importance in the design of light weight thin-walled structures. Their nonlinear behaviour has been studies by a number of researchers.

Barut *et al.* (2000) presented a nonlinear FE formulation for moderately thick flat and curved laminated panels subjected to non-uniform thermal loading over the panel surface and across the thickness. The material properties were assumed independent of the temperature changes. The principle of virtual work along with the co-rotational form of the total Lagrangian formulation were used to derive the governing equations. Sze *et al.* (2004) presented eight sets of geometric nonlinear benchmark problems on cylindrical and spherical shells. Fukuchi *et al.* (2006) presented an improved FEM for elastic-plastic analysis of shallow shells. Their approach was based on a hybrid model in which the stress distribution across the panel thickness was expressed as a continuous function using the membrane forces and bending moments for elastic-plastic materials and the delta-sequence function.

[1] Based on the works reported by Khazaeinejad and Usmani (2016a).

A meshless local Petrov-Galerkin (MLPG) method was employed by Sladek *et al.* (2008a) to solve thick shallow shell problems under mechanical static and dynamic loads. Albuquerque and Aliabadi (2008) presented a boundary element formulation for the analysis of isotropic shallow shells. They showed that the formulation of thin shallow shells can be used for shells with small ratio between curvature radius and edge length. Recently, Sabik and Kreja (2013) numerically studied the load capacity of thermally loaded multi-layered shells under uniform thermal loading based on the first order shear deformation theory and without taking into account the thermal degradation of material properties at high temperatures.

Analytical and semi-analytical approaches are successfully applied to the shell nonlinear problems. Nie (2003) presented a nonlinear analysis of an imperfect shallow spherical shell on a Pasternak foundation subjected to uniform loads. The shell was assumed elastically restrained against rotational, transverse and in-plane displacements. The asymptotic iteration method was applied to obtain an analytical expression for the external load and the central deflection of the shell. Heuer and Ziegler (2004) studied the thermal snap-through in symmetrically layered shallow shells of a polygonal planform with immovable straight edges using a two DoFs model derived from a Ritz-Galerkin approximation. Amabili (2005) investigated the large amplitude of the response of simply supported doubly-curved shallow shells with rectangular planform to static and dynamic loads. He used the Donnell and Novozhilov shell theories retaining in-plane inertia to obtain geometrically nonlinear shell responses.

In this chapter, a nonlinear mathematical model is developed to analyse the large displacements of thin shallow shells with single or double curvature (i.e. shallow hyperbolic paraboloidal shell, shallow spherical shell, and shallow cylindrical shell) under thermomechanical loading conditions.

7.2 Basic hypothesis

A shallow shell typically has a rise of less than one-fifth of the smallest dimension of its planform. Consider a thin shallow shell with single or double curvature (see Figure 7.1) under non-uniform through-depth thermal gradients, while it is being subjected to a transverse mechanical load. In line with the assumptions of the shallow shell theory, it is assumed that the rise of the shell is relatively small in comparison to

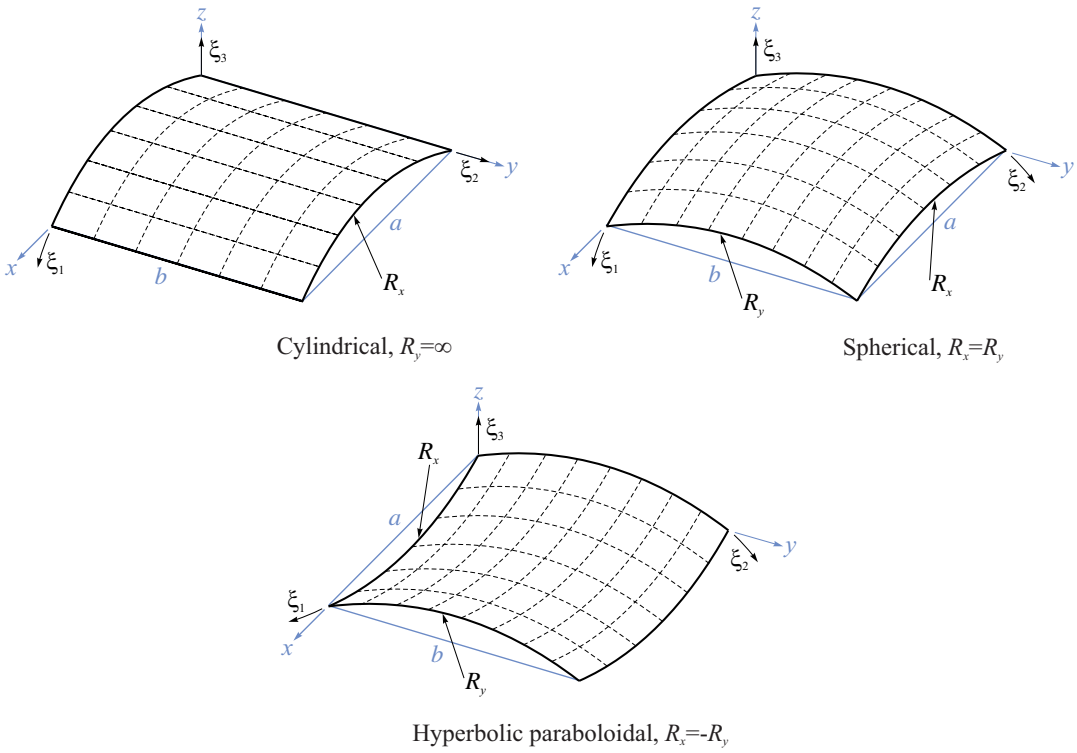

Figure 7.1 Types of shallow shells with single and double curvature on a rectangular platform.

its other dimensions (see Figure 3.2). The basic relations of shallow shells are similar but not identical to the equations (5.1) and (5.2).

7.3 Derivation of governing equations

Under quasi-static conditions, the nonlinear response of a thermomechanically loaded shallow shell can be determined by solving compatibility and equilibrium equations simultaneously. The compatibility equation can be obtained by taking the second derivatives of the strains and combining the resulting expressions as follows

$$\frac{\partial^2 \varepsilon_{xx}}{\partial y^2} + \frac{\partial^2 \varepsilon_{yy}}{\partial x^2} - \frac{\partial^2 \gamma_{xy}}{\partial x \partial y} = \left(\frac{\partial^2 w}{\partial x \partial y}\right)^2 - \left(\frac{\partial^2 w}{\partial x^2}\right)\left(\frac{\partial^2 w}{\partial y^2}\right) + \frac{1}{R_y}\left(\frac{\partial^2 w}{\partial x^2}\right) + \frac{1}{R_x}\left(\frac{\partial^2 w}{\partial y^2}\right) - \frac{2}{R_{xy}}\left(\frac{\partial^2 w}{\partial x \partial y}\right) \tag{7.1}$$

Substituting equations (3.35) and (5.2) in the above equation, gives the compatibility equation of the problem to be solved in terms of the stress function and the out-of-plane displacement as follows

$$\begin{aligned}&\frac{\partial^4 F}{\partial x^4}+2\frac{\partial^4 F}{\partial x^2\partial y^2}+\frac{\partial^4 F}{\partial y^4}\\&-E\left[\left(\frac{\partial^2 w}{\partial x\partial y}\right)^2-\left(\frac{\partial^2 w}{\partial x^2}\right)\left(\frac{\partial^2 w}{\partial y^2}\right)+\frac{1}{R_x}\left(\frac{\partial^2 w}{\partial y^2}\right)+\frac{1}{R_y}\left(\frac{\partial^2 w}{\partial x^2}\right)-\frac{2}{R_{xy}}\left(\frac{\partial^2 w}{\partial x\partial y}\right)\right]\\&+\frac{1}{h}\left(\frac{\partial^2 N^\theta}{\partial x^2}+\frac{\partial^2 N^\theta}{\partial y^2}\right)=0\end{aligned} \tag{7.2}$$

The equilibrium equation of the shell can be expressed by adding the effect of shell curvature to the equation (5.21)

$$\begin{aligned}&\frac{\partial^2 M_{xx}}{\partial x^2}+2\frac{\partial^2 M_{xy}}{\partial x\partial y}+\frac{\partial^2 M_{yy}}{\partial y^2}+N_{xx}\frac{\partial^2 w}{\partial x^2}+N_{yy}\frac{\partial^2 w}{\partial y^2}\\&+2N_{xy}\frac{\partial^2 w}{\partial x\partial y}-\left(\frac{N_{xx}}{R_x}+\frac{N_{yy}}{R_y}+\frac{2N_{xy}}{R_{xy}}\right)+q(x,y)=0\end{aligned} \tag{7.3}$$

After substitution from equation (3.28) into equation (7.3), the equilibrium equation of the shell can be derived as follows

$$\begin{aligned}&D\left(\frac{\partial^4 w}{\partial x^4}+2\frac{\partial^4 w}{\partial x^2\partial y^2}+\frac{\partial^4 w}{\partial y^4}\right)\\&-h\left[\frac{\partial^2 F}{\partial y^2}\left(\frac{\partial^2 w}{\partial x^2}-\frac{1}{R_x}\right)+\frac{\partial^2 F}{\partial x^2}\left(\frac{\partial^2 w}{\partial y^2}-\frac{1}{R_y}\right)-2\frac{\partial^2 F}{\partial x\partial y}\left(\frac{\partial^2 w}{\partial x\partial y}-\frac{1}{R_{xy}}\right)\right]\\&+\left(\frac{\partial^2 M^\theta}{\partial x^2}+\frac{\partial^2 M^\theta}{\partial y^2}\right)-q(x,y)=0\end{aligned} \tag{7.4}$$

In the case of flat shells, the radii of curvatures are equal to infinity and the governing equations (7.2) and (7.4) simplify to the ones previously reported for the plate.

7.4 Solution of governing equations

Similar to the plate analysis, two common types of support conditions are considered for shell problems:

1. Edges laterally unrestrained, thereby permitting lateral translation, while transverse translations are restrained along the shell edges and rotations about the edge axis are free.

2. Edges laterally restrained where all translations are restricted along the shell edges, while rotations about the edge axis remains free.

These BCs are suitable for cases where rotational restraints are not important. The suitable solutions for the out-of-plane displacement, the thermal resultants, the transverse mechanical loading and the stress function may be assumed in the same form as equations (5.23)-(5.31). For the laterally restrained BC, the following expressions are obtained from the elongation of the shell in the x direction

$$\int_0^a \frac{\partial u}{\partial x}\mathrm{d}x = \int_0^a \left[\frac{1}{E}\left(\frac{\partial^2 F}{\partial y^2} - \nu\frac{\partial^2 F}{\partial x^2}\right) - \frac{1}{2}\left(\frac{\partial w}{\partial x}\right)^2 - \frac{w}{R_x} + \frac{N^\theta}{Eh}\right]\mathrm{d}x \tag{7.5}$$

and in the y direction

$$\int_0^b \frac{\partial v}{\partial y}\mathrm{d}y = \int_0^b \left[\frac{1}{E}\left(\frac{\partial^2 F}{\partial x^2} - \nu\frac{\partial^2 F}{\partial y^2}\right) - \frac{1}{2}\left(\frac{\partial w}{\partial y}\right)^2 - \frac{w}{R_y} + \frac{N^\theta}{Eh}\right]\mathrm{d}y \tag{7.6}$$

Setting the edge displacements to zero after some manipulations, yields the following expressions for the reaction loads at the shell edges

$$\begin{aligned} P_x = {} & \frac{Ebh\pi^2 w_{mn}^2}{8(1-\nu^2)}\left(\frac{m^2}{a^2} + \nu\frac{n^2}{b^2}\right) + \frac{hn\left[-1+(-1)^m\right]\left[-1+(-1)^n\right]F_{mn}}{mb} \\ & + \frac{Eah\left[-1+(-1)^m\right]\left[-1+(-1)^n\right]w_{mn}}{mn\pi^2(1-\nu^2)}\left(\frac{1}{R_x} + \frac{\nu}{R_y}\right) - \frac{bN^\theta}{(1-\nu)} \end{aligned} \tag{7.7a}$$

$$\begin{aligned} P_y = {} & \frac{Eah\pi^2 w_{mn}^2}{8(1-\nu^2)}\left(\nu\frac{m^2}{a^2} + \frac{n^2}{b^2}\right) + \frac{hm\left[-1+(-1)^m\right]\left[-1+(-1)^n\right]F_{mn}}{na} \\ & + \frac{Eah\left[-1+(-1)^m\right]\left[-1+(-1)^n\right]w_{mn}}{mn\pi^2(1-\nu^2)}\left(\frac{\nu}{R_x} + \frac{1}{R_y}\right) - \frac{aN^\theta}{(1-\nu)} \end{aligned} \tag{7.7b}$$

Substituting equations (5.23)-(5.31) into equations (7.2) and (7.4) leads to the following compatibility equation

$$\begin{aligned}&\left(\frac{m^2}{a^2}+\frac{n^2}{b^2}\right)^2 F_{mn}S_{mn}-\left(\frac{m^2}{a^2}+\frac{n^2}{b^2}\right)\frac{N^{\theta}_{mn}S_{mn}}{h\pi^2}\\&-\frac{E}{a^2b^2}\left(mnrs\,C_{mn}C_{rs}-m^2s^2\,S_{mn}S_{rs}\right)w_{mn}w_{rs}\\&+\frac{E}{\pi^2}\left(\frac{n^2S_{mn}}{b^2}\frac{1}{R_x}+\frac{m^2S_{mn}}{a^2}\frac{1}{R_y}+\frac{mnC_{mn}}{ab}\frac{2}{R_{xy}}\right)w_{mn}=0\end{aligned}\tag{7.8}$$

and equilibrium equation for the shell

$$\begin{aligned}&\left[D\left(\frac{m^2}{a^2}+\frac{n^2}{b^2}\right)^2+\frac{1}{ab\pi^2}\left(\frac{m^2P_x}{a}+\frac{n^2P_y}{b}\right)\right]w_{mn}S_{mn}\\&-\left(\frac{m^2}{a^2}+\frac{n^2}{b^2}\right)\frac{M^{\theta}_{mn}S_{mn}}{\pi^2}\\&-\frac{h\left[(m^2s^2+r^2n^2)\,S_{mn}S_{rs}-2mrns\,C_{mn}C_{rs}\right]}{a^2b^2}F_{rs}w_{mn}\\&-\frac{h}{\pi^4}\left[\left(-\frac{P_x}{bh}+\frac{s^2\pi^2}{b^2}F_{rs}S_{rs}\right)\frac{1}{R_x}+\left(-\frac{P_y}{ah}+\frac{r^2\pi^2}{a^2}F_{rs}S_{rs}\right)\frac{1}{R_y}\right.\\&\left.+\frac{2rs\pi^2C_{rs}}{ab}F_{rs}\frac{1}{R_{xy}}\right]-\frac{q_{mn}S_{mn}}{\pi^4}=0\end{aligned}\tag{7.9}$$

Ignoring the mathematical coupling between higher order terms in the governing equations (i.e., $m=r$ and $n=s$), as discussed in previous chapters, results in a simplified version of the compatibility equation

$$\begin{aligned}&\left(\frac{m^2}{a^2}+\frac{n^2}{b^2}\right)^2 F_{mn}S_{mn}-\left(\frac{m^2}{a^2}+\frac{n^2}{b^2}\right)\frac{N^{\theta}_{mn}S_{mn}}{h\pi^2}-\frac{Em^2n^2(C^2_{mn}-S^2_{mn})}{a^2b^2}w^2_{mn}\\&+\frac{E}{\pi^2}\left(\frac{n^2S_{mn}}{b^2}\frac{1}{R_x}+\frac{m^2S_{mn}}{a^2}\frac{1}{R_y}+\frac{mnC_{mn}}{ab}\frac{2}{R_{xy}}\right)w_{mn}=0\end{aligned}\tag{7.10}$$

and the equilibrium equation for the shell

$$\begin{aligned}
&\left[D\left(\frac{m^2}{a^2}+\frac{n^2}{b^2}\right)^2+\frac{1}{ab\pi^2}\left(\frac{m^2P_x}{a}+\frac{n^2P_y}{b}\right)\right]w_{mn}S_{mn}\\
&-\left(\frac{m^2}{a^2}+\frac{n^2}{b^2}\right)\frac{M^{\theta}_{mn}S_{mn}}{\pi^2}-\frac{2hm^2n^2(S^2_{mn}-C^2_{mn})}{a^2b^2}F_{mn}w_{mn}\\
&-\frac{h}{\pi^4}\left[\left(-\frac{P_x}{bh}+\frac{n^2\pi^2}{b^2}F_{mn}S_{mn}\right)\frac{1}{R_x}+\left(-\frac{P_y}{ah}+\frac{m^2\pi^2}{a^2}F_{mn}S_{mn}\right)\frac{1}{R_y}\right.\\
&\left.+\frac{2mn\pi^2C_{mn}}{ab}F_{mn}\frac{1}{R_{xy}}\right]-\frac{q_{mn}S_{mn}}{\pi^4}=0
\end{aligned}\tag{7.11}$$

It should be noted that in the case of untwisted shallow shells, the twist radius R_{xy} is infinite and therefore the whole terms containing $1/R_{xy}$ vanish. Using the expansion theorem as discussed in previous chapters, the following equations are established

$$\begin{aligned}
&\left(\frac{m^2}{a^2}+\frac{n^2}{b^2}\right)^2F_{mn}-\left(\frac{m^2}{a^2}+\frac{n^2}{b^2}\right)\frac{N^{\theta}_{mn}}{h\pi^2}\\
&-4EH_{mn}\left(\frac{mn}{ab}\right)^2w^2_{mn}+\frac{E}{\pi^2}\left(\frac{n^2}{b^2}\frac{1}{R_x}+\frac{m^2}{a^2}\frac{1}{R_y}\right)w_{mn}=0
\end{aligned}\tag{7.12}$$

$$\begin{aligned}
&\left[D\left(\frac{m^2}{a^2}+\frac{n^2}{b^2}\right)^2+\frac{1}{ab\pi^2}\left(\frac{m^2P_x}{a}+\frac{n^2P_y}{b}\right)\right]w_{mn}\\
&-\left(\frac{m^2}{a^2}+\frac{n^2}{b^2}\right)\frac{M^{\theta}_{mn}}{\pi^2}+8hH_{mn}F_{mn}\left(\frac{mn}{ab}\right)^2w_{mn}\\
&+\frac{4[-1+(-1)^m][-1+(-1)^n]}{mn\pi^6}\left(\frac{P_x}{b}\frac{1}{R_x}+\frac{P_y}{a}\frac{1}{R_y}\right)\\
&-\frac{h}{\pi^2}\left(\frac{n^2}{b^2}\frac{1}{R_x}+\frac{m^2}{a^2}\frac{1}{R_y}\right)F_{mn}-\frac{q_{mn}}{\pi^4}=0
\end{aligned}\tag{7.13}$$

Substituting equation (7.12) into equation (7.13), gives the following characteristic load-deflection equation for the shell

$$\varsigma_1\,w^3_{mn}+\varsigma_2\,w^2_{mn}+\varsigma_3\,w_{mn}+\varsigma_4=0\tag{7.14}$$

which has the following coefficients

$$\varsigma_1 = \frac{32Ehm^4n^4H_{mn}^2}{\left(m^2b^2+n^2a^2\right)^2} \tag{7.15a}$$

$$\varsigma_2 = -\frac{12EhH_{mn}a^2b^2}{\pi^2\left(m^2b^2+n^2a^2\right)^2}\left(\frac{m^2n^4}{b^2}\frac{1}{R_x}+\frac{m^4n^2}{a^2}\frac{1}{R_y}\right) \tag{7.15b}$$

$$\begin{aligned}\varsigma_3 = {} & D\left(\frac{m^2}{a^2}+\frac{n^2}{b^2}\right)^2+\frac{8N_{mn}^{\theta}H_{mn}m^2n^2}{\pi^2(m^2b^2+n^2a^2)}+\frac{1}{ab\pi^2}\left(\frac{m^2P_x}{a}+\frac{n^2P_y}{b}\right) \\ & +\frac{Eh}{\pi^4\left(m^2b^2+n^2a^2\right)^2}\left(n^2a^2\frac{1}{R_x}+m^2b^2\frac{1}{R_y}\right)^2\end{aligned} \tag{7.15c}$$

$$\begin{aligned}\varsigma_4 = {} & -\left(\frac{m^2}{a^2}+\frac{n^2}{b^2}\right)\frac{M_{mn}^{\theta}}{\pi^2}-\frac{N_{mn}^{\theta}a^2b^2}{\pi^4\left(m^2b^2+n^2a^2\right)}\left(\frac{n^2}{b^2}\frac{1}{R_x}+\frac{m^2}{a^2}\frac{1}{R_y}\right) \\ & -\frac{q_{mn}}{\pi^4}+\frac{4\left[-1+(-1)^m\right]\left[-1+(-1)^n\right]}{mn\pi^6}\left(\frac{P_x}{b}\frac{1}{R_x}+\frac{P_y}{a}\frac{1}{R_y}\right)\end{aligned} \tag{7.15d}$$

There are three solutions for the above nonlinear equation, one real solution and two complex solutions. The deflection must be calculated for adequate series terms to make the final solution more accurate for both the chosen BCs. The membrane tractions of the shell can be calculated from

$$N_{xx} = \frac{P_x}{b}-\sum_{m=1}^{\infty}\sum_{n=1}^{\infty}\frac{hn^2\pi^2}{b^2}\,S_{mn}\,F_{mn} \tag{7.16a}$$

$$N_{yy} = \frac{P_y}{a}-\sum_{m=1}^{\infty}\sum_{n=1}^{\infty}\frac{hm^2\pi^2}{a^2}\,S_{mn}\,F_{mn} \tag{7.16b}$$

$$N_{xy} = -\sum_{m=1}^{\infty}\sum_{n=1}^{\infty}\frac{hmn\pi^2}{ab}\,C_{mn}\,F_{mn} \tag{7.16c}$$

To investigate the accuracy and performance of the proposed method, a number of examples are solved for square thin shallow shells with both the chosen BCs. In these examples, shells are subjected to a UDL and/or a through-depth thermal gradient.

7.4.1 Shallow shell subject to UDL

In addition to the dimensionless parameters in Table 5.1, a list of new dimensionless parameters are considered which are listed in Table 7.1. Results of dimensionless deflection of a shallow spherical shell with the laterally unrestrained BC subjected to a UDL only are compared with results obtained from the MLPG formulation (Sladek *et al.*, 2008a), as shown in Figure 7.2a. The bottom surface of the shell is subjected to a UDL of 2.07×10^6 N/m^2 directed upwards (bottom surface loading). The shell has the same material and geometrical properties as the previous case. Only for this example, the deflection is presented in a different dimensionless form, namely deflection of shallow shell over deflection of its corresponding flat shell ($R_x = R_y = \infty$). Figure 7.2a shows that the maximum deflection at the centre of the laterally unrestrained shallow shell differ by 20 percent from the deflection for its corresponding flat shell. The convergence of the solution for the central deflection is demonstrated in Figure 7.2b. As can be seen, the solutions presented match well with those solutions obtained from the MLPG method. It may also be noticed that this reasonable accuracy may be achieved by considering only one series term in the solutions.

As stated earlier, the curvature allows a thin shell to deliver useful load-carrying capacity. To better understand this feature, the influence of the curvature of a shallow cylindrical shell on its nonlinear response to a UDL is investigated using the proposed model and the FE software ABAQUS. Four different shallow cylindrical shells subjected to a UDL of 10 directed downwards (top surface loading) are modelled in ABAQUS using an S4R5 element, as shown in Figure 7.3. The dimensionless deflections of these shells are presented in Tables 7.2 and 7.3, for the laterally unrestrained and restrained BCs, respectively. The rise of the shell above its planform is denoted by H and is calculated from $R - \sqrt{R^2 - a^2/4}$, as illustrated in Figure 3.2.

Table 7.1 Definitions of dimensionless quantities for geometrically nonlinear shallow shell problems

Description	Definition
Thickness to span ratio	h/a
Rise to thickness ratio	H/h
Radius of curvature to span ratio	R_x/a and R_y/a
Dimensionless x-coordinate parameter	x/a

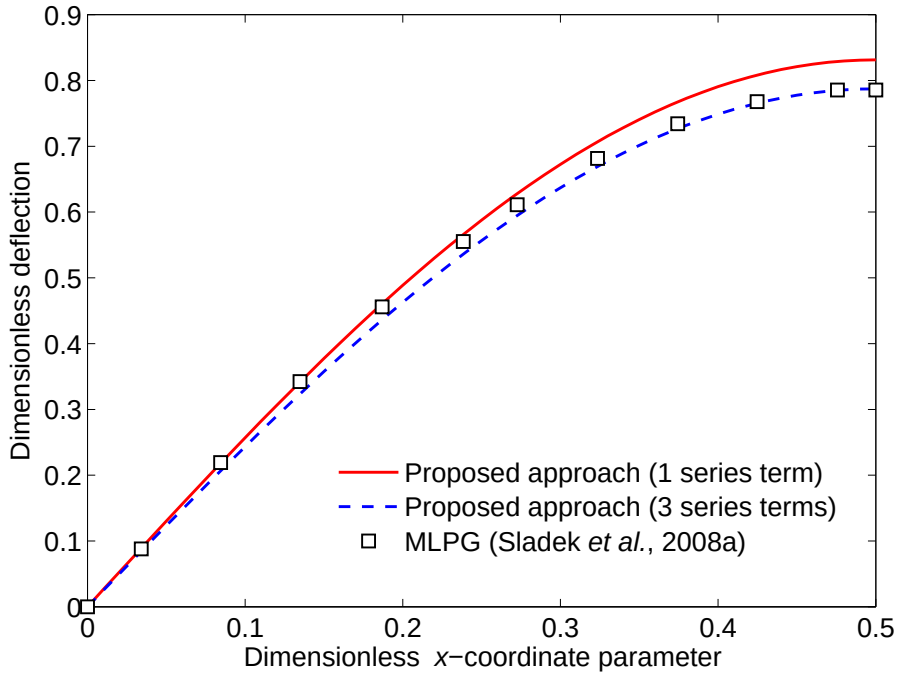

(a)

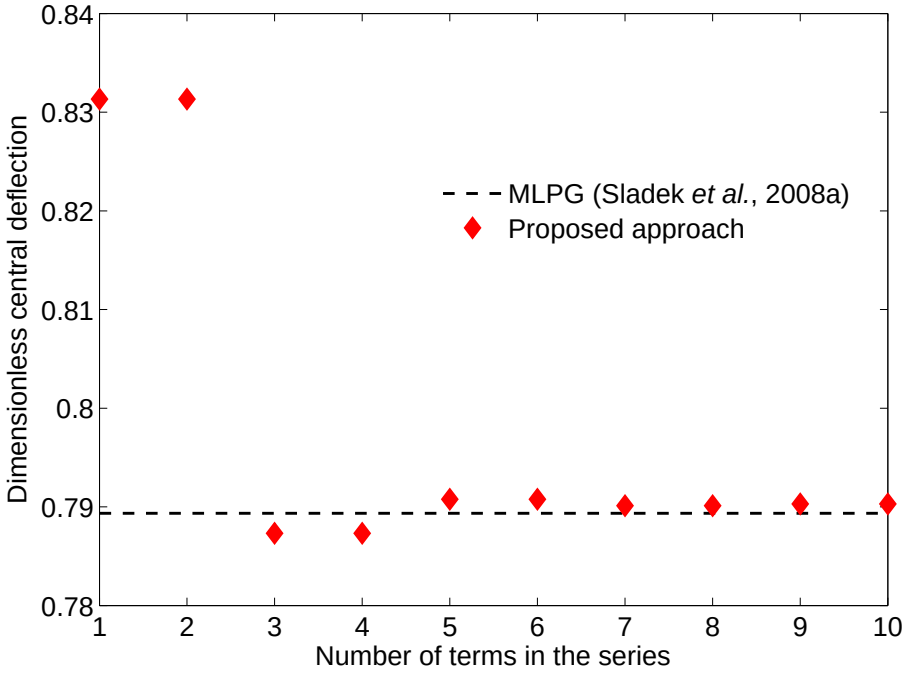

(b)

Figure 7.2 Comparison of deflection for a shallow spherical shell with the laterally unrestrained BC subject to UDL. Figure (a) shows the variation of dimensionless deflection (i.e. deflection of the shallow shell over deflection of its corresponding flat shell) with the dimensionless x-coordinate parameter and Figure (b) demonstrates the convergence of the dimensionless central deflection. Note that, the denominator of the MLPG and the proposed solutions are determined from the same method used for the calculation of the deflection of the curved shell.

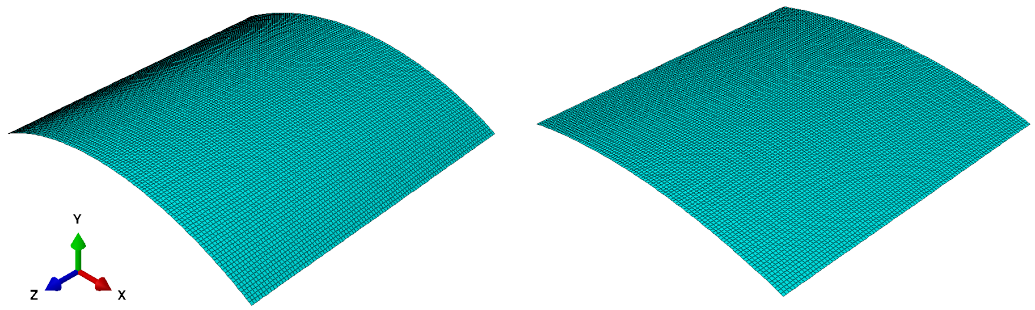

(a) R_x/a=1 **(b)** R_x/a=2

(c) R_x/a=3 **(d)** R_x/a=5

Figure 7.3 FE meshes for shallow cylindrical shell examples.

It can be observed that the deflection values decrease with an increase in the curvature of the shell. This is due to increasing flexural rigidity of the shell caused by the curvature. The accuracy of the proposed method decreases significantly for relatively deep shells with the laterally unrestrained BC. Therefore, the present approach is not accurate enough for determining the nonlinear responses of such shells. However, in the case of shells with the laterally restrained BC, the proposed method has a better performance when compared with the ABAQUS solutions. This is very promising since the laterally restrained BC is practically more useful than the laterally unrestrained BC.

For extremely shallow shells ($R_x/a = 5$) in Tables 7.2 and 7.3, quiver plots of all principal stresses on the top and bottom surfaces of the shell are shown in Figures 7.4 and 7.5. These figures are obtained using the proposed approach and ABAQUS for thin square shallow cylindrical shells with laterally restrained and unrestrained BCs. The lengths of the vectors are proportional to their magnitudes. Both Figures 7.4

Table 7.2 Comparison of dimensionless nonlinear central deflection for a shallow cylindrical shell with the the laterally unrestrained BC under UDL using one series term

R_x/a	H/h	Angle subtended[a]	Proposed approach[b]	ABAQUS simulation
1	4.47	60	-0.053	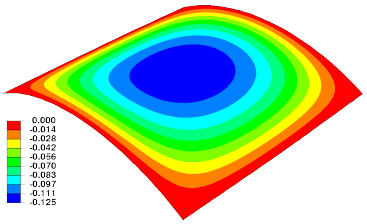
2	2.12	28.95	-0.172	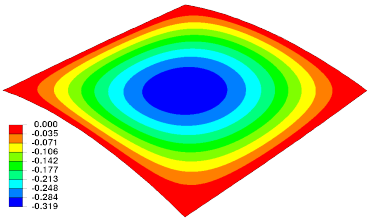
3	1.40	19.2	-0.297	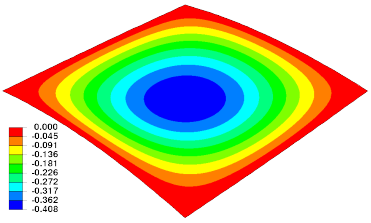
5	0.83	11.5	-0.427	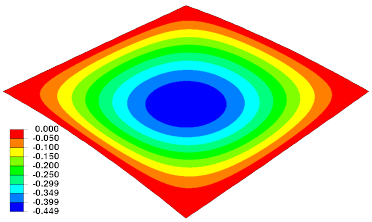

[a] See Figure 3.2.

[b] For this BC, the present formulation is only valid for extremely shallow shells (e.g. $R_x/a = 5$).

and 7.5 show that the top surface of the shell under both BCs is predominantly under compression, while predominantly tension occurs at the bottom surface of the shell, which suggests a behaviour not unlike plate bending. However, closer inspection shows that the stress trajectories and distribution patterns are quite different for the two BCs. The case of the unrestrained BC shows that the tensile stresses at the bottom surface are concentrated towards the centre with a large area of compression surrounding them, similar to a compressive ring surrounding laterally unrestrained plates under large deflections. It can also be seen from Figures 7.4 and 7.5 that the

Table 7.3 Comparison of dimensionless nonlinear central deflection for a shallow cylindrical shell with the laterally restrained BC under UDL using three series terms

R_x/a	H/h	Angle subtended[a]	Proposed approach[b]	ABAQUS simulation
1	4.47	60	-0.010	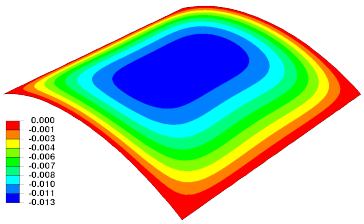
2	2.12	28.95	-0.055	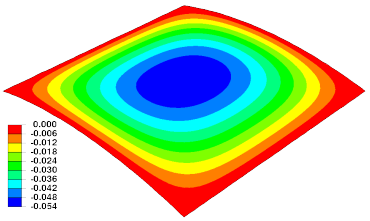
3	1.40	19.2	-0.122	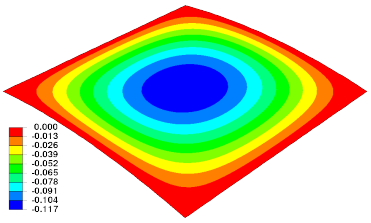
5	0.83	11.5	-0.278	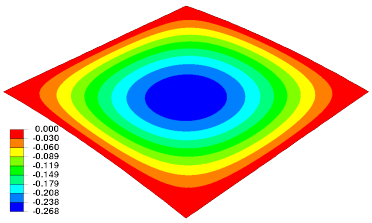

[a] See Figure 3.2.

general stress patterns predicted by the proposed approach match quite well with those predicted by the ABAQUS.

The load-deflection relationship for various types of shallow shells is depicted in Figures 7.6 and 7.7 for both the chosen BCs. The shell has elastic modulus of 27×10^9 N/m^2, Poisson's ratio of 0.3, and thickness to span ratio of 0.03 and is subjected to a UDL at its top and bottom surfaces. For both BCs, the maximum deflection of the shell (at the centre) increases nonlinearly as the UDL increases. It is clear that the top surface loading produces a downwards deflection whereas the bottom

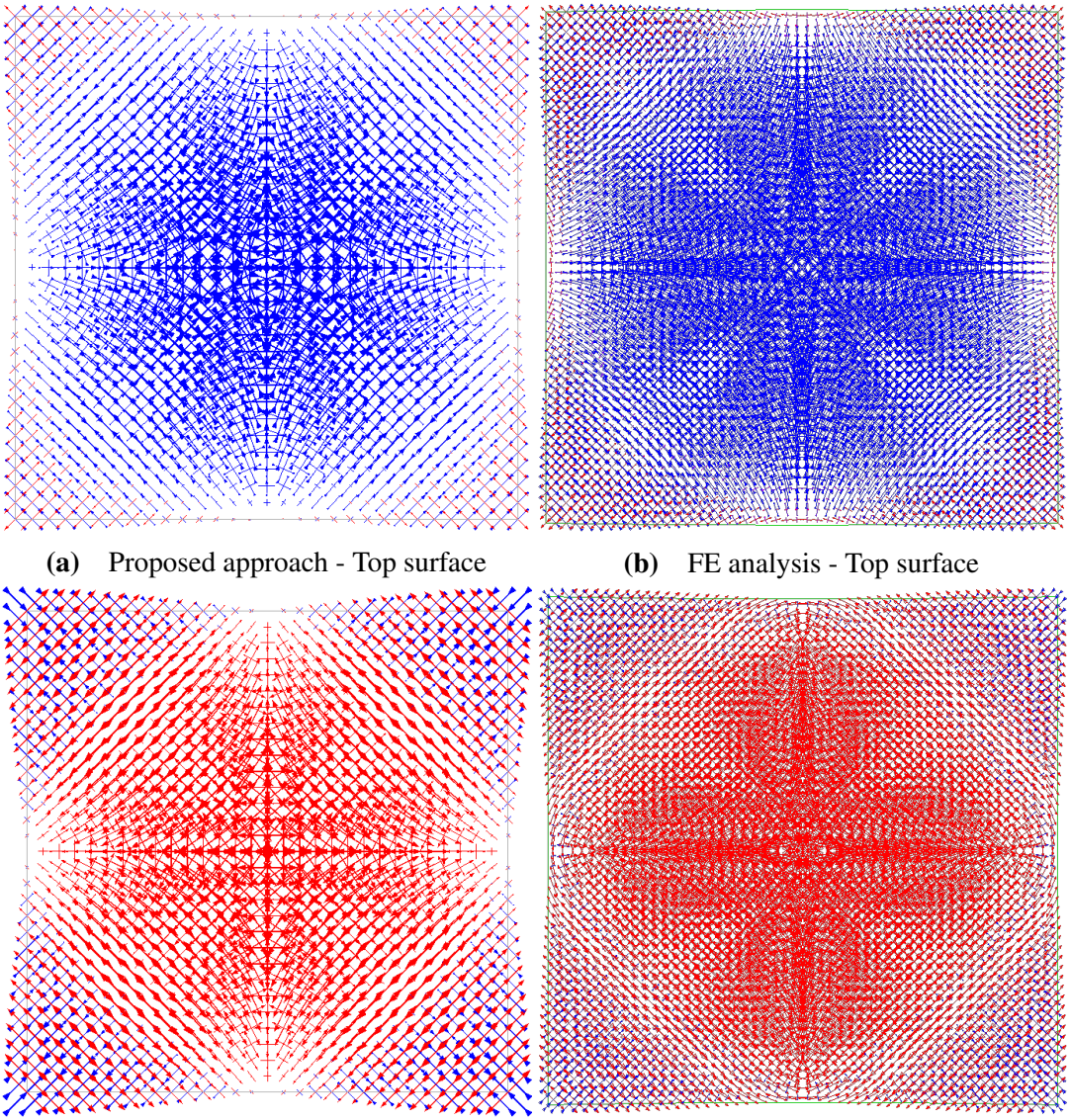

(a) Proposed approach - Top surface **(b)** FE analysis - Top surface

(c) Proposed approach - Bottom surface **(d)** FE analysis - Bottom surface

Figure 7.4 Quiver plots of principal stresses on the top and bottom surfaces of a square isotropic shallow cylindrical shell with laterally unrestrained BC subject to a UDL. Blue arrows represent compressive stresses and the red ones represent tensile stresses. Five series terms are used in the proposed formulation to produce the stress trajectories.

surface loading produces an upwards deflection, according to the sign convention in Figure 7.1. It is also interesting to note how the nonlinear behaviour of a shell is changed due to a change in the radius of shell curvature. As can be seen in Figures 7.6 and 7.7, under both upwardly and downwardly directed mechanical loading, the shallow spherical shell is deflected less than the other two types of shallow shells. As such, the largest deflection has been produced by the shallow hyperbolic paraboloidal and cylindrical shells, depending upon the intensity of the UDL applied. For instance, under downwardly directed UDL of 20, the shallow cylindrical shell has produced the

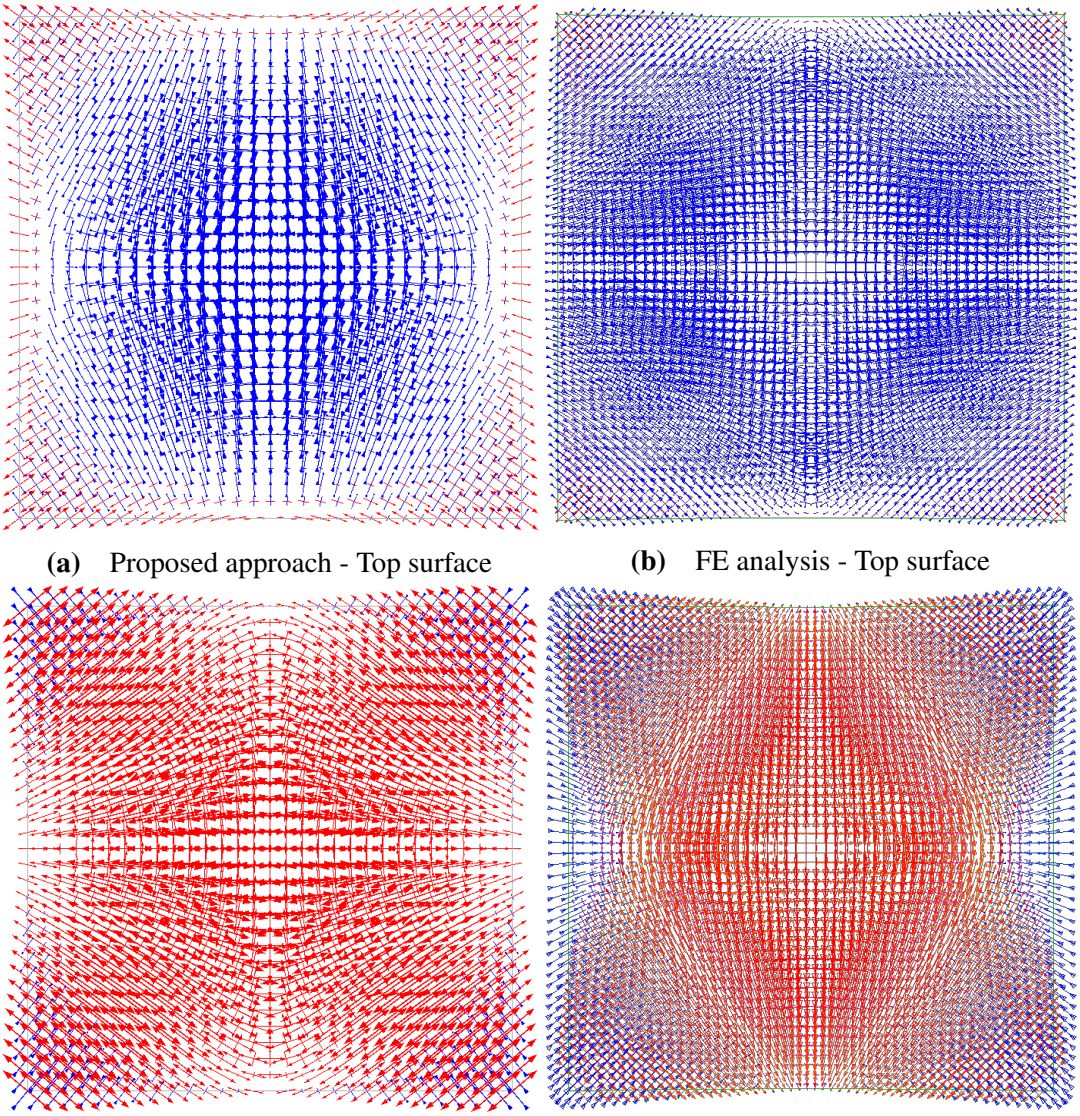

(a) Proposed approach - Top surface

(b) FE analysis - Top surface

(c) Proposed approach - Bottom surface

(d) FE analysis - Bottom surface

Figure 7.5 Quiver plots of principal stresses on the top and bottom surfaces of a square isotropic shallow cylindrical shell with laterally restrained BC subject to a UDL. Blue arrows represent compressive stresses and the red ones represent tensile stresses. Five series terms are used in the proposed formulation to produce the stress trajectories.

largest deflection, while under the same UDL when upwardly directed, the shallow hyperbolic paraboloidal shell has produced the largest deflection.

7.4.2 Shallow shell subject to thermal effects

To investigate the thermal effects on the nonlinear response of shallow shells, results of dimensionless deflection for a shallow spherical shell with the laterally unrestrained BC under thermal loading are compared with results obtained from a MLPG formulation (Sladek *et al.*, 2008b) and a FEM analysis (Sladek *et al.*, 2008b). The results are plotted in Figure 7.8. The shell has elastic modulus of 0.6895×10^{10} N/m^2,

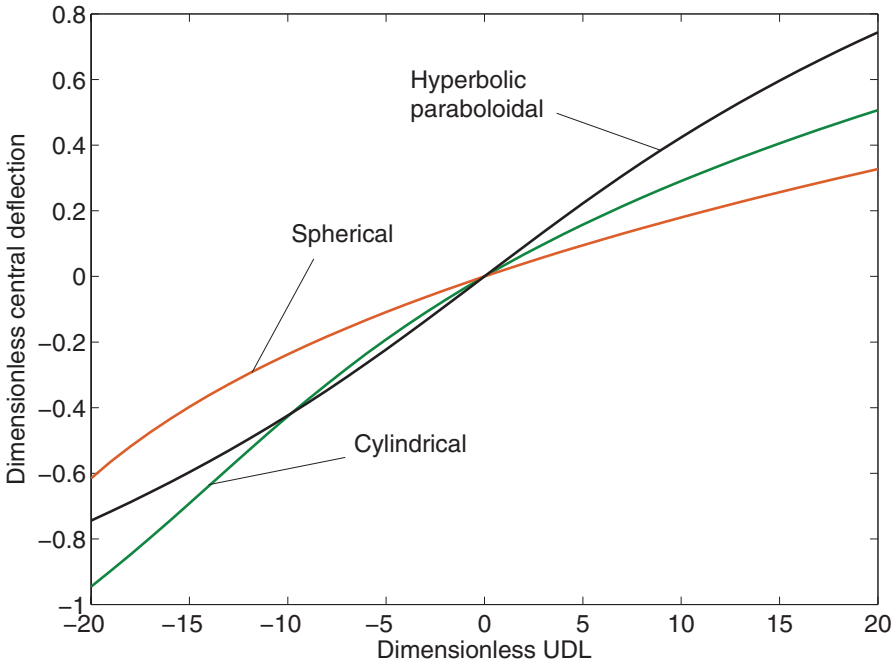

Figure 7.6 Dimensionless central deflection for various types of shallow shells with the laterally unrestrained BC subject to UDL. The data are calculated using only one series term.

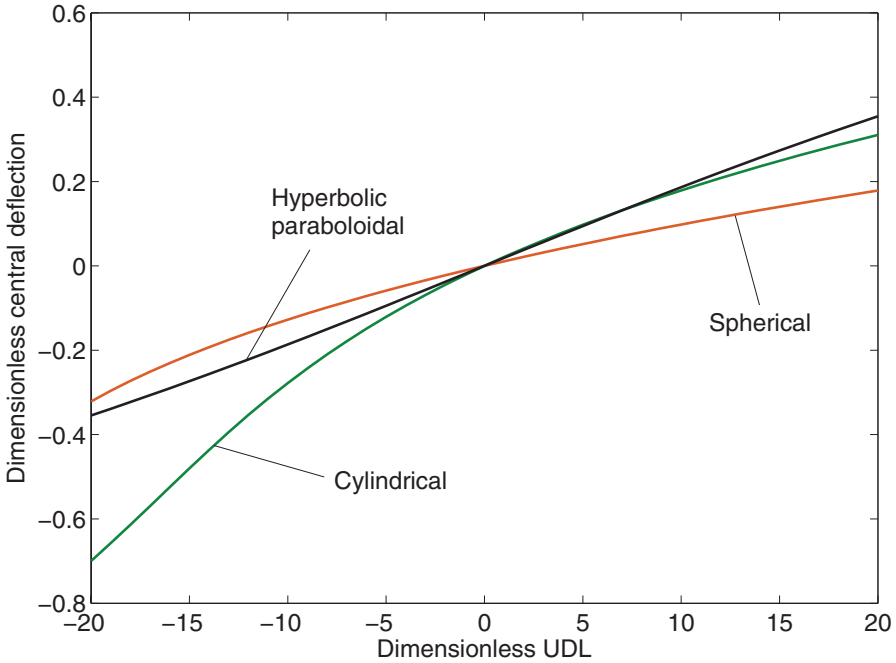

Figure 7.7 Dimensionless central deflection for various types of shallow shells with the laterally restrained BC subject to UDL. The data are calculated using three series terms.

coefficient of thermal expansion of 1×10^{-5} 1/°C, Poisson's ratio of 0.3, thickness to span ratio of 0.05, and radius of curvature to span ratio of 10. A uniformly distributed temperature of 1°C is applied on the top surface of the shell, while the temperature at

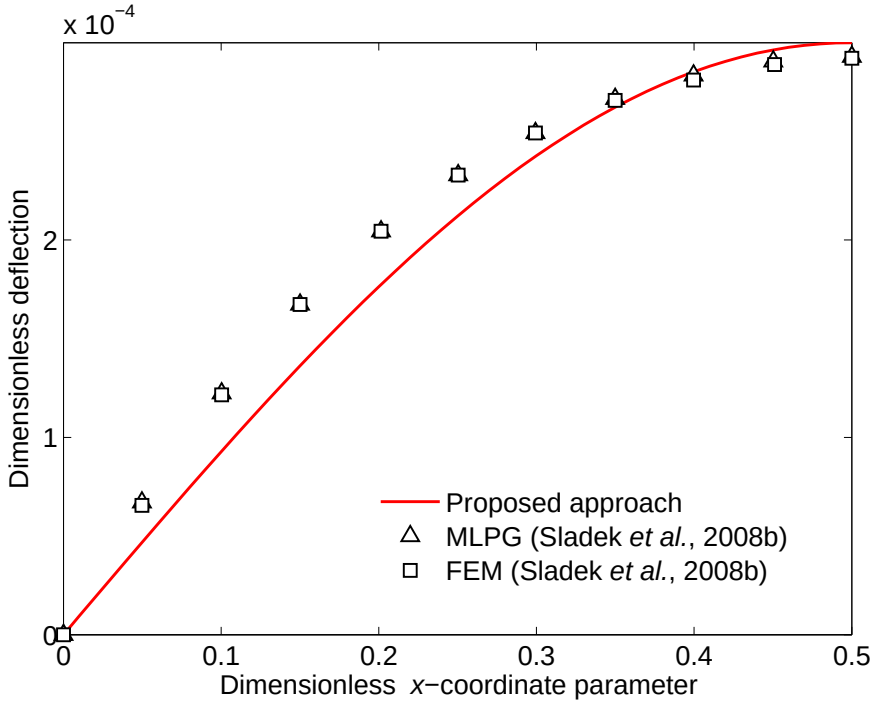

Figure 7.8 Variation of dimensionless deflection with the dimensionless x-coordinate parameter for a shallow spherical shell with the laterally unrestrained BC subject to thermal loading.

the bottom surface of the shell is kept at zero. It can be seen that the solutions of the proposed method are in close agreement with the solutions obtained from both the MLPG method and FEM with a rather rapid convergence (with considering only one series term in the solutions).

7.4.3 Shallow shell subject to combined thermomechanical loads

As another example, the central deflection of a shallow hyperbolic paraboloidal shell (i.e $R_x/a = -R_y/a = -5$) subjected to UDL and linear thermal gradient is considered. The temperature at the top surface of the shell was assumed to be the ambient temperature (20°C) and it assumed to vary linearly through the depth of the shell to temperatures of 20°C, 100°C, and 200°C at the bottom surface. Such temperature profiles may also be represented by an equivalent thermal gradient of $\Delta\theta/z$ and an equivalent mean temperature of $\Delta\theta$. The coefficient of thermal expansion of the shell is taken as 8×10^{-6} 1/°C. Other material and geometrical properties are the same as those stated in the previous example. The dimensionless maximum deflection of the shell is depicted in Figures 7.9 and 7.10 for both the chosen BCs. These figures show that for the cases where a downwardly directed UDL is applied on the top surface

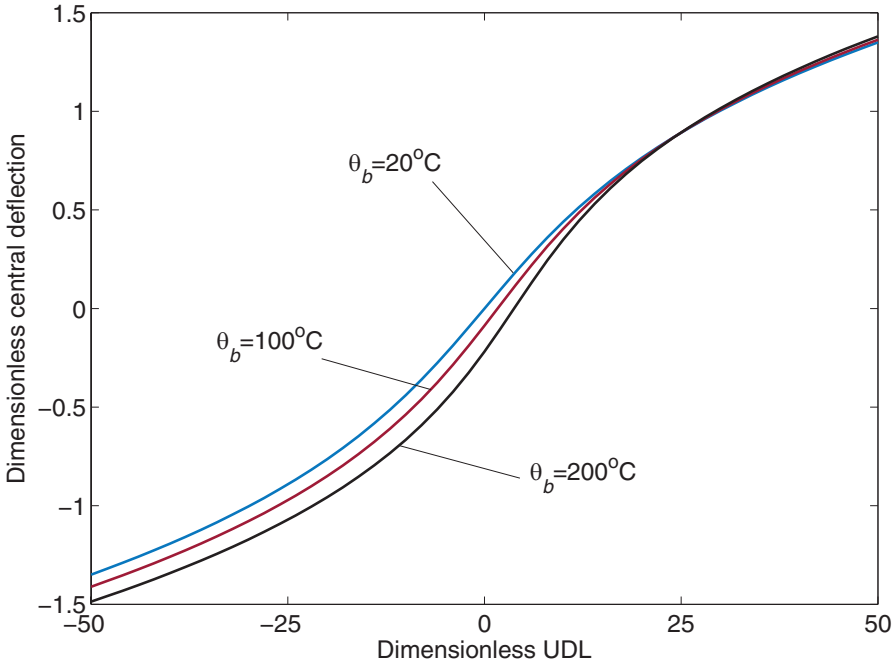

Figure 7.9 Dimensionless central deflection for a shallow hyperbolic paraboloidal shell with the laterally unrestrained BC subject to UDL and linear temperature gradient. The data are calculated using one series term.

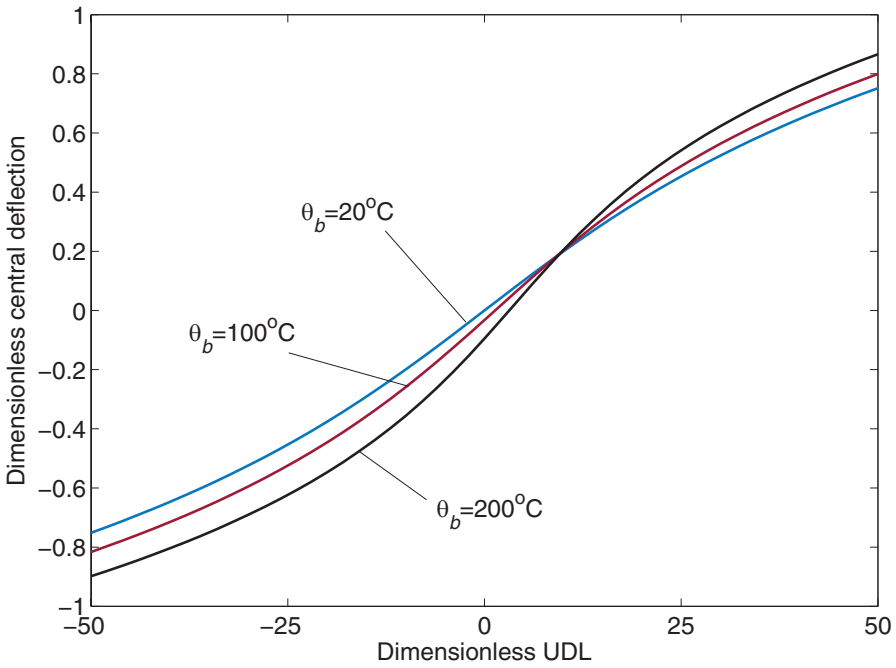

Figure 7.10 Dimensionless central deflection for a shallow hyperbolic paraboloidal shell with the laterally restrained BC subject to UDL and linear temperature gradient. The data are calculated using three series terms.

of the shell, larger temperature gradients result in larger deflections. However, the opposite behaviour is seen where an upwardly directed UDL is applied on the bottom surface of the shell. Moreover, as expected, adding lateral restraint at the shell edges has resulted in lower values for the shell maximum deflections as compared with those obtained for the laterally unrestrained shells.

7.5 Summary

A mathematical model was developed for the geometrically nonlinear analysis of shallow shells in rectangular planforms subject to thermmechanical loads. Two types of support conditions were assumed, bracketing reasonable conditions that may be found in real shell structures applications. It was found that using three terms in the series solutions give results that are reasonably accurate for laterally restrained shallow shells. A notable feature of the proposed approach is its good performance and its relatively rapid convergence for shallow shells with the laterally restrained BC. In the case of shells with the laterally unrestrained BC, this is, however, only achieved for 'extremely shallow shells'. The reason for poor agreement for this BC is the significant change in curvature which is not able to be captured by the formulation. The mention of curvature change with respect to the unrestrained boundaries is related to the structure moving from larger to smaller curvature. The model seems to work significantly better for smaller curvatures than for larger curvatures. By increasing the curvature of the shallow shell, the snap-through and snap-back behaviours of shells can be observed. This was beyond the scope of this research and therefore was not reported in this work. It should be noted that in order to quantify the evolution of the membrane action in the shallow shells, a limited number of terms should be retained in the series solutions. The solutions developed were restricted to elastic nonlinear shallow shells but will be extended in the next chapter for use in cases where severe thermal loading (high temperature) is present to include consequent material nonlinearity.

Chapter 8

Geometrically and Materially Nonlinear Behaviour of Shallow Shells[1]

8.1 Introduction

Composite shallow shells are widely used in buildings (typically as roof structures), aerospace vehicles, ship hulls, pressure vessels and car bodies. Most of these structures are potentially at risk of being exposed to severe non-uniform thermal gradients, while also externally loaded, such as those resulting from a fire. The consequences of such loading conditions may lead to a reduction of the strength and stiffness of the structure and the development of large displacements, leading to the failure of the structure under the most severe cases. Research in this area has been often focused towards developing efficient shell finite elements (see e.g., Surana and Orth, 1991; Bose and Surana, 1993; Ling and Surana, 1994; Vu-Quoc *et al.*, 2000; Vu-Quoc *et al.*, 2001; Talamona and Franssen, 2005; Jeffers, 2013; Jeffers and Beata, 2014; Jeffers, 2015). However, development of appropriate theoretical models is equally important for visualising internal structures in composite shells in order to develop much deeper insights into their load-carrying mechanisms.

Using an analytical method, Woo and Meguid (2001) studied the nonlinear analysis of simply supported (laterally unrestrained) shallow spherical shells with FG material properties subjected to transverse mechanical loads and through-depth thermal gradients. The governing equations were established based on the von Kármán type of

[1] Based on the works reported by Khazaeinejad and Usmani (2016b).

large displacement theory and were solved using series solutions. It was revealed that considering combined thermomechanical loading conditions can affect the nonlinear response of the shells. Jin *et al.* (2002) performed an FE investigation for the thermal post-buckling behaviour of patched cylindrical composite panels under uniform and non-uniform through-depth temperature distributions. Their analysis was based on the Hellinger-Reissner principle. Shen studied the post-buckling behaviour of FG cylindrical shells in thermal environments under axial compression (Shen, 2002b; Shen, 2002a), lateral pressure (Shen, 2003), and a uniform temperature rise (Shen, 2004) using the classical shell theory with the von Kármán-Donnell-type of kinematic nonlinearity assumptions. Material properties of the shell were assumed to be temperature-dependent and graded in the thickness direction according to a simple power law distribution. A boundary layer theory of shell buckling which includes the effects of nonlinear pre-buckling deformations, large deflections in the post-buckling range, and initial geometric imperfections of the shell was used. A singular perturbation technique was employed to obtain the buckling loads and post-buckling equilibrium paths.

Yang *et al.* (2006) evaluated the effects of thermal loads, temperature-dependent properties, initial geometric imperfection, volume fraction index, and geometrical parameters on the post-buckling behaviour of FG cylindrical panels with either simply supported (laterally unrestrained) or clamped edges subjected to a combined initial axial force and a uniform temperature change. Their analysis was based on the classical shell theory and von Kármán-Donnell type kinematic relations. The critical buckling temperature and the post-buckling temperature-deflection curves were determined using a semi-analytical differential quadrature-Galerkin method associated with an iterative algorithm. They reported that both the buckling temperature and the equilibrium path in the post-buckling regime become lower when the temperature-dependent properties are taken into account in the analysis. Arciniega and Reddy developed a tensor-based FE formulation using high order Lagrange elements for the geometrically nonlinear analysis of composite (Arciniega and Reddy, 2007b) and FG shells (Arciniega and Reddy, 2007a). The formulation was based on the first order shear deformation theory. The material properties of the FG shell were assumed to vary across the depth of the shell. They reported that patterns of the load-displacement

equilibrium curves of FG shells are similar to those of isotropic and homogeneous shells.

Kim *et al.* (2008) studied the nonlinear bending behaviour of FG shells using the FSDT with a full definition of the Green's strain tensor that includes membrane, bending, and transverse shear stresses in the geometric stiffness. A four-node shell element was developed based on the quasi-conforming formulation. Zhao and Liew (2009) used the element-free *kp*-Ritz method to investigate the nonlinear response of FG ceramic-metal cylindrical shell panels under mechanical and thermal loads. Their formulation was based on a modified version of Sander's nonlinear shell theory which accounts for transverse shear strains, rotary inertia, and moderate rotations in the von Kármán geometric nonlinearity sense. They showed that for FG shell panels under thermomechanical loads, the temperature field plays a significant role on the evolution of the shell stress profile. Albuquerque and Aliabadi (2010) presented a boundary element formulation for the analysis of laminated composite shallow shells. Duc and Van Tung (2010) studied the nonlinear response of FG cylindrical panels to uniform lateral pressure as well as uniform and through-depth thermal gradients by an analytical approach associated with a Galerkin method. Formulation was based on the classical shell theory, considering the von Kármán-Donnell type of kinematic nonlinearity and initial geometrical imperfection. Three BCs were considered in their analysis, arising from restriction on the lateral movement of curved and straight edges of the cylindrical panel. Temperature-dependency of the material properties of the panel were not taken into consideration. Their numerical results revealed that in-plane restraint and temperature conditions play major roles in dictating the response of the FG cylindrical panels.

An analytical approach was employed by Bich and Van Tung (2011) to study the nonlinear stability of perfect and imperfect FG shallow spherical shells under uniform external pressure with and without considering the effects of uniform and through-depth thermal gradients. In their approach, one term approximation of deflection was used to determine the extremum buckling loads and load-deflection curves for laterally restrained and unrestrained shallow spherical shells. Material properties were assumed to be temperature-independent. Their results showed that while the

effect of temperature field on the nonlinear response of FG shallow spherical shells under thermomechanical loads is significant, the effect of initial imperfection on the nonlinear response of mechanically loaded FG shallow spherical shells is weak. The nonlinear buckling behaviour of homogeneous and non-homogeneous orthotropic thin-walled truncated conical shells under axial loads was presented by Sofiyev and Kuruoglu (2013). The stability and compatibility equations of the problem were derived using the large deformation theory with the von Kármán-Donnell type of kinematic nonlinearity. It was reported that for long truncated conical shells, the effect of non-homogeneity on the nonlinear axial buckling load is negligible.

A coupled numerical methodology was used by Civalek (2014) to study the geometrically nonlinear static and dynamic analyses of shallow spherical shells resting on elastic foundation. The formulation of the shell was based on the Donnell theory. He concluded that both the static and dynamic responses of a shell decreases with an increase in the value of its foundation parameter. Recently, Zhang (2015) used the physical neutral surface and high order shear deformation theory to model the nonlinear static responses of FG infinite cylindrical shallow shells. His formulation was based on the nonlinear von Kármán strain-displacement relationships with considering temperature-dependent material properties. He reported that the intensity of the snap-through in cylindrical shallow shells with immovable (vertically restrained) simply supported and clamped edges increases with an increase in the geometrical property and the temperature of the shell.

In most composite shell analyses, spatially varying material properties are not employed and the analysis has been often limited to temperature sensitive material properties. Hence, in this chapter, the formulation proposed in the previous chapter is extended to account for the temperature-dependent nonlinear response of shallow shells with single and double curvatures on a rectangular planform. Same as the loading conditions for the plate, the shallow shell is subject to a transverse mechanical load, while it is imposed to a full non-uniform temperature field over its surface and through its depth. In the context of structural performance under extreme thermal actions, the short hot and long cool fire conditions are assumed for the shallow shell.

8.2 Derivation of governing equations

Consider a shallow shell with a rectangular planform as illustrated in Figure 7.1. The shell is assumed to undergo large deflections. The material properties of the shell is assumed to vary with temperature.

By rearranging equation (3.37) along with using equation (6.1), the middle plane strains in the shallow shells can be written as

$$\begin{Bmatrix} \frac{\partial u}{\partial x}+\frac{1}{2}\left(\frac{\partial w}{\partial x}\right)^2 \\ \frac{\partial v}{\partial y}+\frac{1}{2}\left(\frac{\partial w}{\partial y}\right)^2 \\ \frac{\partial u}{\partial y}+\frac{\partial v}{\partial x}+\left(\frac{\partial w}{\partial x}\right)\left(\frac{\partial w}{\partial y}\right) \end{Bmatrix} + \begin{Bmatrix} \frac{w}{R_x} \\ \frac{w}{R_y} \\ \frac{2w}{R_{xy}} \end{Bmatrix} = \begin{pmatrix} a_{11} & a_{12} & a_{16} \\ & a_{22} & a_{26} \\ \text{symm.} & & a_{66} \end{pmatrix} \begin{Bmatrix} \frac{\partial^2 F}{\partial y^2} \\ \frac{\partial^2 F}{\partial x^2} \\ -\frac{\partial^2 F}{\partial x \partial y} \end{Bmatrix} + \begin{pmatrix} b_{11} & b_{12} & b_{16} \\ & b_{22} & b_{26} \\ \text{symm.} & & b_{66} \end{pmatrix} \begin{Bmatrix} \frac{\partial^2 w}{\partial x^2} \\ \frac{\partial^2 w}{\partial y^2} \\ 2\frac{\partial^2 w}{\partial x \partial y} \end{Bmatrix} + \begin{pmatrix} a_{11} & a_{12} & a_{16} \\ & a_{22} & a_{26} \\ \text{symm.} & & a_{66} \end{pmatrix} \begin{Bmatrix} N^{\theta}_{xx} \\ N^{\theta}_{yy} \\ N^{\theta}_{xy} \end{Bmatrix} \tag{8.1}$$

Substituting equations (6.1) and (8.1) into the strain compatibility equation (7.1) the following nonlinear equation is derived

$$\begin{aligned} &a_{22}\frac{\partial^4 F}{\partial x^4} - 2a_{26}\frac{\partial^4 F}{\partial x^3 \partial y} + (2a_{12}+a_{66})\frac{\partial^4 F}{\partial x^2 y^2} - 2a_{16}\frac{\partial^4 F}{\partial x \partial y^3} + a_{11}\frac{\partial^4 F}{\partial y^4} \\ &- \left(\frac{\partial^2 w}{\partial x \partial y}\right)^2 + \left(\frac{\partial^2 w}{\partial x^2}\right)\left(\frac{\partial^2 w}{\partial y^2}\right) + b_{12}\frac{\partial^4 w}{\partial x^4} + (2b_{26}-b_{16})\frac{\partial^4 w}{\partial x^3 \partial y} \\ &+ (b_{11}+b_{22}-2b_{66})\frac{\partial^4 w}{\partial x^2 \partial y^2} + (2b_{16}-b_{26})\frac{\partial^4 w}{\partial x \partial y^3} + b_{12}\frac{\partial^4 w}{\partial y^4} - \frac{1}{R_x}\left(\frac{\partial^2 w}{\partial y^2}\right) \\ &- \frac{1}{R_y}\left(\frac{\partial^2 w}{\partial x^2}\right) + 2\frac{1}{R_{xy}}\left(\frac{\partial^2 w}{\partial x \partial y}\right) = -a_{12}\frac{\partial^2 N^{\theta}_{xx}}{\partial x^2} + a_{16}\frac{\partial^2 N^{\theta}_{xx}}{\partial x \partial y} - a_{11}\frac{\partial^2 N^{\theta}_{xx}}{\partial y^2} \\ &- a_{22}\frac{\partial^2 N^{\theta}_{yy}}{\partial x^2} + a_{26}\frac{\partial^2 N^{\theta}_{yy}}{\partial x \partial y} - a_{12}\frac{\partial^2 N^{\theta}_{yy}}{\partial y^2} - a_{26}\frac{\partial^2 N^{\theta}_{xy}}{\partial x^2} + a_{66}\frac{\partial^2 N^{\theta}_{xy}}{\partial x \partial y} - a_{16}\frac{\partial^2 N^{\theta}_{xy}}{\partial y^2} \end{aligned} \tag{8.2}$$

In the above equation, F and w are both unknown. Therefore, another equation is required, that is the equilibrium equation of the shell which relates the axial forces

to the out-of-plane displacement of the shell. From substituting equations (8.1) into equation (3.38), the moment resultants can be rewritten as

$$\begin{aligned}
\left\{\begin{array}{c} M_{xx} \\ M_{yy} \\ M_{xy} \end{array}\right\} &= \left(\begin{array}{ccc} c_{11} & c_{12} & c_{16} \\ & c_{22} & c_{26} \\ \text{symm.} & & c_{66} \end{array}\right) \left\{\begin{array}{c} \frac{\partial u}{\partial x} + \frac{1}{2}\left(\frac{\partial w}{\partial x}\right)^2 \\ \frac{\partial v}{\partial y} + \frac{1}{2}\left(\frac{\partial w}{\partial y}\right)^2 \\ \frac{\partial u}{\partial y} + \frac{\partial v}{\partial x} + \left(\frac{\partial w}{\partial x}\right)\left(\frac{\partial w}{\partial y}\right) \end{array}\right\} \\
&+ \left(\begin{array}{ccc} c_{11} & c_{12} & c_{16} \\ & c_{22} & c_{26} \\ \text{symm.} & & c_{66} \end{array}\right) \left\{\begin{array}{c} \frac{w}{R_x} \\ \frac{w}{R_y} \\ \frac{2w}{R_{xy}} \end{array}\right\} \\
&+ \left(\begin{array}{ccc} d_{11} & d_{12} & d_{16} \\ & d_{22} & d_{26} \\ \text{symm.} & & d_{66} \end{array}\right) \left\{\begin{array}{c} -\frac{\partial^2 w}{\partial x^2} \\ -\frac{\partial^2 w}{\partial y^2} \\ -2\frac{\partial^2 w}{\partial x \partial y} \end{array}\right\} \\
&+ \left(\begin{array}{ccc} c_{11} & c_{12} & c_{16} \\ & c_{22} & c_{26} \\ \text{symm.} & & c_{66} \end{array}\right) \left\{\begin{array}{c} N_{xx}^{\theta} \\ N_{yy}^{\theta} \\ N_{xy}^{\theta} \end{array}\right\} - \left\{\begin{array}{c} M_{xx}^{\theta} \\ M_{yy}^{\theta} \\ M_{xy}^{\theta} \end{array}\right\}
\end{aligned} \tag{8.3}$$

Upon substitution of equation (8.3) into equation (7.3), a nonlinear equilibrium equation can be obtained as

$$\begin{aligned}
&d_{11}\frac{\partial^4 w}{\partial x^4} + 2d_{16}\frac{\partial^4 w}{\partial x^3 \partial y} + 2(d_{12}+2d_{66})\frac{\partial^4 w}{\partial x^2 y^2} + 4d_{26}\frac{\partial^4 w}{\partial x \partial y^3} + d_{22}\frac{\partial^4 w}{\partial y^4} \\
&- \frac{\partial^2 F}{\partial y^2}\left(\frac{\partial^2 w}{\partial x^2} - \frac{1}{R_x}\right) + 2\frac{\partial^2 F}{\partial x \partial y}\left(\frac{\partial^2 w}{\partial x \partial y} - \frac{1}{R_{xy}}\right) - \frac{\partial^2 F}{\partial x^2}\left(\frac{\partial^2 w}{\partial y^2} - \frac{1}{R_y}\right) - c_{12}\frac{\partial^4 F}{\partial x^4} \\
&- (2c_{26} - c_{16})\frac{\partial^4 F}{\partial x^3 \partial y} - (c_{11} + c_{22} - 2c_{66})\frac{\partial^4 F}{\partial x^2 y^2} - (2c_{16} - c_{26})\frac{\partial^4 F}{\partial x \partial y^3} - c_{12}\frac{\partial^4 F}{\partial y^4} = q \\
&+ c_{11}\frac{\partial^2 N_{xx}^{\theta}}{\partial x^2} + c_{12}\frac{\partial^2 N_{xx}^{\theta}}{\partial y^2} + 2c_{16}\frac{\partial^2 N_{xx}^{\theta}}{\partial x \partial y} + c_{12}\frac{\partial^2 N_{yy}^{\theta}}{\partial x^2} + c_{22}\frac{\partial^2 N_{yy}^{\theta}}{\partial y^2} + 2c_{26}\frac{\partial^2 N_{yy}^{\theta}}{\partial x \partial y} \\
&+ c_{16}\frac{\partial^2 N_{xy}^{\theta}}{\partial x^2} + c_{26}\frac{\partial^2 N_{xy}^{\theta}}{\partial y^2} + 2c_{66}\frac{\partial^2 N_{xy}^{\theta}}{\partial x \partial y} - \frac{\partial^2 M_{xx}^{\theta}}{\partial x^2} - \frac{\partial^2 M_{yy}^{\theta}}{\partial y^2} - 2\frac{\partial^2 M_{xy}^{\theta}}{\partial x \partial y}
\end{aligned} \tag{8.4}$$

Depending upon how the support conditions are specified for the shell, suitable trigonometric functions are used in the following to solve the differential governing equations.

8.3 Solution of governing equations

The solution functions for the shell can be taken as those introduced in (5.23)-(5.31). In the case of laterally restrained BC, reaction loads at the shell edges can be obtained using the following expressions for the elongation of the shell in the x and y directions

$$\int_0^a \frac{\partial u}{\partial x} dx = \int_0^a \left(a_{11} \frac{\partial^2 F}{\partial y^2} + a_{12} \frac{\partial^2 F}{\partial x^2} + b_{11} \frac{\partial^2 w}{\partial x^2} + b_{12} \frac{\partial^2 w}{\partial y^2} + a_{11} N_{xx}^{\theta} + a_{12} N_{yy}^{\theta} - \frac{1}{2} \left(\frac{\partial w}{\partial x} \right)^2 - \frac{w}{R_x} \right) \mathrm{d}x \tag{8.5a}$$

$$\int_0^b \frac{\partial v}{\partial y} dy = \int_0^b \left(a_{12} \frac{\partial^2 F}{\partial y^2} + a_{22} \frac{\partial^2 F}{\partial x^2} + b_{12} \frac{\partial^2 w}{\partial x^2} + b_{22} \frac{\partial^2 w}{\partial y^2} + a_{12} N_{xx}^{\theta} + a_{22} N_{yy}^{\theta} - \frac{1}{2} \left(\frac{\partial w}{\partial y} \right)^2 - \frac{w}{R_y} \right) \mathrm{d}y \tag{8.5b}$$

Setting the edge displacements to zero after some manipulations gives the following expressions for the reaction loads

$$P_x = F_{mn} \bar{n}^2 \frac{bh\zeta_2}{\zeta_1} + w_{mn} \frac{bh\zeta_3}{\zeta_1} + \frac{1}{2} w_{mn}^2 \frac{bh\zeta_4}{\zeta_1} - bhN_{xx}^{\theta} \tag{8.6a}$$

$$P_y = F_{mn} \bar{m}^2 \frac{ah\zeta_2}{\zeta_1} + w_{mn} \frac{ah\zeta_5}{\zeta_1} + \frac{1}{2} w_{mn}^2 \frac{ah\zeta_4}{\zeta_1} - ahN_{yy}^{\theta} \tag{8.6b}$$

where the coefficients can be calculated by

$$\zeta_1 = \int_0^a \int_0^b \left(a_{11} a_{22} - a_{12}^2 \right) \mathrm{d}y \, \mathrm{d}x \tag{8.7a}$$

$$\zeta_2 = \int_0^a \int_0^b \left(a_{11} a_{22} - a_{12}^2 \right) S_{mn} \, \mathrm{d}y \, \mathrm{d}x \tag{8.7b}$$

$$\zeta_3 = \int_0^a \int_0^b \left[\left(a_{22} b_{11} - a_{12} b_{12} \right) \bar{m}^2 + \left(a_{22} b_{12} - a_{12} b_{22} \right) \bar{n}^2 + \frac{a_{22}}{R_x} - \frac{a_{12}}{R_y} \right] S_{mn} \, \mathrm{d}y \, \mathrm{d}x \tag{8.7c}$$

$$\zeta_4 = \int_0^a \int_0^b \left(a_{22}\bar{m}^2 \cos^2 \bar{m}x \sin^2 \bar{n}y - a_{12}\bar{n}^2 \sin^2 \bar{m}x \cos^2 \bar{n}y\right) \, \mathrm{d}y \, \mathrm{d}x \quad (8.7d)$$

$$\zeta_5 = \int_0^a \int_0^b \left[\left(a_{11}b_{12} - a_{12}b_{11}\right)\bar{m}^2 + \left(a_{11}b_{22} - a_{12}b_{12}\right)\bar{n}^2 + \frac{a_{12}}{R_x} - \frac{a_{11}}{R_y}\right] S_{mn} \, \mathrm{d}y \, \mathrm{d}x \quad (8.7e)$$

$$\zeta_6 = \int_0^a \int_0^b \left(a_{11}\bar{n}^2 \sin^2 \bar{m}x \cos^2 \bar{n}y - a_{12}\bar{m}^2 \cos^2 \bar{m}x \sin^2 \bar{n}y\right) \, \mathrm{d}y \, \mathrm{d}x \quad (8.7f)$$

For through-depth thermal loading conditions, these equations are simplified as

$$\begin{aligned} P_x = {} & \frac{bh\left(a_{22}\bar{m}^2 - a_{12}\bar{n}^2\right)}{8\left(a_{11}a_{22} - a_{12}^2\right)} w_{mn}^2 + \frac{[-1+(-1)^m][-1+(-1)^n]\, bh\bar{n}^2}{mn\pi^2} F_{mn} \\ & + \frac{bh[-1+(-1)^m][-1+(-1)^n]\left[(a_{22}b_{11} - a_{12}b_{12})\bar{m}^2 + (a_{22}b_{12} - a_{12}b_{22})\bar{n}^2\right]}{mn\pi^2\left(a_{11}a_{22} - a_{12}^2\right)} w_{mn} \\ & + \frac{[-1+(-1)^m][-1+(-1)^n]\, bh}{mn\pi^2(a_{11}a_{22} - a_{12}^2)} \left(\frac{a_{22}}{R_x} - \frac{a_{12}}{R_y}\right) w_{mn} - bhN_{xx}^{\theta} \end{aligned} \quad (8.8a)$$

$$\begin{aligned} P_y = {} & \frac{ah\left(a_{11}\bar{n}^2 - a_{12}\bar{m}^2\right)}{8\left(a_{11}a_{22} - a_{12}^2\right)} w_{mn}^2 + \frac{[-1+(-1)^m][-1+(-1)^n]\, ah\bar{m}^2}{mn\pi^2} F_{mn} \\ & + \frac{ah[-1+(-1)^m][-1+(-1)^n]\left[(a_{11}b_{12} - a_{12}b_{11})\bar{m}^2 + (a_{11}b_{22} - a_{12}b_{12})\bar{n}^2\right]}{mn\pi^2\left(a_{11}a_{22} - a_{12}^2\right)} w_{mn} \\ & + \frac{[-1+(-1)^m][-1+(-1)^n]\, ah}{mn\pi^2(a_{11}a_{22} - a_{12}^2)} \left(\frac{a_{11}}{R_y} - \frac{a_{12}}{R_x}\right) w_{mn} - ahN_{yy}^{\theta} \end{aligned} \quad (8.8b)$$

When the laterally unrestrained BC is imposed, the in-plane displacements can be obtained as

$$u = \sum_{m=1}^{\infty} \sum_{n=1}^{\infty} \left[-\frac{\bar{m}^2}{4}\left(x + \frac{\sin 2\bar{m}x}{2\bar{m}}\right) w_{mn}^2 \sin^2 \bar{n}y + \eta_1 w_{mn} + \eta_2 F_{mn} + \eta_3\right] \quad (8.9a)$$

$$v = \sum_{m=1}^{\infty} \sum_{n=1}^{\infty} \left[-\frac{\bar{n}^2}{4}\left(y + \frac{\sin 2\bar{n}y}{2\bar{n}}\right) w_{mn}^2 \sin^2 \bar{m}x + \eta_4 w_{mn} + \eta_5 F_{mn} + \eta_6\right] \quad (8.9b)$$

where the coefficients are defined by the following expressions

$$\eta_1 = -\int_0^a \left(\bar{b}_{11}\bar{m}^2 + \bar{b}_{12}\bar{n}^2 - \frac{1}{R_x}\right) S_{mn}\,\mathrm{d}x \tag{8.10a}$$

$$\eta_2 = -\int_0^a \left(\bar{a}_{12}\bar{m}^2 + \bar{a}_{11}\bar{n}^2\right) S_{mn}\,\mathrm{d}x \tag{8.10b}$$

$$\eta_3 = \int_0^a \left(\bar{a}_{11}N_{xx}^{\theta} + \bar{a}_{12}N_{yy}^{\theta}\right)\,\mathrm{d}x \tag{8.10c}$$

$$\eta_4 = -\int_0^b \left(\bar{b}_{12}\bar{m}^2 + \bar{b}_{22}\bar{n}^2 - \frac{1}{R_y}\right) S_{mn}\,\mathrm{d}y \tag{8.10d}$$

$$\eta_5 = -\int_0^b \left(\bar{a}_{22}\bar{m}^2 + \bar{a}_{12}\bar{n}^2\right) S_{mn}\,\mathrm{d}y \tag{8.10e}$$

$$\eta_6 = \int_0^b \left(\bar{a}_{12}N_{xx}^{\theta} + \bar{a}_{22}N_{yy}^{\theta}\right)\,\mathrm{d}y \tag{8.10f}$$

The above equations can be simplified for the through-depth thermal loading conditions as follows

$$\begin{aligned} u = \sum_{m=1}^{\infty}\sum_{n=1}^{\infty}\Bigg[& -\frac{\bar{m}^2}{4}w_{mn}^2\left(x + \frac{\sin 2\bar{m}x}{2\bar{m}}\right)\sin^2\bar{n}y \\ & + \frac{b_{11}\bar{m}^2 + b_{12}\bar{n}^2}{\bar{m}}w_{mn}\cos\bar{m}x\sin\bar{n}y + \frac{w_{mn}}{\bar{m}R_x}\cos\bar{m}x\sin\bar{n}y \\ & + \frac{a_{12}\bar{m}^2 + a_{11}\bar{n}^2}{\bar{m}}F_{mn}\cos\bar{m}x\sin\bar{n}y + aa_{11}N_{xx}^{\theta} + aa_{12}N_{yy}^{\theta}\Bigg] \end{aligned} \tag{8.11a}$$

$$\begin{aligned} v = \sum_{m=1}^{\infty}\sum_{n=1}^{\infty}\Bigg[& -\frac{\bar{n}^2}{4}w_{mn}^2\sin^2\bar{m}x\left(y + \frac{\sin 2\bar{n}y}{2\bar{n}}\right) \\ & + \frac{b_{12}\bar{m}^2 + b_{22}\bar{n}^2}{\bar{n}}w_{mn}\sin\bar{m}x\cos\bar{n}y + \frac{w_{mn}}{\bar{n}R_y}\sin\bar{m}x\cos\bar{n}y \\ & + \frac{a_{22}\bar{m}^2 + a_{12}\bar{n}^2}{\bar{n}}F_{mn}\sin\bar{m}x\cos\bar{n}y + ba_{12}N_{xx}^{\theta} + ba_{22}N_{yy}^{\theta}\Bigg] \end{aligned} \tag{8.11b}$$

Substituting equations (5.23)-(5.31) into the governing equations (8.2) and (8.4), the compatibility and equilibrium equations are obtained as

$$\sum_{m=1}^{\infty}\sum_{n=1}^{\infty}\left\{\chi_1 F_{mn} + \chi_2 W_{mn}^2 + \chi_3 W_{mn} + \chi_4\right\} = 0 \tag{8.12a}$$

$$\sum_{m=1}^{\infty}\sum_{n=1}^{\infty}\left\{\chi_5 W_{mn} + \chi_6 F_{mn}W_{mn} + \chi_7 F_{mn} + \chi_8\right\} = 0 \tag{8.12b}$$

where the coefficients are defined by the following expressions

$$\chi_1 = \int_0^a \int_0^b \left[a_{22}\bar{m}^4 S_{mn}^2 + 2a_{26}\bar{m}^3\bar{n}S_{mn}C_{mn} + (2a_{12}+a_{66})\bar{m}^2\bar{n}^2 S_{mn}^2 + 2a_{16}\bar{m}\bar{n}^3 S_{mn}C_{mn} + a_{11}\bar{n}^4 S_{mn}^2\right] \mathrm{d}y\,\mathrm{d}x \tag{8.13a}$$

$$\chi_2 = \int_0^a \int_0^b \bar{m}^2\bar{n}^2\left(S_{mn}^2 - C_{mn}^2\right) S_{mn}\,\mathrm{d}y\,\mathrm{d}x \tag{8.13b}$$

$$\begin{aligned}\chi_3 &= \int_0^a \int_0^b \\ &= \Bigg[b_{12}\bar{m}^4 S_{mn}^2 - (2b_{26}-b_{16})\bar{m}^3\bar{n}S_{mn}C_{mn} \\ &\quad + (b_{11}+b_{22}-2b_{66})\bar{m}^2\bar{n}^2 S_{mn}^2 - (2b_{16}-b_{26})\bar{m}\bar{n}^3 S_{mn}C_{mn} + b_{12}\bar{n}^4 S_{mn}^2 \\ &\quad + \frac{\bar{n}^2}{R_x}S_{mn}^2 + \frac{\bar{m}^2}{R_y}S_{mn}^2 + \frac{2\bar{m}\bar{n}}{R_{xy}}S_{mn}C_{mn}\Bigg]\,\mathrm{d}y\,\mathrm{d}x\end{aligned} \tag{8.13c}$$

$$\begin{aligned}\chi_4 = -\int_0^a \int_0^b \Big[&(a_{12}N_{mnxx}^{\theta} + a_{22}N_{mnyy}^{\theta} + a_{26}N_{mnxy}^{\theta})\bar{m}^2 S_{mn}^2 \\ &+ (a_{11}N_{mnxx}^{\theta} + a_{12}N_{mnyy}^{\theta} + a_{16}N_{mnxy}^{\theta})\bar{n}^2 S_{mn}^2 \\ &+ (a_{16}N_{mnxx}^{\theta} + a_{26}N_{mnyy}^{\theta} + a_{66}N_{mnxy}^{\theta})\bar{m}\bar{n}S_{mn}C_{mn}\Big]\,\mathrm{d}y\,\mathrm{d}x\end{aligned} \tag{8.13d}$$

$$\chi_5 = \int_0^a \int_0^b \left[d_{11}\bar{m}^4 S_{mn}^2 - 2d_{16}\bar{m}^3\bar{n}S_{mn}C_{mn} + (2d_{12}+4d_{66})S_{mn}^2\bar{m}^2\bar{n}^2 - 4d_{26}\bar{m}\bar{n}^3 S_{mn}C_{mn} + \bar{d}_{22}\bar{n}^4 S_{mn}^2 + \frac{P_x\bar{m}^2}{bh}S_{mn}^2 + \frac{P_y\bar{n}^2}{ah}S_{mn}^2\right]\mathrm{d}y\,\mathrm{d}x \tag{8.13e}$$

$$\chi_6 = \int_0^a \int_0^b 2\bar{m}^2\bar{n}^2\left(C_{mn}^2 - S_{mn}^2\right) S_{mn}\,\mathrm{d}y\,\mathrm{d}x \tag{8.13f}$$

$$\begin{aligned}\chi_7 = \int_0^a \int_0^b \Bigg[&-c_{12}\bar{m}^4 S_{mn}^2 + (2C_{26}-C_{16})\bar{m}^3\bar{n}S_{mn}C_{mn} \\ &- (c_{11}+c_{22}-2c_{66})\bar{m}^2\bar{n}^2 S_{mn}^2 + (2C_{16}-C_{26})\bar{m}\bar{n}^3 S_{mn}C_{mn} - c_{12}\bar{n}^4 S_{mn}^2 \\ &- \frac{\bar{n}^2}{R_x}S_{mn}^2 - \frac{\bar{m}^2}{R_y}S_{mn}^2 - 2\frac{\bar{m}\bar{n}}{R_{xy}}S_{mn}C_{mn}\Bigg]\,\mathrm{d}y\,\mathrm{d}x\end{aligned} \tag{8.13g}$$

$$\begin{aligned}\chi_8 = \int_0^a \int_0^b \Big[&(c_{11}N_{mnxx}^{\theta} + c_{12}N_{mnyy}^{\theta} + c_{16}N_{mnxy}^{\theta})\bar{m}^2 S_{mn}^2 \\ &- 2(C_{16}N_{mnxx}^{\theta} + C_{26}N_{mnyy}^{\theta} + C_{66}N_{mnxy}^{\theta})\bar{m}\bar{n}S_{mn}C_{mn} \\ &+ (c_{12}N_{mnxx}^{\theta} + c_{22}N_{mnyy}^{\theta} + c_{26}N_{mnxy}^{\theta})\bar{n}^2 S_{mn}^2 - \bar{m}^2 M_{mnxx}^{\theta} S_{mn}^2 - \bar{n}^2 M_{mnyy}^{\theta} S_{mn}^2 \\ &- q_{mn}S_{mn}^2 + \frac{P_x}{bhR_x}S_{mn} + \frac{P_y}{ahR_y}S_{mn}\Big]\,\mathrm{d}y\,\mathrm{d}x\end{aligned} \tag{8.13h}$$

In the case of a laminated shell, the quantities N_{xy}^{θ}, M_{xy}^{θ}, Q_{16}, Q_{26} are zero. It is clear that the coefficients of the in-plane displacements are also temperature-dependent. Considering only through-depth thermal loading, we obtain

$$\begin{aligned}
&\left[a_{22}\bar{m}^4+(2a_{12}+a_{66})\bar{m}^2\bar{n}^2+a_{11}\bar{n}^4\right]F_{mn}S_{mn}-\bar{m}^2\bar{n}^2w_{mn}^2\left(C_{mn}^2-S_{mn}^2\right)\\
&+\left[(b_{11}+b_{22}-2b_{66})\bar{m}^2\bar{n}^2+b_{12}\bar{m}^4+b_{12}\bar{n}^4+\frac{\bar{n}^2}{R_x}+\frac{\bar{m}^2}{R_y}\right]w_{mn}S_{mn}\\
&-\left[\left(a_{12}N_{mnxx}^{\theta}+a_{22}N_{mnyy}^{\theta}\right)\bar{m}^2+\left(a_{11}N_{mnxx}^{\theta}+a_{12}N_{mnyy}^{\theta}\right)\bar{n}^2\right]S_{mn}=0
\end{aligned}\tag{8.14}$$

$$\begin{aligned}
&\left[d_{11}\bar{m}^4+(2d_{12}+4d_{66})\bar{m}^2\bar{n}^2+d_{22}\bar{n}^4\right]w_{mn}S_{mn}\\
&-\left[c_{12}\bar{m}^4+(c_{11}+c_{22}-2c_{66})\bar{m}^2\bar{n}^2+c_{12}\bar{n}^4+\frac{\bar{n}^2}{R_x}+\frac{\bar{m}^2}{R_y}\right]F_{mn}S_{mn}\\
&+\left(\frac{P_x\bar{m}^2}{bh}+\frac{P_y\bar{n}^2}{ah}\right)w_{mn}S_{mn}\\
&-2\bar{m}^2\bar{n}^2F_{mn}w_{mn}\left(S_{mn}^2-C_{mn}^2\right)+\frac{P_x}{bhR_x}+\frac{P_y}{ahR_y}\\
&+\left[\left(c_{11}N_{mnxx}^{\theta}+c_{12}N_{mnyy}^{\theta}\right)\bar{m}^2+\left(c_{12}N_{mnxx}^{\theta}+c_{22}N_{mnyy}^{\theta}\right)\bar{n}^2\right]S_{mn}\\
&-\left(\bar{m}^2M_{mnxx}^{\theta}+\bar{n}^2M_{mnyy}^{\theta}\right)S_{mn}-q_{mn}S_{mn}=0
\end{aligned}\tag{8.15}$$

Using the expansion theorem, the following two algebraic equations can be derived

$$\begin{aligned}
F_{mn}=\frac{1}{(a_{22}\bar{m}^4+(2a_{12}+a_{66})\bar{m}^2\bar{n}^2+a_{11}\bar{n}^4)}&\left[4\bar{m}^2\bar{n}^2H_{mn}w_{mn}^2\right.\\
&-\left[b_{12}\bar{m}^4+(b_{11}+b_{22}-2b_{66})\bar{m}^2\bar{n}^2+b_{12}\bar{n}^4+\frac{\bar{n}^2}{R_x}+\frac{\bar{m}^2}{R_y}\right]w_{mn}\\
&\left.+\left[\left(a_{12}N_{mnxx}^{\theta}+a_{22}N_{mnyy}^{\theta}\right)\bar{m}^2+\left(a_{11}N_{mnxx}^{\theta}+a_{12}N_{mnyy}^{\theta}\right)\bar{n}^2\right]\right]
\end{aligned}\tag{8.16}$$

Likewise, the following load-deflection equation is derived from the equilibrium equation (8.15)

$$\varsigma_1w_{mn}+\varsigma_2F_{mn}+\varsigma_3F_{mn}w_{mn}+\varsigma_4=0\tag{8.17}$$

where the coefficients are defined by

$$\varsigma_1 = \frac{P_x\bar{m}^2}{bh} + \frac{P_y\bar{n}^2}{ah} + d_{11}\bar{m}^4 + (2d_{12} + 4d_{66})\bar{m}^2\bar{n}^2 + d_{22}\bar{n}^4 \tag{8.18a}$$

$$\varsigma_2 = -\left[c_{12}\bar{m}^4 + (c_{11} + c_{22} - 2c_{66})\bar{m}^2\bar{n}^2 + c_{12}\bar{n}^4 + \frac{\bar{n}^2}{R_x} + \frac{\bar{m}^2}{R_y}\right] \tag{8.18b}$$

$$\varsigma_3 = 8\bar{m}^2\bar{n}^2 H_{mn} \tag{8.18c}$$

$$\begin{aligned}\varsigma_4 = {} & \frac{4[-1+(-1)^m][-1+(-1)^n]}{mn\pi^2}\left(\frac{P_x}{bhR_x} + \frac{P_y}{ahR_y}\right) \\ & + \left(c_{11}N^{\theta}_{mnxx} + c_{12}N^{\theta}_{mnyy}\right)\bar{m}^2 + \left(c_{12}N^{\theta}_{mnxx} + c_{22}N^{\theta}_{mnyy}\right)\bar{n}^2 \\ & - \left(\bar{m}^2 M^{\theta}_{mnxx} + \bar{n}^2 M^{\theta}_{mnyy}\right) - q_{mn}\end{aligned} \tag{8.18d}$$

In the following section, a number of examples are solved for isotropic, orthotropic FG, and temperature-dependent shallow shells with both the chosen BCs. For all these examples, representations of either principal stresses or membrane tractions in the shell are graphically illustrated to gain a deeper insight into the nonlinear response of shallow shells with single or double curvature. The definition of dimensionless quantities are the same as those presented in the previous chapters.

8.3.1 Shallow shell subject to UDL

In this section, an FG shallow shell under large displacements is analysed. For an orthotropic FG shell, the elastic moduli referring to the axes x and y are taken in the form of

$$\begin{Bmatrix} E1(z) \\ E2(z) \end{Bmatrix} = \begin{Bmatrix} E1_t - E1_b \\ E2_t - E2_b \end{Bmatrix}\left(\frac{1}{2} + \frac{z}{h}\right)^{\lambda} + \begin{Bmatrix} E1b \\ E2b \end{Bmatrix} \tag{8.19}$$

where $\lambda(\geq 0)$ is the volume fraction index and subscripts Ei_t and Ei_b represent the material properties of the top and bottom surfaces of layer i in the shell, respectively.

Figure 8.1a shows results of dimensionless maximum deflection of a square orthotropic FG shallow spherical shell with the laterally unrestrained BC subjected

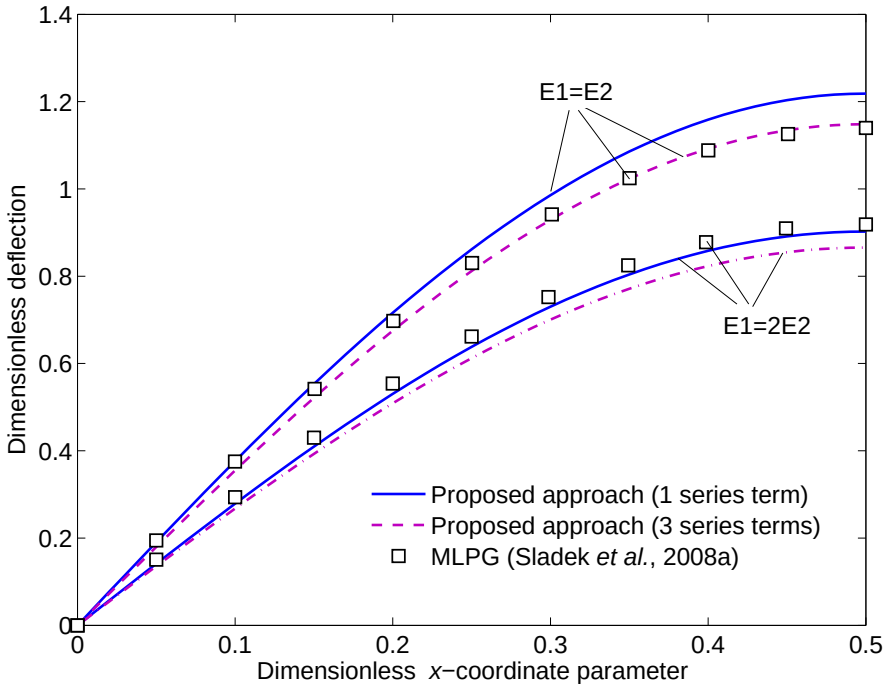

(a)

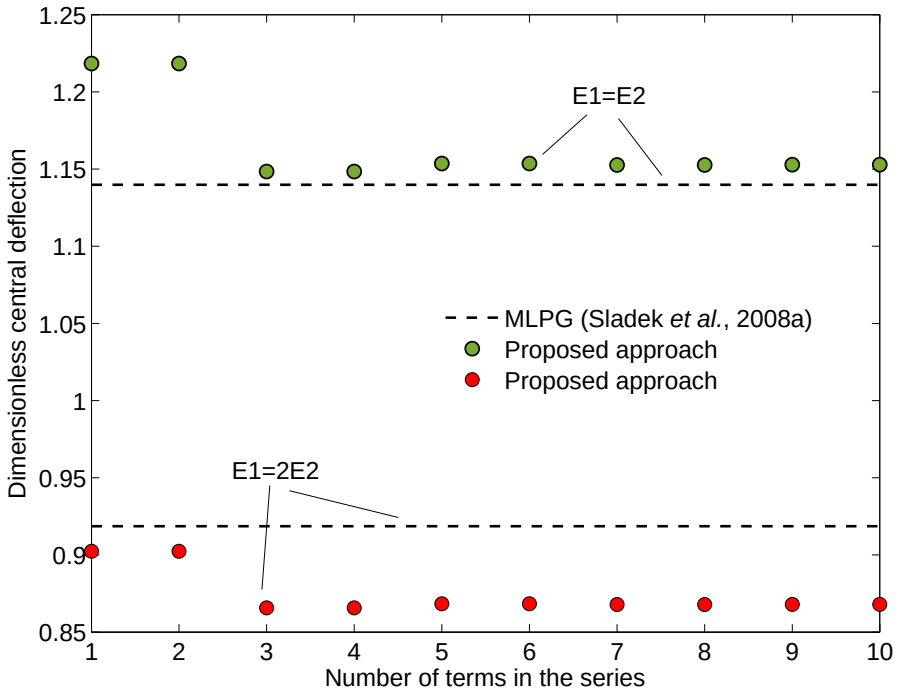

(b)

Figure 8.1 Comparison of deflection for an orthotropic FG shallow spherical shell with the laterally unrestrained BC subject to a UDL. Figure (a) shows the variation of dimensionless deflection (i.e. deflection of the shallow shell over deflection of its corresponding flat shell) with the dimensionless x-coordinate parameter and Figure (b) demonstrates the convergence of the dimensionless central deflection. Note that, the denominator of the MLPG and the proposed solutions are determined from the same method used for the calculation of the deflection of the curved shell.

to a UDL which are compared with the results obtained from a MLPG formulation (Sladek *et al.*, 2008a). The shell has thickness of 0.0127 m, span of 0.254 m, and radius of curvature to span ratio of 10. It is subjected to a UDL of 2.07×10^6 N/m^2 directed upwards (i.e. bottom surface loading). A quadratic variation of the elastic moduli is considered ($\lambda = 2$) with the elastic modulus at the bottom surface being $E1_b = 0.6895 \times 10^{10} N/m^2$ and $E2_b = E1_b/2$ and the elastic modulus at the top surface being $E2_t = 0.6895 \times 10^{10} N/m^2$ and $E1_t = 2E2_t$. For this example, the deflection is presented in a different dimensionless form, namely deflection of shallow shell over deflection of its corresponding flat shell ($R_x = R_y = \infty$) which is calculated from the same method. Figure 8.1a shows that an acceptable level of accuracy can be achieved for extremely shallow spherical shells with the laterally unrestrained BC using the proposed approach. This is justified by the convergence of the solution in Figure 8.1b which shows that the FE prediction is closer to the theoretical prediction obtained using three series terms in the calculations. It is also found that the maximum deflection value at the centre of an orthotropic FG shallow shell is about 1.13 times greater than the maximum deflection of its corresponding flat shell because of the low magnitude of elastic modulus chosen at the bottom surface of the shell.

Quiver plots of all dimensionless principal membrane tractions (forces) for the same orthotropic FG shallow shell with both the laterally unrestrained and restrained are illustrated in Figures 8.2 and 8.3, respectively. As expected, a completely symmetric distribution is formed for both the BCs. Since an upwardly directed UDL is applied, the behaviour of the shell with laterally restrained BC is completely dominated by tensile membrane forces. However, in the case of laterally unrestrained BC, compressive membrane stresses occur around the shell corners, while tensile membrane forces are formed in the central zone of the shell.

8.3.2 Shallow shell subject to combined thermomechanical loads

In order to investigate the structural response of shallow shells under fire conditions, a temperature-dependent concrete shallow hyperbolic paraboloidal shell (as the most general case) which is exposed to through-depth thermal gradients resulting from fire conditions has been analysed. Assuming a heat source at the bottom surface of

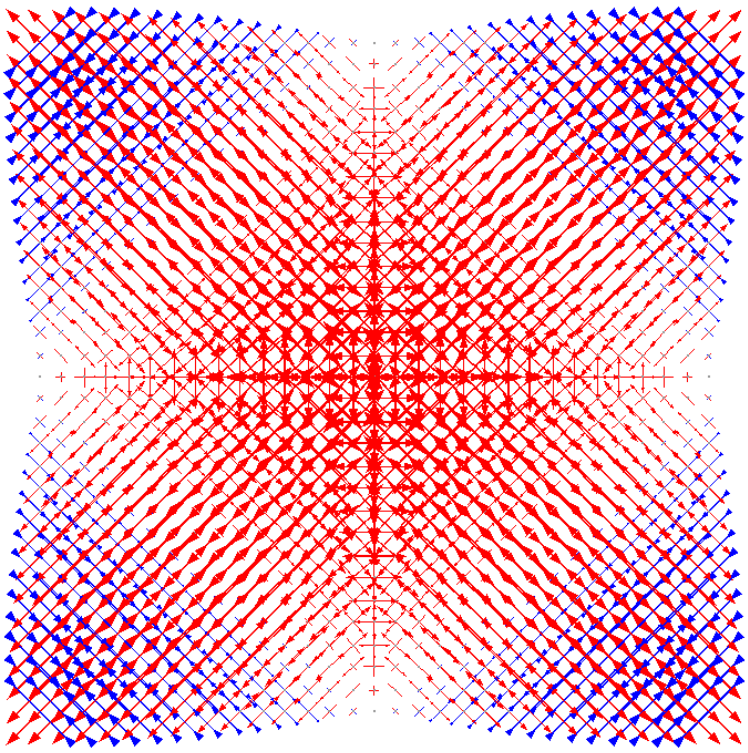

Figure 8.2 Distribution of all the dimensionless principal membrane tractions in a square orthotropic FG shallow cylindrical shell with laterally unrestrained BC subject to a UDL. Blue arrows represent compressive forces and the red ones represent tensile forces.

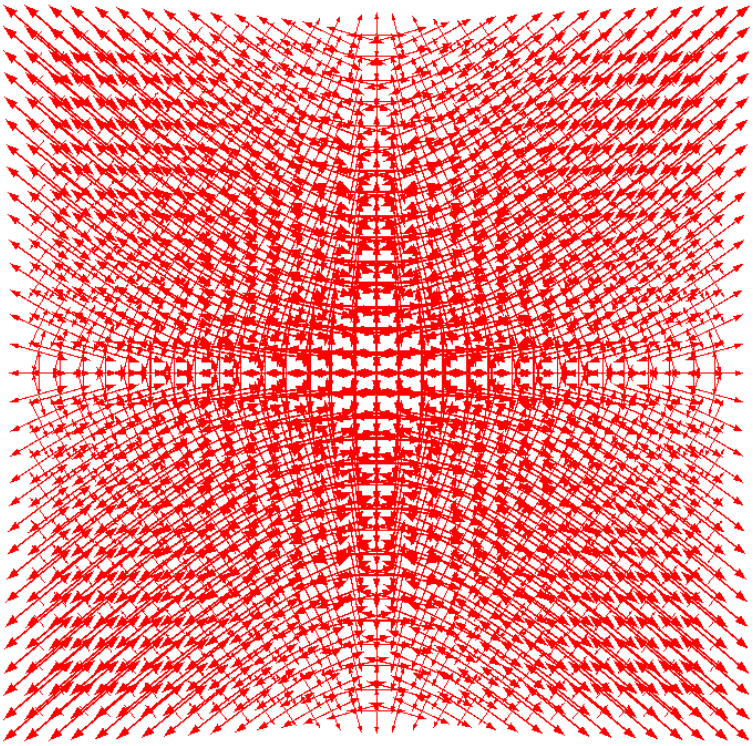

Figure 8.3 Distribution of all the dimensionless principal tensile membrane tractions in a square orthotropic FG shallow cylindrical shell with laterally restrained BC subject to a UDL.

a shell of thickness 0.15 m, two extreme cases of high and low rates of heating are considered:

i. A "short hot" exponential fire representing a high heating rate ($\eta = 0.005$) with a maximum temperature of 1000°C when the bottom surface of the plate was heated for 1,200 s.

ii. A "long cool" exponential fire representing a low heating rate ($\eta = 0.001$) with a maximum temperature of 650°C when the bottom surface of the plate was heated for 21,600 s.

An FE heat transfer analysis (Huang and Usmani, 1994; Usmani *et al.*, 2003) is carried out to determine the temperature history of the imposed heating regimes. As illustrated in Figures 8.4 and 8.5, the temperature may vary slowly with time or may be sustained over long periods of time. The corresponding through-depth temperature distributions for different times are shown in Figure 8.6. In this analysis, the curve at 1111 s is chosen to represent the short hot fire condition and the curve at 3637 s is chosen to represent the long cool fire condition. Using curve fitting, the following expressions are obtained for the short hot fire

$$\theta(z) = 20.01 + 585.30 \exp\left[-9\left(\frac{z}{h} + \frac{1}{2}\right)\right] \tag{8.20}$$

and for the long cool fire

$$\theta(z) = 23.39 + 271.53 \exp\left[-4.5\left(\frac{z}{h} + \frac{1}{2}\right)\right] \tag{8.21}$$

The above non-uniform temperature fields can readily be used to study the structural performance of shallow shells under two extreme fire scenarios with different rates of heating and likely to produce different mechanical responses. For a temperature-dependent concrete shell, the stiffness coefficients are given by

$$\mathbf{Q} = \begin{pmatrix} \frac{E(\theta,z)}{1-\nu^2} & \frac{E(\theta,z)\nu}{1-\nu^2} & 0 \\ & \frac{E(\theta,z)}{1-\nu^2} & 0 \\ \text{symm.} & & \frac{E(\theta,z)}{2(1+\nu)} \end{pmatrix} \tag{8.22}$$

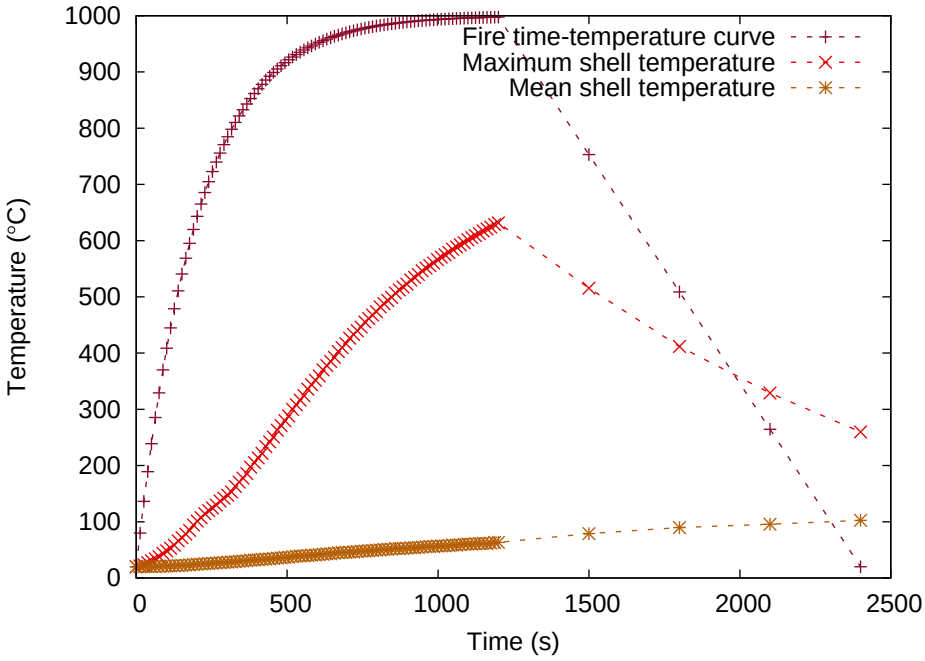

(a) Maximum and minimum temperatures

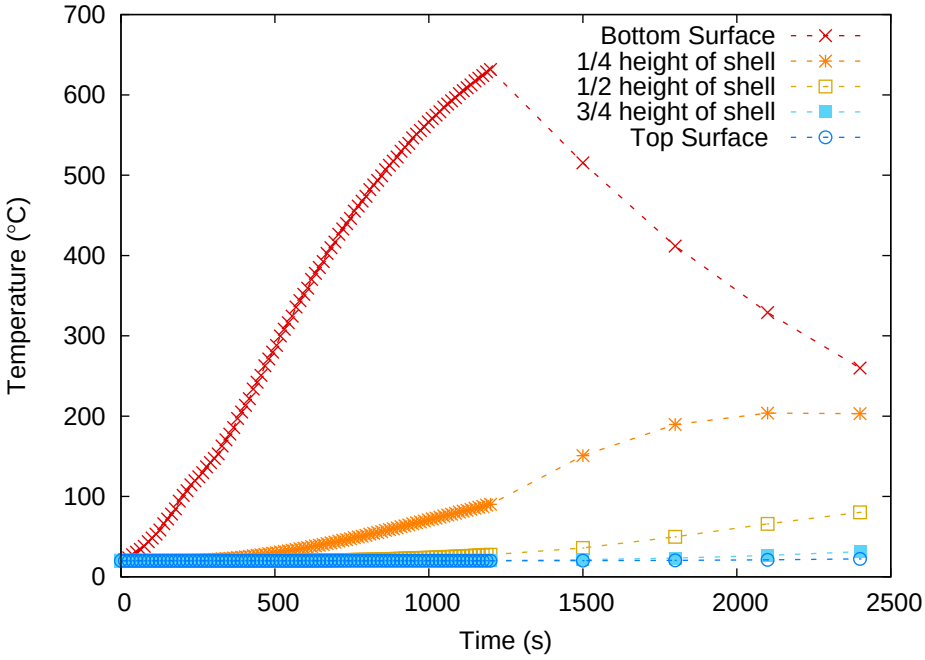

(b) Temperature at various heights

Figure 8.4 Time-temperature curves for the short hot fire scenario.

The elastic modulus and the coefficient of thermal expansion of the concrete at elevated temperatures are calculated using the equation (2.4). The load-deflection relationship for a shallow hyperbolic paraboloidal shell is shown in Figures 8.8 and 8.9 for both the chosen BCs. It can be seen that under a downwardly directed UDL, larger deflections are produced in the case of the short hot fire. Moreover, the effect

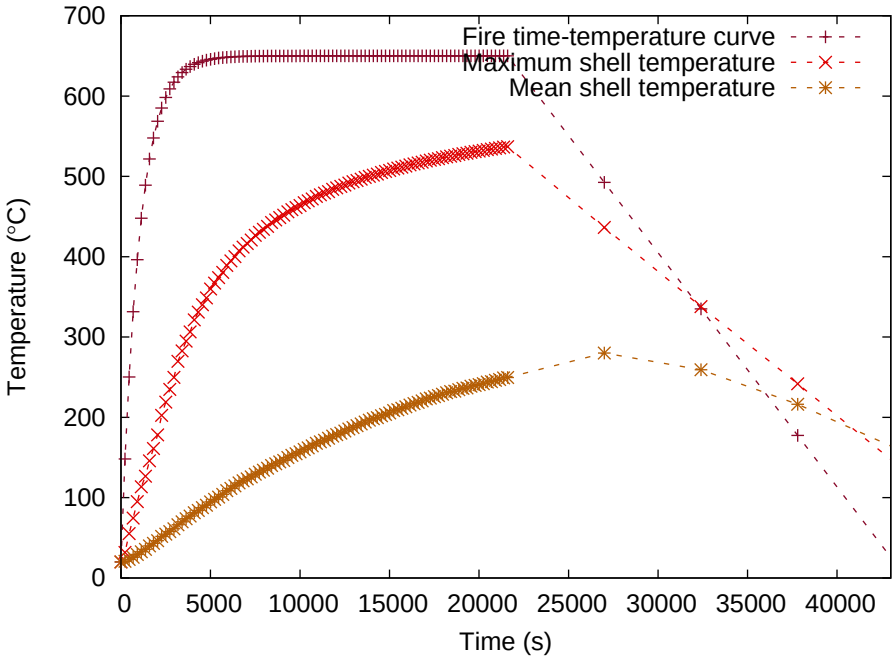

(a) Maximum and minimum temperatures

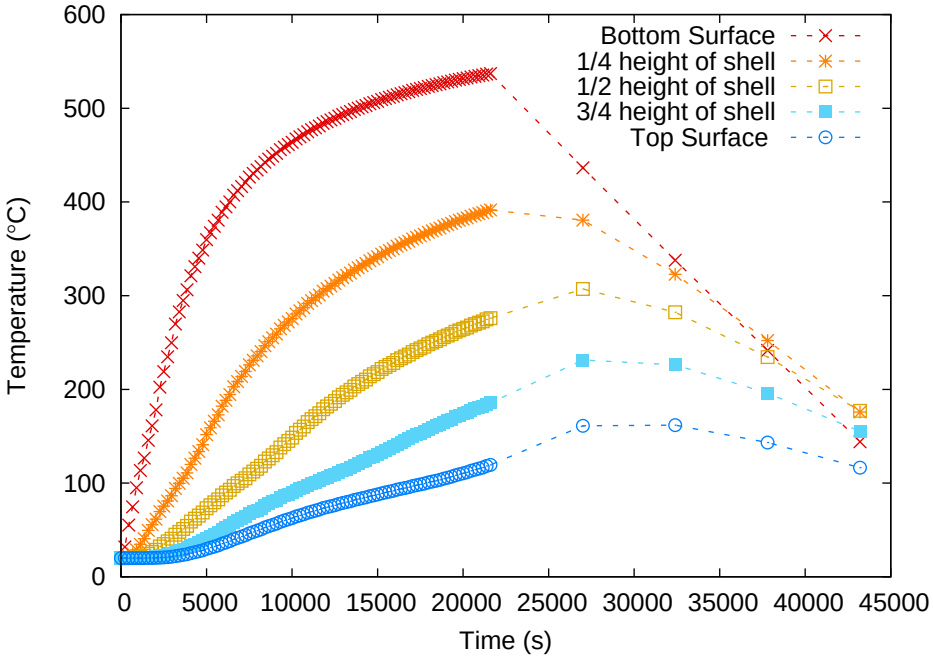

(b) Temperature at various heights

Figure 8.5 Time-temperature curves for the long cool fire scenario.

of TDMP on the nonlinear response of the shell is more considerable for the short hot fire condition compared with the long cool fire condition. Adding lateral restraint at the shell edges has clearly resulted in lower values for the shell maximum deflection as compared with those values obtained for the laterally unrestrained shells.

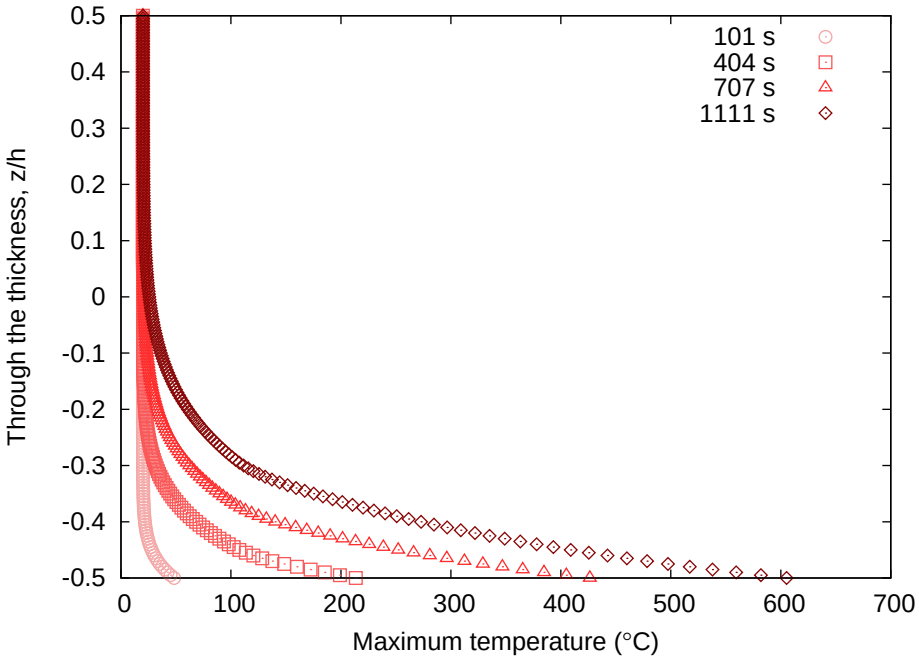

(a) Short hot fire

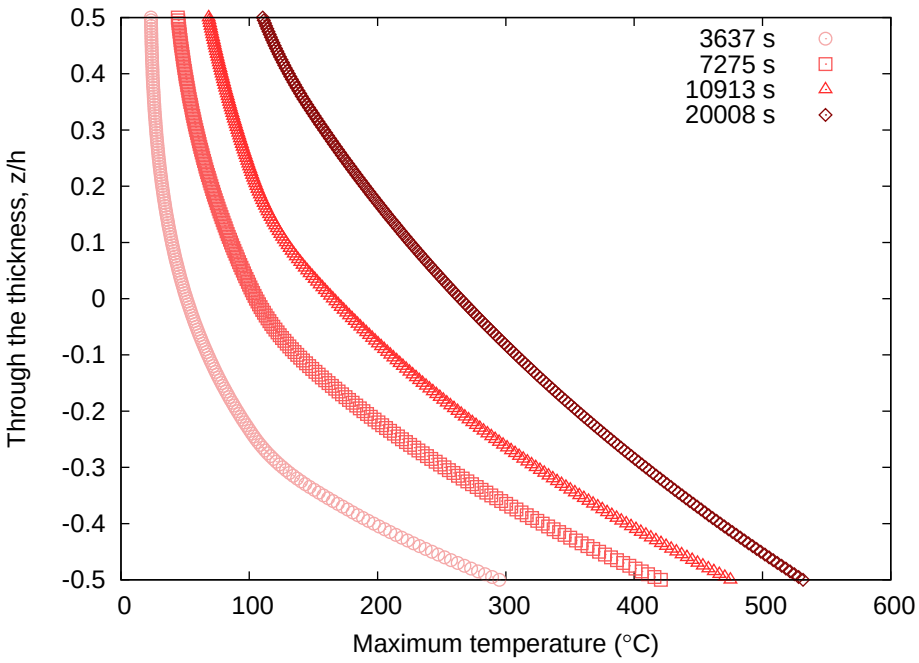

(b) Long cool fire

Figure 8.6 Fire induced through-depth temperature distribution for a shell.

Quiver plots of all dimensionless principal membrane tractions (forces) of the same shallow hyperbolic paraboloidal shell under short hot fire exposure condition are illustrated in Figure 8.10 for laterally unrestrained BC and in Figure 8.11 for laterally restrained BC. Figure 8.11 shows the compressive forces dominating the shell as a result of lateral restraint along the shell boundaries, producing maximum tensile forces

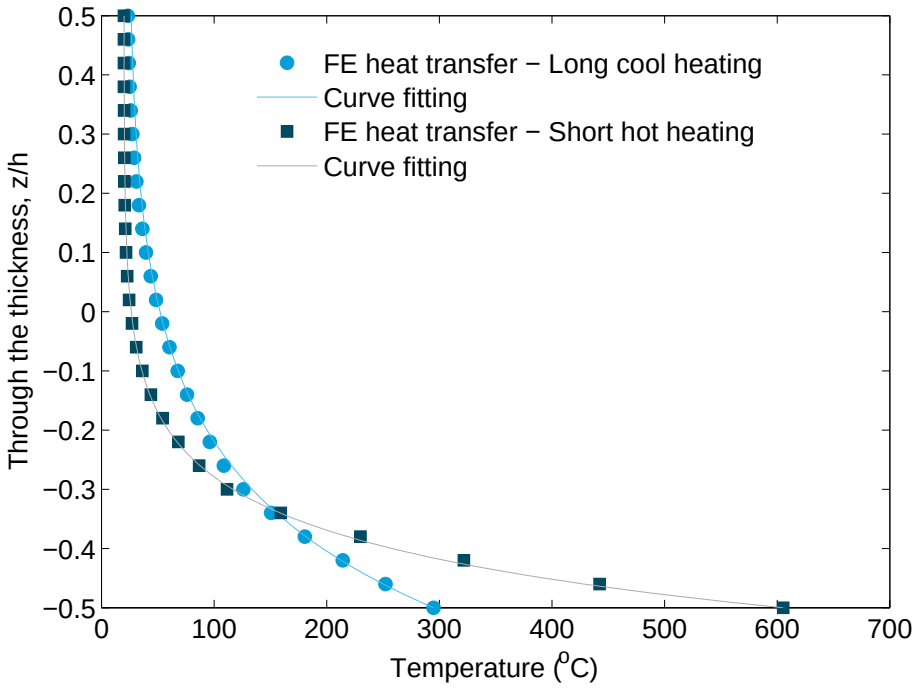

Figure 8.7 Non-uniform through-depth temperature distributions for the shell. The assumed curve fitting functions correspond to the high and low rates of heating.

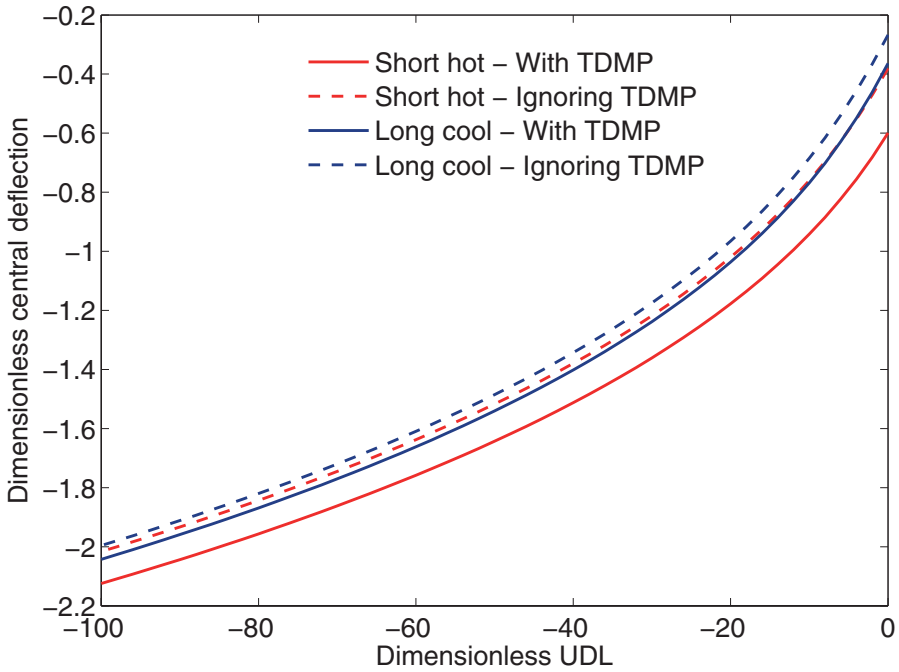

Figure 8.8 Dimensionless central deflection of square shallow hyperbolic paraboloidal shells ($h/a = 0.03$ and $R_x/a = -R_y/a = -5$) with laterally unrestrained BC subject to UDL and short hot and long cool fire scenarios.

around the shell corners. By moving away from the corners, the forces become more uniform. However, as Figure 8.10 depicts, in the case of the laterally unrestrained

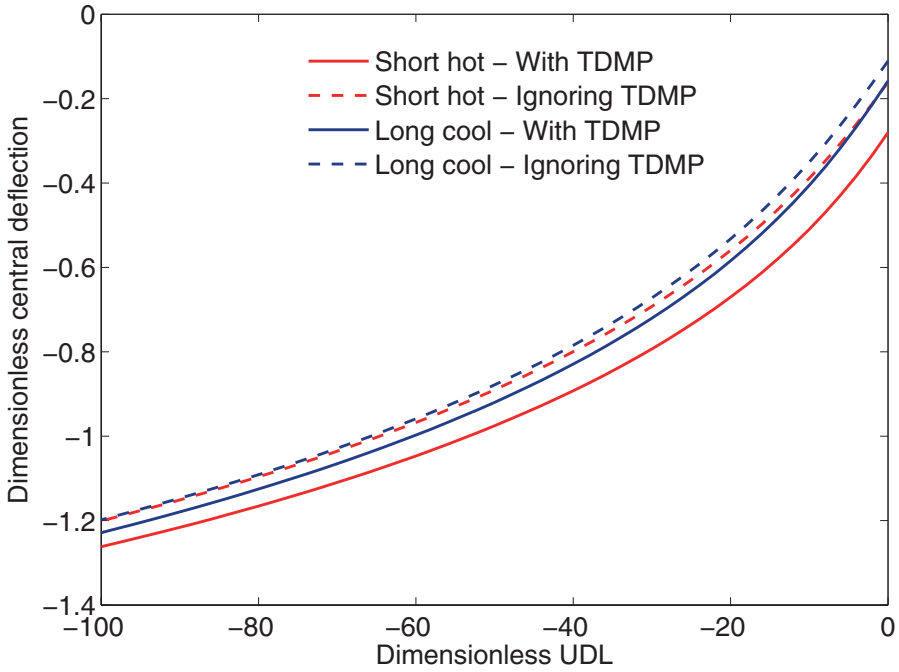

Figure 8.9 Dimensionless central deflection of square shallow hyperbolic paraboloidal shells ($h/a = 0.03$ and $R_x/a = -R_y/a = -5$) with laterally restrained BC subject to UDL and short hot and long cool fire scenarios.

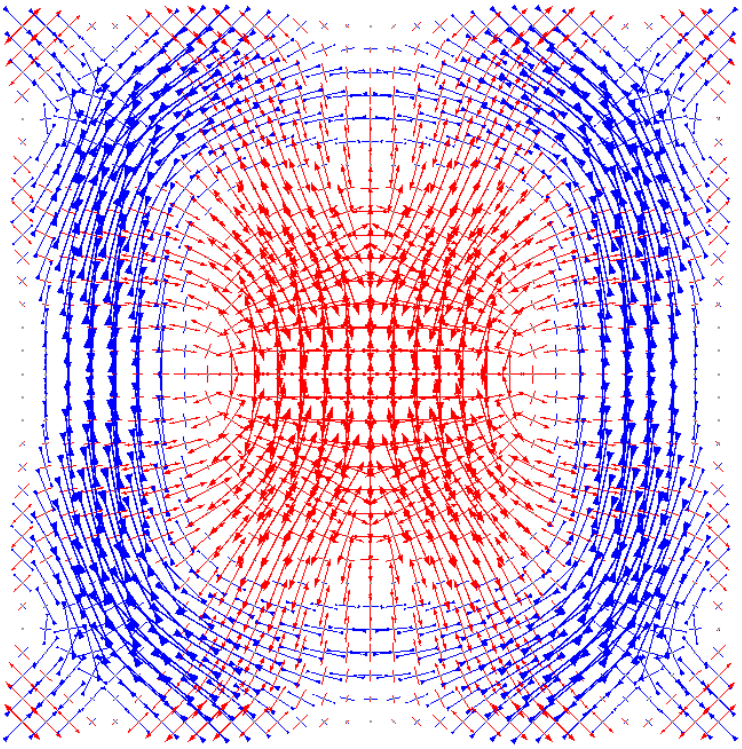

Figure 8.10 Distribution of the all dimensionless principal membrane tractions in a square temperature-dependent concrete shallow hyperbolic paraboloidal shell with laterally unrestrained BC under UDL and short hot fire exposure condition. Blue arrows represent compressive forces and the red ones represent tensile forces.

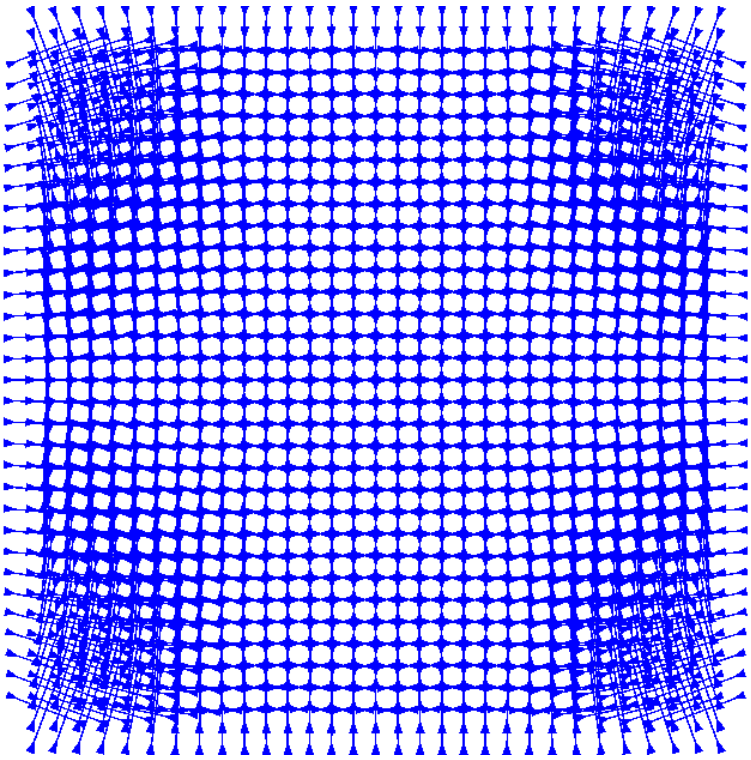

Figure 8.11 Distribution of all dimensionless compressive principal membrane tractions in a square temperature-dependent concrete shallow hyperbolic paraboloidal shell with laterally restrained BC under UDL and short hot fire exposure condition.

BC, compressive forces develop along the two shell edges with positive curvature, whereas at the centre of the shell only tensile forces are formed. The highest value of compressive forces occurs in the shell corners and the overall pattern suggests a clear development of a compressive ring, supporting the tension in the middle.

8.4 Summary

A geometrically and materially nonlinear analysis of temperature-dependent shallow shells subjected to thermo-mechanical loads was presented. Rotations along the shell boundaries were assumed to be free in all cases considered, while translations across the boundaries could be free or restrained. Quiver plots of principal stresses and membrane tractions are graphically illustrated for the examples considered. Comparison studies between the results obtained from the proposed formulation and those obtained from FE analyses show that the proposed approach offers a rapid convergence rate as well as an adequate level of accuracy for ‘extremely shallow shells’. However, based on the analyses carried out, for relatively deep shallow shells, it can offer sufficiently good performance for the case of laterally restrained BC. The formulation developed is versatile and appropriate for other applications,

such as laminated composite or orthotropic FG shallow shells. It can be used for the nonlinear analysis of extremely shallow shells when subjected to non-uniform through-depth thermal gradients, while also considering nonlinear and temperature-dependent material behaviour.

Chapter 9

Conclusions and Recommendations

9.1 Introduction

The series of studies in this thesis were designed to establish robust theoretical formulations to study the nonlinear elastic behaviour of beams, plates, and shallow shells exposed to varying regimes of external heating, while also externally loaded. It must be mentioned that plasticity or fracture were not in the current study. The solutions developed can be of considerable use in assessing the results from more rigorous numerical analyses as well as in hybrid-type computational approaches to construct advanced basis functions. Moreover, they can be used for visualising internal load paths and stress trajectories in complex structural components such as composite shells that can help engineers develop deeper insights into the relevant mechanics. The proposed formulations were capable of capturing engineering concepts such as “compressive ring” supporting TMA in slabs in fire and “thermal snap-through” and “thermal snap-back” in plates and shells undergoing large thermomechanical displacements. However, the latter was beyond the scope of this research and thus was not reported in this thesis. The chief conclusions that could be drawn from the current studies are given in the subsequent section.

9.2 Conclusions

- The beam analyses showed that in the case of laterally restrained beams under thermal loading regimes, an initial displacement is accommodated by the downward deflection of the beam due to longitudinal thermal expansions. It

was also observed that the pattern of the development of axial forces in single beams is largely governed by the thermal expansion, the thermal bowing, and the degree of restraint at the beam supports. The variation of mean temperature and thermal bowing can produce completely different responses for the beam, ranging from compressive forces to tensile forces. In beams with finite axial restraint, the axial force first increased but then reduced during heating due to cancelling out of the restrained thermal expansion by the thermal bowing induced curvature.

- Adding lateral restraint at the edges of the plates and shells resulted in lower values for maximum nonlinear deflection than those obtained for the laterally unrestrained BC. This, however, could change by increasing the mean temperature relative to the temperature gradient.

- In the case of laterally restrained BC, comparison studies show that sufficiently good performance for the plates and shells can be obtained using three series terms in the calculations. However, in the case of laterally unrestrained BC, only one series term might be adequate to achieve a satisfactory level of accuracy for plates and extremely shallow shells.

- In terms of accuracy and convergence rate, the proposed approach was found to be efficient for predicting the nonlinear behaviour of rectangular plates at both ambient and elevated temperatures (assuming thermal degradation of properties). However, due to significant changes in the shell curvature, good performance of the proposed approach has been only verified for shells with the restrained boundaries.

- Despite the larger area under the long cool fire time-temperature curve, which traditionally represented the fire severity, the effect of the short hot fire on the behaviour of beams, plates, and shells was more pronounced. It was found to be the most detrimental fire exposure condition in terms of the structural response.

- In the numerical analyses carried out, the effect of considering the temperature-dependency of material properties appeared to be minimal for the long cool fire condition. This effect was more significant when the short hot fire exposure condition was imposed since at high temperatures the material stiffness declines faster than at lower temperatures.

- The stress trajectories and principal stress distribution patterns obtained from the proposed approach were found to be very similar to the ones obtained from the FE analysis. These patterns can be explored and exploited to visualise internal structures in composite flat and curved shells in order to develop much deeper insights into the load-carrying mechanisms of thin shallow shells.

9.3 Recommendation for future research

The research described in this thesis has taken the understanding of the underlying mechanics of beams, plates, and shells further, but inevitably there are a number of important issues that must be investigated further.

9.3.1 Further development of theoretical models

The theoretical formulations developed in this thesis can provide relatively quick and accurate solutions for component level analyses. However, further research could be made to improve the formulations developed in the current study. These include:

- As previously discussed, an important limitation in this research is that due to significant changes in the shell curvature the performance of the proposed formulation was relatively poor for relatively deep shells. A different solution method would be required for such problems.

- The analysis was carried out assuming quasi-static conditions ignoring any dynamic effect. The proposed approach can be extended to include time-dependent nonlinear responses of beams, plates, and shells to thermomechanical actions.

- Future research may also consider the development of reliable theoretical methods for structures with plastic deformations, arbitrary size and boundary conditions other than those assumed in this thesis.

9.3.2 Development of efficient computational tools

A considerable amount of further research will be necessary to establish a highly efficient formulation for shell structures under more severe thermomechanical actions. As mentioned previously, the solutions developed could potentially be used in the hybrid-type computational approaches to establish an efficient computational tool for analysing complex engineering structures. This can be accomplished by combining the advantages of FEM and fundamental solutions developed in this study in a hybrid-type FE strategy. The requisite theoretical framework for this has been developed and reported in Appendix A, which can be used to develop such elements and implement on an appropriate software platform. Initial results which have so far been achieved are summarised in Table 9.1.

Table 9.1 Comparison of maximum central deflection and moment for a simply supported square plate ($E = 2.1 \times 10^6$ kg cm^{-2}, $\rho = 8 \times 10^{-6}$ kg s^{2}cm^{-4}, $\nu = 0.25$, $a = 25$ cm and $h = 5$cm) subjected to a uniform pulse load (of 10 kg cm^{-2})

Solution method	time, $\Delta t(\mu s)$		
	5	10	15
Deflection ($10^{-3}cm$)			
Proposed HT solution	-1.383	-1.402	-1.410
Exact solution (Akay, 1980)		-1.360	
Boundary element method (Qin, 1996b)	-1.381	-1.404	-1.412
Hybrid-Trefftz FEM (Qin, 1996c)	-1.383	-1.402	-1.410
Moment ($kg\ cm^{-1}$)			
Proposed HT solution	-630.1	-633.2	-642.3
Exact solution (Akay, 1980)		-613.8	
Boundary element method (Qin, 1996b)	-632.9	-635.3	-640.5
Hybrid-Trefftz FEM (Qin, 1996c)	-630.1	-633.2	-642.3

9.3.3 Discovering details of internal load-carrying mechanisms

Structures carry loads by developing internal stress patterns based on the loading and support conditions. Analogies of internal structures within structural members are often used in the design of structures. For instance, truss analogy is commonly used for estimating shear reinforcement required in beams. With the advent of 3D printing and the potential revolution this may bring to the future of the construction industry, it is important to develop a systematic approach for manufacturing structural members by enabling highly customised designs optimised for cost, function and aesthetic appearance. Such an approach can only be established if engineers and architects

collaborate much more intimately and have the tools available to examine and explore the internal structures hidden in the structural members that they design.

Current approaches of structural shape optimisation (involving removal of under-stressed regions) potentially offer a solution, however, such analyses are highly computationally intensive. Such an approach is justified for mechanical parts that once designed may be produced in their thousands or even millions, however, it may not be cost-effective for a building made of 100s or 1000s of customised structural members, each of which may potentially be unique. A relatively quick and computationally efficient visualisation approach could produce a viable alternative to this, which could also be adapted to guide the manufacturing process through 3D printing.

Appendix A

A hybrid-type FE model

In engineering problems, the terminology 'hybrid FEM' is typically referred to as the method of Lagrange multipliers, in which independent interpolation functions are constructed for stresses and displacements. The domain of the problem under consideration is divided into either sub-domains or sub-elements. Continuity is then enforced on the common boundary between any two adjacent domains or elements by adding additional terms to the variational functional. In the literature, Trefftz FEM, hybrid fundamental solution-based FEM, and enriched FEM have been successfully used to overcome many difficulties in solid and structural mechanics problems. A brief description of these FE strategies is given subsequently.

A.1 Trefftz FEM

The Trefftz FE strategy is named after the German mathematician and physicist Erich Immanuel Trefftz (1888 - 1937). In 1926, Trefftz presented an analogue to the variational method of Rayleigh-Ritz in order to solve partial differential equations of boundary value problems (Trefftz, 1926). In his variational formulation, instead of using approximate solutions that satisfy *a priori* all the essential BCs, he suggested using parametric functions satisfying *a priori* the differential equation(s) of the problem under consideration. In this FE strategy, as illustrated in Figure A.1, the domain of the problem is divided into a number of elements and for each element internal and boundary displacement fields are independently defined in the domain and on the boundary of the element, respectively.

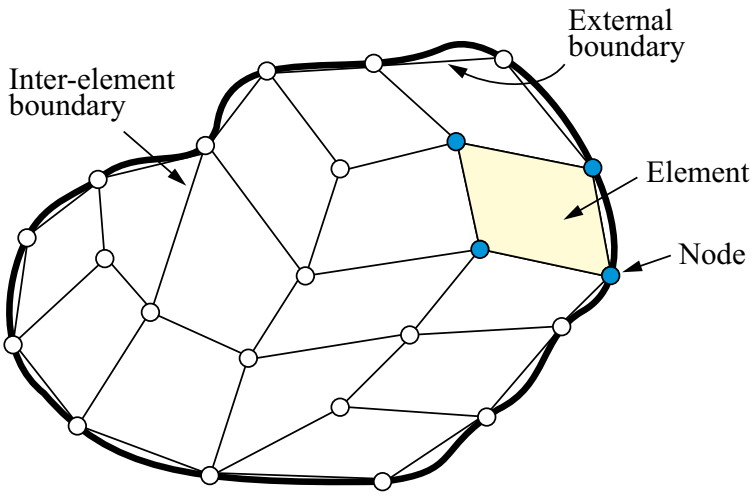

Figure A.1 Configuration of a Trefftz element. The domain is sub-divided into a number of polygonal sub-domains highlighted in yellow colour.

The internal field satisfies *a priori* the governing equation(s) of the problem and approximates the variation of potential within the domain of the element. It is represented as the sum of homogeneous and particular solutions of the governing equation(s). The homogeneous Trefftz functions which are also known as T-complete (Trefftz-complete) functions or T-complete set of homogeneous solutions, are chosen as basis functions. The mathematical basis of these functions was first developed by Herrera (1977) but was named T-complete functions or T-complete set of homogeneous solutions, in honour of its originator (Qin, 2005b). Since then, the terminology 'hybrid Trefftz' has been commonly used to refer to such system of equations.

The boundary displacement field, however, is approximated using the conventional FE shape functions. Additional terms are added to the variational functional to enforce the displacement and traction continuity conditions on the common boundary of two adjacent elements. The stiffness equations are established via the stationary condition of the variational functional.

The Trefftz method is basically classified into two types:

i. *Direct Trefftz method,* which is an extension of the displacement hybrid method and was developed by Jirousek (Jirousek and Leon, 1977; Jirousek, 1978). The analytical solutions of different sub-regions in the domain of the problem under consideration are used to construct the global solution through a suitable criterion. Non-singular homogeneous solutions of the problems are adopted as

trial and weighting functions. The former is interpolated by conventional FEMs, while the latter is approximated by the Trefftz-complete functions. In this method, unknowns are physical and coefficients of conventional interpolation functions.

ii. *Indirect Trefftz method,* in which depending upon the choice, trial functions can be either Trefftz collocation or Trefftz Galerkin. In this method, unknowns are non-physical and coefficients of Trefftz functions (see e.g., Chang *et al.* (2003) and Chang and Liu (2004)).

The fundamental concepts of Trefftz FEMs has been expanded by many researchers, particularly by Jirousek and his co-workers (Jirousek and Leon, 1977; Jirousek, 1978) and Herrera and his co-workers (Celia and Herrera, 1987; Celia *et al.*, 1989). This method has been successfully applied to a wide range of engineering problems including elastic and elasto-plastic problems (Qin, 2005a; Cao *et al.*, 2012a), plate and shell problems (Vörös, 1992; Choo *et al.*, 2010; Cen *et al.*, 2014; Rezaiee-Pajand and Karkon, 2014), material science problems (Cao *et al.*, 2012b; Cao *et al.*, 2013), nonlinear problems (Wang *et al.*, 2007), and heat conduction problems (Cao *et al.*, 2012c). A comprehensive overview on the hybrid Trfftz finite element methods (HT-FEM) and its application can be found in Qin (2005b). The main advantages of such methods include (Qin, 2005b):

i. Higher-order continuity between elements by introducing an auxiliary independent displacement field for inside the elemental domain under consideration;

ii. Improving the capability of the boundary element methods for handling local effects (e.g. imperfections, cracks and holes) in solid and structural mechanics via developing special elements using the introduced inter-element displacement field;

iii. Integration along the element boundaries, thereby providing more flexibility for generating complex elements such as curve sided elements;

Table A.1 Comparison between FEM and HT-FEM for solid and structural mechanics problems

Features	FEM	HT-FEM
Interpolation functions for element domain and boundary	Same functions	Two independent fields
Integration on boundary and domain	On both	Only on boundary
Generating complex elements	Generally difficult	Relatively easy
Mesh distortion	Not very sensitive	Insensitive
Mesh adjustment for local effects	Required	Not necessarily
Flexibility in boundary and initial conditions	No	Yes

iv. Representing the optimal expansion bases for hybrid-type elements where satisfaction of inter-element continuity *a priori* is not necessary (e.g. in generating quasi-conforming plate bending element).

These features are compared in Table A.1 with the features of conventional FEMs. Like any other numerical method, the HT-FEM has intrinsic limitations. The main challenges are:

i. finding and implementing suitable Trefftz functions that can satisfy the governing equations of the problem(s) under consideration;

ii. dealing with numerical instability caused by a notoriously ill-conditioned interpolation matrix. It may lead to inaccurate results which limits the applicability of the method to certain cases;

iii. generating nonlinear elements as the HT-FEM is not well-suited for materially and/or geometrically nonlinear problems. The method is mainly more versatile and appropriate for isotropic and linearly elastic problems.

To overcome the major drawbacks in the HT-FEMs, new hybrid-type FEMs have been developed.

A.2 Hybrid fundamental solution based FEM

Method of fundamental solutions (Hui and Qinghua, 2007) led to address the difficulty in generating Trefftz functions (Wang and Qin, 2009; Wang and Qin, 2010b; Wang

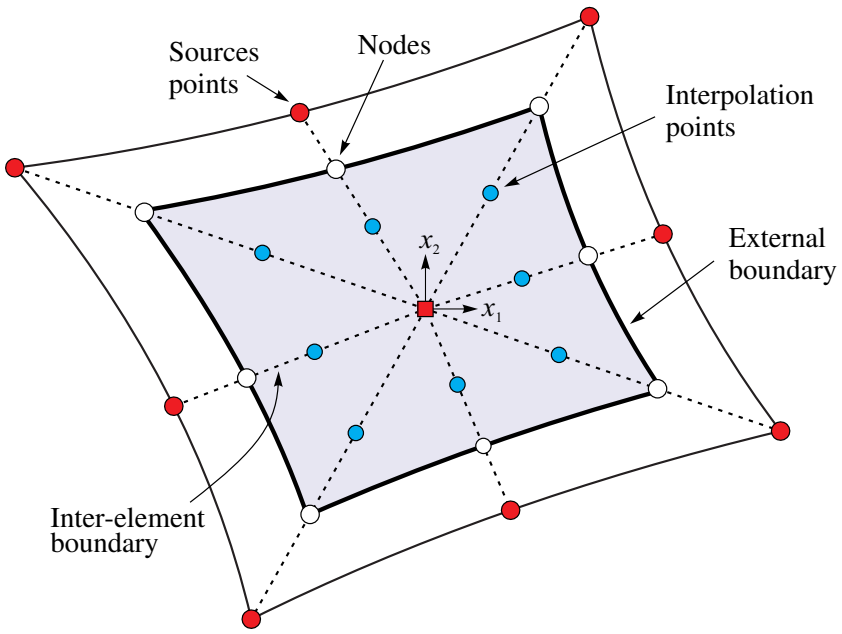

Figure A.2 Configuration of an HFS-FEM element.

and Qin, 2010a; Wang and Qin, 2011; Wang *et al.*, 2012a; Wang and Qin, 2012a; Wang and Qin, 2012b; Wang *et al.*, 2012b; Qin and Wang, 2013; Zhang *et al.*, 2014). In their alternative approach, which is called hybrid fundamental solution based finite element method (HFS-FEM), the basic idea of HT strategy has remaind the same and the intra-element and auxiliary frame fields are independently defined in the domain and on element boundary, respectively, but the field variable is interpolated by regular and special fundamental solutions (Green's functions). As illustrated in Figure A.2, a linear combination of the fundamental solutions at different source points outside the element domain of the problem(s) under consideration is used to approximate the non-conforming internal field variable. As a consequence, a new modified variational functional has been introduced to establish the stiffness matrix equations. It ensures that the inter-element continuity requirements is satisfied *a priori* in the problem(s) domain.

A.3 Enriched FEM

The refinement of mesh in the standard FEMs is not always efficient to model the propagation of various discontinuities. To deal with this, Dolbow and Belytschko (1999) developed an extended FEM based on the generalized FEM and the partition of unity method. Their main idea was describing localised features by appropriate set of basis enrichment functions. As such, the method requires *a priori* knowledge of the

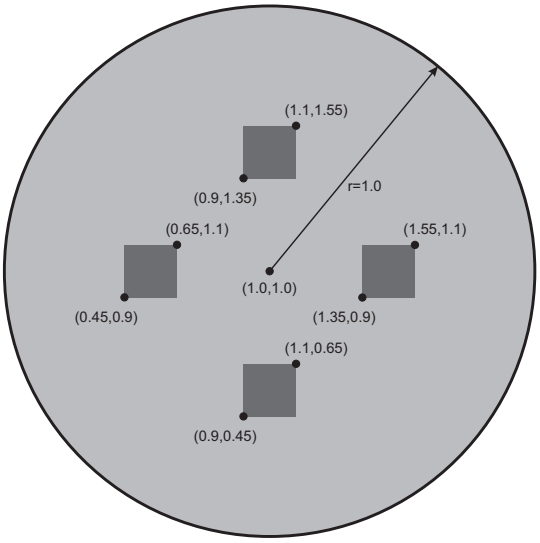

Figure A.3 An Enriched example for a multiple heat sources problem. The numbers in parenthesis refer to the coordinates in meters (Shadi Mohamed *et al.*, 2013).

functions that approximate the solution such as analytical solutions of the problem(s). A key feature of this approach in time-dependent problems is that the FE enrichment is not required to be updated at each time step. This strategy has been shown to reduce errors in computational analyses.

Recently, it has been efficiently used to solve problems with multiple heat sources (Shadi Mohamed *et al.*, 2013), as shown in Figure A.3. Three meshes considered in the simulation are shown in Figure A.4, indicating that the lowest number of DoFs is used for the enriched partition of unity FEM (PUFEM). As can be seen in Figure A.5, for the temperature at different sources, very similar results are obtained by the PUFEM compared to the reference solution based on the finest mesh and the FEM solution. This FE strategy has the advantage of obtaining accurate solutions for less number of DoFs in comparison with conventual FEM. This is particularly useful for modelling structures under localised heating.

A.4 A HT formulation

In an HT formulation, the internal displacement field may be written as the total of two homogeneous and particular parts as follows

$$\begin{aligned} \mathbf{u}_e &= \mathbf{u}_{\mathbf{p}_e} + \sum_{j=1}^{m} N_{ej} c_{ej} \\ &= \mathbf{u}_{\mathbf{p}_e} + \mathbf{N}_e \mathbf{c}_e \end{aligned} \tag{A.1}$$

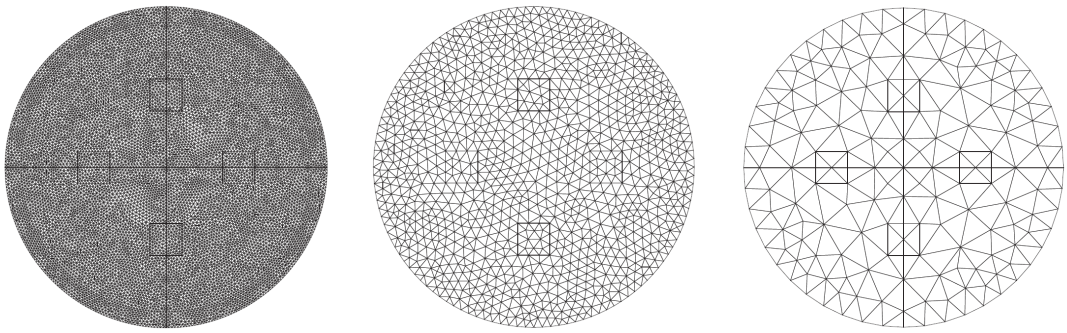

(a) FEM1 11041 modes and 21732 elements

(b) FEM2 1076 nodes and 203 elements

(c) PUFEM6DoFs 178 nodes and 306 elements

Figure A.4 FE meshes for the Enriched example with multiple heat sources (Shadi Mohamed *et al.*, 2013).

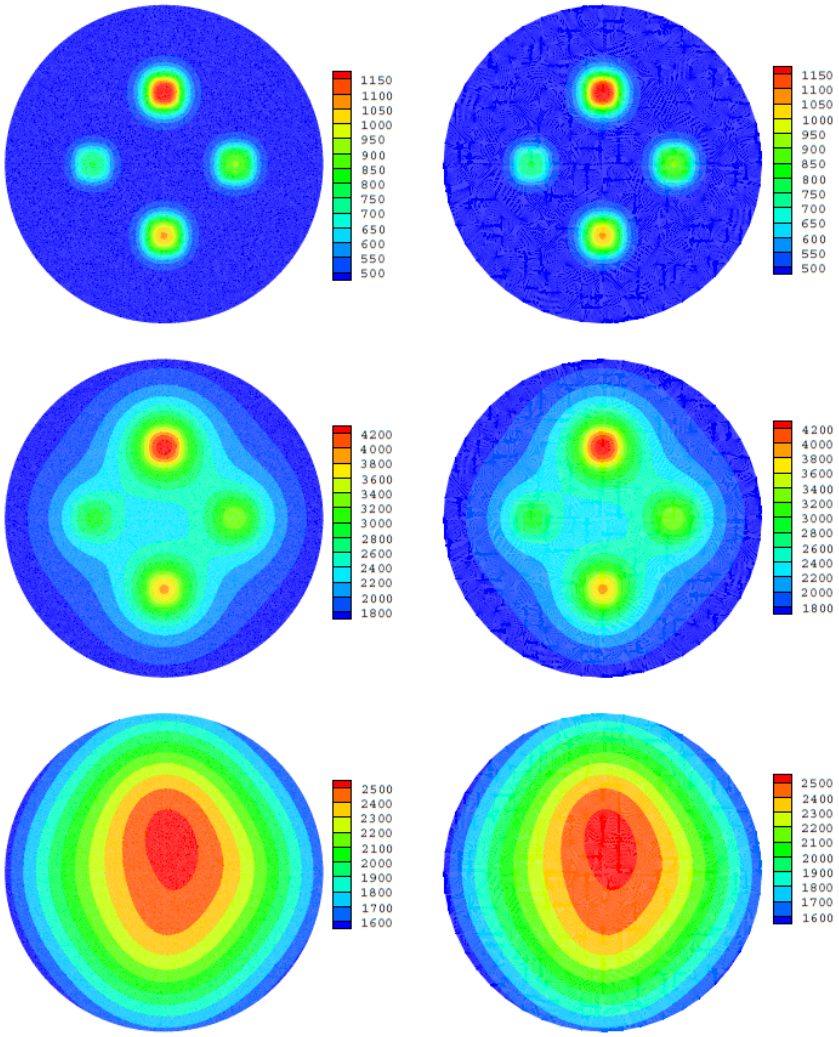

Figure A.5 Temperature distributions at different simulation times (from top to bottom, 0.5 s, 5 s, and 10 s) obtained for the Enriched example with multiple heat sources (Shadi Mohamed *et al.*, 2013).

where $\mathbf{u}_{\mathbf{p}_e}$ and $\mathbf{N}_e$ are the particular and homogeneous solutions to governing equation(s), respectively, and $\mathbf{c}_e$ is the undetermined coefficients vector. The number of

truncated Trefftz functions m is suggested to be equal or greater than the difference between the number of nodal DoFs of the element and the number of rigid body modes.

The boundary tractions along the element boundary can then be derived as

$$\begin{aligned} \mathbf{T}_e &= \mathbf{T}_{\mathbf{p}_e} + \sum_{j=1}^{m} \Upsilon_{ej} c_{ej} \\ &= \mathbf{T}_{\mathbf{p}_e} + \Upsilon_e \mathbf{c}_e \end{aligned} \tag{A.2}$$

where $\mathbf{T}_{\mathbf{p}_e}$ and Υ_e correspond to $\mathbf{u_p}$ and $\mathbf{N}_e$, respectively.

The boundary (frame) displacements at the boundary Γ_e of a particular element can be approximated by conventional FE shape functions as follows

$$\begin{aligned} \tilde{\mathbf{u}}_e &= \sum_{i=1}^{N} \tilde{N}_{ei} d_{ei} \\ &= \tilde{\mathbf{N}}_e \mathbf{d}_e \end{aligned} \tag{A.3}$$

where $\tilde{\mathbf{N}}_e$ and $\mathbf{d}_e$ are the shape functions matrix and nodal DoFs vector, respectively. It should be noted that, the assumed frame displacement is restricted to the element boundary Γ_e. The BCs are given by

$$\mathbf{u} = \bar{\mathbf{u}} \quad \text{on } \Gamma_{\mathrm{u}} \tag{A.4a}$$

$$\mathbf{T} = \mathbf{n}\sigma = \bar{\mathbf{T}} \quad \text{on } \Gamma_{\mathrm{T}} \tag{A.4b}$$

where $\bar{\mathbf{u}}$ and $\bar{\mathbf{T}}$ are prescribed boundary displacement and traction vector, respectively, and $\Gamma(=\Gamma_u \cup \Gamma_T)$ represents the boundary of the solution domain Ω. Moreover, inter-element continuity for any two neighboring elements such as $e1$ and $e2$ can be satisfied with the following requirements

$$\mathbf{u}_{e1} = \mathbf{u}_{e2} \quad on\ \Gamma_{e1} \cap \Gamma_{e2} \tag{A.5a}$$

$$\mathbf{T}_{e1} + \mathbf{T}_{e2} = 0 \quad on\ \Gamma_{e1} \cap \Gamma_{e2} \tag{A.5b}$$

The HT variational formulation is based on a multi-field functional. It can be established from the total potential energy principle. Using the two displacement fields introduced in equations (A.1) and (A.3), the HT functional can be written as

$$\begin{aligned}\Pi(\mathbf{u},\tilde{\mathbf{u}}) &= \sum_e \Pi_e(\mathbf{u},\tilde{\mathbf{u}}) \\ &= \sum_e \left[\int_{\Omega_e} W_e \, \mathrm{d}\Omega - \int_{\Omega_e} \mathbf{b}^{\mathrm{T}}\mathbf{u}_e \, \mathrm{d}\Omega - \int_{\Gamma_{eT}} \bar{\mathbf{T}}^{\mathrm{T}}\tilde{\mathbf{u}} \, \mathrm{d}\Gamma - \int_{\Gamma_{eu}} \bar{\mathbf{T}}_e^{\mathrm{T}}(\tilde{\mathbf{u}} - \bar{\mathbf{u}}) \, \mathrm{d}\Gamma \right. \\ &\qquad \left. - \oint_{\Gamma_e} \mathbf{T}_e^{\mathrm{T}}(\mathbf{u} - \tilde{\mathbf{u}}) \, \mathrm{d}\Gamma \right]\end{aligned} \tag{A.6}$$

where $W_e = \frac{1}{2}\boldsymbol{\sigma}_e^{\mathrm{T}}\boldsymbol{\varepsilon}_e$ is the strain energy density function in the domain, $\mathbf{b}$ is the vector of body forces (per unit volume), $\mathbf{T}$ are the tractions along element boundary Γ_e, and Γ_{eT} and Γ_{eu} are portions of the element boundary on which either boundary tractions $\bar{\mathbf{T}}$ or displacements $\bar{\mathbf{u}}$ are prescribed. The first integral term on the right hand side of the equal sign is commonly used in establishing the functional of conventional FEMs. As a consequence, element continuity is not strongly guaranteed. However, in the HT-FE strategy, additional terms are added to the functional in order to meet the displacement and traction continuity requirements on the adjacent elements. More specifically, the fourth integral term on the right hand side of the equal sign ensures that $\tilde{\mathbf{u}}$ and $\bar{\mathbf{u}}$ have the same value on the element boundary Γ, while the fifth term ensures that continuity condition for $\mathbf{u}$ and $\tilde{\mathbf{u}}$ is satisfied.

The stationary condition of equation (A.6) is formed by

$$\begin{aligned}\delta\Pi|_{\delta\mathbf{u}} = \sum_e \left[\int_{\Omega_e} \delta W \, \mathrm{d}\Omega - \int_{\Omega_e} \mathbf{b}^{\mathrm{T}}\delta\mathbf{u}_e \, \mathrm{d}\Omega - \int_{\Gamma_{eu}} \delta\mathbf{T}_e^{\mathrm{T}}(\tilde{\mathbf{u}} - \bar{\mathbf{u}}) \, \mathrm{d}\Gamma \right. \\ \left. - \oint_{\Gamma_e} \delta\mathbf{T}_e^{\mathrm{T}}(\mathbf{u} - \tilde{\mathbf{u}}) \, \mathrm{d}\Gamma + \oint_{\Gamma_e} \mathbf{T}_e^{\mathrm{T}}\delta\mathbf{u}_e \, \mathrm{d}\Gamma \right]\end{aligned} \tag{A.7}$$

and

$$\delta\Pi|_{\delta\tilde{\mathbf{u}}} = \sum_e \left[- \int_{\Gamma_{eu}} \mathbf{T}_e^{\mathrm{T}}\delta\tilde{\mathbf{u}} \, \mathrm{d}\Gamma - \int_{\Gamma_{eT}} \bar{\mathbf{T}}^{\mathrm{T}}\delta\tilde{\mathbf{u}} \, \mathrm{d}\Gamma + \oint_{\Gamma_e} \mathbf{T}_e^{\mathrm{T}}\delta\tilde{\mathbf{u}} \, \mathrm{d}\Gamma \right] \tag{A.8}$$

Using the divergence theorem (also known as Gauss's theorem), the first term on the right hand side of equation (A.7) can be transformed into the boundary integral form as follows

$$\delta\Pi|_{\delta\mathbf{u}} = \sum_e \left[-\int_{\Omega_e} \left(\frac{\partial \sigma_{ij}}{\partial x_j} + b_i \right) \delta u_i \, d\Omega - \int_{\Gamma_{eu}} \delta T_i (u_i - \tilde{u}_i) \, d\Gamma \right] \tag{A.9}$$

For quasi-static problems, the first integral term in the equation (A.9) is zero since it is satisfied by the equilibrium equation. Therefore, the stationary condition of the functional reduces to the following variational principles

$$\sum_e \left[\oint_{\Gamma_e} \delta \mathbf{T}_e^{\mathrm{T}} (\mathbf{u} - \tilde{\mathbf{u}}) \, \mathrm{d}\Gamma \right] = 0 \tag{A.10a}$$

$$\sum_e \left[\oint_{\Gamma_e} \mathbf{T}_e^{\mathrm{T}} \delta \tilde{\mathbf{u}} \, \mathrm{d}\Gamma - \int_{\Gamma_{eT}} \bar{\mathbf{T}}^{\mathrm{T}} \delta \tilde{\mathbf{u}} \, \mathrm{d}\Gamma \right] = 0 \tag{A.10b}$$

Substituting the determined displacements and traction into the above equations gives the following expression for the element parameters $\mathbf{c}_e$

$$\mathbf{c}_e = \mathbf{H_1}_e^{-1} \mathbf{H_2}_e \mathbf{d}_e - \mathbf{H_1}_e^{-1} \mathbf{H_3}_e \tag{A.11}$$

where

$$\mathbf{H_1}_e = \int_{\Gamma_e} \Upsilon_e^{\mathrm{T}} \, \mathbf{N}_e \, \mathrm{d}\Gamma \tag{A.12a}$$

$$\mathbf{H_2}_e = \int_{\Gamma_e} \Upsilon_e^{\mathrm{T}} \, \tilde{\mathbf{N}}_e \, \mathrm{d}\Gamma \tag{A.12b}$$

$$\mathbf{H_3}_e = \int_{\Gamma_e} \Upsilon_e^{\mathrm{T}} \, \mathbf{u_p}_e \, \mathrm{d}\Gamma \tag{A.12c}$$

and the nodal DoFs vector $\mathbf{d}_e$ is defined by

$$\mathbf{d}_e = \mathbf{K}_e^{\mathrm{T}} \, \mathbf{F}_e \tag{A.13}$$

in which the element stiffness matrix $\mathbf{K}_e$ and the equivalent nodal forces $\mathbf{F}_e$ are given by

$$\mathbf{K}_e^{\mathrm{T}} = \mathbf{H_2}_e^{\mathrm{T}}\, \mathbf{H_1}_e\, \mathbf{H_2}_e \tag{A.14a}$$

$$\mathbf{F}_e = \mathbf{H_4}_e - \mathbf{H_2}_e^{\mathrm{T}}\, \mathbf{H_1}_e^{-1}\, \mathbf{H_2}_e \tag{A.14b}$$

and

$$\mathbf{H_4}_e = \oint_{\Gamma_e} \tilde{\mathbf{N}}_e^{\mathrm{T}} \left(\mathbf{T_p}_e - \bar{\mathbf{T}}_e \right) \mathrm{d}\Gamma \tag{A.15}$$

Appendix B

Degradation of structural steel at elevated temperature - Eurocode

The empirical data for the reduction in structural steel at elevated temperatures are given in tabular form in Eurocode (2005). These data are listed in Table B.1 in which E_a is the elastic modulus of steel at ambient temperature, $E_{a,\theta}$ is the slope of the linear elastic range for steel at elevated temperature θ_a, f_{ap} is the proportional limit for steel at ambient temperature, $f_{ap,\theta}$ is its counterpart at elevated temperature, f_{au} is the maximum stress level or effective yield strength for steel at ambient temperature, and $f_{au,\theta}$ is its counterpart at elevated temperature.

Table B.1 Reduction factors for structural steel at elevated temperatures (extracted from Eurocode (2005))

Steel Temperature, θ_a [°C]	$k_{E,\theta} = \frac{E_{a,\theta}}{E_a}$	$k_{p,\theta} = \frac{f_{ap,\theta}}{f_{ay}}$	$k_{y,\theta} = \frac{f_{ay,\theta}}{E_{ay}}$	$k_{u,\theta} = \frac{f_{au,\theta}}{f_{ay}}$
20	1	1	1	1.25
100	1	1	1	1.25
200	0.9	0.807	1	1.25
300	0.8	0.613	1	1.25
400	0.7	0.420	1	
500	0.6	0.360	0.78	
600	0.31	0.180	0.47	
700	0.13	0.075	0.23	
800	0.09	0.050	0.11	
900	0.0675	0.0375	0.06	
1000	0.0450	0.0250	0.04	
1100	0.0225	0.0125	0.02	
1200	0	0	0	

Appendix C

Degradation of concrete at elevated temperature - Eurocode

The empirical data for the reduction in concrete at elevated temperatures are given in tabular form in Eurocode (2005). These data are listed in Table C.1 in which f_c is the compressive strength of concrete at ambient temperature, $f_{c,\theta}$ is its counterpart at elevated temperature, ε_{cu} is the corresponding strain of concrete at ambient temperature, and $\varepsilon_{cu,\theta}$ is its counterpart at elevated temperature.

Table C.1 Reduction factors for normal weight concrete and lightweight concrete at elevated temperatures (extracted from Eurocode (2005))

Concrete Temperature, θ [°C]	$k_{c,\theta} = \frac{f_{c,\theta}}{f_c}$		$\varepsilon_{cu,\theta} \times 10^3$
	Normal weight	Lightweight	Normal weight
20	1	1	2.5
100	1	1	4
200	0.95	1	5.5
300	0.85	1	7
400	0.75	0.88	10
500	0.6	0.76	15
600	0.45	0.64	25
700	0.3	0.52	25
800	0.15	0.40	25
900	0.08	0.28	25
1000	0.04	0.16	25
1100	0.01	0.04	25
1200	0	0	-

References

Abu, A. K., Burgess, I. W., and Plank, R. J. (2013). Tensile membrane action of thin slabs exposed to thermal gradients. *Journal of Engineering Mechanics* **139**(11): 1497–1507 (see p. 69).

Abu-Farsakh, G., Barakat, S., and Al-Zoubi, N. (2000). Effect of material nonlinearity in unidirectional composites on the behavior of beam structures. *International Journal of Solids and Structures* **37**(19): 2673–2694 (see p. 43).

Akay, H. (1980). Dynamic large deflection analysis of plates using mixed finite elements. *Computers & Structures* **11**: 1–11 (see p. 171).

Al-Gahtani, H. J. and Naffa'a, M. (2009). RBF meshless method for large deflection of thin plates with immovable edges. *Engineering Analysis with Boundary Elements* **33**(2): 176–183 (see pp. 68, 87, 89).

Albuquerque, E. and Aliabadi, M. (2008). A boundary element formulation for boundary only analysis of thin shallow shells. *CMES: Computer Modeling in Engineering & Sciences* **29**(2): 63–73 (see p. 127).

Albuquerque, E. and Aliabadi, M. (2010). A boundary element analysis of symmetric laminated composite shallow shells. *Computer Methods in Applied Mechanics and Engineering* **199**(41): 2663–2668 (see p. 147).

Alinia, M. and Ghannadpour, S. (2009). Nonlinear analysis of pressure loaded FGM plates. *Composite Structures* **88**(3): 354–359 (see pp. 77, 99).

Amabili, M (2005). Non-linear vibrations of doubly curved shallow shells. *International Journal of Non-Linear Mechanics* **40**(5): 683–710 (see p. 127).

Arciniega, R. and Reddy, J. (2007a). Large deformation analysis of functionally graded shells. *International Journal of Solids and Structures* **44**(6): 2036–2052 (see p. 146).

Arciniega, R. and Reddy, J. (2007b). Tensor-based finite element formulation for geometrically nonlinear analysis of shell structures. *Computer Methods in Applied Mechanics and Engineering* **196**(4): 1048–1073 (see p. 146).

Asghari, M, Kahrobaiyan, M., and Ahmadian, M. (2010). A nonlinear Timoshenko beam formulation based on the modified couple stress theory. *International Journal of Engineering Science* **48**(12): 1749–1761 (see p. 44).

Ayad, R. and Rigolot, A. (2002). An improved four-node hybrid-mixed element based upon Mindlin's plate theory. *International Journal for Numerical Methods in Engineering* **55**(6): 705–731 (see p. 66).

Ayad, R., Dhatt, G., and Batoz, J. L. (1998). A new hybrid-mixed variational approach for Reissner–Mindlin plates. The MiSP model. *International Journal for Numerical Methods in Engineering* **42**(7): 1149–1179 (see p. 66).

Bailey, C. (2003). Efficient arrangement of reinforcement for membrane behaviour of composite floor slabs in fire conditions. *Journal of Constructional Steel Research* **59**(7): 931–949 (see p. 98).

Bailey, C. and Moore, D. (2000). The structural behaviour of steel frames with composite floorslabs subject to fire: Part 2: design. *Structural Engineer* (see p. 97).

Bailey, C. G. (2001). Membrane action of unrestrained lightly reinforced concrete slabs at large displacements. *Engineering Structures* **23**(5): 470–483 (see p. 3).

Bailey, C. G. (2004). Membrane action of slab/beam composite floor systems in fire. *Engineering Structures* **26**(12): 1691–1703 (see pp. 3, 98).

Bailey, C. G. and Toh, W. S. (2007). Small-scale concrete slab tests at ambient and elevated temperatures. *Engineering Structures* **29**(10): 2775–2791 (see p. 98).

Bailey, C. G. (1995). Simulation of the structural behaviour of steel-framed buildings in fire. PhD Thesis. Department of Civil and Structural Engineering, University of Sheffield, UK (see p. 21).

Barut, A, Madenci, E, and Tessler, A. (2000). Nonlinear thermoelastic analysis of composite panels under non-uniform temperature distribution. *International Journal of Solids and Structures* **37**(27): 3681–3713 (see p. 126).

Bathe, K.-J. and Dvorkin, E. N. (1985). A four-node plate bending element based on Mindlin/Reissner plate theory and a mixed interpolation. *International Journal for Numerical Methods in Engineering* **21**(2): 367–383 (see p. 66).

Bathe, K.-J. and Dvorkin, E. N. (1986). A formulation of general shell elements–the use of mixed interpolation of tensorial components. *International Journal for Numerical Methods in Engineering* **22**(3): 697–722 (see p. 66).

Batoz, J. and Lardeur, P (1989). A discrete shear triangular nine D.O.F. element for the analysis of thick to very thin plates. *International Journal for Numerical Methods in Engineering* **28**(3): 533–560 (see p. 66).

Belytschko, T, Tsay, C., and Liu, W. (1981). A stabilization matrix for the bilinear Mindlin plate element. *Computer Methods in Applied Mechanics and Engineering* **29**(3): 313–327 (see p. 66).

Belytschko, T. and Tsay, C.-S. (1983). A stabilization procedure for the quadrilateral plate element with one-point quadrature. *International Journal for Numerical Methods in Engineering* **19**(3): 405–419 (see p. 66).

Berger, H. M. (1955). A new approach to the analysis of large deflections of plates. *Journal of Applied Mechanics* **22**(465): 465–472 (see p. 66).

Bich, D. H. and Van Tung, H. (2011). Non-linear axisymmetric response of functionally graded shallow spherical shells under uniform external pressure including temperature effects. *International Journal of Non-Linear Mechanics* **46**(9): 1195–1204 (see p. 147).

Bose, A and Surana, K. (1993). Piecewise hierarchical p-version axisymmetric shell element for non-linear heat conduction in laminated composites. *Computers & Structures* **47**(1): 1–18 (see p. 145).

Byklum, E. and Amdahl, J. (2002). A simplified method for elastic large deflection analysis of plates and stiffened panels due to local buckling. *Thin-Walled Structures* **40**(11): 925–953 (see p. 69).

Cao, C, Qin, Q.-H., and Yu, A (2012a). A new hybrid finite element approach for three-dimensional elastic problems. *Archives of Mechanics* **64**(3): 261–292 (see p. 175).

Cao, C. and Qin, Q.-H. (2015). Hybrid Fundamental Solution Based Finite Element Method: Theory and Applications. *Advances in Mathematical Physics* **2015** (see p. 3).

Cao, C., Yu, A., and Qin, Q.-H. (2013). A novel hybrid finite element model for modeling anisotropic composites. *Finite Elements in Analysis and Design* **64**: 36–47 (see p. 175).

Cao, L.-L., Qin, Q.-H., and Zhao, N. (2012b). Hybrid graded element model for transient heat conduction in functionally graded materials. *Acta Mechanica Sinica* **28**(1): 128–139 (see p. 175).

Cao, L., Wang, H., and Qin, Q.-H. (2012c). Fundamental solution based graded element model for steady-state heat transfer in FGM. *Acta Mechanica Solida Sinica* **25**(4): 377–392 (see p. 175).

Celia, M. and Herrera, I. (1987). Solution of general ordinary differential equations using the algebraic theory approach. *Numerical Methods for Partial Differential Equations* **3**(2): 117–129 (see p. 175).

Celia, M. A., Herrera, I., Bouloutas, E., and Kindred, J. S. (1989). A new numerical approach for the advective-diffusive transport equation. *Numerical Methods for Partial Differential Equations* **5**(3): 203–226 (see p. 175).

Cen, S., Shang, Y., Li, C.-F., and Li, H.-G. (2014). Hybrid displacement function element method: A simple hybrid-Trefftz stress element method for analysis of Mindlin–Reissner plate. *International Journal for Numerical Methods in Engineering* **98**(3): 203–234 (see p. 175).

Chan, H. and Chung, W. (1989). Geometrically nonlinear analysis of shallow shells using higher order finite elements. *Computers & Structures* **31**(3): 329–338 (see p. 36).

Chang, J.-r., Liu, R.-f., Kuo, S.-r., and Yeih, W. (2003). Application of symmetric indirect Trefftz method to free vibration problems in 2D. *International Journal for Numerical Methods in Engineering* **56**(8): 1175–1192 (see p. 175).

Chang, J. and Liu, R. (2004). An asymmetric indirect Trefftz method for solving free-vibration problems. *Journal of Sound and Vibration* **275**(3): 991–1008 (see p. 175).

Cheng, S., Li, L.-y., and Kim, B. (2015). Buckling analysis of cold-formed steel channel-section beams at elevated temperatures. *Journal of Constructional Steel Research* **104**: 74–80 (see p. 45).

Chia, C.-Y. (1988). Geometrically nonlinear behavior of composite plates: a review. *Applied Mechanics Reviews* **41**(12): 439–451 (see p. 98).

Choo, Y. S., Choi, N., and Lee, B. C. (2010). A new hybrid-Trefftz triangular and quadrilateral plate elements. *Applied Mathematical Modelling* **34**(1): 14–23 (see p. 175).

Civalek, Ö (2014). Geometrically nonlinear dynamic and static analysis of shallow spherical shell resting on two-parameters elastic foundations. *International Journal of Pressure Vessels and Piping* **113**: 1–9 (see p. 148).

Civalek, Ö. (2007). Nonlinear analysis of thin rectangular plates on Winkler–Pasternak elastic foundations by DSC–HDQ methods. *Applied Mathematical Modelling* **31**(3): 606–624 (see p. 68).

Coffin, D. W. and Bloom, F. (1999). Elastica solution for the hygrothermal buckling of a beam. *International Journal of Non-Linear Mechanics* **34**(5): 935–947 (see p. 42).

Dang, T. D. and Hung, N.-D. (2013). A hybrid element model for structural mechanics problems. *European Journal of Mechanics-A/Solids* **42**: 469–479 (see p. 3).

De Holanda, A. and Gonçalves, P. (2003). Postbuckling analysis of plates resting on a tensionless elastic foundation. *Journal of Engineering Mechanics* **129**(4): 438–448 (see p. 69).

Di Capua, D. and Mari, A. R. (2007). Nonlinear analysis of reinforced concrete cross-sections exposed to fire. *Fire Safety Journal* **42**(2): 139–149 (see p. 44).

Dolbow, J. and Belytschko, T (1999). A finite element method for crack growth without remeshing. *International Journal for Numerical Methods in Engineering* **46**(1): 131–150 (see p. 177).

Donnell, L. H. (1976). *Beams, Plates and Shells*. Vol. 8. McGraw-Hill New York (see pp. 35, 36).

Drysdale, D. (2011). *An Introduction to Fire Dynamics*. John Wiley & Sons (see p. 45).

du Béton, C. (2010). *CEB-FIP model code 2010, first completed draft*. Lausanne, Switzerland (see p. 115).

Duc, N. D. and Quan, T. Q. (2013). Nonlinear postbuckling of imperfect eccentrically stiffened P-FGM double curved thin shallow shells on elastic foundations in thermal environments. *Composite Structures* **106**: 590–600 (see p. 100).

Duc, N. D. and Quan, T. Q. (2014). Nonlinear response of imperfect eccentrically stiffened FGM cylindrical panels on elastic foundation subjected to mechanical loads. *European Journal of Mechanics-A/Solids* **46**: 60–71 (see p. 100).

Duc, N. D. and Thang, P. T. (2014). Nonlinear response of imperfect eccentrically stiffened ceramic–metal–ceramic FGM thin circular cylindrical shells surrounded on elastic foundations and subjected to axial compression. *Composite Structures* **110**: 200–206 (see p. 100).

Duc, N. D. and Van Tung, H. (2010). Nonlinear response of pressure-loaded functionally graded cylindrical panels with temperature effects. *Composite Structures* **92**(7): 1664–1672 (see p. 147).

Erkmen, R. E. and Bradford, M. A. (2009). Nonlinear elastic analysis of composite beams curved in-plan. *Engineering Structures* **31**(7): 1613–1624 (see p. 44).

Eurocode (2002). *EN 1993-1-2, Eurocode 0: Basis of Structural Design*. Brussels: European Committee for Standardization (see p. 1).

Eurocode (2005). *EN 1993-1-2, Eurocode 3: Design of Steel Structures, Part 1-2: General rules - Structural fire design*. Brussels: European Committee for Standardization (see pp. 14, 15, 100, 184, 185).

Flügge, W and Elling, R. (1972). Singular solutions for shallow shells. *International Journal of Solids and Structures* **8**(2): 227–247 (see p. 35).

Franssen, J. (2011). User's Manual for SAFIR 2011 a Computer Program for Analysis of Structures Subjected to Fire. *University of Liege, Belgium* (see p. 21).

Fukuchi, N., Okada, K., and Sugita, N. (2006). An elastic–plastic analysis of large deflection of thin shell structure using a delta-sequence function. *Thin-Walled Structures* **44**(1): 91–101 (see p. 126).

GhannadPour, S. and Alinia, M. (2006). Large deflection behavior of functionally graded plates under pressure loads. *Composite Structures* **75**(1): 67–71 (see p. 110).

Ghugal, D. Y. M. and Kulkarni, S. (2011). Thermal stress analysis of cross-ply laminated plates using refined shear deformation theory. *Journal of Experimental & Applied Mechanics* **2**(1) (see p. 110).

Gillie, M., Usmani, A. S., and Rotter, J. M. (2002). A structural analysis of the Cardington British steel corner test. *Journal of Constructional Steel Research* **58**(4): 427–442 (see p. 3).

Gillie, M., Usmani, A., and Rotter, M. (2004). Bending and membrane action in concrete slabs. *Fire and Materials* **28**(2-4): 139–157 (see p. 3).

He, X.-T., Chen, Q., Sun, J.-Y., and Zheng, Z.-L. (2012). Large-deflection axisymmetric deformation of circular clamped plates with different moduli in tension and compression. *International Journal of Mechanical Sciences* **62**(1): 103–110 (see p. 68).

Herrera, I. (1977). General variational principles applicable to the hybrid element method. *Proceedings of the National Academy of Sciences* **74**(7): 2595–2597 (see p. 174).

Heuer, R. and Ziegler, F. (2004). Thermoelastic stability of layered shallow shells. *International Journal of Solids and Structures* **41**(8): 2111–2120 (see p. 127).

Hill, R. (1965). A self-consistent mechanics of composite materials. *Journal of the Mechanics and Physics of Solids* **13**(4): 213–222 (see p. 17).

Hinton, E and Huang, H. (1986). A family of quadrilateral Mindlin plate elements with substitute shear strain fields. *Computers & Structures* **23**(3): 409–431 (see p. 66).

Huang, H.-C. and Usmani, A. S. (1994). *Finite Element Analysis for Heat Transfer*. Springer (see pp. 60, 160).

Huang, Z., Burgess, I. W., and Plank, R. J. (1999). Nonlinear analysis of reinforced concrete slabs subjected to fire. *ACI Structural Journal* **96**(1) (see p. 97).

Huang, Z., Burgess, I. W., and Plank, R. J. (2003a). Modeling membrane action of concrete slabs in composite buildings in fire. I: Theoretical development. *Journal of Structural Engineering* (see p. 98).

Huang, Z., Burgess, I. W., and Plank, R. J. (2003b). Modeling membrane action of concrete slabs in composite buildings in fire. II: Validations. *Journal of Structural Engineering* **129**(8): 1103–1112 (see p. 98).

Hughes, T. J., Taylor, R. L., and Kanoknukulchai, W. (1977). A simple and efficient finite element for plate bending. *International Journal for Numerical Methods in Engineering* **11**(10): 1529–1543 (see p. 66).

Hui, W. and Qinghua, Q. (2007). Some problems with the method of fundamental solution using radial basis functions. *Acta Mechanica Solida Sinica* **20**(1): 21–29 (see p. 176).

Ibrahimbegović, A. (1993). Quadrilateral finite elements for analysis of thick and thin plates. *Computer Methods in Applied Mechanics and Engineering* **110**(3): 195–209 (see p. 66).

Imam, B and Chryssanthopoulos, M. (2010). A review of metallic bridge failure statistics. in: *Bridge Maintenance, Safety and Management: Proceedings of the Fifth International IABMAS Conference*, pp. 3275–3282 (see p. 2).

Iyengar, K. S. R. and Naqvi, M. M. (1966). Large deflections of rectangular plates. *International Journal of Non-Linear Mechanics* **1**(2): 109–122 (see p. 66).

Izzuddin, B. (1996). Quartic formulation for elastic beam-columns subject to thermal effects. *Journal of Engineering Mechanics* **122**(9): 861–871 (see p. 21).

Jang, T. (2013). A new semi-analytical approach to large deflections of Bernoulli–Euler-v. Karman beams on a linear elastic foundation: nonlinear analysis of infinite beams. *International Journal of Mechanical Sciences* **66**: 22–32 (see p. 44).

Javaheri, R and Eslami, M. (2002). Thermal buckling of functionally graded plates. *AIAA Journal* **40**(1): 162–169 (see p. 17).

Jayakumar, K, Yadav, D, and Nageswara Rao, B (2013). Moderately large deflection analysis of simply supported piezo-laminated composite plates under uniformly distributed transverse load. *International Journal of Non-Linear Mechanics* **49**: 137–144 (see p. 77).

Je˛kot, T. (1996). Nonlinear problems of thermal postbuckling of a beam. *Journal of Thermal Stresses* **19**(4): 359–367 (see p. 42).

Jeffers, A. E. (2013). Heat transfer element for modeling the thermal response of non-uniformly heated plates. *Finite Elements in Analysis and Design* **63**: 62–68 (see p. 145).

Jeffers, A. E. (2015). Triangular shell heat transfer element for the thermal analysis of nonuniformly heated structures. *Journal of Structural Engineering*: 04015084 (see p. 145).

Jeffers, A. E. and Beata, P. A. (2014). Generalized shell heat transfer element for modeling the thermal response of non-uniformly heated structures. *Finite Elements in Analysis and Design* **83**: 58–67 (see p. 145).

Jeyaraj, P (2013). Buckling and free vibration behavior of an isotropic plate under nonuniform thermal load. *International Journal of Structural Stability and Dynamics* **13**(03) (see p. 100).

Jiang, J. and Usmani, A. (2013). Modeling of steel frame structures in fire using OpenSees. *Computers & Structures* **118**: 90–99 (see p. 21).

Jiang, J., Khazaeinejad, P., and Usmani, A. (2012). Nonlinear analysis of shell structures in fire using OpenSees. in: *Proceedings of the 20th UK Conference of the Association for Computational Mechanics in Engineering (ACME2012)*. Manchester, UK (see p. 21).

Jiang, J., Usmani, A., and Li, G.-Q. (2014). Modelling of steel-concrete composite structures in fire using OpenSees. *Advances in Structural Engineering* **17**(2): 249–264 (see p. 21).

Jin, L. J., Oh, I.-K., Lee, I., and Yeom, C. H. (2002). Thermal post-buckling behavior of patched laminated panels under uniform and non-uniform temperature distributions. *Composite Structures* **55**(2): 137–145 (see p. 146).

Jirousek, J. (1978). Basis for development of large finite elements locally satisfying all field equations. *Computer Methods in Applied Mechanics and Engineering* **14**(1): 65–92 (see pp. 174, 175).

Jirousek, J. and Leon, N. (1977). A powerful finite element for plate bending. *Computer Methods in Applied Mechanics and Engineering* **12**(1): 77–96 (see pp. 174, 175).

Johansen, K. W. (1962). *Yield-Line Theory*. London, UK: Cement and Concrete Association (see p. 3).

Kaju, K. K. and Venkateswara Kao, G (1984). Thermal postbuckling behavior of tapered columns. *AIAA Journal* **22**(10): 1499–1501 (see p. 42).

Kanaka Raju, K and Venkateswara Rao, G (1993). Thermal postbuckling of uniform columns on elastic foundation. *Journal of Engineering Mechanics* **119**(3): 626–629 (see p. 42).

Katili, I. (1993a). A new discrete Kirchhoff-Mindlin element based on Mindlin–Reissner plate theory and assumed shear strain fields–part II: An extended DKQ element for thick-plate bending analysis. *International Journal for Numerical Methods in Engineering* **36**(11): 1885–1908 (see p. 66).

Katili, I. (1993b). A new discrete Kirchhoff-Mindlin element based on Mindlin-Reissner plate theory and assumed shear strain fields–part I: An extended DKT element for thick-plate bending analysis. *International Journal for Numerical Methods in Engineering* **36**(11): 1859–1883 (see p. 66).

Katsikadelis, J. and Tsiatas, G. (2003). Large deflection analysis of beams with variable stiffness. *Acta Mechanica* **164**(1-2): 1–13 (see p. 43).

Khandan, R., Noroozi, S., Sewell, P., and Vinney, J. (2012). The development of laminated composite plate theories: A review. *Journal of Materials Science* **47**(16): 5901–5910 (see p. 99).

Khazaeinejad, P and Najafizadeh, M. (2010). Mechanical buckling of cylindrical shells with varying material properties. *Proceedings of the Institution of Mechanical Engineers, Part C: Journal of Mechanical Engineering Science* **224**(8): 1551–1557 (see p. 17).

Khazaeinejad, P and Usmani, A. (2016a). On thermo-mechanical nonlinear behaviour of shallow shells. *International Journal of Non-Linear Mechanics*: in press (see p. 126).

Khazaeinejad, P and Usmani, A. (2016b). Temperature-dependent nonlinear response of shallow shells: A theoretical approach. *Composite Structures*: in press (see p. 145).

Khazaeinejad, P and Usmani, A. S. (2014). Analytical solutions for nonlinear response of plates under thermal loading. in: *Proceedings of the 8th International Conference on Structures in Fire (SiF'14)*. Shanghai, China (see p. 97).

Khazaeinejad, P, Najafizadeh, M., Jenabi, J, and Isvandzibaei, M. (2010). On the buckling of functionally graded cylindrical shells under combined external pressure and axial compression. *Journal of Pressure Vessel Technology* **132**(6): 064501 (see p. 17).

Khazaeinejad, P, Usmani, A. S., and Laghrouche, O (2012). Nonlinear stress analysis of plates under thermo-mechanical loads. in: *Journal of Physics: Conference Series*. Vol. 382. IOP Publishing, p. 012022 (see p. 66).

Khazaeinejad, P, Usmani, A., and Laghrouche, O (2014). An analytical study of the nonlinear thermo-mechanical behaviour of thin isotropic rectangular plates. *Computers & Structures* **141**: 1–8 (see p. 66).

Khazaeinejad, P, Usmani, A., and Laghrouche, O (2015). Temperature-dependent nonlinear behaviour of thin rectangular plates exposed to through-depth thermal gradients. *Composite Structures* **132**: 652–664 (see pp. 14, 97).

Khorasani, N. E., Garlock, M. E., and Quiel, S. E. (2015). Modeling steel structures in OpenSees: Enhancements for fire and multi-hazard probabilistic analyses. *Computers & Structures* **157**: 218–231 (see p. 21).

Kim, K.-D., Lomboy, G. R., and Han, S.-C. (2008). Geometrically non-linear analysis of Functionally Graded Material (FGM) plates and shells using a four-node quasi-conforming shell element. *Journal of composite materials* **42**(5): 485–511 (see p. 147).

Kim, N. (2015). *Introduction to Nonlinear Finite Element Analysis*. New York: Springer (see p. 13).

Kirchhoff, G. (1850). Über das gleichgewichi und die bewegung einer elasishem scheibe. *Journal Fuer die Reine und Angewandte Mathematik* **49**: 51–88 (see p. 29).

Koizumi, M. (1997). FGM activities in Japan. *Composites Part B: Engineering* **28**(1): 1–4 (see p. 16).

Krenk, S. (2001). *Mechanics and Analysis of Beams, Columns and Cables: A Modern Introduction to the Classic Theories*. Springer Science & Business Media (see p. 26).

Lee, S. and Reddy, J. (2005). Non-linear response of laminated composite plates under thermomechanical loading. *International Journal of Non-Linear Mechanics* **40**(7): 971–985 (see p. 98).

Lee, S. and Wong, S. (1982). Mixed formulation finite elements for Mindlin theory plate bending. *International Journal for Numerical Methods in Engineering* **18**(9): 1297–1311 (see p. 66).

Levy, S. (1942). *Bending of Rectangular Plates with Large Deflections*. Tech. rep. Washington, DC: NACA (see pp. 66, 77).

Li, Q., Liu, J., and Xiao, H. (2004). A new approach for bending analysis of thin circular plates with large deflection. *International Journal of Mechanical Sciences* **46**(2): 173–180 (see p. 76).

Li, S.-R., Zhang, J.-H., and Zhao, Y.-G. (2007). Nonlinear thermomechanical post-buckling of circular FGM plate with geometric imperfection. *Thin-Walled Structures* **45**(5): 528–536 (see p. 99).

Li, S. and Zhou, Y. (2003). Geometrically nonlinear analysis of Timoshenko beams under thermomechanical loadings. *Journal of Thermal Stresses* **26**(9): 861–872 (see p. 43).

Li, S., Zhou, Y.-H., and Zheng, X. (2002). Thermal post-buckling of a heated elastic rod with pinned-fixed ends. *Journal of Thermal Stresses* **25**(1): 45–56 (see p. 43).

Lin, R., Lim, M., and Du, H (1994). Large deflection analysis of plates under thermal loading. *Computer Methods in Applied Mechanics and Engineering* **117**(3): 381–390 (see p. 69).

Ling, C. S. and Surana, K. (1994). *p*-Version least squares finite element formulation for axisymmetric heat conduction with temperature-dependent thermal conductivities. *Computers & Structures* **52**(2): 353–364 (see p. 145).

Love, A. E. H. (1888). The small free vibrations and deformation of a thin elastic shell. *Philosophical Transactions of the Royal Society of London. A*: 491–546 (see p. 29).

Luo, A. C. (2000). An approximate theory for geometrically nonlinear thin plates. *International Journal of Solids and Structures* **37**(51): 7655–7670 (see p. 68).

Ma, L. and Wang, T. (2003). Nonlinear bending and post-buckling of a functionally graded circular plate under mechanical and thermal loadings. *International Journal of Solids and Structures* **40**(13): 3311–3330 (see pp. 69, 99).

Madhukar, S and Singha, M. (2013). Geometrically nonlinear finite element analysis of sandwich plates using normal deformation theory. *Composite Structures* **97**: 84–90 (see p. 99).

Marguerre, K (1938). Zur theorie der gekrümmten platte grosser formänderung. in: *Proceedings of the 5th International Congress for Applied Mechanics*, pp. 93–101 (see p. 35).

Martin, D and Moore, D (1999). *The Behaviour of Multi-Storey Steel Framed Buildings in Fire*. European Joint Research Programme Cardington Test Report. British Steel PLC Rotherham, UK (see p. 97).

Matsunaga, H. (2009). Stress analysis of functionally graded plates subjected to thermal and mechanical loadings. *Composite Structures* **87**(4): 344–357 (see p. 110).

Mindlin, R. (1951). Influence of rotatory inertia and shear on flexural motions of isotropic, elastic plates. *ASME Journal of Applied Mechancis* **18**: 31–38 (see pp. 29, 110).

Mohamed, M. S., Seaid, M., Trevelyan, J., and Laghrouche, O. (2013). Time-independent hybrid enrichment for finite element solution of transient conduction–radiation in diffusive grey media. *Journal of Computational Physics* **251**: 81–101 (see p. 3).

Mori, T and Tanaka, K (1973). Average stress in matrix and average elastic energy of materials with misfitting inclusions. *Acta Metallurgica* **21**(5): 571–574 (see p. 17).

Na, K.-S. and Kim, J.-H. (2006). Nonlinear bending response of functionally graded plates under thermal loads. *Journal of Thermal Stresses* **29**(3): 245–261 (see p. 99).

Najafizadeh, M., Hasani, A, and Khazaeinejad, P (2009). Mechanical stability of functionally graded stiffened cylindrical shells. *Applied Mathematical Modelling* **33**(2): 1151–1157 (see p. 17).

Najafizadeh, M., Mahdavian, M, and Khazaeinejad, P (2010). Superposition buckling analysis of rectangular plates composed of functionally graded materials subjected to non-uniform distributed in-plane loading. *Proceedings of the Institution of Mechanical Engineers, Part C: Journal of Mechanical Engineering Science* **224**(11): 2299–2307 (see p. 17).

Navazi, H. and Haddadpour, H (2008). Nonlinear cylindrical bending analysis of shear deformable functionally graded plates under different loadings using analytical methods. *International Journal of Mechanical Sciences* **50**(12): 1650–1657 (see p. 99).

Nie, G. (2003). Analysis of non-linear behaviour of imperfect shallow spherical shells on pasternak foundation by the asymptotic iteration method. *International Journal of Pressure Vessels and Piping* **80**(4): 229–235 (see p. 127).

Oberkampf, W. L., Sindir, M., and Conlisk, A. (1998). Guide for the verification and validation of computational fluid dynamics simulations. *American Institute of Aeronautics and Astronautics* (see p. 22).

Olszak, W. (1980). *Thin Shell Theory: New Trends and Applications*. Springer (see p. 35).

Oñate, E., Zienkiewicz, O., Suarez, B, and Taylor, R. (1992). A general methodology for deriving shear constrained Reissner-Mindlin plate elements. *International Journal for Numerical Methods in Engineering* **33**(2): 345–367 (see p. 66).

Plaut, R. H. (2014). A generalized reissner theory for large axisymmetric deflections of circular plates. *Journal of Applied Mechanics* **81**(3): 034502 (see p. 66).

Qatu, M. S. (2004). *Vibration of Laminated Shells and Plates*. Elsevier (see p. 36).

Qin, Q. (1994). Hybrid Trefftz finite-element approach for plate bending on an elastic foundation. *Applied Mathematical Modelling* **18**(6): 334–339 (see p. 67).

Qin, Q. (1995). Postbuckling analysis of thin plates by a hybrid Trefftz finite element method. *Computer Methods in Applied Mechanics and Engineering* **128**(1): 123–136 (see p. 67).

Qin, Q. (1996a). Nonlinear analysis of thick plates by HT FE approach. *Computers & Structures* **61**(2): 271–281 (see p. 67).

Qin, Q. and Diao, S (1996). Nonlinear analysis of thick plates on an elastic foundation by HT FE with *p*-extension capabilities. *International Journal of Solids and Structures* **33**(30): 4583–4604 (see p. 67).

Qin, Q.-H. (1996b). New algorithms for transient plate bending analysis by BEM. *Engineering Analysis with Boundary Elements* **17**: 175–180 (see p. 171).

Qin, Q.-H. (1996c). Transient plate bending analysis by hybrid Trefftz element approach. *Communications in Numerical Methods in Engineering* **12**(10): 609–616 (see p. 171).

Qin, Q. H. (1997). Postbuckling analysis of thin plates on an elastic foundation by HT FE approach. *Applied Mathematical Modelling* **21**(9): 547–556 (see p. 67).

Qin, Q.-H. (2000). *The Trefftz Finite and Boundary Element Method*. Wit Press (see p. 3).

Qin, Q.-H. (2005a). Formulation of hybrid Trefftz finite element method for elastoplasticity. *Applied Mathematical Modelling* **29**(3): 235–252 (see p. 175).

Qin, Q.-H. (2005b). Trefftz finite element method and its applications. *Applied Mechanics Reviews* **58**(5): 316–337 (see pp. 3, 174, 175).

Qin, Q. H. and Wang, H. (2013). Special circular hole elements for thermal analysis in cellular solids with multiple circular holes. *International Journal of Computational Methods* **10**(04) (see p. 177).

Reddy, J. (2000). Analysis of functionally graded plates. *International Journal for Numerical Methods in Engineering* **47**(1-3): 663–684 (see p. 17).

Reddy, J. and Chin, C. (1998). Thermomechanical analysis of functionally graded cylinders and plates. *Journal of Thermal Stresses* **21**(6): 593–626 (see p. 19).

Reddy, J. N. (2004). *Mechanics of Laminated Composite Plates and Shells: Theory and Analysis*. CRC press (see p. 87).

Reissner, E. (1945). The effect of transverse shear deformation on the bending of elastic plates. *ASME Journal of Applied Mechanics* **12**(2): 69–77 (see p. 29).

Reissner, E. (1946). Stresses and small displacements of shallow spherical shells. *Journal of Mathematics and Physics* **25**(4): 279–300 (see p. 35).

Rezaiee-Pajand, M. and Karkon, M. (2014). Two higher order hybrid-Trefftz elements for thin plate bending analysis. *Finite Elements in Analysis and Design* **85**: 73–86 (see p. 175).

Sabik, A and Kreja, I (2013). Large thermo-elastic displacement and stability FEM analysis of multilayered plates and shells. *Thin-Walled Structures* **71**: 119–133 (see pp. 100, 127).

Salminen, M. and Heinisuo, M. (2014). Numerical analysis of thin steel plates loaded in shear at non-uniform elevated temperatures. *Journal of Constructional Steel Research* **97**: 105–113 (see p. 100).

Sepahi, O, Forouzan, M., and Malekzadeh, P (2010). Large deflection analysis of thermo-mechanical loaded annular FGM plates on nonlinear elastic foundation via DQM. *Composite Structures* **92**(10): 2369–2378 (see p. 99).

Shadi Mohamed, M, Seaid, M., Trevelyan, J., and Laghrouche, O. (2013). A partition of unity FEM for time-dependent diffusion problems using multiple enrichment functions. *International Journal for Numerical Methods in Engineering* **93**(3): 245–265 (see pp. 178, 179).

Shen, H.-S. (2002a). Postbuckling analysis of axially loaded functionally graded cylindrical panels in thermal environments. *International Journal of Solids and Structures* **39**(24): 5991–6010 (see p. 146).

Shen, H.-S. (2002b). Postbuckling analysis of axially-loaded functionally graded cylindrical shells in thermal environments. *Composites Science and Technology* **62**(7): 977–987 (see p. 146).

Shen, H.-S. (2003). Postbuckling analysis of pressure-loaded functionally graded cylindrical shells in thermal environments. *Engineering Structures* **25**(4): 487–497 (see p. 146).

Shen, H.-S. (2004). Thermal postbuckling behavior of functionally graded cylindrical shells with temperature-dependent properties. *International Journal of Solids and Structures* **41**(7): 1961–1974 (see p. 146).

Shen, H.-S. (2007). Thermal postbuckling behavior of shear deformable FGM plates with temperature-dependent properties. *International Journal of Mechanical Sciences* **49**(4): 466–478 (see p. 99).

Shen, H.-S. and Wang, Z.-X. (2010). Nonlinear bending of FGM plates subjected to combined loading and resting on elastic foundations. *Composite Structures* **92**(10): 2517–2524 (see p. 111).

Shepherd, P. G. and Burgess, I. (2011). On the buckling of axially restrained steel columns in fire. *Engineering Structures* **33**(10): 2832–2838 (see p. 43).

Shirong, L. and Changjun, C. (2000). Analysis of thermal post-buckling of heated elastic rods. *Applied Mathematics and Mechanics* **21**(2): 133–140 (see p. 43).

Shukla, K. and Nath, Y (2000). Nonlinear analysis of moderately thick laminated rectangular plates. *Journal of Engineering Mechanics* **126**(8): 831–838 (see p. 99).

Singha, M., Prakash, T, and Ganapathi, M (2011). Finite element analysis of functionally graded plates under transverse load. *Finite elements in Analysis and Design* **47**(4): 453–460 (see p. 99).

Sladek, J and Sladek, V (2003). A meshless method for large deflection of plates. *Computational Mechanics* **30**(2): 155–163 (see p. 67).

Sladek, J, Sladek, V, Zhang, C., and Solek, P (2008a). Static and dynamic analysis of shallow shells with functionally graded and orthotropic material properties. *Mechanics of Advanced Materials and Structures* **15**(2): 142–156 (see pp. 127, 134, 158).

Sladek, J, Sladek, V, Solek, P, Wen, P., and Atluri, S. (2008b). Thermal analysis of Reissner-Mindlin shallow shells with FGM properties by the MLPG. *CMES: Computer Modeling in Engineering & Sciences* **30**(2): 77–97 (see p. 140).

Sladek, J, Sladek, V, Solek, P, and Wen, P. (2008c). Thermal bending of Reissner-Mindlin plates by the MLPG. *CMES: Computer Modeling in Engineering & Sciences* **28**(1): 57–76 (see p. 67).

Sladek, J, Sladek, V, Krahulec, S, and Pan, E (2013). The MLPG analyses of large deflections of magnetoelectroelastic plates. *Engineering Analysis with Boundary Elements* **37**(4): 673–682 (see p. 67).

Sofiyev, A. and Kuruoglu, N (2013). Buckling analysis of nonhomogeneous orthotropic thin-walled truncated conical shells in large deformation. *Thin-Walled Structures* **62**: 131–141 (see p. 148).

Soh, A., ZhiFei, L, and Song, C (1999). A Mindlin plate triangular element with improved interpolation based on Timoshenko's beam theory. *Communications in Numerical Methods in Engineering* **15**(7): 527–532 (see p. 66).

Sokolinsky, V. S., Shen, H., Vaikhanski, L., and Nutt, S. R. (2003). Experimental and analytical study of nonlinear bending response of sandwich beams. *Composite Structures* **60**(2): 219–229 (see p. 43).

Standards Australia (1998). *Steel Structures, AS4100*. Sydney, Australia (see p. 14).

Standards Australia (2001). *Concrete Structures, AS3600*. Sydney, Australia (see p. 14).

Stern-Gottfried, J. and Rein, G. (2012). Travelling fires for structural design-Part II: Design methodology. *Fire Safety Journal* **54**: 96–112 (see p. 6).

Sun, R., Huang, Z., and Burgess, I. W. (2012). Progressive collapse analysis of steel structures under fire conditions. *Engineering Structures* **34**: 400–413 (see p. 68).

Surana, K. and Orth, N. (1991). *p*-Version hierarchical three dimensional curved shell element for heat conduction. *Computational Mechanics* **7**(5-6): 341–353 (see p. 145).

Sze, K., Liu, X., and Lo, S. (2004). Popular benchmark problems for geometric nonlinear analysis of shells. *Finite Elements in Analysis and Design* **40**(11): 1551–1569 (see pp. 44, 126).

Talamona, D. and Franssen, J.-M. (2005). A quadrangular shell finite element for concrete and steel structures subjected to fire. *Journal of Fire Protection Engineering* **15**(4): 237–264 (see p. 145).

Taylor, R. L. and Auricchio, F. (1993). Linked interpolation for Reissner-Mindlin plate elements: Part II–A simple triangle. *International Journal for Numerical Methods in Engineering* **36**(18): 3057–3066 (see p. 66).

Thai, H.-T. and Kim, S.-E. (2015). A review of theories for the modeling and analysis of functionally graded plates and shells. *Composite Structures* **128**: 70–86 (see p. 100).

Timoshenko, S. and Woinowsky-Krieger, S. (1959). *Theory of Plates and Shells*. Vol. 2. McGraw-hill New York (see pp. 30, 66, 75, 77–79).

Touloukian, Y. (1967). *Thermophysical Properties of High Temperature Solid Materials*. New York: MacMillan (see pp. 19, 20).

Trefftz, E. (1926). Ein gegenstuck zum ritzschen verfahren. in: *Proceedings of the 2nd International Congress of Applied Mechanics*. Zurich, Switzerland, pp. 131–137 (see p. 173).

Tsiatas, G. (2010). Nonlinear analysis of non-uniform beams on nonlinear elastic foundation. *Acta Mechanica* **209**(1-2): 141–152 (see p. 43).

Usmani, A. and Cameron, N. (2004). Limit capacity of laterally restrained reinforced concrete floor slabs in fire. *Cement and Concrete Composites* **26**(2): 127–140 (see pp. 90, 91, 98).

Usmani, A., Drysdale, D., Rotter, J., Sanad, A., Gillie, M, Lamont, S, O'Connor, M., O'Callaghan, D, Elghazouli, A., Izzuddin, B., Richardson, A., Bailey, C., and Newman, G. (2000). *Behaviour of Steel Framed Structures Under Fire Conditions*. Tech. rep. School of Civil and Environmental Engineering, The University of Edinburgh (see pp. 3, 4, 125).

Usmani, A., Rotter, J., Lamont, S, Sanad, A., and Gillie, M (2001). Fundamental principles of structural behaviour under thermal effects. *Fire Safety Journal* **36**(8): 721–744 (see pp. 44, 53).

Usmani, A., Chung, Y., and Torero, J. L. (2003). How did the WTC towers collapse: A new theory. *Fire Safety Journal* **38**(6): 501–533 (see pp. 5, 60, 160).

Vel, S. S. and Batra, R. (2002). Exact solution for thermoelastic deformations of functionally graded thick rectangular plates. *AIAA Journal* **40**(7): 1421–1433 (see p. 16).

Venkateswara Rao, G and Kanaka Ruju, K (1984). Thermal postbuckling of columns. *AIAA Journal* **22**(6): 850–851 (see p. 42).

von Kármán, T (1910). Festigkeitsprobleme im Maschinenbau. *Encyclopädie der Mathematischen Wissenschaften* **4**: 311–385 (see p. 29).

Vörös, G. (1992). Application of the hybrid-Trefftz finite element model to thin shell analysis. *Periodica Polytechnica, Mechanical Engineering* **36**(1-2): 23–40 (see p. 175).

Vu-Quoc, L, Deng, H, and Tan, X. (2000). Geometrically-exact sandwich shells: The static case. *Computer Methods in Applied Mechanics and Engineering* **189**(1): 167–203 (see p. 145).

Vu-Quoc, L, Deng, H, and Tan, X. (2001). Geometrically exact sandwich shells: The dynamic case. *Computer Methods in Applied Mechanics and Engineering* **190**(22): 2825–2873 (see p. 145).

Wang, D. and El-Sheikh, A. (2005). Large-deflection mathematical analysis of rectangular plates. *Journal of Engineering Mechanics* **131**(8): 809–821 (see pp. 69, 77, 79, 86–88).

Wang, H. and Qin, Q.-H. (2009). Hybrid FEM with fundamental solutions as trial functions for heat conduction simulation. *Acta Mechanica Solida Sinica* **22**(5): 487–498 (see p. 176).

Wang, H. and Qin, Q.-H. (2010a). Fundamental-solution-based finite element model for plane orthotropic elastic bodies. *European Journal of Mechanics-A/Solids* **29**(5): 801–809 (see p. 176).

Wang, H. and Qin, Q.-H. (2010b). *Fundamental Solution-Based Hybrid Finite Element Analysis for Non-Linear Minimal Surface Problems*. WIT Press, p. 309 (see p. 176).

Wang, H. and Qin, Q.-H. (2011). Fundamental-solution-based hybrid FEM for plane elasticity with special elements. *Computational Mechanics* **48**(5): 515–528 (see p. 177).

Wang, H. and Qin, Q.-H. (2012a). A fundamental solution-based finite element model for analyzing multi-layer skin burn injury. *Journal of Mechanics in Medicine and Biology* **12**(05) (see p. 177).

Wang, H. and Qin, Q.-H. (2012b). A new special element for stress concentration analysis of a plate with elliptical holes. *Acta Mechanica* **223**(6): 1323–1340 (see p. 177).

Wang, H., Qin, Q.-H., and Arounsavat, D. (2007). Application of hybrid Trefftz finite element method to non-linear problems of minimal surface. *International Journal for Numerical Methods in Engineering* **69**(6): 1262–1277 (see p. 175).

Wang, H., Cao, L., and Qin, Q.-H. (2012a). Hybrid graded element model for nonlinear functionally graded materials. *Mechanics of Advanced Materials and Structures* **19**(8): 590–602 (see p. 177).

Wang, H., Qin, Q.-H., and Liang, X.-P. (2012b). Solving the nonlinear Poisson-type problems with F-Trefftz hybrid finite element model. *Engineering Analysis with Boundary Elements* **36**(1): 39–46 (see p. 177).

Wang, H., Qin, Q.-H., and Han, M.-Y. (2014). Hybrid finite element simulation for bioheat transfer in the human eye. *Ophthalmological Imaging and Applications*: 409 (see p. 3).

Wang, W.-Y., Li, G.-Q., and Kodur, V. (2012c). Approach for modeling fire insulation damage in steel columns. *Journal of Structural Engineering* **139**(4): 491–503 (see p. 44).

Wen, P. and Hon, Y. (2007). Geometrically nonlinear analysis of Reissner-Mindlin plate by meshless computation. *Computer Modeling in Engineering and Sciences* **21**(3): 177–191 (see p. 67).

Wen, P., Aliabadi, M., and Young, A (2005). Large deflection analysis of Reissner plate by boundary element method. *Computers & Structures* **83**(10): 870–879 (see p. 67).

Wen, P., Aliabadi, M., and Young, A (2006). Post buckling analysis of Reissner plates by the boundary element method. *The Journal of Strain Analysis for Engineering Design* **41**(3): 239–252 (see p. 67).

Woo, J and Meguid, S. (2001). Nonlinear analysis of functionally graded plates and shallow shells. *International Journal of Solids and structures* **38**(42): 7409–7421 (see pp. 76, 145).

Yang, J, Liew, K., Wu, Y., and Kitipornchai, S (2006). Thermo-mechanical post-buckling of FGM cylindrical panels with temperature-dependent properties. *International Journal of Solids and Structures* **43**(2): 307–324 (see p. 146).

Yanga, J and Shen, H.-S. (2003). Non-linear analysis of functionally graded plates under transverse and in-plane loads. *International Journal of Non-Linear Mechanics* **38**(4): 467–482 (see p. 99).

Zhang, D.-G. (2015). Nonlinear static analysis of FGM infinite cylindrical shallow shells based on physical neutral surface and high order shear deformation theory. *Applied Mathematical Modelling* **39**(5): 1587–1596 (see p. 148).

Zhang, H. and Kuang, J. (2007). Eight-node Reissner–Mindlin plate element based on boundary interpolation using Timoshenko beam function. *International Journal for Numerical Methods in Engineering* **69**(7): 1345–1373 (see p. 66).

Zhang, Y. and Yang, C. (2009). Recent developments in finite element analysis for laminated composite plates. *Composite Structures* **88**(1): 147–157 (see p. 98).

Zhang, Z. W., Wang, H., and Qin, Q. H. (2014). Analysis of transient bioheat transfer in the human eye using hybrid finite element model. *Applied Mechanics and Materials* **553**: 356–361 (see p. 177).

Zhao, X, Liu, G., Dai, K., Zhong, Z., Li, G., and Han, X (2008). Geometric nonlinear analysis of plates and cylindrical shells via a linearly conforming radial point interpolation method. *Computational Mechanics* **42**(1): 133–144 (see p. 68).

Zhao, X. and Liew, K. M. (2009). Geometrically nonlinear analysis of functionally graded shells. *International Journal of Mechanical Sciences* **51**(2): 131–144 (see p. 147).

Zienkiewicz, O., Taylor, R., and Too, J. (1971). Reduced integration technique in general analysis of plates and shells. *International Journal for Numerical Methods in Engineering* **3**(2): 275–290 (see p. 66).

Zienkiewicz, O. C., Xu, Z., Zeng, L. F., Samuelsson, A., and Wiberg, N.-E. (1993). Linked interpolation for Reissner-Mindlin plate elements: Part I–A simple quadrilateral. *International Journal for Numerical Methods in Engineering* **36**(18): 3043–3056 (see p. 66).